Investigation of Crystal Structures and Ultra-Low Thermal Conductivities in Novel Group 14 and 15 Chalcogenides

by

Luke T. Menezes

A thesis

presented to the University of Waterloo

in fulfillment of the

thesis requirement for the degree of

Doctor of Philosophy

in

Chemistry

Waterloo, Ontario, Canada, 2023

Examining Committee Membership

The following served on the Examining Committee for this thesis. The decision of the Examining Committee is by majority vote.

External Examiner	Andrew Grosvenor Professor (University of Saskatchewan)
Supervisor(s)	Holger Kleinke Professor (University of Waterloo)
Internal Members	Pavle Radovanovic Professor (University of Waterloo)
Internal-external member	Will Percival Professor (University of Waterloo)
Other Member(s)	Kathryn Preuss Professor (University of Guelph)

Author's Declaration

I hereby declare that I am the sole author of this thesis. This is a true copy of the thesis including any required final revisions, as accepted by my examiners. I understand that my thesis may be made electronically available to the public.

Abstract

The crystal structures and physical properties of several new group 14 and 15 chalcogenides are discussed in this thesis. The thesis discusses the chalcoantimonates $TlLa_2Sb_3Se_9$ and $La_{12+z}Sb_{9-y}Se_{38-z}$ (simplified as $La_{12}Sb_9Se_{38}$). $TlLa_2Sb_3Se_9$ crystallizes in an ordered variant of the $KLa_2Sb_3S_9$ structure type (space group = $P2_12_12_1$). The thermoelectric properties of $TlLa_2Sb_3Se_9$ were enhanced through *p*-type doping by replacing La^{3+} with Ca^{2+}. The largest thermoelectric figure-of-merit was 0.078 at 623 K in the $TlLa_{0.95}Ca_{0.05}Sb_3Se_9$ sample.

The $La_{12}Sb_9Se_{38}$ ($Pm\bar{3}$) structure type features La^{3+}/Sb^{3+} disorder and S^{2-}/S_2^{2-} disorder, making it possible to produce nonstoichiometric compounds within a narrow phase width. The low thermal conductivities of samples with the nominal compositions $La_{12.17}Sb_{8.5}S_{38}$ and $La_{12.17}Sb_{8.5}S_{37.75}$ were around 1 W m^{-1} K^{-1}.

The latter half of this document focusses on Si, Ge, and Sn selenides. $Ba_6Ge_2Se_{12}$ ($P2_1/c$) and $Ba_7Ge_2Se_{17}$ (*Pnma*) adopt new structure types—both possess positional disorder confirmed *via* a single crystal, Rietveld, and pair distribution function models. The $Ba_6Ge_2Se_{12}$ structure contains disordered Se_2^{2-} dumbbells which may align for quasi-infinite 1D chains, whereas the $Ba_7Ge_2Se_{17}$ structure contains disordered $[GeSe_5]^{4-}$ anions. The thermal conductivities of $Ba_6Ge_2Se_{12}$ and $Ba_7Ge_2Se_{17}$ range from 0.3 – 0.4 W m^{-1} K^{-1}.

Substituting Si into the Ge compound $Ba_6Ge_2Se_{12}$ compounded produced the new compound $Ba_6Si_2Se_{12}$ ($P\bar{1}$). Up to 75% of the Si atoms in the $Ba_6Si_2Se_{12}$ structure may be replaced with Ge while preserving the triclinic structure. The Si^{4+}/Ge^{4+} disorder and the positional disorder in the Se_2^{2-} dumbbells were studied using powder X-ray diffraction patterns collected using

synchrotron radiation. The ultra-low thermal conductivity of $Ba_6Si_2Se_{12}$ ranges from 0.3 to 0.5 W m^{-1} K^{-1}.

The final chapters discuss Sr compounds as well as Ba compounds. $Sr_8Ge_4Se_{17}$ ($P\bar{1}$) and $Ba_8Sn_4Se_{17}$ ($C2/c$) share stoichiometries but adopt different structure types. The $Ba_8Sn_4Se_{17}$ unit cell may be regarded as a 2 × 1 × 4 supercell of the $Sr_8Ge_4Se_{17}$ unit cell. The structures of these two compounds were finalized using Rietveld refinements on powder X-ray diffraction data collected using synchrotron radiation, as no disorder was observed in these structures. Despite not having structural disorder, the ultra-low thermal conductivity of $Ba_8Sn_4Se_{17}$ was found to be as low as 0.3 W $m^{-1}K^{-1}$ due to its complex structure.

The final compound discussed is the noncentrosymmetric compound $Sr_6Ge_3OSe_{11}$ ($P3m1$). This chapter explores partial isovalent substitution to design noncentrosymmetric structures by promoting the alignment of $[GeOSe_3]^{4-}$ anions. The second-order nonlinear susceptibilities (d_{il}) of $Sr_6Ge_3OSe_{11}$ were calculated to be d_{15} = -12.9 pm V^{-1}, d_{22} = -15.4 pm V^{-1}, d_{33} = 15.0 pm V^{-1} and d_{eff} = 17.0 pm V^{-1}. Size-dependent second harmonic generation intensity experiments revealed that $Sr_6Ge_3OSe_{11}$ is phase matchable at 1064 nm with an intensity equal to 0.62 × KH_2PO_4.

Acknowledgements

I am immensely grateful to all those who have supported and guided me throughout my journey toward completing this Ph.D. thesis. Their expertise, encouragement, and unwavering dedication have been instrumental in shaping the course of my research and in the realization of this work.

I am deeply grateful to my supervisor, Dr. Holger Kleinke, whose profound insights, unyielding support, and constructive feedback have been indispensable. Your mentorship has enhanced the quality of my research and inspired me to strive for excellence in all aspects of academia.

I would like to express my sincere appreciation to my committee members and examiners, Dr. Linda Nazar, Dr. Pavle Radovanovic, Dr. Rodney Smith, Dr. Andrew Grosvenor, Dr. Kathryn Preuss, and Dr. Will Percival. Your comprehensive evaluation and constructive comments have provided valuable insights for further improvement.

I am grateful to my collaborators, Dr. Abdeljalil Assoud, Dr. Michelle Dolgos, Brooke Richtik, Dr. P. Shiv Halasyamani, and Dr. Mingli Liang, for their expertise and sense of community that has enriched my graduate experience.

Lastly, I am indebted to my parents Elvira and Lino and sister Laura as well as my friends for their unwavering support. I look forward to the future accomplishments of the current group members, especially Madi Donohoe whose capable hands I can pass the reigns to.

Table of Contents

List of Figures

List of Tables

List of Abbreviations

EDS	Electron dispersive X-ray spectroscopy
SEM	Scanning electron microscopy
(s,p)XRD	(Single crystal, powder) X-ray Diffraction
EXAFS	Extended X-ray absorption fine structure
PDF	Pair distribution function
SHG	Second harmonic generation
SFG	Sum frequency generation
DFG	Difference frequency generation
NLO	Nonlinear optics
NCS	Non-centrosymmetric
LDT	Laser damage threshold
AGS	$AgGaS_2$
AGSe	$AgGaSe_2$
ZGP	$ZnGeP_2$
KDP	KH_2PO_4
(N)PM	(Non-) Phase Matching
DFT	Density functional theory
PBE	Perdew–Burke–Ernzerhof exchange-correlation
GGA	Generalized gradient approximation
FP-LAPW	Full-potential linearized augmented plane wave
VASP	Vienna Ab initio Simulation Package
CASTEP	CAmbridge Serial Total Energy Package
SOS	Sum-over-states
LAST	Lead, antimony, silver, tellurium

DSC	Differential scanning calorimetry
TGA	Thermal gravimetric analysis
GUI	Graphical user interface
C.N.	Coordination number
FTIR	Fourier transform infrared spectroscopy
PIAS	Partial isovalent anion substitution
PMT	Photomultiplier tube
ELF	Electron localization function
(Ho,Nd):YAG	(Holmium, Neodymium) Yttrium Aluminum Garnet

List of Symbols

at.-%	Atomic percent
θ	Angle
d	Lattice spacing
λ	Wavelength
$\boldsymbol{n}$	Diffraction order
F (F_c, F_o)	Structure factor (calculated, observed)
R_1	Residual factor (single crystal)
wR_2	Weighted residual factor (single crystal)
y (y_c, y_o)	Intensity (calculated, observed)
R_p	Residual factor (powder profile)
wR_P	Weighted residual factor (powder profile)
Z	Formula units per unit cell
σ (σ_0)	Electrical Conductivity (pre-exponential factor)
S	Seebeck Coefficient
κ (κ_{tot}, κ_{ele}, κ_{lat}, κ_{glass}, κ_{diff})	Thermal conductivity (total, electrical, lattice, amorphous, diffuson)
zT	Dimensionless figure-of-merit
T	Temperature
n	Charge carrier concentration
μ	Charge carrier mobility
e	Elementary charge
ΔV	Voltage difference
ΔT	Temperature difference
D	Thermal diffusivity
C_P	Specific heat

ρ	Density
R	Ideal gas constant
M_{avg}	Average atomic mass
L	Path length
$t_{1/2}$	Thermograph half-maximum time
n	Number density (atoms m^{-3})
k_B	Boltzmann's Constant
v_S	Arithmetic average of the speed of sound
$P(t)$	Polarizability
ε_0	The permittivity of free space
$\chi^{(1)}$	First-order/linear susceptibility
$\chi^{(2)}_{ij}$, d_{ij}	Second-order susceptibility
$E(t)$	Optical field strength
c	Speed of light in a vacuum
v	Speed of light through a medium
n_{ii}	The refractive index in *i*'th axis
ε_{ii}	Dielectric constant in *i*'th axis
ω	Frequency
k	Wave vector
I	Intensity
r	Particle size
E_g, E_F	Band-gap energy, Fermi energy
U_{eq}, U_{ani}, U_{iso}	Equivalent, anisotropic, isotropic atomic displacement parameter
α/S	Absorption/Scattering factor
R	Percent Reflectance
θ_D	Debye temperature

Q_{damp}, Q_{broad}, Q_{max}	Q space resolution effects (dampening, broadening, maximum)
$G_o(r_i)$	Reduced pair distribution function (radial distance)

CHAPTER 1

Introduction

1.1 Chalcogenide Background

Within materials science, researchers have long been fascinated by chalcogenides' remarkable structural diversity and appealing semiconducting properties. These materials have garnered significant interest in nonlinear optics,[1] ferroelectrics,[2,3] and thermoelectric materials.[4] The complex structures formed by the chalcogenides of group 14 and 15 elements give rise to various properties of significant interest. One characteristic of these elements is that they can form various so-called building blocks that can be packed together to form novel structure types. For example, the group 14 element, Ge, can form a variety of polyatomic anions due to its capability to adopt the 4+ and, less commonly, 3+ oxidation states when paired with S or Se. Compounds containing chalco-germanate structural motifs such as $[GeQ_4]^{4-}$ (Q = S, Se), $[GeQ_5]^{4-}$, $[Ge_2Q_5]^{4-}$, $[Ge_2Q_7]^{6-}$, $[Ge_2Q_6]^{6-}$, and $[Ge_4Q_{10}]^{8-}$ have already been observed.[5,6] Se can generate multiple selenide anions, including Se_2^{2-}, Se_3^{2-}, and Se_5^{4-}.[7,8] In contrast to the isolated building blocks of the group 14 elements chalco-antimonates tend to form quasi-infinite edge sharing sheets.[9,10] Additionally, the sterically active lone pair around Sb^{3+} results in Sb^{3+} being able to accommodate a variety of distorted coordination spheres. Despite numerous reported compounds within this phase space, the vast potential for structural diversity within these elements suggests that researchers have only begun to explore the myriad of possible stoichiometries available.

1.2 Motivations

The physical properties of a material are intimately connected to the atomic structure of the material. By understanding and manipulating the structural arrangements of atoms within a crystal lattice, researchers can harness the inherent properties of materials to achieve desired functionalities.

Ultra-low thermal conductivity has garnered significant interest due to its relevance in thermoelectric materials. In the mid-twentieth century, radioisotope batteries were developed, which converted the heat emitted from the decay of radioactive isotopes to electricity.[11] This technology found use in deep-space satellites, which are too far from the Sun to utilize solar panels. More recent applications of thermoelectric generators are present in gadgets powered by body heat,[12–14] cooling systems,[15–18] and sensors.[19,20] The prospective significance of thermoelectric materials may be in the "Internet of Things," a concept that refers to internet-connected electronics and future items embedded with microprocessors.[21] The combination of thermoelectric materials alongside microprocessors enables the creation of devices with extended lifespans that are less dependent on batteries.[22,23]

Thermoelectric materials maintain a temperature gradient by inhibiting heat flow while simultaneously conducting charge carriers through the material. It is well understood that complex structures with large unit cells, such as those found in the skutterudite family, have low thermal conductivities owing to Umklapp scattering and the reduced number of short phonon modes in large unit cells.[24,25] We successfully synthesized several new compounds with novel complex structure types by incorporating large cations with high coordination numbers into compounds with group 14 and 15 structural motifs.

Complex structures have not only found usefulness as thermoelectric materials but also in nonlinear optics. Nonlinear optical materials can convert lasers' frequencies through processes such as second harmonic generation. However, a compound must adopt a noncentrosymmetric crystal structure to be nonlinearly active. The design goals for new nonlinear optical materials are strong second-harmonic generation and a large laser damage threshold. These two goals are at odds in practice since the laser damage threshold is increased by widening the optical band gap. This comes at the cost of second harmonic generation intensity as materials with wider band gaps have greater ionicity and, thus, lower polarizability. In recent years researchers have looked at fluorooxyborates and oxychalcogenides in the ultra-violet (UV) and infrared regions (IR), respectfully to combine large polarizable groups with electronegative elements to minimize tradeoffs.[26–31]

While it is possible to consistently create noncentrosymmetric structures by crystallizing a single enantiomer of a chiral molecule, chemists have focused on synthesizing inorganic compounds for their higher tolerance to laser damage. Additionally, substitutions can be made in existing noncentrosymmetric structure types, such as the chalcopyrite structure (double zincblende), to design new noncentrosymmetric compounds.[7,32–35] Most commercial infrared nonlinear optical materials adopt the chalcopyrite structure but suffer from low laser damage thresholds, leading to continued exploration for competitive alternatives.[36] Since several inorganic compounds have unique structure types, researchers have tried to implement a few strategies to increase the likelihood that their eventual new compound adopts a noncentrosymmetric space group. Strategies to design noncentrosymmetric compounds include using cations which undergo second-order Jahn-Teller distortions, using cations which contain a non-bonding lone pair of electrons, and incorporating NCS building blocks such as tetrahedrally coordinated polyatomic

anions.[37] These factors decrease the local symmetry around a coordinated cation. Second order Jahn-Teller distortions commonly occur in d^0 cations such as Ti^{4+}, V^{5+}, and W^{6+} with non-degenerate ground-states and low-lying excited states. Cations such as Tl^{+}, Pb^{2+}, Bi^{3+}, and Te^{4+} distort neighbouring atoms with a non-bonding lone pair of electrons.[38–41] Finally, pertinent to this work is to include noncentrosymmetric building blocks like trigonal planar and tetrahedral anions. By extension, in recent years, chemists have begun to develop noncentrosymmetric building blocks that contain several anions to create a net polarity to the anion that can align head-to-tail with other like anions and avoid tetrahedra from aligning antiparallel to each other.

1.3 Thesis Overview

The following is an overview of this thesis: Chapter 2, presents a summary of the physical phenomena pertinent to later chapters, including a physical description of thermoelectricity, second harmonic generation, and X-ray diffraction. Concepts such as single-crystal, Rietveld, and pair distribution functions are also described. Further, we discuss the experimental methods used in synthesizing the compounds of interest and the measurements of the physical properties thereof.

Chapter 3 is dedicated to the crystal structure and thermoelectric properties of $TlLa_2Sb_3Se_9$. $TlLa_2Sb_3Se_9$ adopts an ordered variant of the $KLa_2Sb_3S_9$ structure type. $TlLa_2Sb_3Se_9$ is a lustrous grey solid semiconductor with a narrow band gap. We opted to investigate the thermoelectric properties of $TlLa_2Sb_3Se_9$ since it was a candidate to have relatively high intrinsic electrical conductivity and low thermal conductivity due to its narrow band gap and complex structure, respectively. Theoretical investigations of the electronic structure revealed that the electronic bands are relatively flat. This is an indication of low charge carrier mobility through the structure. Initial measurements of the transport properties showed that $TlLa_2Sb_3Se_9$ is a *p*-type

semiconductor with low intrinsic conductivity. To boost the electrical conductivity of $TlLa_2Sb_3Se_9$, we attempted to increase the number of positive charge carriers by doping La^{3+} sites with Ca^{2+} ions. We will show that Ca^{2+} doping increased the thermoelectric figure-of-merit resulting from increased electrical conductivity.

In Chapter 4, the new lanthanum antimony sulphide, $La_{12+x}Sb_{9-y}S_{38-z}$, is introduced. For simplicity, the compounds will be abbreviated as $La_{12}Sb_9S_{38}$. $La_{12}Sb_9S_{38}$ was discovered during exploratory reactions searching for the hypothetical sulphide "$LaSbS_4$." Despite the complex stoichiometry, $La_{12}Sb_9S_{38}$ crystallizes in the highly symmetric cubic space group $Pm\bar{3}$. The structure $La_{12}Sb_9S_{38}$ structure type features a variety of disordered sites, including disordered La/Sb sites and S_2^{2-} dumbbells disordered with lone sulphide ions (S^{2-}). Due to the disorder in the structure, the ratios of La, Sb, and S were altered to explore the narrow phase width of these compounds. Three compounds with the nominal formulas $La_{12.17}Sb_{8.5}S_{37.75}$, $La_{12.17}Sb_{8.5}S_{38}$, and $La_{12}Sb_{8.67}S_{38}$ were synthesized to study the phase width. By dint of the large unit cell and point defects in the structure, $La_{12}Sb_9S_{38}$ has ultra-low thermal conductivity despite its relatively low molecular weight.

From Chapter 5, we move away from antimony chalcogenides and explore the structures and properties of novel group 14 selenides. Beginning with the barium selenogermanates $Ba_6Ge_2Se_{12}$ and $Ba_7Ge_2Se_{17}$, we study the positional disorder in both structures. In $Ba_6Ge_2Se_{12}$, Se_2^{2-} anions exist in two possible orientations: The Se_2^{2-} may be aligned to form chains or rotated perpendicular to the chain. In $Ba_7Ge_2Se_{17}$, the positional disorder consists of a $[GeSe_5]^{4-}$ anion that can exist in two possible overlapping orientations that are flipped with respect to each other. Since positional disorder is relatively uncommon, we performed refinements of the long-range structure

(single-crystal and Rietveld refinements) and the short-range order (pair distribution function analysis) to confirm the presence of disorder in these structures.

Chapter 6 builds upon the work of Chapter 5. Starting with $Ba_6Ge_2Se_{12}$ and $Ba_7Ge_2Se_{17}$, we attempted to substitute Ge with Si in their structures. Of these two stoichiometries, only the 6:2:12 ratio could be produced with Ba, Si, and Se. $Ba_6Si_2Se_{12}$ crystallizes in a different structure type than $Ba_6Ge_2Se_{12}$. Our attempts to make a solid solution of $Ba_6Ge_2Se_{12}$ and $Ba_6Si_2Se_{12}$ were successful and led to a series of samples with 25%, 50%, and 75% of the Si atoms substituted with Ge while maintaining the $Ba_6Si_2Se_{12}$ structure type. We present the results of Rietveld refinements on the powder, including the occupancies of the disordered Si/Ge sites and Se_2^{2-} sites. Additionally, the lattice parameters of all the phases are plotted, and the relationship with Vergard's law is discussed. Finally, the effect of maximizing the configurational entropy of Si and Ge has on thermal conductivity.

In Chapter 7, we expand the scope of the new compounds with Sr and Sn. $Sr_8Ge_4Se_{17}$ and $Ba_8Sn_4Se_{17}$ share the exact stoichiometry but adopt different crystal structure types. The structures differ in size and symmetry. At first glance, the structures appear unrelated; however, we analyze the structural motifs that link the two structure types and document their ultra-low thermal conductivities arising from their complex structures and large unit cells.

Chapter 8 will culminate with a study of the new nonlinear optical properties of the new oxyselenide $Sr_6Ge_3OSe_{11}$. $Sr_6Ge_3OSe_{11}$ was found by attempting to substitute a small fraction of the Se in $Sr_8Ge_4Se_{17}$ with O. A strategy of partial isovalent anion substitution has been extremely popular in recent years for synthesizing novel noncentrosymmetric compounds. We could synthesize the new noncentrosymmetric compound reported here by utilizing this strategy. We

analyze the crystal structure of $Sr_6Ge_3OSe_{11}$ and highlight how adding oxygen helps align the nonlinearly active $[GeOSe_3]^{4-}$ anions. We use computational and experimental methods to compare the second harmonic generation intensity of $Sr_6Ge_3OSe_{11}$ with other recently reported oxyselenides and state-of-the-art nonlinearly active materials.

CHAPTER 2

Methods and Concepts

2.1 Synthesis

All the compounds reported in this thesis have been synthesized through high-temperature solid-state synthesis, which involves combining the elements in the stoichiometric ratio of the target compound and heating the sample in the absence of air. Except for $La_{12}Sb_9S_{38}$ in Chapter 4, pure compounds could be produced by combining stoichiometric amounts of the constituent elements into a silica tube inside an Ar-filled glove box. For Sr- and Ba-rich samples, it was insufficient to only create a protective C-coating on the inside of silica tubes because of the high reactivities and large proportions of these elements. Therefore, glassy C crucibles contained the reactants for the Sr and Ba samples.

Standard operating conditions inside the glove box have O_2 and H_2O concentrations below 0.1 ppm. The Ar-filled tubes containing the elements are then evacuated to at least $< 2.5 \times 10^{-3}$ mbar to avoid a pressure build-up inside the tubes as the sample is heated. The evacuated tubes are then flame-sealed on an H_2/O_2 torch to make sealed ampules. Specific heating conditions for each compound will be discussed in their respective chapters. Any samples not pure after the first heating were homogenized in a mortar and pestle and resealed in a silica tube using the procedure above to be heated for a more extended period.

Table 2.1. Summary of the elements used and their purities.

Element	Form	Purity	Manufacturer
Calcium	Granules	99.5%	Alfa Aesar
Strontium	Granules	99%	Alfa Aesar
Barium	Pieces	99.7%	Strem Chemicals
Lanthanum	Chips	99.6%	Strem Chemicals
Thallium	Granules	99.99%	Alfa Aesar
Antimony	Lumps	99.5%	Fisher Scientific
Silicon	Powder	99.9%	Alfa Aesar
Germanium	Chunk	99.999%	American Element
Tin	Granules	99.99%	Alfa Aesar
Sulpher	Pieces	99.999%	Alfa Aesar
Selenium	Pellets	99.99%	Sigma Aldrich

For $La_{12}Sb_9S_{38,}$ the binary La_3S_4 was synthesized first and combined with a stoichiometric amount of Sb and S in a ball mill under an Ar atmosphere. La_3S_4, Sb, S, and ZrO_2 balls were sealed inside a ZrO_2-lined ball mill jar under an Ar atmosphere to overcome this. The jars were placed in a Planetary Micro Mill Pulverisette 7 ball-mill (FRITSCH) and spun at high speeds to produce the desired compound through high-energy collisions between the balls.[42] The binary La_3S_4 was produced first since reactive metals can damage the lining of the jars.[43] This more involved procedure was required because, in the traditional solid-state synthesis was unable to produce the homogeneous conditions necessary to produce a single product. When heating Sb and S the high vapour pressures of these two elements resulted in the formation of Sb_2S_3 at the top of the silica

tube (i.e. the colder end) akin to crystal growth *via* chemical vapour transport. As a result solid La was left at the bottom of the tube, leaving it to react with any Sb and S that hasn't formed Sb_2S_3.

A final step in the sample preparation was to densify the phase-pure samples into pellets for physical property measurements *via* hot-pressing. Since all samples contained electropositive elements, these selenides are subject to oxidation if heated in air. We used the Oxy-Gon hot-press furnace system to make all the dense pellets for the thermal conductivity and second-harmonic generation property measurements. The powdered samples are loaded into a graphite die pressed vertically in this press. While under pressure, the furnace is heated inductively as an inert atmosphere (Ar) or a reducing atmosphere (95% Ar: 5% H_2) is passed through the chamber. The specific temperatures and pressures at which the pellets were formed are stated in each respective chapter. To ensure that the pellets are dense at this point, their densities are measured *via* the Archimedes method, which determines the density of a sample based on the difference in weight of the sample while in the air or submerged in a liquid.

For nonstoichiometric compounds like $La_{12+x}Sb_{9-y}S_{38-z}$ and $Ba_6Si_{2-x}Ge_xSe_{12,}$ which are discussed, the samples must be homogenous to ensure that the nominal composition of the sample describes the composition throughout the sample. One method of testing the atomic composition of the samples is through electron dispersive X-ray spectroscopy (EDAX). EDAX ionizes surface atoms using the electron beam of a scanning electron microscope (SEM). As the atoms decay back into their ground states, characteristic X-rays associated with a particular element are emitted proportionately to atomic percent of that element (at.-%). Without a standard, the quantification of EDAX is quite good (typically 1-2%). For this work, a QuantaFeg 250/Oxford Instrument x-act system was used to quantify the compositions of the nonstoichiometric compounds.

2.2 X-ray Diffraction

X-ray diffraction (XRD) is a powerful tool for compositional analysis and determining the purity of a sample. The X-rays are generated by accelerating electrons at an anode, which ionizes the atoms and emits X-rays of characteristic wavelengths depending on the element. For Cu, Kα1, Kα2, and Kβ are the most intense energies of X-ray photons produced along with a broad background of *Bremsstrahlung* radiation. In practice, all but the most intense wavelengths are filtered before the X-rays are ready for use.

XRD operates on the principle that when X-rays interact with the periodic lattice of a crystal, the X-rays become phase-shifted after scattering off parallel lattice planes of varying depths. The phase-shifted X-rays will undergo constructive or destructive interference. The angles (θ) at which Bragg's Law describes the phase shifts in the diffracted X-rays which result in constructed interference are given by:

$$2dsin\theta = \boldsymbol{n}\lambda \tag{2.3.1}$$

Where *d* is the spacing between lattice planes, λ is the wavelength of the X-rays, and $\boldsymbol{n}$ represents higher-order wavelengths that would also satisfy the conditions for constructive interference but can be regarded as $\boldsymbol{n} = 1$ in practice.

This phenomenon is not unique to X-rays; however, their wavelength is on the same scale as atomic lattices. The lattice points which describe the periodic structure of the crystal are imaginary points in space that describe the translational symmetry of the unit cells of the crystal structure. In a lattice of atoms, the X-rays scatter elastically (Thomson scattering) off of electrons around the atoms. Heavier elements with more electrons scatter more strongly than lighter

elements with only a few electrons. The difference in scattering intensities can help identify the elements present in the crystal. However, this can also make it difficult to differentiate elements with similar numbers of electrons.

The two most common forms of XRD are powder and single-crystal samples. In single-crystal X-ray Diffraction (sXRD), the crystal must be mounted and rotated on a four-circle goniometer to expose every lattice plane to the X-ray source. The diffracted X-rays are detected to give a series of peaks of the corresponding lattice in reciprocal space. These reflections are indexed, and using a program such as SHELXTL, a model of the unit cell and its contents is constructed based on the intensities and the corresponding structure factors (F).[44,45] Based on the discrepancies between the calculated structure factors (F_c) of the model and observed structure factors (F_o), a residual factor (R_1) may be calculated to measure the agreement of the model to the experimental data.

$$R_1 = \frac{\sum \left| {F_o}^2 - {F_c}^2 \right|}{\sum {F_o}^2} \tag{2.3.2}$$

The weighted residual factor (wR_2) is scaled by the factor w, which is analogous to the standard deviation in the model and observed data (σ).

$$w = \frac{1}{\sigma^2} \tag{2.3.3}$$

$$wR_2 = \frac{\sum w \left| {F_o}^2 - {F_c}^2 \right|}{\sum w {F_o}^2} \tag{2.3.4}$$

In powder X-ray diffraction (pXRD), it is assumed that the powdered sample contains small crystallites in every possible orientation to capture all the angles that would satisfy Bragg's

Law. This is useful for quickly determining the purity of bulk samples since peaks can be easily checked against the simulated patterns of a database of reference patterns. Like single-crystal refinements, it is possible to refine the structural model of a compound from powder data using a program such as GSAS-II.[46] For compounds that are difficult to crystallize, Rietveld refinements is a powerful technique to study changes in the crystal structure, such as defects, disorder, or lattice parameter changes. Rietveld refinements compare the simulated intensities (y_c) of a crystallographic model with the observed intensities (y_o), giving R_p and wR_P.[47]

$$R_p = \frac{\sum|y_o - y_c|}{\sum y_o} \tag{2.3.5}$$

$$wR_p = \left[\frac{\sum w(y_o - y_c)^2}{\sum w{y_o}^2}\right]^{1/2} \tag{2.3.6}$$

In Chapters 6 and 7, Rietveld refinements were carried out on diffraction patterns collected at the High Energy Wiggler Beamline of the Canadian Light Source. Synchrotrons produce X-rays far more intense than possible under laboratory conditions by accelerating electrons in a large circular path. These intense X-rays enabled us to acquire high-quality diffraction patterns of $Ba_6Si_{2-x}Ge_xSe_{12}$, $Sr_8Ge_4Se_{17,}$ and $Ba_8Ge_4Se_{17,}$ all of which have diffraction patterns with thousands of peaks due to low symmetries and large *d*-spacing.

XRD reveals information about the average structure of the crystal, but techniques such as extended X-ray absorption fine structure (EXAFS) or pair distribution function (PDF) analysis are required to determine the local structure around atoms. In Chapter 5 PDFgui was used to support the evidence of positional disorder in $Ba_6Ge_2Se_{12}$ and $Ba_7Ge_2Se_{17}$ using data collected at the 11-ID-B beamline at the Argonne National Laboratory.[48]

2.3 Thermoelectric Properties

Thermoelectric materials are characterized by their ability to convert heat energy into electrical by creating an electric potential across the material as charge carriers diffuse from the hot side (i.e. high-energy) to the cold side (i.e. low-energy). For charge carriers to efficiently move across this temperature gradient, the material must have a high electrical conductivity (σ), high Seebeck coefficient (S), and low thermal conductivity (κ). The thermoelectric efficiency of a material may be described using the dimensionless figure-of-merit, zT.

$$zT = \frac{S^2\sigma}{\kappa}T \tag{2.3.1}$$

From equation (2.3.1), one can see that to maximize zT. One must maximize the σ and S while simultaneously minimizing the κ. However, many of these parameters are interrelated, making optimization difficult when improvements to one parameter come at the cost of another.

The σ of a material depends upon the number of charge carriers (n), the mobility of those charge carriers (μ), and their charge (e). The S may be regarded as a measure of the entropy of the charge carriers in the materials with respect to their charge. On the macroscopic scale, this is equivalent to the change in electric potential (ΔV) with respect to the temperature difference across the material (ΔT). S is inversely proportional to n due to the lower entropy of a smaller number of charge carriers. Consequently, any gains in σ usually come to the detriment of S.

$$\sigma = n\mu e \tag{2.3.2}$$

$$S = \frac{\Delta V}{\Delta T} \tag{2.3.3}$$

The $TlLa_2Sb_3Se_9$ compound discussed in Chapter 3 had all its thermoelectric properties measured using the ULVAC-Riko ZEM-3. This instrument creates a temperature gradient across a vertical bar by heating the base of the bar. The base and top of the bars are held between two electrodes while two thermocouples make contact with the side of the bar, creating 4 points of contact for 4-probe measurements of the electrical conductivity and voltages. Since the two probes making contact with the side of the bar are also thermocouples, they can read the temperature difference between the hot side (bottom) and cold (top) to determine ΔT in addition to ΔT.

For most samples in this thesis, the intrinsic number of charge carriers was too low their σ to be measured on the ULVAC-Riko ZEM-3. For this reason, only their ultra-low κ could be measured. The κ of a material depends upon its thermal diffusivity (D), specific heat (C_P), and density (ρ). Since thermoelectric materials are often tested at high temperatures, it is usually sufficient to use the Dulong-Petit approximation where $C_P = 3R/M_{avg}$ (M_{avg}: average molecular mass) since this is the limit that the C_P of a material approaches at high temperatures. However, we can measure the C_P of the material using an external standard we opted to utilize in most cases.

$$\kappa = DC_P\rho \tag{2.3.4}$$

To measure κ, we use a TA Instruments Laser Flash DLF-1 with the Environmental Module EM-1200. The laser flash method does not determine the κ directly but instead determines the D, which one must combine with C_P and ρ determined through other means to obtain the final κ. In a laser flash method, a laser pulse is shot at a sample of a known thickness (L), and an infrared detector on the opposite side of the pellet creates a thermogram with respect to time as the opposite side of the pellet begins to heat up from the laser pulse. The D may be determined using equation (2.3.5), where $t_{1/2}$ is the time for the thermogram to reach its half-maximum.

$$D = 0.1388 \frac{L^2}{t_{1/2}} \tag{2.3.5}$$

κ may be further broken down into its constituents κ_{ele} and $\kappa_{lat,}$ representing the thermal conductivity of charge carriers and the conductivity of phonons in the lattice, respectively. For all of the compounds reported in this thesis, the contribution of κ_{ele} is negligible due to the low σ and, therefore $\kappa \approx \kappa_{lat}$.

$$\kappa = \kappa_{ele} + \kappa_{lat} \tag{2.3.6}$$

The κ of the materials in this thesis may be regarded as "ultra-low" since they are on the order of < 1 W $m^{-1}K^{-1}$. For ultra-low κ, it is helpful to use the diffuson model of thermal transport instead of the phonon model since the complex structure or defects scatter most short wavelength phonons.[49] Equations (2.3.7) and (2.3.8) represent the thermal conductivities of amorphous or heavily disordered materials (κ_{glass}) and the thermal conductivity derived from the diffuson model (κ_{diff}), respectively. While κ_{glass} approximates thermal conductivity for heavily disordered materials, κ_{diff} is more analogous to the minimum thermal conductivity (κ_{min}) of the material. In these expressions, n represents the number density of the material (atoms m^{-3}), k_B is Boltzmann's constant, and v_s is the sound velocity through the material. The sound velocities of the compounds were measured on hot-pressed pellets coupled to the 5 MHz transducer of a Walfront Smart Sensor Sound Velocity Meter using silicone oil.

$$\kappa_{glass} = 1.21 n^{2/3} k_B v_s \tag{2.3.7}$$

$$\kappa_{diff} = 0.76 n^{2/3} k_B v_s \tag{2.3.8}$$

For novel thermoelectric materials, one must understand the thermodynamic properties of a material before attempting to measure its properties at high temperatures. To achieve this, we use differential scanning calorimetry (DSC) and thermogravimetric analysis (TGA) to understand the limits of a material before it is heated. DSC detects any exothermic or endothermic phase transitions or decomposition in a sample by measuring a standard in parallel and comparing the heats of the two samples. TGA measures changes in the mass of a sample as it is heated. Any loss in mass suggests that volatile compounds such as S or Se are leaving the system and that the sample should exceed that temperature during measurements. Likewise, if the DSC measures a large endothermic peak indicating that the compound has melted that temperature should be avoided as well. For or purposes we use a Netzsch STA 409 PC under a constant flow of argon during heating.

2.4 Linear Optics

Polarization in materials may be expressed with the linear expression:

$$P(t) = \varepsilon_0 \chi^{(1)} E(t) \tag{2.4.1}$$

Where $P(t)$ is the dipole moment per unit volume or polarization, ε_0 is the permittivity of free space, $\chi^{(1)}$ is a proportionality constant known as the linear susceptibility and $E(t)$ is the optical field strength. In physics, linear optics is the subdiscipline which describes lenses, mirrors, and diffraction gratings. In the context of material science, linear optics is also responsible for the refractive index of a material. The refractive index of a medium, n, is the ratio of the speed of light in a vacuum (c) and the speed of light travelling through that medium (v).

$$\mathrm{n} = \frac{c}{v} \tag{2.4.2}$$

In cubic crystal systems (and isotropic systems), where the *x*, *y*, and *z* directions are all equivalent, the *n* is constant regardless of the direction the light travels through the material. The material will have the same refractive indices as unique axes for lower symmetry crystal systems. The refractive indices may be determined from the diagonalized dielectric tensor of material since the refractive indices, n_{xx}, n_{yy}, and n_{zz}, are related to the dielectric constants, ε_{xx}, ε_{yy}, and ε_{zz} *via* equation (2.4.3)

$$\sqrt{\varepsilon_{ii}} = n_{ii} \tag{2.4.3}$$

Table 2.2 Relationship between the number of unique crystallographic axes and the corresponding dielectric tensor. Isotropic materials include those without long-range ordering, such as gases, liquids, and amorphous solids.

Birefringence	Crystal Class	Dielectric Tensor
Biaxial Birefringence	Triclinic, Monoclinic, Orthorhombic	$\begin{bmatrix} \varepsilon_{xx} & 0 & 0 \\ 0 & \varepsilon_{yy} & 0 \\ 0 & 0 & \varepsilon_{zz} \end{bmatrix}$
Uniaxial Birefringence	Tetragonal, Trigonal, Hexagonal	$\begin{bmatrix} \varepsilon_{xx} & 0 & 0 \\ 0 & \varepsilon_{xx} & 0 \\ 0 & 0 & \varepsilon_{zz} \end{bmatrix}$
No Birefringence	Cubic, Isotropic	$\begin{bmatrix} \varepsilon_{xx} & 0 & 0 \\ 0 & \varepsilon_{xx} & 0 \\ 0 & 0 & \varepsilon_{xx} \end{bmatrix}$

2.5 Nonlinear Optics

Under intense optical fields, the polarizability of the medium deviates from linearity, and higher-order terms are introduced into the expression for $P(t)$.

$$P(t) = \varepsilon_0\left[\chi^{(1)}E(t) + \chi^{(2)}E^2(t) + \chi^{(3)}E^3(t) \ldots\right] \quad (2.5.1)$$

The second and third terms are associated with second and third harmonics. Several phenomena are associated with second-order nonlinear optical susceptibility, such as second harmonic generation (SHG), sum frequency generation (SFG), and difference frequency generation (DFG). Figure 2.1 visualizes the physical phenomena governed by the second-order nonlinear optical susceptibility term. SHG occurs when two photons of equal frequency are destroyed, and a photon equal to two times the frequency of the original photons is emitted. Third harmonic generation is the analogous process where three photons are destroyed, and a photon equal to three times the original frequency is emitted. SFG involves destroying two photons of different frequencies and producing a single photon with the total energy of the starting two photons. DFG involves breaking up a high-energy photon into two lower-energy photons.

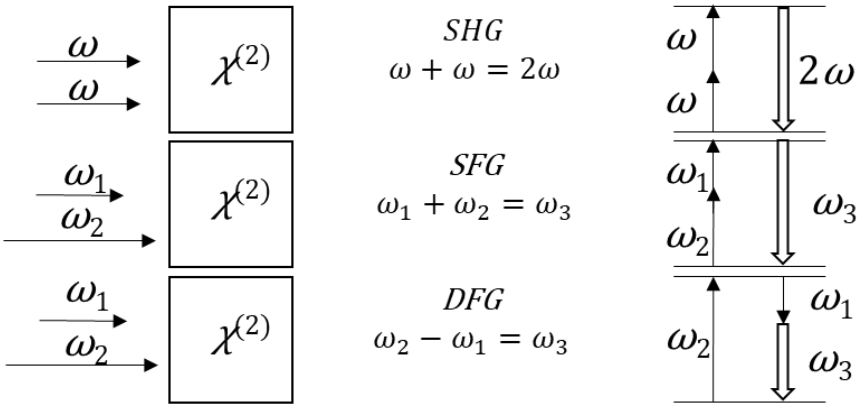

Figure 2.1. Geometric representations and energy level diagrams of SHG (top), SFG (middle), and DFG (bottom).

A prerequisite for SHG is for the material to belong to one of the 21 non-centrosymmetric (NCS) crystal classes. NCS crystal classes do not have an inversion center; therefore, the dipole

moments of the atoms may not cancel each other, leading to polar crystal classes. The consequence of having inversion symmetry is that the even powered terms in the polarization power series vanish completely since the positive and negative polarizations with respect to time sum to zero.

$$P^{(2)}(t) = \chi^{(2)}E^2(t) \tag{2.5.2}$$

Changing the direction (i.e. sign) of the applied electric field must also change the sign of the polarization in a centrosymmetric medium.

$$-P^{(2)}(t) = \chi^{(2)}[-E(t)]^2 \tag{2.5.3}$$

$$-P^{(2)}(t) = \chi^{(2)}E^2(t) \tag{2.5.4}$$

Since equations (2.5.2) and (2.5.4) are equivalent $\chi^{(2)}$ must be zero for $P(t)$ to be qual to $-P(t)$. Since the second-order linear susceptibility vanishes to zero, nonlinear optical (NLO) phenomena such as SHG are impossible within materials with centrosymmetric crystal classes.

Although the lack of inversion symmetry is crucial for SHG, the specific NCS point group adds additional restrictions upon the second-order nonlinear optical susceptibility coefficient. Therefore, describing $\chi^{(2)}$ as a scalar value is no longer enough. $\chi^{(2)}$ can now be written instead as a third-order tensor to encapsulate the symmetries of the crystal system along its three crystallographic axes *x*, *y*, and *z*, which are denoted as 1, 2, and 3, respectively, as the subscripts for $\chi^{(2)}$.

$$\begin{bmatrix} P_x^{\omega 1+\omega 2} \\ P_y^{\omega 1+\omega 2} \\ P_z^{\omega 1+\omega 2} \end{bmatrix} = 2\varepsilon_0 \begin{bmatrix} d_{11} & d_{12} & d_{13} & d_{14} & d_{15} & d_{16} \\ d_{21} & d_{22} & d_{23} & d_{24} & d_{25} & d_{26} \\ d_{31} & d_{32} & d_{33} & d_{34} & d_{35} & d_{36} \end{bmatrix} \begin{bmatrix} E_x^{\omega 1} E_x^{\omega 2} \\ E_y^{\omega 1} E_y^{\omega 2} \\ E_z^{\omega 1} E_z^{\omega 2} \\ E_y^{\omega 1} E_z^{\omega 2} + E_y^{\omega 2} E_z^{\omega 1} \\ E_z^{\omega 1} E_x^{\omega 2} + E_z^{\omega 2} E_x^{\omega 1} \\ E_x^{\omega 1} E_y^{\omega 2} + E_x^{\omega 2} E_y^{\omega 1} \end{bmatrix} \quad (2.5.5)$$

The second-order nonlinear optical susceptibility tensor is now expressed as d where $2d = \chi^{(2)}$. Additionally, contracted notation is used to index the d – tensor elements such that the last two indices are replaced to denote the position of the tensor element in the matrix. 11, 22, 33, 23, 13, and 12 are replaced by 1, 2, 3, 4, 5, and 6, respectively.

The second-order nonlinear optical susceptibility tensor expression in equation (2.5.5) may be simplified using Kleinman symmetry, which states that NLO susceptibility tensor elements are independent of frequency.[50] This assumption is valid at low frequencies since the frequencies participating in SHG are much smaller than the resonant frequency of the material. In practical terms, this means that crystallographic directions of the tensor elements commute and can, therefore, be permutated freely. Several tensor elements become equivalent under Kleinman symmetry through these permutations of crystallographic directions. For example:

$$d_{12} \equiv d_{122} = d_{212} \equiv d_{26} \quad (2.5.6)$$

As a result, the degeneracies under Kleinman symmetry, the d – tensor reduces from 18 unique elements to 10 unique elements.

$$\begin{bmatrix} d_{11} & d_{12} & d_{13} & d_{14} & d_{31} & d_{21} \\ d_{21} & d_{22} & d_{23} & d_{32} & d_{14} & d_{12} \\ d_{31} & d_{32} & d_{33} & d_{23} & d_{13} & d_{14} \end{bmatrix} \quad (2.5.7)$$

Equation (1.2.10) represents the d – tensor for the triclinic 1 point group under Kleinman symmetry. For higher symmetry NCS point groups, there can be fewer than 10 unique elements. When there are more operations, several tensor elements vanish entirely. Research into NLO materials is based on discovering compounds with high d_{ij} values. High d_{ij} values correspond to efficient SHG; a high-quality crystal would be oriented along the crystallographic with the largest d_{ij} value.

For exploratory research into NLO materials, growing high-quality single crystals of the compound is unnecessary. The SHG signal can be measured on NCS powdered samples and a signal corresponding to a combination of all non-zero d_{ijk}, known as d_{eff}.[51]

$$\langle (d_{\text{eff}})^2 \rangle = \frac{19}{105}\sum_{i}(d_{iii})^2 + \frac{13}{105}\sum_{i\neq j} d_{iii}d_{ijj} + \frac{44}{105}\sum_{i\neq j}(d_{iij})^2 + \frac{13}{105}\sum_{ijk,cyclic} d_{iij}d_{jkk} + \frac{5}{7}(d_{ijk})^2 \tag{2.5.8}$$

The SHG intensity of the sample is compared to the SHG intensity of a standard with known d_{ij} values such as $AgGaS_2$ (AGS) or $AgGaSe_2$ (AGSe).

To have efficient SHG, energy and momentum must be conserved, known as phase-matching. The intensity of the SHG signal drops rapidly when phase-matching conditions are not met. Energy conservation is described in terms of the frequencies of the source (ω_1) and generated photons (ω_2).

$$\omega_1 + \omega_1 = \omega_2 \tag{2.5.9}$$

Conservation of momentum is described by the wavevectors of the source and generated photons, k_1 and k_2, respectively.

$$k_1 + k_1 = k_2 \tag{2.5.10}$$

$$k = \frac{\omega}{v} \tag{2.5.11}$$

Substituting equations (2.5.2) and (2.6.11) into (2.6.12), the relationship between refractive index and conservation of momentum becomes clear.

$$\frac{\omega_1 \mathrm{n}_1}{c} + \frac{\omega_1 \mathrm{n}_1}{c} = \frac{\omega_2 \mathrm{n}_2}{c} \tag{2.5.12}$$

For phase-matching conditions to be perfectly met, the refractive index of the medium at ω_1 must be the same as the refractive index at ω_2. This condition is impossible to meet without birefringence due to the frequency dependence of the refractive index. The refractive index increases with increasing frequency. In a material which displays birefringence, it is possible to cross over to a different refractive index curve to keep the refractive index the same at the new frequency, thus conserving momentum. In practice, to achieve phase-matching using the inherent birefringence of a crystal, the source light is polarized along the crystallographic direction corresponding to the lower refractive index, n_1. If these two source photons must be polarized parallel to each other, this is known as "type I" phase-matching, and if the source photons must be orthogonal to each other, then this is known as "type II" phase-matching. The lack of birefringence ends up limiting the SHG intensity of many cubic materials with large nonlinear susceptibility values, such as GaAs, which adopts the zincblende structure with the point group $\bar{4}3m$.[52] The intensity of SHG as it relates to the conservation of momentum is described by equations (2.6.13) and (2.6.14).

$$\Delta k = k_2 - 2k_1 \tag{2.5.13}$$

$$I = I_{max}\left[\frac{\sin\left(\frac{\Delta kL}{2}\right)}{\frac{\Delta kL}{2}}\right]^2 \quad (2.5.14)$$

Where I is the intensity of SHG and L is the path length for the laser through the crystal. For maximum SHG intensity to be achieved, Δk must be zero. Otherwise, the intensity drops dramatically.

To determine whether a crystal can phase-match, one must determine whether the material is phase matchable at a given wavelength. Kurtz and Perry at Bell Labs found that the phase-matching ability of a material could be tested on powdered samples.[51] It is assumed that the particles are oriented randomly in powder and that the SHG intensity increases additively as light passes through more particles. The laser passes through L/r particles in the powdered sample where L is the path length through the powdered sample and r is the average size of a particle in the powdered sample. In type I phase-matching, there is no angular dependence between the particles, so the SHG intensity for smaller particles is weak due to the increased amount of scattering from the more significant number of particles. Eventually, the SHG intensity plateaus once the particles are large enough. When the compound does not type I phase to match, the SHG intensity reaches a maximum before decreasing with increasing particle size. This is because there is a small range of angles at which the incident light must hit the particle for SHG to occur. For larger particle sizes, the incident beam passes through fewer particles, meaning there will be fewer in the correct orientation to perform SHG.

An experimental d_{eff} may be calculated by comparing the SHG intensity of a new sample and the SHG intensity of a standard.[53] If the new sample exhibits phase-matching, it must be compared using a phase-matching (PM) standard like $LiNbO_3$; alternatively, if the new sample

does not phase match a non-phase-matching (NPM) standard like α-SiO_2. Equations (2.6.15) and (2.6.16) give d_{eff} in SI units (pm V^{-1}). Due to the particle size dependence of SHG intensity, comparing standards and samples that have been sieved to the same particle size ranges is crucial.

$$\langle d_{eff} \rangle_{PM} = \left[\frac{I^{2\omega}(A)}{I^{2\omega}(LiNbO_3)} \times 798 \right]^{1/2} \tag{2.5.15}$$

$$\langle d_{eff} \rangle_{NPM} = \left[\frac{I^{2\omega}(A)}{I^{2\omega}(\alpha - SiO_2)} \times 0.3048 \right]^{1/2} \tag{2.5.16}$$

2.6 Density Functional Theory

Density functional theory (DFT) is a computational modelling method which provides an accurate scheme for overcoming the many-electron problem in quantum mechanical problems. To describe the decrease in electron density further from the nucleus, gradient terms may be added to the density functional, i.e. generalized gradient approximation (GGA).[54] DFT calculations begin with a structural model of a molecule or unit cell. When computing the energy of the unit cell, the program samples a specified number of points in the Brillouin zone known as *k* points. This can be computationally expensive for large unit cells that contain many atoms, so the number of *k* points sampled is reduced for expediency at the cost of accuracy. The computational then relaxes the structure until energy and charge thresholds are met. Then, one may calculate the electronic structure of the material or physical properties with the relaxed structure. WIEN2k was used in this work to calculate these compounds' band structure and density of states (DOS).

In Chapter 8, the NLO properties of $Sr_6Ge_3OSe_{11}$ are calculated using DFT. The second-order susceptibilities may be calculated following the convergence of the self-consistent cycle criteria. Second-order susceptibilities may be calculated by several different DFT software such

as Abinit,[55] Elk.[56] Add-ons for VASP have also been developed by Yong-Fan Zhang, which enable it to calculate the second-order NLO tensor elements.[57,58] An add-on has also been used with CASTEP to calculate NLO susceptibilities.[59,60] The two commonly used approaches for calculating nonlinear susceptibilities are known as the "sum-over-states" (SOS) and the "length-gauge" formalisms developed by Sharma and Sipe, respectively.[61–63] Depending on which software is used for DFT calculations, either approach may be implemented. The SOS formalism will be focused on since it is the method used in the Elk code.

The SOS formalism determines the number of excitations occurring within valence and conduction bands and between bands for a given photon energy. Excitations within the same band are always present and are known as the intraband component of nonlinear susceptibility. Above half the band gap energy of the material excitations from the conduction band dominates second-order nonlinear optical susceptibility. This is the interband component. Half the band gap energy is critical since photons with 2ω that SHG creates have enough energy to excite charge carriers between bands. Finally, the interband and intraband components are added to get the total susceptibility. Since excitations within the band structure are being calculated, having a dense k point mesh is necessary when initializing a DFT calculation. Optical properties require large numbers of k points to reach convergence.[64] Additionally, an accurate experimental band gap energy is crucial to determining optical properties since interband terms depend on this energy value. Since DFT calculations often underestimate the band gap energy, the optical band gap is often obtained experimentally and used to correct the calculated band gap *post hoc* using a scissor operator. The scissor operator raises conduction bands to match the experimental band gap.

To increase the precision of the theoretically calculated optical properties the calculated band gap is often corrected to the experimental value using a scissor operator. For solid samples such as the ones described here the spectrometer is set up to measure the diffuse reflectance of a pelletized sample and the reflectance is then converted to absorbance which is used to determine the optical band gap graphically. For these compounds, the PerkinElmer Lambda 1050 UV/VIS/NIR Spectrometer was used since it allowed for measurements into the near IR region where the band gap for several of these selenogermanates resides. Using the Kubelka-Munk equation, (2.6.1), the reflectance can be converted to absorbance.

$$\frac{\alpha}{S} = \frac{(1-R)^2}{2R} \tag{2.6.1}$$

Where R is the percent reflectance written as a decimal, α is the absorbance, and S is a scattering factor which is approximately constant for material with particles sizes greater than ~ 5 μm. Once the a/S term is determined it is plotted versus wavelength or the corresponding energies. The band gap can then be read from the plot by extrapolating the absorption edge to the baseline.

An alternative method to determine the band gap, which is used in the characterization of $TlLa_2Sb_3Se_9$ in Chapter 3, is to measure the change in σ with respect to temperature. Intrinsic charge carriers can to be thermally activated to cross from the valence band to the conduction band. The relationship between T and σ is given by the Arrhenius equation:

$$\sigma = \sigma_0 e^{-\frac{E_g}{2k_B T}} \tag{2.6.2}$$

Where E_g is the band gap, k_B is the Boltzmann constant, T is temperature and σ_0 is a pre-exponential factor. For semiconductors, plotting $\ln(\sigma)$ versus $1/T$ yields and negative linear relationship with slope equal to $-E_g/2k_B$.

CHAPTER 3

$TlLa_2Sb_3Se_9$

3.1 Introduction

Research into antimonates has led to the discovery of several new compounds due to the structural distortions arising from the sterically active lone pair of electrons of the Sb^{3+} ion. Our initial investigations of the La-Sb-*Q* (*Q* = S, Se, Te) system resulted in the discovery of $La_7Sb_9S_{24}$.[65] Subsequent research involved adding a second heavy atom to the ternary system, yielding the quaternaries $BaLaSb_2S_6$ and $BaLaSb_2Se_6$.[66] $TlLa_2Sb_3Se_9$ was discovered by using Tl^+ as the second heavy cation instead of Ba^{2+}. $TlLa_2Sb_3Se_9$ crystallizes in an ordered variant of its K analogue sulphide $KLa_2Sb_3S_9$.[67]

Chalcoantimonates such as the LAST compounds (Lead-Antimony-Silver-Tellurium)[68] and the tetrahedrites $Cu_{12}Sb_4S_{13}$[69,70] have succeeded as thermoelectric materials. The efficiency of a thermoelectric material depends on the dimensionless figure-of-merit, $zT = S^2\sigma T\,\kappa^{-1}$. Where *S* is the Seebeck coefficient, σ is the electrical conductivity, κ is the thermal conductivity, and *T* is the temperature. Phases with large unit cells and low symmetry, such as the tetrahedrites $TlLa_2Sb_3Se_9$, are known to have low κ since the low symmetry structure scatters short wavelength phonons.[71–75] Additionally, $TlLa_2Sb_3Se_9$ is a lustrous grey material suggesting that it is a narrow band gap

semiconductor. For these reasons, the thermoelectric properties of $TlLa_2Sb_3Se_9$ were determined minneapand enhanced by doping with Ca^{2+} to increase the electrical conductivity, σ.

3.2 Synthesis

All the starting materials were handled within an argon filled glove box. Stoichiometric amounts of the constituent elements Tl (granules, 99.99%, Alfa Aesar), La (chips, 99.6%, Strem Chemicals), Ca (granules, 99.5%, Alfa Aesar), Sb (lumps, 99.5%, Fisher Scientific), and Se (pellets, 99.99%, Sigma Aldrich) were added to a fused silica tube, evacuated to 2.5 × 10-3 mbar, and flame sealed to make an ampule. The sealed ampule was heated over 6 hours to 923 K and left to dwell for 12 hours to complete the reaction of the elements. The furnace was then slowly cooled over 120 hours to 473 K to obtain crystals for single crystal analysis. Thereafter, the furnace was turned off and allowed to cool to room temperature naturally.

The single crystal data were collected at room temperature on a Bruker Kappa Apex II CCD diffractometer equipped with a Mo Kα radiation source. The ω and ϕ directions were scanned in 0.3º steps and data was collected in 30 second intervals.[76] The crystal structure was at first solved using the direct method within the SHELXTL package,[45] and the previously reported solution for $KLa_2Sb_3S_9$[67] was originally used to refine the $TlLa_2Sb_3Se_9$ structure. In the end, the positions were standardized using the STIDY routine.[77]

Powder X-ray diffraction of the ground samples was performed on an Inel powder X-ray diffractometer using Cu $K\alpha_1$ radiation. Diffraction patterns are provided as Figure A.1.

The electronic structure was determined using the Perdew-Burke-Ernzerhof (PBE) functional for the generalized gradient approximation (GGA) included in the Wien2K package.[78]

The convergence criteria of energy changes < 0.001 Ry and charge changes < 0.001 were met for $TlLa_2Sb_3Se_9$ using a 12 × 3 × 2 *k* point mesh.

To perform thermoelectric property measurements, the $TlLa_{2-x}Ca_xSb_3Se_9$ samples were hot pressed into 12.7 mm diameter pellets under 62 MPa of pressure at 623 K for two hours with argon constantly flowing through the Oxy-Gon hot-press furnace system. The densities of these pellets were determined using the Archimedes method; all had densities greater than 96% of the theoretical density. The thermoelectric properties were then determined using the TA Instruments DLF 1200 to determine the thermal diffusivities of the pellets, and the ULVAC ZEM-3 instrument was used to determine the Seebeck coefficients and electrical conductivities of prismatic bars cut from the hot-pressed pellets. The thermal conductivity values were calculated from the product of the thermal diffusivity, density and specific heat derived from the Dulong-Petit law for each sample. The thermoelectric properties were measured at room temperature up to 623 K.

The thermal behavior of $TlLa_2Sb_3Se_9$ was analyzed by differential scanning calorimetry (DSC) and thermal gravimetric analysis (TGA) using a Netzsch STA 409 PC under a flow of argon.

3.3 Crystal Structure

$TlLa_2Sb_3Se_9$ adopts an ordered variant of the $KLa_2Sb_3S_9$ structure type (Figure 3.1), i.e. without the disorder of the chalcogen atoms.[67] The crystallographic data are summarized in Table 3.1, and the atomic positions are in Table A.1. There are six cations and nine anions located on the only *4a* Wyckoff sites in $P2_12_12_1$.

Table 3.1. Crystallographic details of $TlLa_2Sb_3Se_9$.

Parameters	$TlLa_2Sb_3Se_9$
Crystal system	Orthorhombic
Space group	$P2_12_12_1$ (no. 19)
a (Å)	4.2621(2)
b (Å)	15.155(9)
c (Å)	25.5005(9)
Unit cell volume ($Å^3$)	1647.5(1)
Crystal size (mm)	0.100 x 0.010 x 0.005
Formula units per unit cell, *Z*	4
Molecular weight (g mol^{-1})	1558.08
Density (g cm^{-3})	6.28
Radiation, wavelength (Å)	0.71073 (Mo Kα)
Temperature (K)	296
F(000)	2616
Absorption coefficient, μ (mm^{-1})	39.5
Goodness-of-fit	1.01
R_1 [I > 2σ(I)]	0.0488
wR_2 [I > 2σ(I)]	0.0910
Largest diff. peak, hole (e $Å^{-3}$)	3.43, -3.62

The Sb^{3+} cations are surrounded by six Se atoms in two different distorted octahedral geometries, a [5+1] coordination sphere for Sb1 and a [3+3] coordination sphere for Sb2 and Sb3.

These coordinations are very common for the Sb^{3+} cation, observed in many chalco-antimonates due to their stereochemical active lone pair. The [$SbSe_6$] distorted octahedra share four common edges to form a {SbSe} slab (Figure 3.1). These slabs are connected *via* corner through the longest Sb-Se contact (above 3 Å) to form columns similar to many selenoantimonates, including $BaLaSb_2Q_6$ (*Q* = S, Se),[66] $Tl_{2.35}Sb_{8.65}Se_{14}$,[79] $Pb_4Sb_6Se_{13}$ and $Pb_6Sb_6Se_{17}$,[80] $FePb_4Sb_6S_{14}$,[81,82], and $Ba_4LaSbGe_3Se_{13}$.[83] Two crystallographically independent La^{3+} cations are in ninefold coordination in form of tri-capped trigonal prisms by two different Se anions: Se^{2-} and Se^{-}. [$La1Se_9$] and [$La2Se_9$] polyhedra share a common edge formed by a Se_2^{2-} dumbbell and share common faces (Figure 3.2). The coordination of the Tl^{+} cation is also ninefold in the form of a tri-capped trigonal prism with bond lengths ranging from 3.28 Å to 3.66 Å, similar to those found in many thallium selenides. The [$TlSe_9$] polyhedra share common faces forming an infinite linear chain along the *a* axis (Figure 3.3).

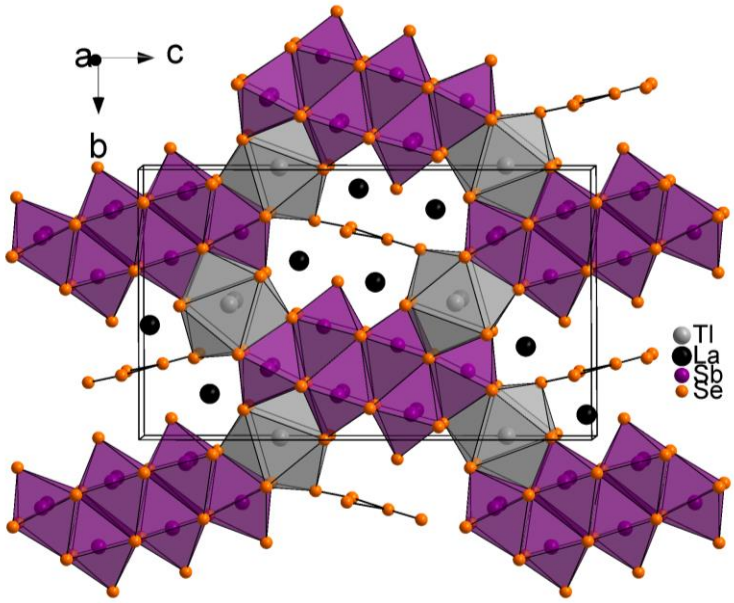

Figure 3.1. Crystal structure of $TlLa_2Sb_3Se_9$ with edge-sharing [$SbSe_6$] polyhedra and {TlSe} chains.

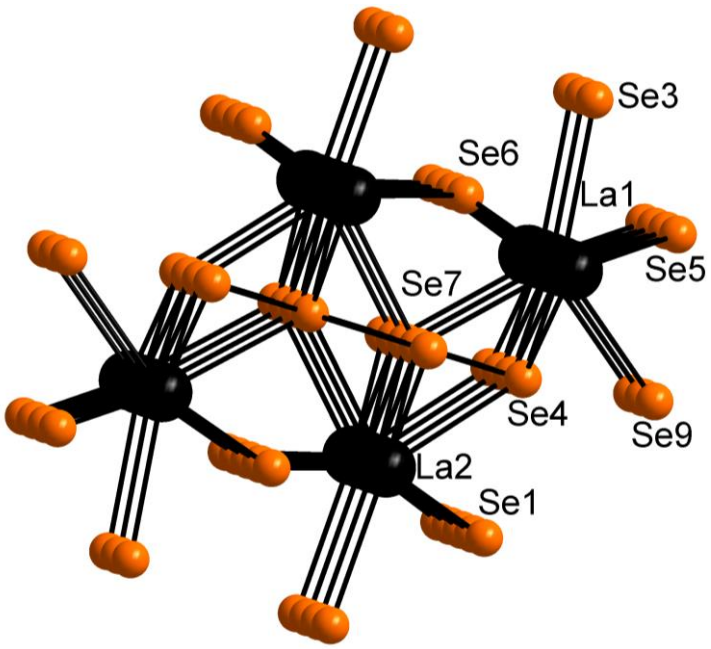

Figure 3.2. Two double chains of $LaSe_9$ polyhedra.

There are also nine crystallographically independent Se atoms, which are fully ordered, while in the case of $KLaSb_3S_9$, two of the sulphur sites were split into two different positions with almost 50:50 occupancy. A similar scenario was also observed in the cases of $Pb_6Sb_6S_{17}$ and $Pb_6Sb_6Se_{17}$. Two of the Se atoms, Se4 and Se7, form a Se_2^{2-} dumbbell, with a Se-Se bond of 2.48 Å, longer than in most cases but similar to those found in the polyselenides $BaLaSb_2Se_6$ (2.45 Å) and $Sr_{19-x}Pb_xGe_{11}Se_{44}$ (2.45 Å – 2.46 Å).[84] Each dumbbell is connected to two others *via* contacts of 3.10 Å between two Se7 atoms, resulting in an infinite ribbon of four Se atoms running along the *a* axis. The next Se4-Se7 distance is 3.48 Å, likely nonbonding (Figure 3.3). Treating the dumbbells as Se_2^{2-} ions, a charge balanced formula results with $(Tl^+)(La^{3+})_2(Sb^{3+})_3(Se^{2-})_7(Se_2^{2-})$.

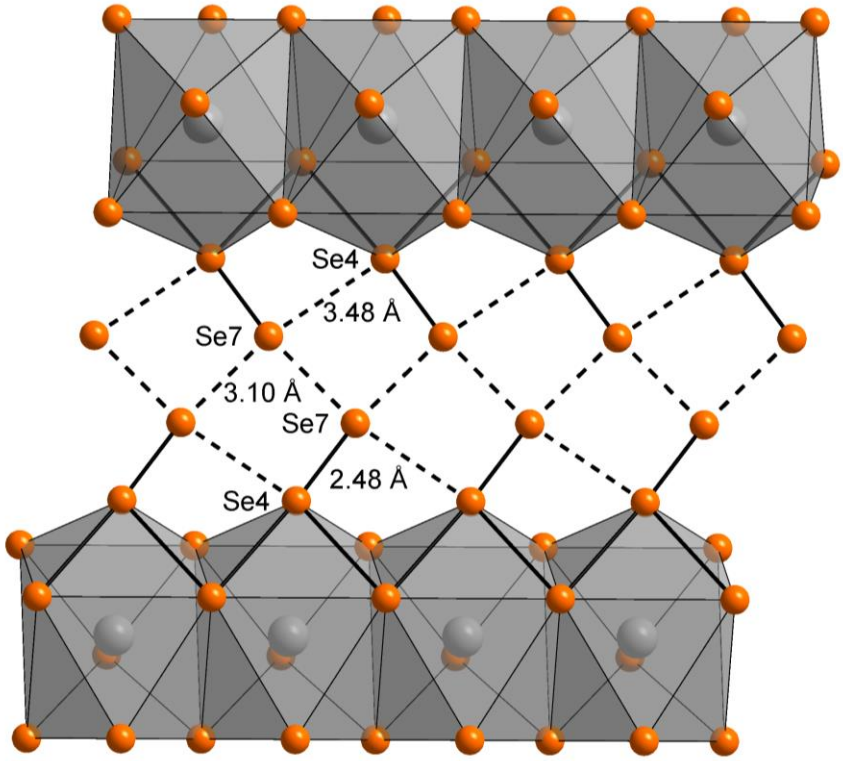

Figure 3.3. {TlSe} chains joined by Se-Se interactions.

3.4 Theoretical Studies

The band structure calculated revealed a band gap of 0.47 eV separating the valence band from the conduction band (Figure 3.4). Se p states dominate the top of the valence band, while the sharp peak around +3 eV in the conduction band mainly consists of La *d* states. The bands near the Fermi level are primarily flat throughout the *k* space, especially below the Fermi level, which should lead to low charge carrier mobility and a high Seebeck coefficient.

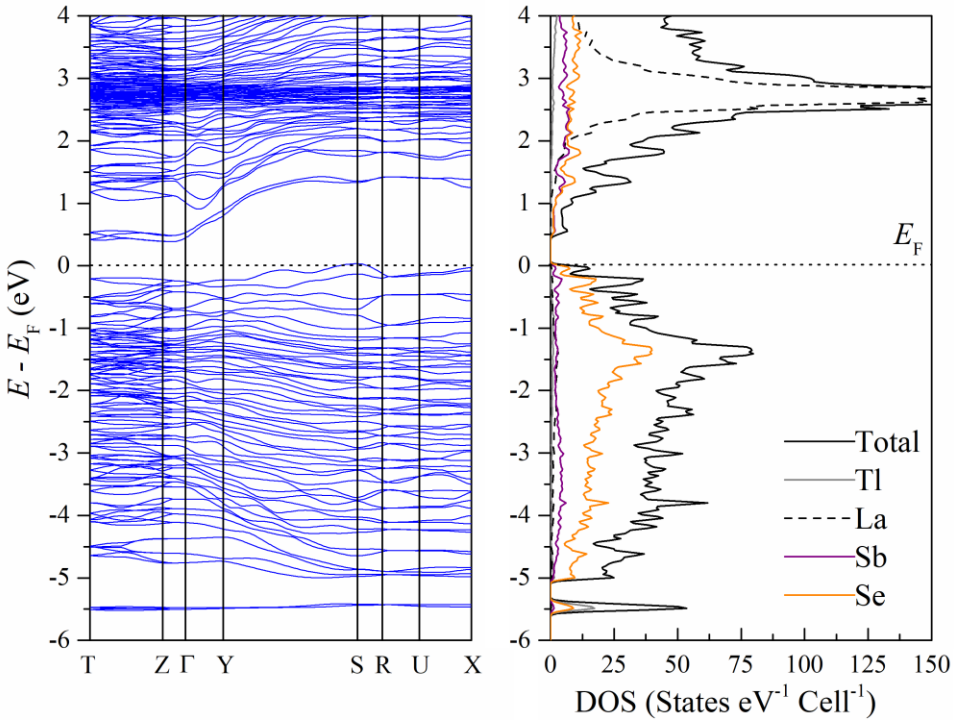

Figure 3.4. Band structure (left) and density of states (DOS, right) of $TlLa_2Sb_3Se_9$.

3.5 Thermoelectric Properties

3.5.1 Electrical Conductivity

To know what temperature $TlLa_2Sb_3Se_9$ could be safely heated to during the thermoelectric property measurements, differential scanning calorimetry (DSC) and thermal gravimetric analysis (TGA) were performed. As seen in Figure A.2, the DSC curve of the $TlLa_2Sb_3Se_9$ sample shows a sharp endothermic peak at 857 K, which did not reappear upon cooling the sample. This indicates that the sample melted incongruently at this temperature, leaving behind simpler phases. Above the incongruent melting point of $TlLa_2Sb_3Se_9$, the volatility of Se significantly increases, and approximately 5% of the mass is lost above this temperature. Smaller peaks occur at 639 K upon heating and 690 K upon cooling. Thus, the physical property measurements were performed up to 623 K.

Using the DSC/TGA results, the thermoelectric property measurements of the hot-pressed samples were kept below 623 K not to decompose the samples. Undoped $TlLa_2Sb_3Se_9$ has abysmal electrical conductivity (< 0.01 Ω^{-1} cm^{-1}), and a signal could not be obtained at room temperature. Ca was chosen as a dopant since Ca^{2+} has a comparable ionic radius to La^{3+} (1.12 Å and 1.16 Å).[85] All Ca-containing samples could be measured at 323 K instead of 373 K for the undoped sample, but a signal at room temperature was still unobtainable. The electrical conductivity values for the $TlLa_{2-x}Ca_xSb_3Se_9$ samples rise exponentially with respect to temperature (Figure 3.5), indicative of increasing thermal activation of the intrinsic charge carriers, with the Ca-containing samples exhibiting significantly higher values of up to σ = 1.8 $\Omega^{-1}cm^{-1}$ at 623 K, compared to 0.7 $\Omega^{-1}cm^{-1}$ for the Ca-free sample. Such relatively low values, compared to advanced thermoelectric materials with σ >> 100 $\Omega^{-1}cm^{-1}$, along with the observed thermal activation, indicate the absence of significant amounts of extrinsic charge carriers, pointing to charge compensation within the Ca-containing samples *via* defects.

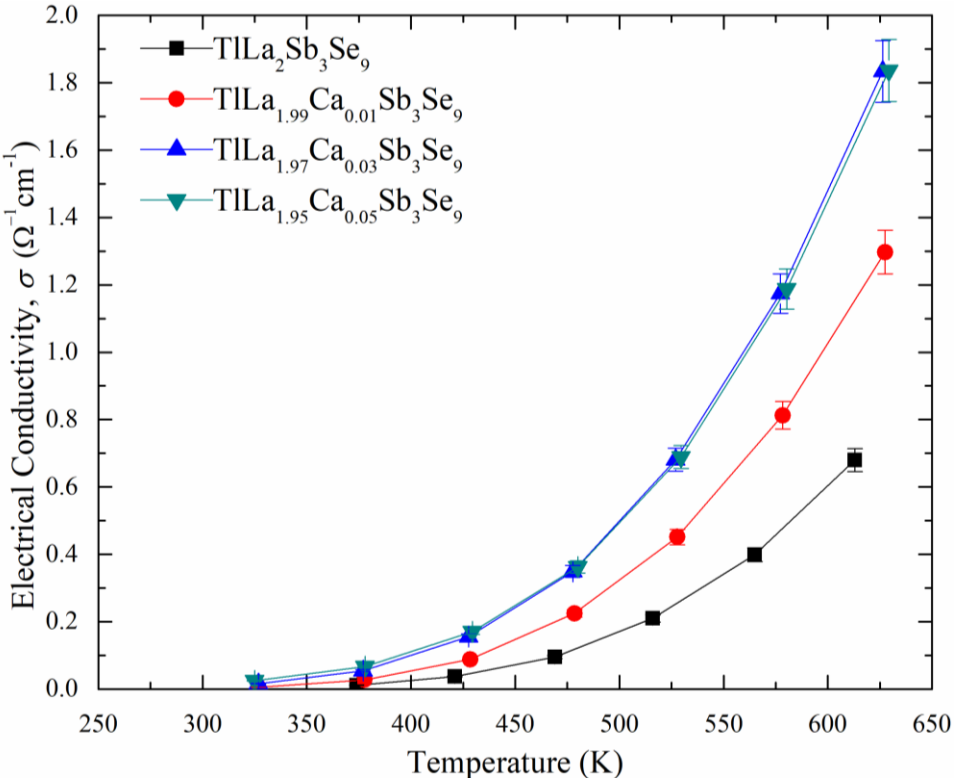

Figure 3.5. Electrical conductivity of $TlLa_{2-x}Ca_xSb_3Se_9$ (x = 0, 0.01, 0.03, 0.05).

Since $TlLa_2Sb_3Se_9$ behaves as an intrinsic semiconductor, the experimental band gap could be determined using the Arrhenius equation:

$$\sigma = \sigma_0 e^{\left(\frac{-E_g}{2k_B T}\right)} \tag{3.4.1}$$

Where σ_0 is a pre-exponential factor, E_g is the band-gap energy, k_B is the Boltzmann constant, and T is the absolute temperature. Linear regression of the curve gave an experimental band gap value of 0.68 eV for $TlLa_2Sb_3Se_9$ (Figure A.3). This is in qualitative agreement with the calculated value of 0.47 eV, noting that calculated band gaps based on density functional theory are often underestimated.

3.5.2 Seebeck Coefficient

$TlLa_2Sb_3Se_9$ is a *p*-type semiconductor with a positive Seebeck coefficient. The Seebeck data follow – as is commonly observed – the opposite trend compared to the electrical conductivity data: increasing Ca content occurs with values. The curves begin to merge at higher temperatures (Figure 3.6). The low concentration and mobility of charge carriers lead to an excellent Seebeck coefficient of approximately 500 $\mu V\ K^{-1}$ for all samples at 623 K. These experimental observations are in line with the flat bands near the Fermi level that were calculated in the band structure of $TlLa_2Sb_2Se_9$.

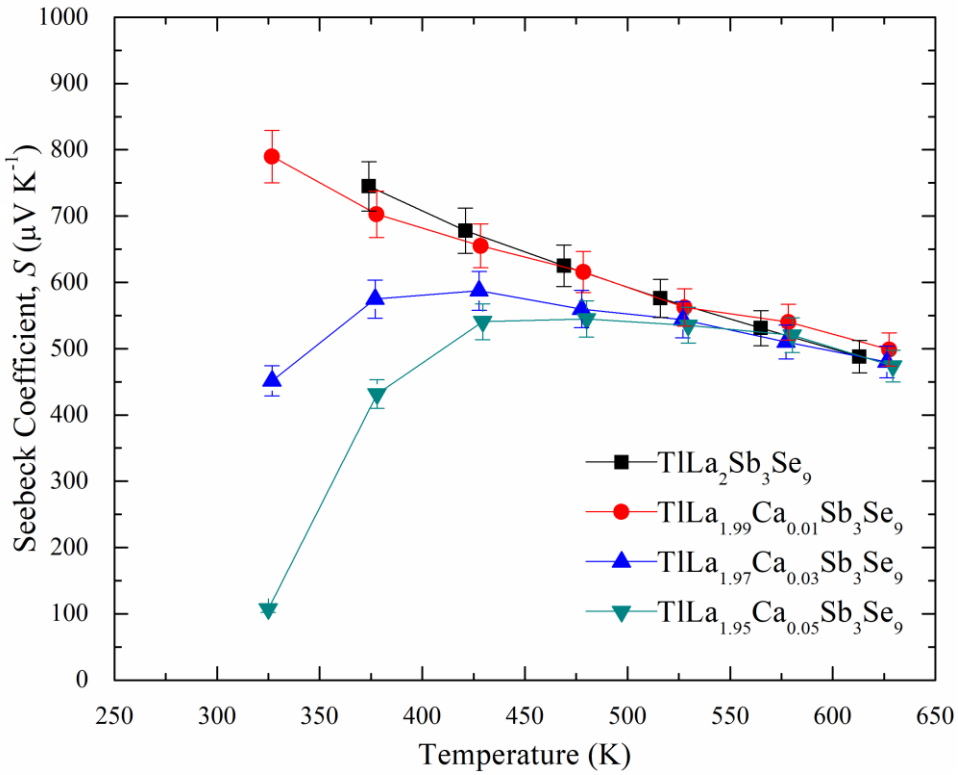

Figure 3.6. Seebeck coefficient of $TlLa_{2-x}Ca_xSb_3Se_9$ (x = 0, 0.01, 0.03, 0.05).

3.5.3 Thermal Conductivity

The thermal conductivity values are below 0.5 W $m^{-1}K^{-1}$, slowly decreasing with increasing temperature (Figure 3.7). Such low values are ideal for thermoelectric materials, but the low electrical conductivity prohibits using these materials for that purpose.

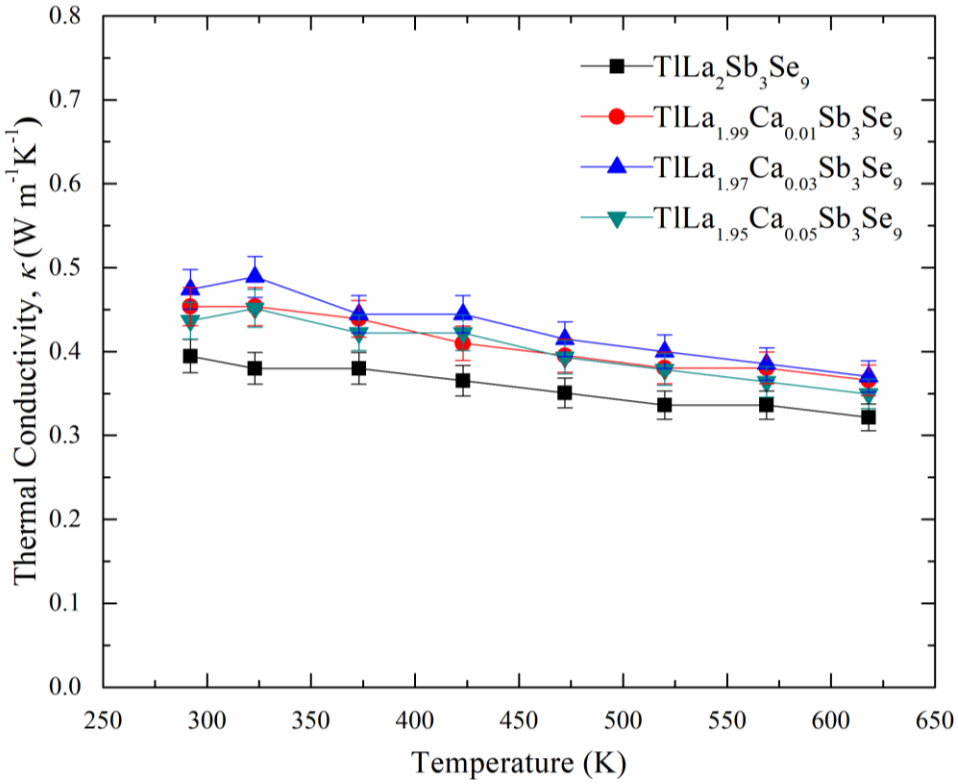

Figure 3.7. Thermal conductivity of $TlLa_{2-x}Ca_xSb_3Se_9$ (x = 0, 0.01, 0.03, 0.05).

The exponential trend in electrical conductivity dominates the *zT* relationship and leads to a maximum *zT* of 0.078 for the $TlLa_{1.95}Ca_{0.05}Sb_3Se_9$ sample at the maximum temperature (Figure 3.8). This is more than double the value for the undoped $TlLa_2Sb_3Se_9$ with its *zT* = 0.031 but well below the values of state-of-the-art thermoelectric materials with *zT* > 1. For comparison, *p*-type chalcoantimonates such as $(Bi_{0.4}Sb_{0.6})_2Te_3$ have reached peak *zT* values up to 1.4.[86]

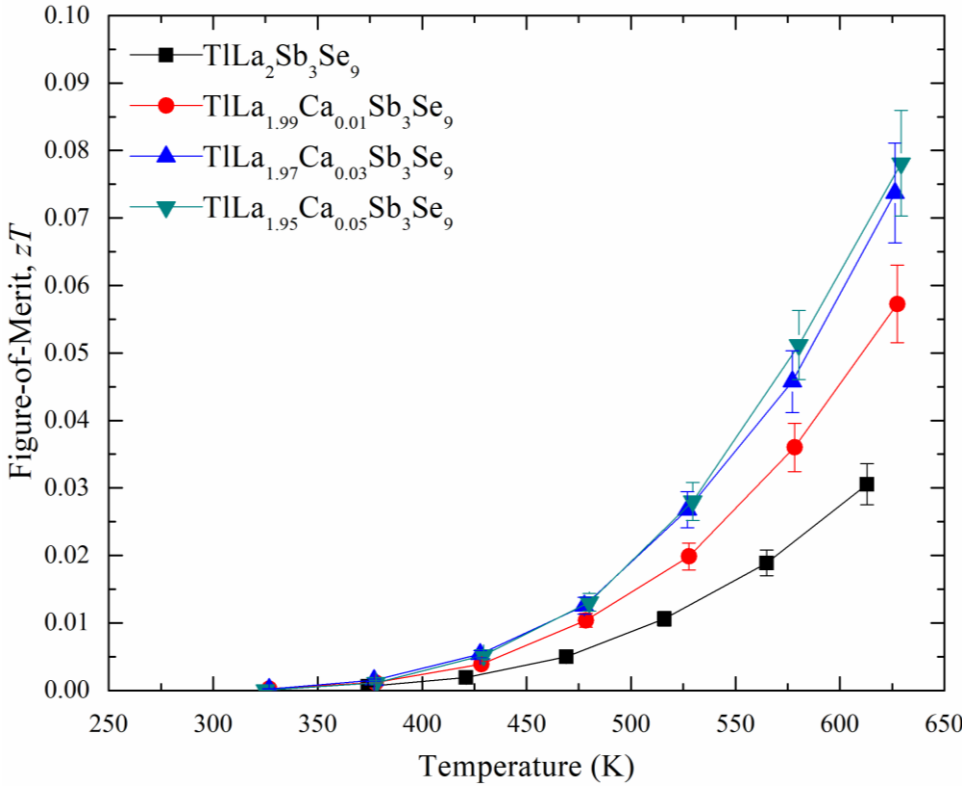

Figure 3.8. Thermoelectric dimensionless figure-of-merit of $TlLa_{2-x}Ca_xSb_3Se_9$ (x = 0, 0.01, 0.03, 0.05).

3.6 Conclusion

$TlLa_2Sb_3Se_9$ is a dark grey semiconductor with an experimental band gap of 0.68 eV, adopting an ordered variant of the $KLa_2Sb_3S_9$ type. Due to the complex crystal structure comprising stereochemically active Sb^{3+} cations, this material is bestowed with ultralow thermal conductivity. Attempts to obtain a competitive electrical conductivity *via* Ca doping were largely unsuccessful. The additon of *p*-type charge carriers did increase the electrical conductivity, but not sufficiently for the trend with respect to temperature to indicate that the material was behaving as an extrinsic semiconductor. Additionally, Se vacancies may be created in the material which largley negates the effects of the Ca dopant.

CHAPTER 4

$La_{12}Sb_9S_{38}$

Portions of this chapter have been reprinted with permission from

J. Mater. Chem. C. 2021, 9, 6553-6559.

4.1 Introduction

Antimony chalcogenides like the tetrahedrites $Cu_{12}Sb_4S_{13}$ [69,70] and the LAST materials (Lead-Antimony-Silver-Tellurium) [68] are at the forefront of research into the thermoelectric energy conversion.[71,74,87] They are also of interest as nonlinear optical materials because the lone pair of Sb^{3+} often causes noncentrosymmetric structures with strong second harmonic generation (SHG) effects.[88–92] Yet to date, only five different ternary lanthanoid antimony sulphides have been characterized, namely $La_7Sb_9S_{24}$,[93] $Yb_4Sb_2S_{11.25}$ along with its isostructural analogue $Tm_4Sb_2Se_{11.68}$,[94] $Pr_8Sb_2S_{15}$ [95] and its isostructural analogues $Ln_8Sb_2S_{15}$ with *Ln* = La, Pr, Nd [88] and $Ce_8Sb_2S_{15}$,[96] $Eu_3Sb_4S_9$ [97] and $Eu_6Sb_6S_{17}$.[98] Of these, only $Yb_4Sb_2S_{11.25}$, $Tm_4Sb_2Se_{11.68}$ and $Eu_6Sb_6S_{17}$ are also polysulfides, containing S_2^{2-} dumbbells and bent S_3^{2-} groups, respectively, and aside from the band gaps of $Yb_4Sb_2S_{11.25}$ and $Tm_4Sb_2Se_{11.68}$ of 1.71 eV and 1.22 eV, no properties have been reported to date.

Our ongoing studies of these systems uncovered the first ternary lanthanum antimony polysulfide, namely $La_{12}Sb_9S_{38}$, with several interesting structural features. These include a La/Sb mixed site, where the La atom is more regularly coordinated to the

surrounding S atoms than the Sb atom, like in $La_7Sb_9S_{24}$,[93] and a disorder of an isolated S^{2-} anion with an S_2^{2-} dumbbell, as also found in $Yb_4Sb_2S_{11.25}$.[94] Similarly, mixed Sm/Sb sites were observed in the oxide halides $Sm_{1.3}Sb_{1.7}O_4Cl$ and $Sm_{1.5}Sb_{1.5}O_4Br$.[99]

4.2 Synthesis

The title compound was initially synthesized from the elements stored in an argon-filled glove box (La: chips, 99.6%, Strem Chemicals; Sb: lumps, 99.5%, Fisher Scientific; S: pieces, 99.999%, Alfa Aesar). The mixtures were loaded into fused silica tubes, sealed under a vacuum and placed into a resistance furnace for heat treatment. They were heated over 6 hours to 923 K, left at this temperature for 12 hours, and over 120 hours cooled to 473 K to acquire crystals, and then turned off to cool down to room temperature.

Two different, red single crystals were obtained from samples with starting elemental ratios of La : Sb : S = 1.15 : 0.85 : 4 and 1 : 1 : 4; optical property measurements were done after solving the crystal structure on a new sample with a ratio of 12 : 9 : 38.

After that, the products were ground for analysis with an INEL powder X-ray diffractometer using Cu-$K\alpha_1$ radiation. The sample of nominal composition $La_{12}Sb_9S_{38}$ contained the target material in high yield with no clear evidence of any significant side products.

To further study the phase width and obtain more pure samples for the transport measurements, we prepared the binary sulphide La_3S_4 [100] to avoid using metallic lanthanum in the ball-mill. Then we carried out three reactions with different amounts of Sb and S according to the nominal target compositions $La_{12.17}Sb_{8.5}S_{38}$, $La_{12.17}Sb_{8.5}S_{37.75}$, and $La_{12}Sb_{8.67}S_{38}$. Each reaction was started in the Planetary Micro Mill Pulverisette 7 ball-mill

(FRITSCH) with a sample-to-ball mass of 1 : 15, using 600 revolutions per minute for eight hours.

After that the samples were pressed to round disks with diameters of 12.7 mm at 54 MPa at 773 K for 9 hours using the hot-press model FR-210-30T (Oxy-Gon Industries). This produced phase-pure samples in the cases of the target compositions $La_{12.17}S_{8.5}S_{38}$ and $La_{12.17}S_{8.5}S_{37.75}$, while minor side product peaks were evident in the X-ray powder patterns of the more Sb-rich sample $La_{12}Sb_{8.67}S_{38}$, identified with an asterisk (*) in Figure 4.1.

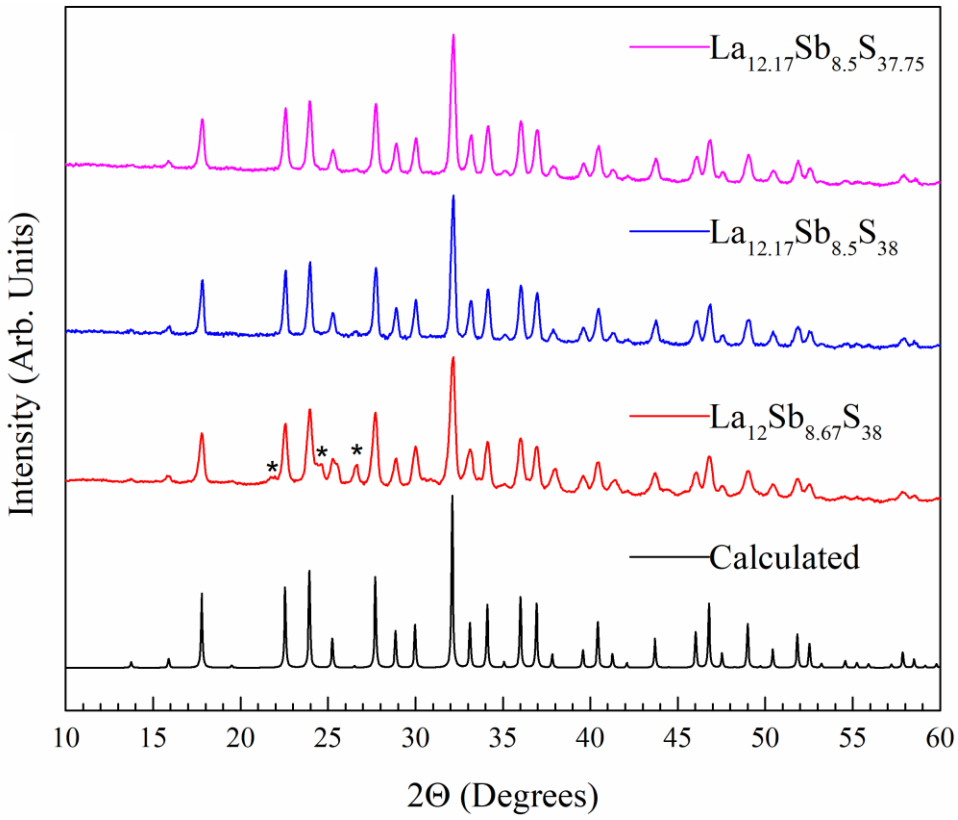

Figure 4.1. Experimental and calculated pXRD diagrams of different $La_{12+x}Sb_{9-y}S_{38-z}$ phases. *: peaks of unidentified side products. The cif of $La_{12.17(1)}Sb_{8.59(2)}S_{37.86(3)}$ was used to obtain the calculated pattern.

We employed a Bruker Kappa Apex II CCD with Mo-Kα radiation for the single crystal structure studies. The data were collected *via* ω scans. The data were corrected for Lorentz and polarization effects. We utilized the empirical multi-scan method *via* SADABS as a part of the APEX II software.[101] The crystal structures were solved and refined using the SHELXTL package,[45] and ultimately standardized *via* the TIDY routine embedded in PLATON.[77]

The structure solution was successful in the space group $Pm\overline{3}$ for the crystal from the nominal composition "$La_{1.15}Sb_{0.85}S_4$" sample, in line with the absence of systematic extinctions. The refinement with all identified positions *via* the direct methods, three La, one Sb, and four S sites resulted in a prominent peak of 44 e Å^{-3} in a physically impossible distance of 0.9 Å to La2, and distances of 2.4 Å – 2.6 Å to the surrounding S atoms, and a likewise impossible Sb1–Sb1 distance across a mirror plane of 0.7 Å. Consequently, we refined La2 as a split La/Sb site – as also observed in $La_7Sb_9S_{24}$ [93] – and Sb1 as 50% occupied, so the unreasonable Sb1–Sb1 distance is avoided throughout the crystal. These two changes lowered the R_1 value from 19.9% to 3.43% and the most significant residual electron density to 8 e Å^{-3}.

Upon closer inspection, we noticed that the S4 site had an unusually high U_{eq} value of 1.6 Å^2, indicative of lower electron density on that site, along with many too-short S4–S4 distances. Thus, the occupancy of this site was freely refined, resulting in an occupancy of 23%, an inconspicuous U_{eq} value and a vastly improved R_1 = 1.50%. Noting that the La2 site stood out with its U_{eq} = 0.019 Å^2 compared to the other La sites with their U_{eq} = 0.010 Å^2, we removed the constraint of a combined 100% occupancy of La2 and Sb2, i.e., freely refined the occupancy of La2 and Sb2. This resulted in occupancies of 53% for La2 and

43% for Sb2, thus a deficiency of 4% = 100% - 53% - 43% on that split position and an improvement from R_1 = 1.50% to R_1 = 1.36%. Tentative refinements of the occupancies of the other sites yielded no significant changes. With that, the formula was refined to $La_{12.17(1)}Sb_{8.59(2)}S_{37.86(3)}$, demonstrating significant deficiencies on cation and anion sites.

The refinements of the second crystal, taken from a different sample with a La : Sb starting ratio of 1 : 1 gave qualitatively the same results, culminating in a refined formula of $La_{12.10(1)}Sb_{8.60(2)}S_{37.79(6)}$ and R_1 = 1.6% (Tables 4.1 and 4.2).

Energy-dispersive X-ray spectroscopy (EDAX) was used to verify the elemental ratios of the refinement, using a QuantaFeg 250/Oxford Instrument x-act system. The average atomic-% of area scans on three separate single crystals were 20(1)% La, 14.4(3)% Sb, and 66(1)% S. This is in good agreement with the refined at.-% values of 20.8%, 14.7%, and 64.6 %.

The electronic structure was determined using the Perdew-Burke-Ernzerhof (PBE) functional for the generalized gradient approximation (GGA)[54] included in the Wien2K package, wherein the full-potential linearized augmented plane wave (FP-LAPW) method is applied within the density functional theory (DFT).[78,102] A model had to be constructed due to the partially occupied sites. The symmetry of this model was reduced from $Pm\overline{3}$ to $P1$ while retaining the original unit cell. The final stoichiometry of the $P1$ model was $La_{12}Sb_9S_{38}$. This model is electron-rich according to the formula $(La^{3+})_{12}(Sb^{3+})_9(S^{2-})_{24}(S_2^{2-})_7(e^-)$, i.e. having part of the conduction band filled. Since removing one La or Sb atom would have removed three electrons, we instead replaced one La atom with one Ba atom, achieving charge balance as in $Ba^{2+}(La^{3+})_{11}(Sb^{3+})_9(S^{2-})_{24}(S_2^{2-})_7$. The alternative, to triple

the unit cell and then remove one La or Sb atom, would have resulted in a too-large unit cell.

Diffuse reflectance spectroscopy was performed on $La_{12}Sb_9S_{38}$ since it is a dark red sample indicating a band gap within the visible light spectrum. A ground $La_{12}Sb_9S_{38}$ sample was mounted by adhering fine $La_{12}Sb_9S_{38}$ powder to a glass slide *via* double-sided tape. A PerkinElmer Lambda 1050 UV/VIS/NIR Spectrometer was used to obtain the diffuse reflectance spectrum. The diffuse reflectance spectrum of $La_{12}Sb_9S_{38}$ was collected from 300 nm to 1300 nm and converted to absorbance *via* the Kubelka-Munk equation: $\alpha/S = (1 - R)^2 / (2 R)$, where α is absorbance, S is the scattering factor, and R is the reflectance.

The thermal diffusivity (D) measurements of the hot-pressed samples $La_{12.17}S_{8.5}S_{38}$ and $La_{12.17}S_{8.5}S_{37.75}$ were performed using the Laser Flash DLF-1 (Environmental Module EM-1200, TA Instruments) under Ar (Figure A.7). The specific heat (C_p) was simultaneously determined using the Vespel standard, resulting in values above the Dulong-Petit limit of up to 20%, especially at elevated temperatures (Figure A.6). The thermal conductivity was calculated *via* $\kappa = D\rho C_p$, with ρ = density as determined using the Archimedes method.[103] The relative densities were 92(1)%. The experimental errors for the thermal conductivity are estimated to be ±5%.

Sound velocity v_S was measured on a hot-pressed pellet using a 5.0 MHz Walfront Smart Sensor Sound Velocity Meter with silicone oil as coupler, with its accuracy reported to be ±0.1 mm or ±7% of the thickness of the pellet.

In addition, Scanning electron microscopy (SEM) and EDAX studies were performed on the surfaces of both pellets used for the thermal conductivity determinations (Figures A.8 and A.9), and Rietveld refinements using GSAS-II[46] were carried on crushed

and ground parts of these pellets to verify composition and purity after these measurements (Figures A.4 and A.5). Notably, no side products were identified, and the refined formulae were equal to the nominal composition within two standard deviations, namely $La_{12.1(2)}Sb_{8.6(2)}S_{37.6(2)}$ in case of the pellet of the nominal composition $La_{12.17}S_{8.5}S_{38}$ and $La_{12.1(2)}Sb_{8.6(2)}S_{37.8(2)}$ in case of $La_{12.17}S_{8.5}S_{37.75}$.

Table 4.1. Crystallographic details of $La_{12.17(1)}Sb_{8.59(2)}S_{37.86(3)}$ and $La_{12.10(1)}Sb_{8.60(2)}S_{37.79(6)}$.

Parameters	$La_{12.17(1)}Sb_{8.59(2)}S_{37.86(3)}$	$La_{12.10(1)}Sb_{8.60(2)}S_{37.79(6)}$
Crystal system	Cubic	Cubic
Space group	$Pm\bar{3}$ (no. 200)	$Pm\bar{3}$ (no. 200)
a (Å)	11.1455(2)	11.151(1)
Unit cell volume (Å^3)	1384.52(7)	1386.5(3)
Crystal size (mm)	0.10 x 0.08 x 0.02	0.06 x 0.04 x 0.02
Formula units per unit cell, Z	1	1
Molecular Weight (g mol^{-1})	3951.55	3939.41
Density (g cm^{-3})	4.74	4.72
Radiation, wavelength (Å)	0.71073 (Mo Kα)	0.71073 (Mo Kα)
Temperature (K)	296	296
F(000)	1738	1733
Absorption coefficient, μ (mm^{-1})	14.71	14.63
Goodness-of-fit	1.18	1.08
R_1 [$I > 2\sigma(I)$][a]	0.014	0.016
wR_2 [$I > 2\sigma(I)$][b]	0.027	0.029
Largest diff. peak, hole (e Å^{-3})	1.53, -1.05	1.20, -1.18

Table 4.2. Interatomic distances (Å) of $La_{12.17(1)}Sb_{8.59(2)}S_{37.86(3)}$.

Atom pair	distance	Atom pair	Distance
La1–S2	3× 3.0212(4)	Sb1–S1	2× 2.4338(8)
La1–S3	3× 3.0191(2)	Sb1–S3	2.676(1)
La1–S1	3× 3.0440(4)	Sb1–S2	2× 3.3310(6)
		Sb1–S3	3.320(1)
La2–S3	2× 2.983(1)	Sb1-S2	2× 3.536(1)
La2–S3	2× 3.020(1)		
La2–S1	4× 3.0787(8)	Sb2–S4	2.618(2)
La2–S4	3.493(4)	Sb2–S3	2× 2.737(1)
		Sb2–S3	2× 2.767(1)
La3–S2	12× 3.1205(8)	Sb2–S1	4× 3.636(1)
		Sb2–S4	3.740(4)
S2–S2	2.085(2)		
S4–S4	2.00(1)		

4.3 Crystal Structure

$La_{12}Sb_9S_{38}$ adopts a new structure type comprising a three-dimensional network of Sb-S polyhedra. In its unit cell, depicted in Figure 4.2, we show all atoms as fully occupied, thus the physically impossible distances. This includes the distance of 0.7 Å across the mirror plane between two half-occupied Sb1 sites and between the split sites of La2 and Sb1 of 0.9 Å. Finally, the S4 sites form a cube around the origin with several too short

distances, namely 1.2 Å along its edge and 1.6 Å across its face. As such, only two of the eight S4 sites in each cube can be occupied, situated on opposing corners so that the shortest S4–S4 distance is along the space diagonal of 2.00 Å (Table 4.2), consistent with an S–S single bond in an S_2^{2-} dumbbell as found in Na_2S_2 (2.13 Å)[104] and LaS_2 (2.11 Å).[105] This works well with the refined occupancies being just below ¼, namely 22% in $La_{12.10}Sb_{8.60}S_{37.79}$ and 23% in $La_{12.17}Sb_{8.59}S_{37.86}$. Thus, each of these cubes contains either the S_2^{2-} dumbbell or an isolated S^{2-} ion, resulting in a 2- charge for each cube in either case. This situation is reminiscent of the one in $Yb_4Sb_2S_{11.25}$, where either the $(S4)^{2-}$ or the $(S5)_2^{2-}$ is present at that position in the crystal.[94] In addition, the S2 atoms also form an S_2^{2-} dumbbell with an S–S single bond of 2.09 Å in $La_{12}Sb_9S_{38}$, while the S1 and S3 sites have no noteworthy S–S contact, indicative of S^{2-} ions.

Treating the S4 site as 25% occupied results in the balanced formula of $((La, Sb)^{3+})_{21-x}(S^{2-})_{24}(S_2^{2-})_7$ with 62 positive and 62 negative charges when x = ⅓. Both refined formulae from the two single crystals studied match this x value well, with x = 0.30 in $La_{12.10}Sb_{8.6}S_{37.80}$ and x = 0.24 in $La_{12.17}Sb_{8.59}S_{37.86}$.

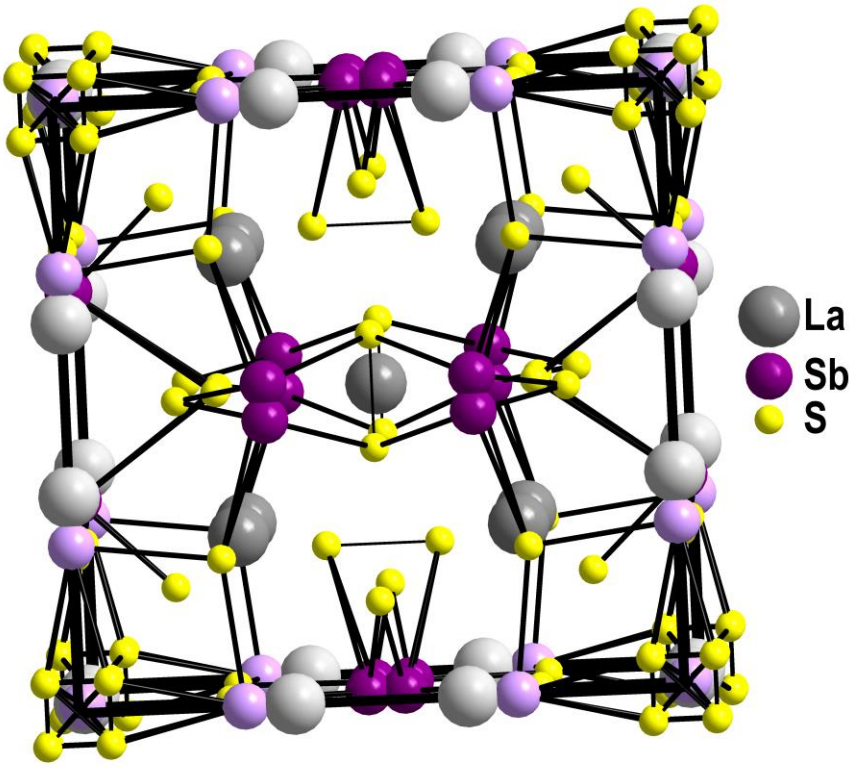

Figure 4.2. Crystal structure of $La_{12}Sb_9S_{38}$. La–S bonds are omitted for more clarity. The La2/Sb2 split sites are emphasized with lighter shades.

The La2/Sb2 split site is a consequence of the tendency of Sb towards shorter distances and more distorted polyhedra because of the free electron pair of Sb^{3+}, as visualized in Figure 4.3. Sb2 is surrounded by five S atoms at short distances between 2.62 Å and 2.76 Å, by five S atoms at 3.64 Å – 3.74 Å, and La2 more regularly by eight S atoms at distances between 2.98 Å and 3.08 Å, and one at 3.49 Å. Similarly, the La1/Sb1 split site in $La_{7+x}Sb_{9-x}S_{24}$ has nine La1–S distances between 2.79 Å and 3.45 Å, and four short Sb1–S distances between 2.54 Å and 2.83 Å and five longer Sb1–S of 3.39 Å to 3.62 Å,[93] and a comparable situation was reported to exist in $K_2Pr_{2-x}Sb_{4+x}Se_{12}$.[9]

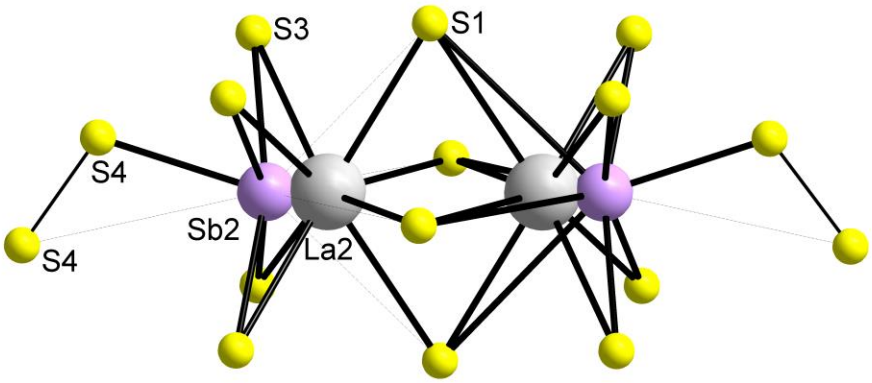

Figure 4.3. Interconnection of two pairs of the (Sb2)S10/(La2)S8 polyhedra. Distances from 3.63 Å to 3.74 Å are shown as dotted lines.

The interconnection of the $(La1)S_9$, $(La3)S_{12}$, and $(Sb1)S_8$ polyhedra is displayed in Figure 4.4. La1 is coordinated to nine S atoms at distances between 3.02 Å and 3.04 Å and shares common vertices with the $(La3)S_{12}$ polyhedron, wherein La3 is bonded to six $(S2)_2^{2-}$ dumbbells. The $(La1)S_9$ polyhedron shares a common edge with the $(Sb1)S_8$ polyhedron. It should be noted that only one of the Sb1 atoms shown can be present in such an $(Sb1)S_8$ polyhedron, each having three short Sb1–S bonds of 2.43 Å – 2.68 Å and five longer ones between 3.32 Å and 3.54 Å. Were the Sb1 atom to sit on the mirror plane (i.e. in the center of the split site shown in Figure 4.4), the most notable differences would be in the two Sb1–S3 distances, which would change from 2.68 Å and 3.32 Å to 2 × 3.00 Å. The split site formation may thus be viewed as yet another distortion arising from the lone pair effect of a Sb^{3+} cation.

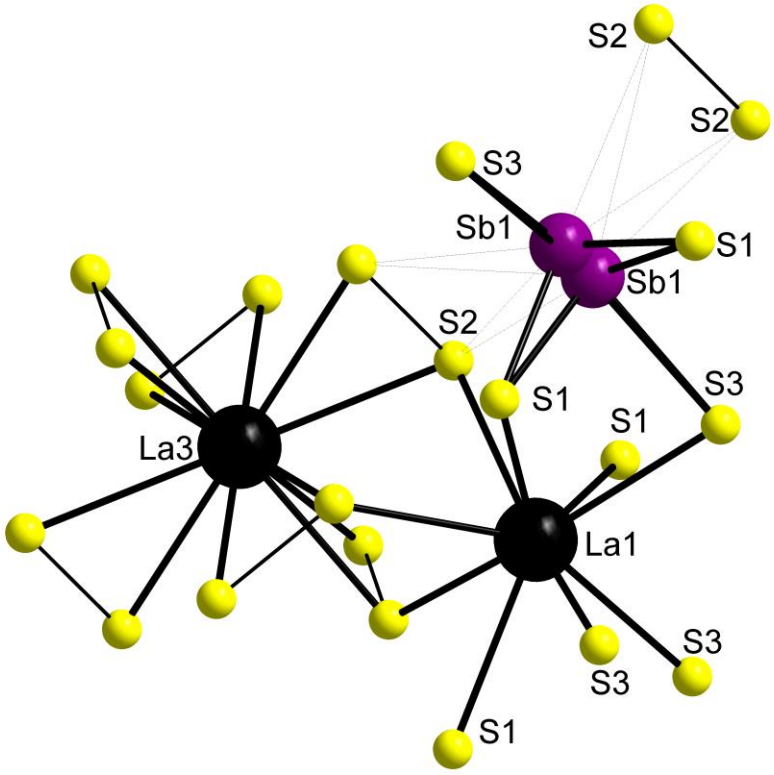

Figure 4.4. Interconnection of La1S9, La3S12, and Sb1S8 polyhedra. Distances from 3.33 Å to 3.53 Å are shown as dotted lines.

4.4 Theoretical Studies

We modelled the electronic structure of the charge-balanced material by replacing one La atom with Ba instead of calculating a tripled unit cell with one La vacancy. The band structure and density of states of the model $BaLa_{11}Sb_9S_{38}$ are depicted in Figure 4.5. $BaLa_{11}Sb_9S_{38}$ is semiconducting, in accord with the formulation $Ba^{2+}(La^{3+})_{11}(Sb^{3+})_9(S^{2-})_{24}(S_2^{2-})_7$ and the experimentally observed red colour. As typical for DFT calculations, the calculated band gap of 0.6 eV underestimates the real gap.

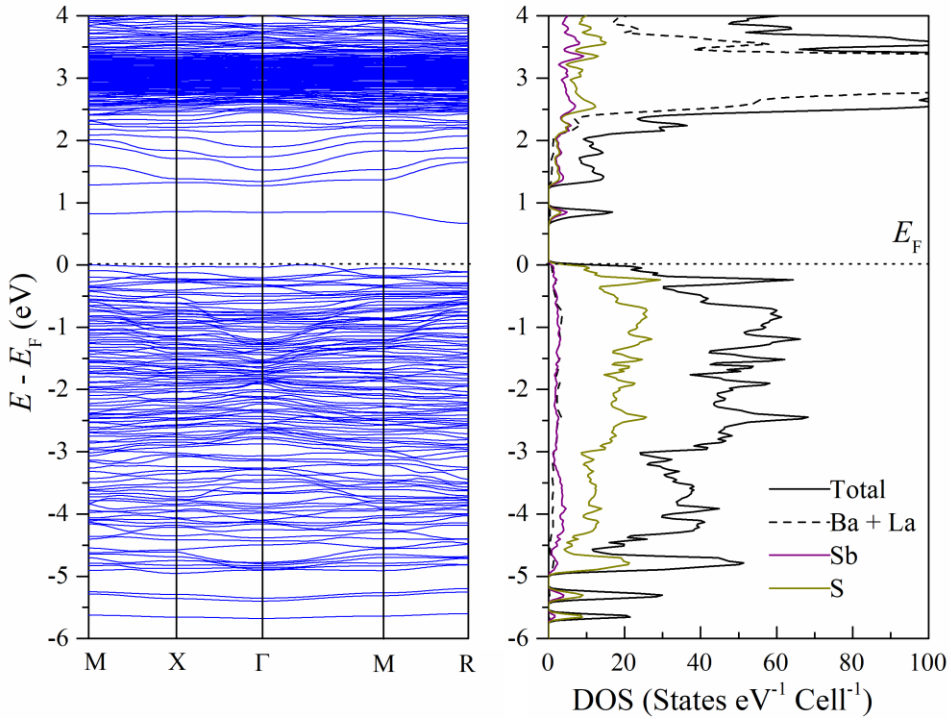

Figure 4.5. Band structure (left) and density of states (right) of the model $BaLa_{11}Sb_9S_{38}$.

Flat bands at the bottom of the conduction band and the top of the valence band indicate a high effective mass, low mobility, a significant Seebeck coefficient and low electrical conductivity. Similarly, flat bands were encountered in the thiospinel $CuCr_{1.75}Sb_{0.25}S_4$, where the additional presence of more dispersed bands enabled $CuCr_{1.7}Sb_{0.3}S_4$ to attain a peak zT of 0.43 around 900 K.[106] The co-existence of the steep and flat band has generally been proven helpful for enhanced power factors, for example, most recently demonstrated for various sulphide perovskites.[107] Unfortunately, this material has no such steep bands, which may be problematic in achieving high thermoelectric performance.

4.5 Physical Properties

4.5.1 UV-Vis-NIR Spectroscopy

Considering the red colour of the title compounds, the above-mentioned charge-balanced formula of $((La,Sb)^{3+})_{20.67}(S^{2-})_{24}(S_2^{2-})_7$, and the model calculation, semiconducting properties are to be expected. Correspondingly, the absorbance spectrum reveals an optical band gap of 1.75 eV (Figure 4.6), as expected based on the dark red colour. The same band gap of 1.71 eV was reported for $Yb_4Sb_2S_{11.25}$, which also contains an S_2^{2-} dumbbell.

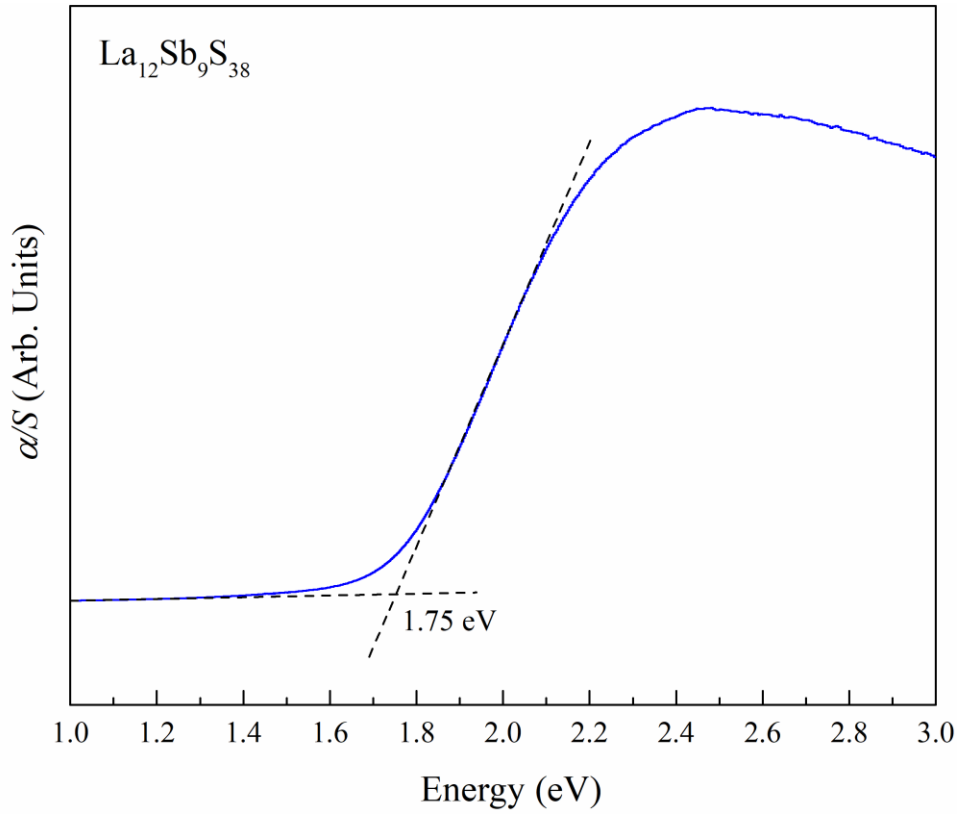

Figure 4.6. Absorbance spectrum of $La_{12}Sb_9S_{38}$.

Moreover, we were unable to measure the electrical conductivity because of the high resistance of the sample, also indicative of semiconducting (or insulating) character.

Thermal conductivity measurements were performed on two samples of nominal compositions $La_{12.17}Sb_{8.5}S_{37.8}$ and $La_{12.17}Sb_{8.5}S_{37.75}$, resulting in insignificant decreases with increasing temperature and overall, very similar curves and low values between 1.05 W $m^{-1}K^{-1}$ and 0.80 W $m^{-1}K^{-1}$ (Figure 4.7). It should be pointed out that the diffusivity curves show a smooth decrease with temperature (Figure A.7) and that the two local minima around 350 K and 520 K stem from the heat capacity measurements using Vespel (Figure A.6), i.e. are experimental artifacts.

4.5.2 Thermal Conductivity

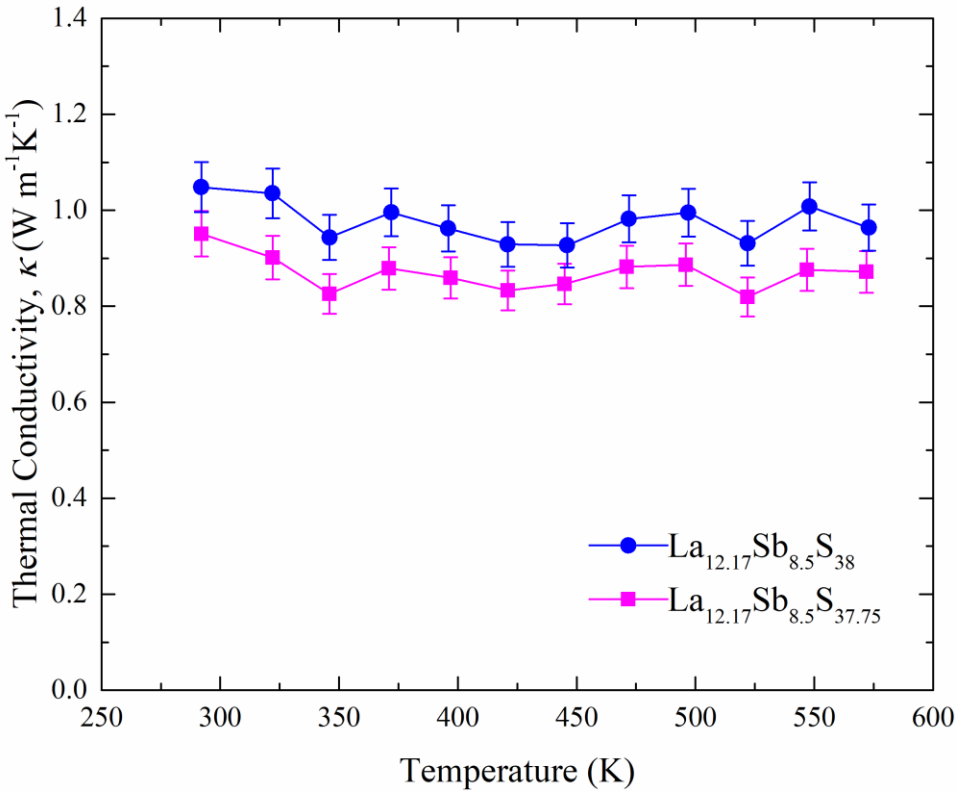

Figure 4.7. Thermal conductivity of $La_{12}Sb_9S_{38}$.

As there is no contribution from the electronic thermal conductivity, the total conductivity equals the lattice thermal conductivity. The values around 1 W $m^{-1}K^{-1}$ are shallow for a sulphide but in line with this complicated crystal structure that includes a La/Sb disorder and Sb and S split sites. For example, bulk PbS with the high molar mass of Pb but the simple NaCl structure type exhibits room temperature lattice thermal conductivity values of 2.2 W $m^{-1}K^{-1}$ – 2.7 W $m^{-1}K^{-1}$, depending on the synthesis method.[108] To compare the impact of the molar mass of Pb, a look at the average molar masses is instructive, namely the molar mass of PbS divided by 2, the number of atoms per formula unit. This yields average molar masses of (207.20 + 32.07) g mol^{-1} / 2 = 119.6 g/mol for PbS and 3951.55 g mol^{-1} /58.62 = 67.4 g/mol for $La_{12.17}Sb_{8.59}S_{37.86}$, which is around 44% less. For comparison, the average molar mass of PbTe is 167.4 g/mol, explaining in part why thermoelectric research has been focussed on tellurides, not sulphides, for decades.

Comparably low thermal conductivity values were achieved in the closer related tetrahedrites, e.g. 0.9 W $m^{-1}K^{-1}$ in undoped $Cu_{12}Sb_4S_{13}$.[69] Therein, the large dynamic displacement of some Cu atoms and the lone pair effect of the Sb site were identified as a cause for the low thermal conductivity.[109] In sulphides with more disorder, such as the bornites with mostly disordered metal atom sites, much lower values of the order of 0.4 W $m^{-1}K^{-1}$ can be attained.[110]

To determine the minimal (glass-like) thermal conductivity κ_{glass} according to Cahill,[111] and the Debye temperature θ_{D}, we measured the speed of sound at room temperature:

$$\kappa_{\mathrm{glass}} = 1.21\, n^{2/3}\ k_{\mathrm{B}}\, v_{\mathrm{S}} \qquad (4.5.1)$$

$$\Theta_{\mathrm{D}} = \frac{\hbar}{k_{\mathrm{B}}} (6\pi^2 n)^{1/3} v_{\mathrm{S}} \tag{4.5.2}$$

Here, $\hbar$ is the reduced Planck constant, k_B is the Boltzmann constant, n is the number density of atoms, and v_S is the arithmetic average of the speed of sound. With the experimentally determined v_S = 2930 m s^{-1}, we obtain κ_{glass} = 0.62 W m^{-1}K^{-1}. We thus note that the disorders observed here are not enough to bring the thermal conductivity down to the Cahill limit. The Debye temperature calculated from the speed of sound at room temperature of θ_D = 304 K lies between the ones of SnS (270 K) and Sb_2S_3 (310 K).

4.6 Conclusion

The first lanthanum antimony polysulfide was presented in this work. $La_{12+x}Sb_{9-y}S_{38-z}$ adopts a new structure type, which is comprised of a La/Sb mixed site with a small deficiency, an Sb split site, and disordered S_2^{2-} dumbbells.

$La_{12+x}Sb_{9-y}S_{38-z}$ is a semiconducting material with an optical band gap of 1.75 eV, in accord with the charge-balanced formula $((La,Sb)^{3+})_{21-x}(S^{2-})_{24}(S_2^{2-})_7$ with 62 positive and 62 negative charges when x = ⅓. Despite its relatively low average molar mass of 67.4 g mol^{-1}, low thermal conductivity values around 1 W m^{-1}K^{-1} were experimentally determined. These values are caused by the complex crystal structure and various disorders, resulting in enhanced phonon scattering. It remains to be explored whether significantly enhanced thermoelectric properties can be attained by optimizing the charge carrier concentration.

CHAPTER 5

$Ba_6Ge_2Se_{12}$ and $Ba_7Ge_2Se_{17}$

Portions of this chapter have been reprinted with permission from

Inorg. Chem. 2023, 62, 1, 285–294.

5.1 Introduction

Zintl compounds are characterized by their adherence to the simple octet counting rules. These materials' compositions are primarily explained by the ionic interactions between group one and two elements with their post-transition metal counterparts. Herein, the ternary Ba-Ge-Se phase space is investigated and expanded to include two previously unreported compounds: $Ba_6Ge_2Se_{12}$ and $Ba_7Ge_2Se_{17}$. So far, only two barium seleno-germanates have been reported, namely Ba_2GeSe_4 and $Ba_2Ge_2Se_5$.[4,6.] The former is a member of a diverse class of compounds with the general formula $M^{II}_2TtQ_4$, where M^{II} is either one or two different divalent cations, the tetrel *Tt* a tetrahedrally coordinated cation such as Si, Ge, or Sn, and *Q* is a chalcogen atom such as S or Se. Exploratory search into M^{II}-*Tt*-*Q* materials has been a reliable strategy for researchers to discover new compounds and structure types.[4,112–116] Many of these compounds have been investigated for their non-linear optical (NLO) properties, partly because they are composed of non-centrosymmetric building blocks into the structure, such as $[TtQ_4]^{4-}$ tetrahedra.[34,117–121] Although neither $Ba_6Ge_2Se_{12}$ (space group $P2_1/c$) nor $Ba_7Ge_2Se_{17}$ (*Pnma*) crystallizes in a non-centrosymmetric space group, they adopt new structure types. Stoichiometric analogs containing Sr, Sn, or S could not be synthesized. Despite this, several chalcogen-rich compounds can be found

in the literature with similar stoichiometries and low symmetries such as $Sr_4Sn_2Se_9$ ($P2_12_12$), [122] $Sr_4Sn_2Se_{10}$ (*Pbam*),[122] Ba_2SnSe_5 ($P2_1/c$ and $P2_12_12_1$),[123–125] Ba_2SnTe_5 ($P2_1/c$),[126] $Ba_{12}Sn_4S_{23}$ ($P2_1/n$)[127], $Ba_7Sn_3S_{13}$ (*Pnma*), [127] $Ba_7Sn_3Se_{13}$ (*Pnma*),[128] $Ba_7Sn_5S_{15}$ ($P6_3cm$),[129] and $Ba_8Sn_4S_{15}$ ($Pca2_1$).[130]

Out of the previously reported barium seleno-germanates and seleno-stannates, only the metastable structure of Ba_2SnSe_5 in space group $P2_1/c$ contains positional disorder.[124] The title compounds $Ba_6Ge_2Se_{12}$ and $Ba_7Ge_2Se_{17}$ both have disordered polyatomic anions. $Ba_6Ge_2Se_{12}$ contains disordered Se_2^{2-} dumbbells, and $Ba_7Ge_2Se_{17}$ contains disordered $[GeSe_5]^{4-}$ anions. Disordered molecular groups are common in the crystal structures of organic compounds that co-crystallize with their solvents or have *tert*-butyl groups but are relatively uncommon in inorganic compounds.[131,132]

5.2 Synthesis

The synthesis of the two title compounds was carried out through high-temperature solid-state reactions. Single crystals of the two new compounds were obtained by loading stoichiometric amounts of elements (Ba: pieces, 99.7%, Strem Chemicals; Ge: pieces, 99.999%, Strem Chemicals; Se: powder, 99.999%, Alfa Aesar) into carbon-coated silica tubes inside a dry argon-filled glove box. The silica tubes containing the elements were evacuated to $< 2.5\times10^{-3}$ bar before finally sealing the ampoules with an H_2/O_2 torch. To produce the crystals suitable for single crystal X-ray diffraction (XRD), the samples were heated to 923 K over 24 h and slowly cooled to room temperature at 2 K h^{-1}.

To produce single-phase bulk samples of $Ba_6Ge_2Se_{12}$ and $Ba_7Ge_2Se_{17}$, a different approach was required to account for the high reactivity of Ba and the high melting points of Ba and Ge, 1000 K and 1211 K, respectively. For the bulk samples, stoichiometric amounts of Ba, Ge and Se

were added to glassy carbon crucibles and lowered into 13 mm diameter silica tubes. The total mass of the elements was restricted to 500 mg to fit into the crucibles easily. The silica tubes were then evacuated, and flame sealed. The $Ba_6Ge_2Se_{12}$ and $Ba_7Ge_2Se_{17}$ samples were placed in programmable furnaces to heat to 923 K over 24 h and held at this temperature for 100 hours. The furnace temperature was then lowered to 623 K and held at this temperature for another 100 hours before being shut off. To determine the purities of the samples, powder X-ray diffraction (XRD) diagrams were collected on an INEL XRG 3000 diffractometer equipped with a Cu-Kα_1 radiation source. Analysis of the powders' diffraction patterns revealed that in addition to the target material, ternary and binary side products that correspond to the following reaction equations were present in the two cases:

$$6\ Ba + 2\ Ge + 12\ Se \rightarrow 2\ Ba_2GeSe_4 + 2\ BaSe_2 \qquad (5.2.1)$$

$$7\ Ba + 2\ Ge + 17\ Se \rightarrow 2\ Ba_2GeSe_4 + 3\ BaSe_3 \qquad (5.2.2)$$

To remove these side products, the samples were ground into homogeneous powders and hot-pressed into dense pellets for further annealing. The powders were hot-pressed into 12.7 mm diameter pellets in an Oxy-Gon model FR-210-30T hot-press at 627 K for 16 hours under 54 MPa of pressure. At this point, $Ba_7Ge_2Se_{17}$ was determined to be a single phase *via* powder XRD, but $Ba_6Ge_2Se_{12}$ still had small impurity peaks in the diffraction pattern. The pellet was sealed again in an evacuated silica tube and annealed in a manual furnace for 10 days at 627 K.

Single crystal structures were performed using a Bruker Kappa Apex II CCD with Mo-Kα radiation. $Ba_6Ge_2Se_{12}$ forms red platelets, and $Ba_7Ge_2Se_{17}$ forms black needle-like crystals. The data was collected in 30 s intervals *via* ω scans. The multi-scan method was used for the absorption correction within SADABS.[133] Both crystal structures were solved and refined using the

SHELXTL package.[44,45] The $Ba_6Ge_2Se_{12}$ crystal was refined as a twin. Finally, the refined atomic positions were standardized *via* the "TIDY" procedure in the PLATON software.[134,135]

Both crystal structures were initially refined without disordered atomic sites, resulting in sizeable residual electron densities. In $Ba_6Ge_2Se_{12}$, two such Q peaks with electron densities of 19 and 15 e $Å^{-3}$ remained, and in $Ba_7Ge_2Se_{17}$, four prominent Q peaks with electron densities of 22 e $Å^{-3}$, 22 e $Å^{-3}$, 21 e $Å^{-3}$, and 13 e $Å^{-3}$ remained, that all had physically impossible distances to the central atoms. These Q positions were identified as Ge or Se sites with low occupancies depending on their coordination environments. Adjacent Ge and Se atoms with the impossibly short distances to the newly added sites also refined their occupancies.

After refining this model for $Ba_6Ge_2Se_{12}$, two Se atoms tended towards ~78% occupancy, whereas the other two sites tended towards 22% occupancy. Similarly, one Ge and three Se sites tended towards 80% occupancy in $Ba_7Ge_2Se_{17}$, whereas the other one Ge and three Se sites tended towards 20% occupancy. Upon visual inspection, it became clear that the groups of atoms with similar occupancies were related to their counterparts through symmetry. In $Ba_6Ge_2Se_{12}$, the disordered Se sites correspond to a pair of Se_2^{2-} dimers that are rotated 90º about the midpoint of their Se-Se bonds. In $Ba_7Ge_2Se_{17}$, two $[GeSe_5]^{4-}$ overlapping polyhedra share Se3 and Se7. For the Ge atoms to remain at the center of each polyhedron, the Ge site must be split, creating a 15º pivot about the Se3 and Se7 axis. With this revelation, the models were again refined using the "PART" instruction in SHELXTL to refine the occupancies of the high occupancy sites with their low occupancy counterparts. The occupancies of the disordered parts were constrained to sum to 100%. The final refined occupancies for the Se_2^{2-} dimers were 0.7837(2) and 0.2163(2) in $Ba_6Ge_2Se_{12}$. The occupancies of the overlapping $[GeSe_5]^{4-}$ polyhedra in $Ba_7Ge_2Se_{17}$ are 0.8093(1) and 0.1907(1), respectively. Since the parts were constrained to sum to 100% occupancy, the charge-

balanced formulas are $(Ba^{2+})_6(Ge^{4+})_2(Se^{2-})_8(Se_2^{2-})_2$ and $(Ba^{2+})_7(Ge^{4+})_2(Se^{2-})_6(Se_2^{2-})_4(Se_3^{2-})$. Crystallographic details of both data collections are summarized in Table 5.1, and atomic positions, U_{eq} values and occupancy factors in Tables A.3 and A.4.

Table 5.1. Crystallographic data for $Ba_6Ge_2Se_{12}$ and $Ba_7Ge_2Se_{17}$ from the sXRD experiments.

Parameters	$Ba_6Ge_2Se_{12}$	$Ba_7Ge_2Se_{17}$
Crystal system	Monoclinic	Orthorhombic
Space group	$P2_1/c$ (no. 14)	*Pnma* (no. 62)
a (Å)	10.0903(2)	12.652(1)
b (Å)	9.3640(2)	20.069(2)
c (Å)	25.7643(5)	12.3067(9)
β (º)	90.303(1)	90
Unit cell volume ($Å^3$)	2434.32(9)	3124.8(4)
Crystal size (mm)	0.13 x 0.04 x 0.02	0.16 x 0.02 x 0.02
Formula units per unit cell, *Z*	4	4
Molecular Weight ($g\ mol^{-1}$)	1916.74	2448.88
Density ($g\ cm^{-3}$)	5.230	5.205
Radiation, wavelength (Å)	0.71073 (Mo Kα)	0.71073 (Mo Kα)
Temperature (K)	296	296
F(000)	3232	4136
Absorption coefficient, μ (mm^{-1})	29.902	30.361
Goodness-of-fit	1.07	1.02
R_1 [$I > 2\sigma(I)$][a]	0.029	0.026
wR_2 [$I > 2\sigma(I)$][b]	0.051	0.056
Largest diff. peak, hole ($e\ Å^{-3}$)	2.23, -2.69	3.02, -1.95

To further support the conclusion that there are disordered parts in the crystal structures of $Ba_6Ge_2Se_{12}$ and $Ba_7Ge_2Se_{17}$, Rietveld refinements were performed in GSAS-II.[46] Refining the powder XRD pattern is helpful to determine if the disordered sites are accurate or an artifact of the twinned crystal data. Only the isotropic thermal displacement parameters (U_{iso}) were refined due to the lower resolution of the one-dimensional powder XRD detector compared to the 2D detectors used for single-crystal refinements. The occupancies of the disordered parts were again constrained to sum to 100%. For comparison, ordered models were also created that only used the sites with greater occupancy. The results from these models were discarded since they led to large U_{iso} associated with the disordered sites signaling that these positions were overly occupied when they had 100% occupancy. For the $Ba_6Ge_2Se_{12}$ sample, three peaks from an unknown phase were visible in the powder XRD. These peaks that could not be linked to Ba_2GeSe_4, $BaSe_2$, or any other barium selenide were excluded from the refinement range (23.9º, 25.5º, and 29.6º).

The pair distribution function (PDF) was also used to understand local disorder within these structures. Total scattering data was collected at 11-ID-B at Advanced Photon Source. The data was transformed *via* a sine Fourier transform using GSAS-II software.[46] The Q_{max} was fixed to 24 $Å^{-1}$. This work opted not to apply the Lorch function, as this function results in a lower spatial resolution of the data, and a higher spatial resolution was necessary to distinguish between the different models during the analysis. Small-box modelling was performed using PDFgui.[48] Data was modelled between 1.85 Å, and 15 Å. Fitting was restrained to the low radius region to probe the local structure of the system. A maximum radius of r = 15 Å was chosen for both systems as this is the distance between the Se chains in $Ba_6Ge_2Se_{12}$ and between the Ge-Se polyhedron layers in $Ba_7Ge_2Se_{17}$. Small-box refinements were performed using refined average structure from single

crystal data as a starting model. The scale, lattice parameters, atomic displacement parameters, and atomic positions were refined. The Q_{damp} and Q_{broad} parameters were refined from a nickel standard. The weighted residual (R_w) was used to evaluate the fit quality. Here R_w is defined as:

$$R_W = \sqrt{\frac{\sum_{i-1}^{N} w(r_i)[G_o(r_i) - G_c(r_i)]^2}{\sum_{i-1}^{N} w(r_i)[G_o(r_i)]^2}} \tag{5.2.3}$$

where $G_o(r_i)$ is the experimental intensity at a radial distance r_i, $G_c(r_i)$ is the calculated intensity from the refined model at r_i, and $w(r_i)$ is the weight of the data point at r_i.

The optical band gaps of these phases were obtained *via* diffuse-reflectance spectroscopy. The powdered samples were cold-pressed into pellets. These pellets were mounted vertically with double-sided tape in a PerkinElmer Lambda 1050 UV/vis/NIR spectrometer. The reflectance data were converted to an absorption spectrum using the Kubelka-Munk equation ($\alpha/S = (1 - R)^2/(2R)$), where α is the absorption, R the reflectance and S a scattering factor, which is constant for particle sizes larger than ~5 μm.

Thermal conductivity measurements were performed on both phases' hot-pressed and annealed pellets. The total thermal conductivity (κ_{tot}) was measured from room temperature up to 573 K in an argon atmosphere using a TA Instruments DLF 1200 instrument. κ_{tot} is calculated from thermal diffusivity (D), specific heat (C_P) and density (ρ) *via* the formula $\kappa_{tot} = DC_P\rho$. The Archimedes method obtained densities which were > 90% of their respective theoretical densities. A Vespel standard was used to obtain the experimental C_P. Alternatively, the C_P can be derived from the Dulong-Petit law. The experimental error of the κ_{tot} measurements is estimated to be 5%. κ_{tot} can be defined as the sum of the lattice component of thermal conductivity and the electrical component of thermal conductivity, i.e. $\kappa_{tot} = \kappa_{lat} + \kappa_{ele.}$ The minimum thermal conductivity (κ_{diff})

may be derived from the sound velocity (v_s) through the material.[49] The v_s was obtained by coupling the pellets with silicone oil to a 5.0 MHz Walfront Smart Sensor Sound Velocity Meter.

Models had to be constructed to calculate the electronic structures of these two phases since some of the atomic sites are partially occupied. We opted to create two models for each compound. One of the models only included the more highly occupied disordered sites, whereas the second model, in each case, only included the less occupied disordered sites. The electronic structures of the two title phases were calculated by density functional theory (DFT) within the WIEN2k package.[78,102] The Perdew-Burke-Ernzerhof (PBE) function with the generalized gradient approximation (GGA) was used until the energy had converged to < 0.001 Ry and the electric charge had converged to < 0.001 e^-.[54] For $Ba_6Ge_2Se_{12}$, a 6 × 6 × 2 *k* point mesh in the reciprocal lattice was used to meet these convergence criteria.[27] The uneven distribution of *k* points along the different axes results from the *c* axis in the $Ba_6Ge_2Se_{12}$ being more than twice as long as the *a* or *b* axes. Similarly, the first Brillouin zone of $Ba_7Ge_2Se_{17}$ was divided into a 5 × 3 × 5 *k* point grid. Using these calculations, the band structures and density of states (DOS) were calculated for both compounds. XCrySDen was used to select the *k* vectors along a path in the Brillouin zone that includes all the high symmetry vertices for the band structure.[136]

The more highly occupied disordered Se sites, Se3 and Se12, form a staggered 1D chain along the *a* direction in $Ba_6Ge_2Se_{12}$. As the polyselenides Se_2^{2-} and Se_3^{2-} are relatively common in Se-rich compounds, we determined the average length of the Se chain in $Ba_6Ge_2Se_{12}$, given the refined occupancies. A C# script was written to track the consecutive instances of either orientation appearing for given probabilities.[137]

5.3 Crystal Structures

5.3.1 $Ba_6Ge_2Se_{12}$

$Ba_6Ge_2Se_{12}$ crystallizes in the monoclinic $P2_1/c$ space group and has a relatively large unit cell volume of 2434.3 $Å^3$. All atoms exist on the low symmetry 4e Wyckoff position. This leads to six Ba, two Ge and fourteen Se positions. Four Se sites are related *via* disordered Se dumbbell pairs, meaning in any given unit cell, only 10 + 4/2 = 12 of the Se sites are occupied. We opted to refer to this compound as $Ba_6Ge_2Se_{12}$ rather than reducing the formula to Ba_3GeSe_6 because of the number of symmetrically unique crystallographic sites.

The major structural motifs of $Ba_6Ge_2Se_{12}$ are the $[GeSe_4]^{4-}$ tetrahedra and the staggered 1D chains of Se_2^{2-} dumbbells (Figure 5.1). These chains run parallel to the *a*-axis of the unit cell and perpendicular to the rows of aligned $[GeSe_4]^{4-}$ tetrahedra. The Se atoms are not evenly spaced throughout the staggered chain. The Se atoms pair up into Se_2^{2-} dumbbells with Se-Se bond distances of 2.33 Å – 2.38 Å. The Se-Se distance between adjacent Se pairs is 2.70 Å. This is much shorter than the distances between the aligned Se_2^{2-} dumbbells in $Ba_{12}In_4Se_{20}$ (3.51 Å).[8] Unevenly spaced Se chains have been observed in other compounds such as the $Ln_4O_4Se_3$ family of compounds where *Ln* = La, Ce, Pr, Nd, or Sm.[138–140] Additionally, each Se dumbbell has a disordered counterpart that is rotated by approximately 90º about the center of the Se-Se bond. Both dumbbell positions are not equally likely, with the Se positions aligned along the *a* axis being occupied 78% of the time and the pairs perpendicular to the *a* axis being occupied 22% of the time. As seen in Figure 5.2, the anisotropy of the Se dumbbells is accentuated in the direction of the chain, whereas the perpendicular dumbbells are in and out of the plane of the figure.

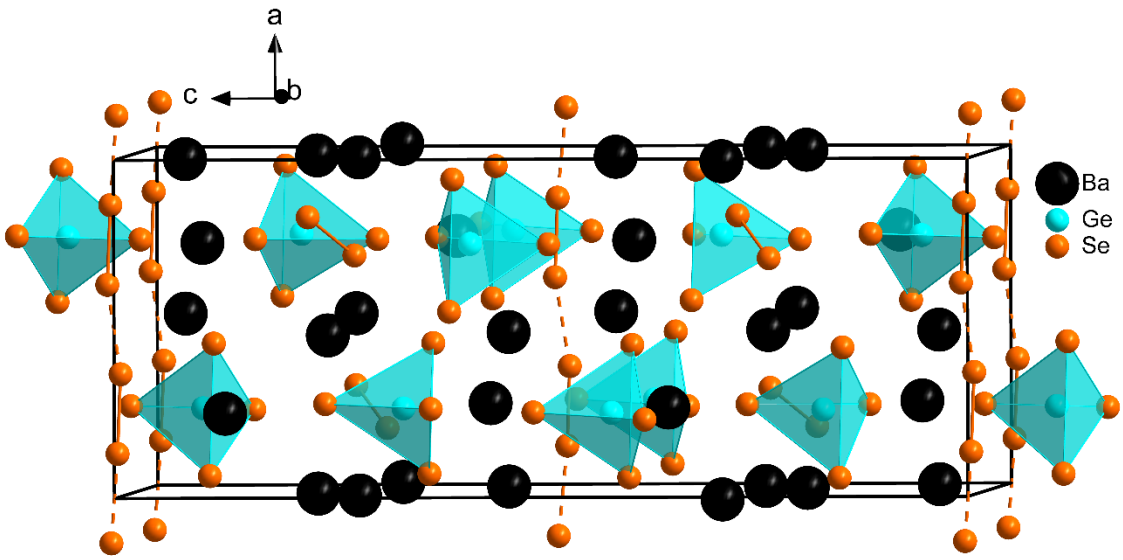

Figure 5.1. Crystal structure of $Ba_6Ge_2Se_{12}$. Se5 and Se13 have been excluded for clarity and to highlight the linear chain of the Se3 and Se12 atoms.

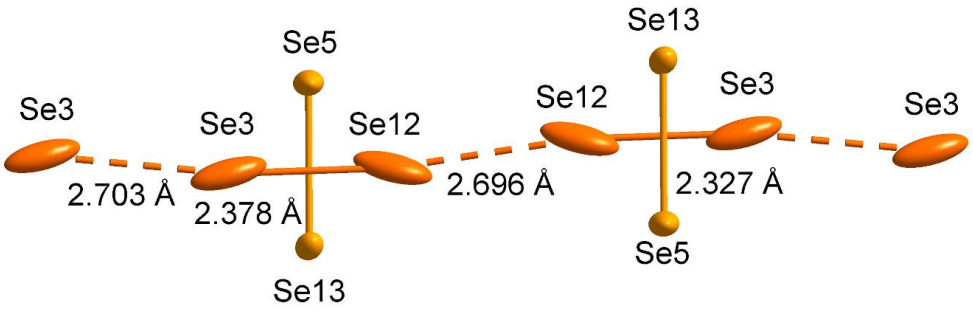

Figure 5.2. Se_2^{2-} disorder in the 1D chain of $Ba_6Ge_2Se_{12}$. Se-Se distances greater than 2.4 Å are shown as dashed lines. The Se sites that are less occupied (Se5 and Se13) are shaded more lightly. The anisotropy of Se5 and Se13 is most pronounced perpendicular to the plane.

There are also isolated Se_2^{2-} anions composed of Se4 and Se9 with a bond length of 2.37 Å (Figure 5.3), which aligns with the Se-Se bond lengths in the 1D chain. The Ge-Se bond lengths in the $[GeSe_4]^{4-}$ tetrahedra range from 2.32 Å – 2.36 Å. This is nearly identical to the range of Ge-Se bond lengths found in Ba_2GeSe_4 (2.33 Å – 2.36 Å).[4]

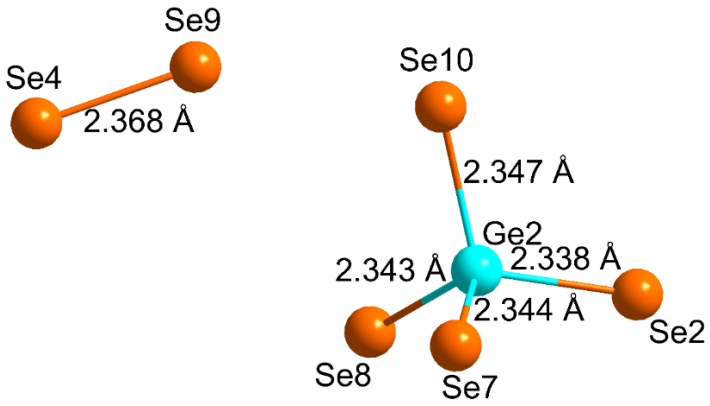

Figure 5.3. Isolated Se_2^{2-} anion (left) and an example of a $[GeSe_4]^{4-}$ tetrahedron (right).

5.3.2 $Ba_7Ge_2Se_{17}$

$Ba_7Ge_2Se_{17}$ crystallizes in the *Pnma* space group and has a large unit cell volume of 3125 $Å^3$. This new structure type contains a variety of anionic motifs, namely $[GeSe_5]^{4-}$, Se_2^{2-} and Se_3^{2-}. The anions are organized into alternating $[GeSe_5]^{4-}$ and polyselenide layers along the *b* direction (Figure 5.4). The $[GeSe_5]^{4-}$ units are tetrahedral like $[GeSe_4]^{4-}$ but with a Se_2^{2-} capping the tetrahedra instead of a single Se ion. The Se-Se bond lengths in Se_2^{2-} are longer than in $Ba_6Ge_2Se_{12}$. The bond length is 2.43 Å in the isolated dumbbell and 2.40 Å in $[GeSe_5]^{4-}$, and 2.33 Å and 2.37 Å in the nonlinear Se_3^{2-} unit (Figure 5.5).

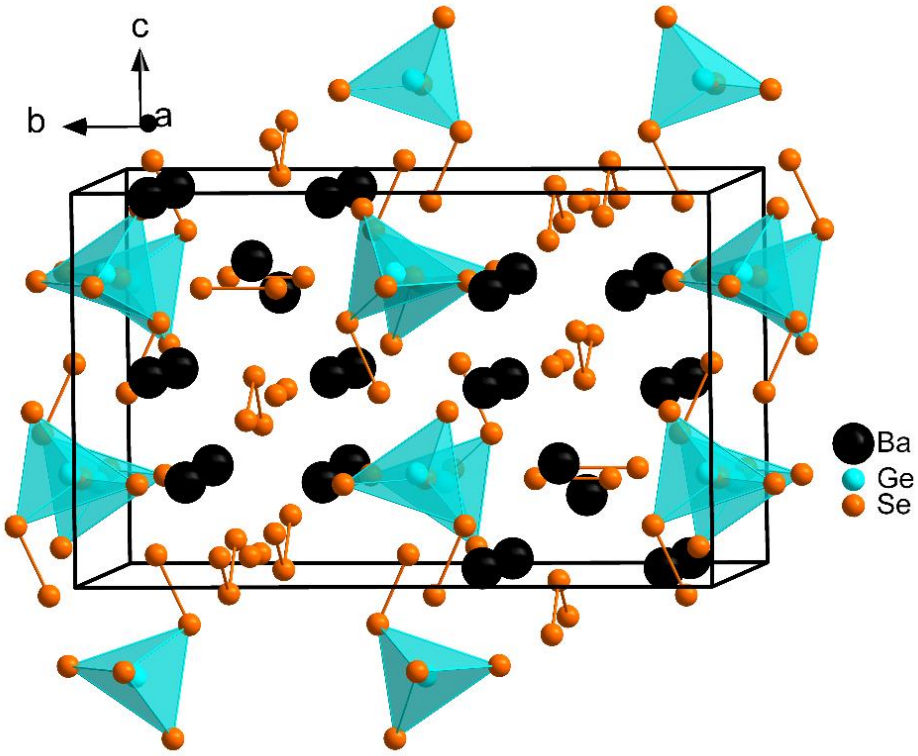

Figure 5.4. Crystal structure of $Ba_7Ge_2Se_{17}$. Only the more highly occupied $[GeSe_5]^{4-}$ anion is portrayed. Ge2, Se1, Se4, and Se6 have been excluded for clarity.

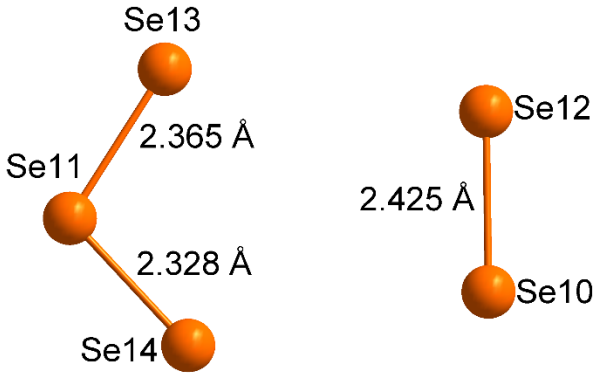

Figure 5.5. The polyselenide motifs in $Ba_7Ge_2Se_{17}$. Left: Se_3^{2-}; right: Se_2^{2-}.

Unlike in $Ba_6Ge_2Se_{12}$, the anion disorder in this structure type is found in the $[GeSe_5]^{4-}$ anion rather than the Se_2^{2-} dumbbells. The $[GeSe_5]^{4-}$ anion is unevenly split across two atomic site sets. Both orientations of the anion share Se3 and Se7, and the remaining Ge and three Se atoms are

topologically related to their counterparts by performing a reflection across the two shared Se sites. The PART1 anion has an 81% occupancy rate, and the PART2 anion has a 19% occupancy rate, according to the refinement of the single crystal data. The Rietveld refinement of $Ba_7Ge_2Se_{17}$ was performed using the disordered $[GeSe_5]^{4-}$ model. The atoms associated with PART1 (Ge1, Se2, Se4, and Se6) had an occupancy of 77% after the refinement, and the atoms associated with PART2 (Ge2, Se2, Se5, and Se9) therefore an occupancy of 23%.

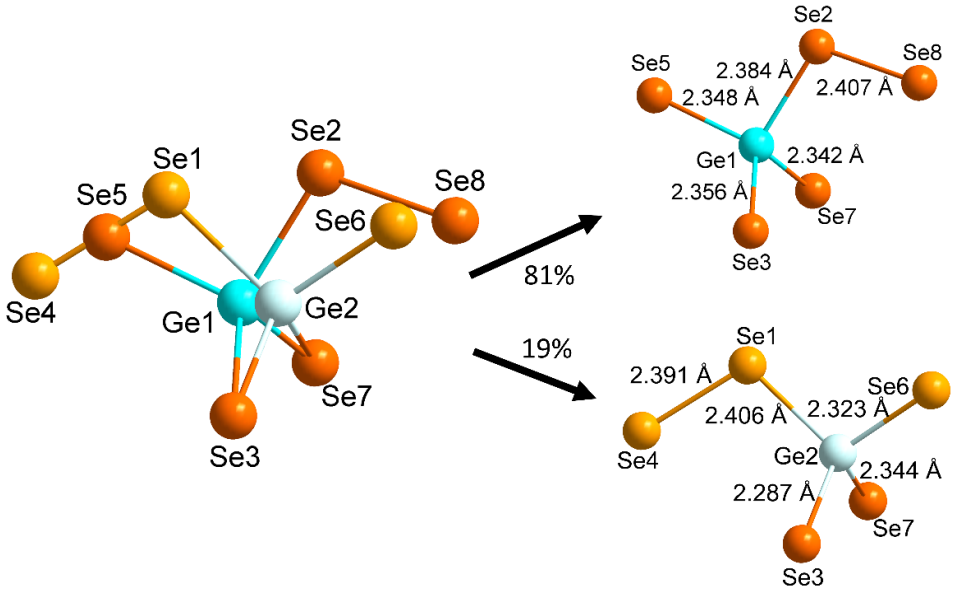

Figure 5.6. $[GeSe_5]^{4-}$ anion disorder with overlapping ions (left) and their structures, along with occupancies and bond lengths (right).

Figure 5.7 depicts the different coordination environments of the Ba atoms with respect to the disordered Se sites. In $Ba_6Ge_2Se_{12}$, the Ba atoms adjacent to the 1D Se chain do not straddle the center of the chain. This leads to short Ba-Se distances (2.92 Å) between Ba3 and Se13. As a result, the Se13 and correspondingly Se5 sites are unfavorable. In $Ba_7Ge_2Se_{17}$ the Ba-Se distances associated with PART1 range from 3.31 Å – 3.57 Å, and the Ba-Se distances from PART2 range from 3.15 Å – 3.40 Å. The slightly shorter Ba-Se distances may account for the disparity in the

occupancy between the two sets of atomic sites. Additionally, the coordination number of Ba2 increases from C.N. = 8 to 9 when the Se4 site of PART2 is occupied.

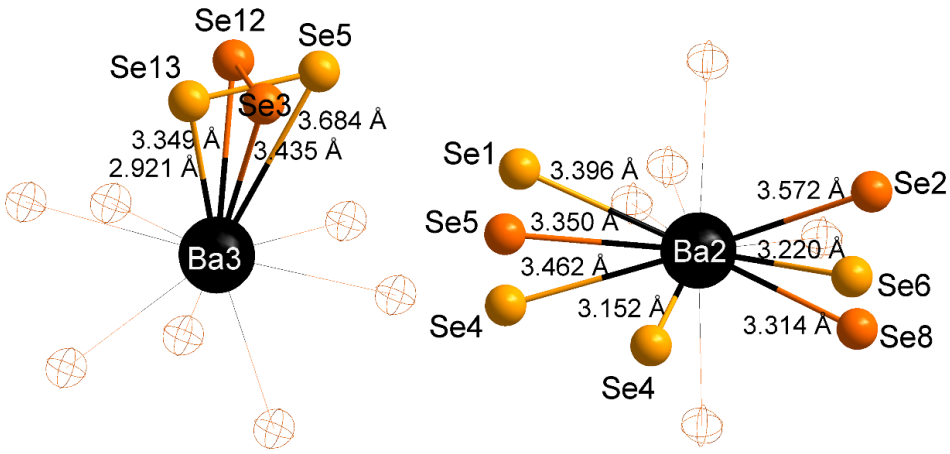

Figure 5.7. Ba3 coordination sphere in $Ba_6Ge_2Se_{12}$ (left) and Ba2 coordination sphere in $Ba_7Ge_2Se_{17}$ (right). Se atoms with 100% occupancy are only depicted as outlines.

5.3.3 Single Crystal and Rietveld Refinements

The Rietveld refinement of the polycrystalline $Ba_6Ge_2Se_{12}$ sample (Figure 5.8) leads to similar occupancies of the Se_2^{2-} pairs in the staggered chain. The Rietveld refinement decreased the occupancy of PART1 from 78% to 73% and correspondingly increased the occupancy of PART2 from 22% to 27%.

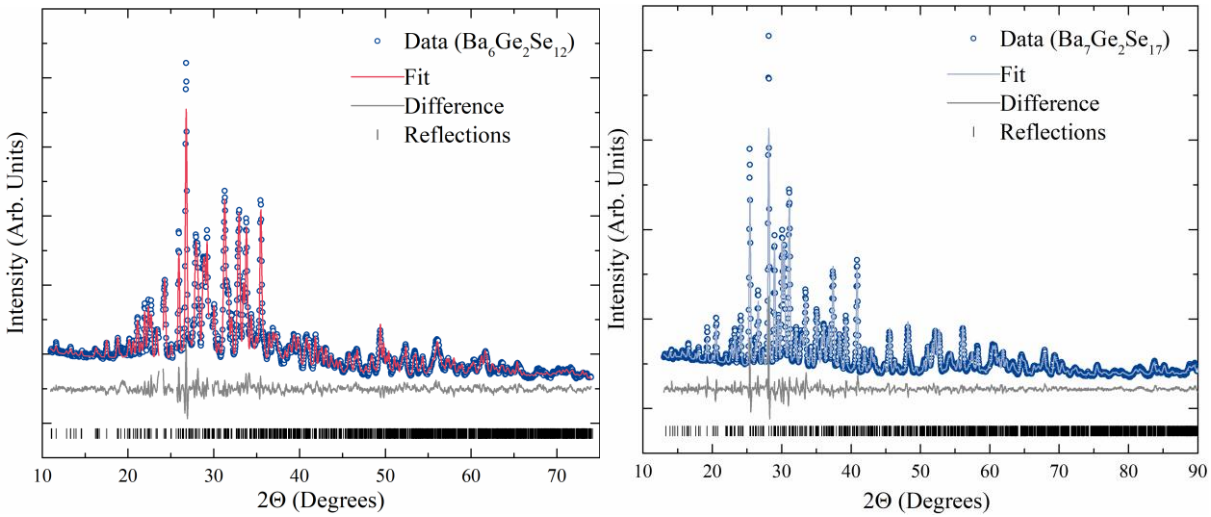

Figure 5.8. Rietveld refinement fits. $Ba_6Ge_2Se_{12}$ (left) and $Ba_7Ge_2Se_{17}$ (right) data.

A simulation was run using the probabilities obtained from the single-crystal refinement to determine the distribution of Se atom chain lengths. It was observed that the number of consecutively oriented dumbbells was most likely to be only one unit long. Se_2^{2-} aligned along the *a* axis have a 78% probability of being occupied, and there is a 22% chance that the length of this chain is one unit long. 99% of Se atom chains along the *a* axis are 18 units (i.e. 36 Se atoms) long or less. The number of consecutive antiparallel dumbbells decays rapidly due to its lower occupancy rate. 78% of antiparallel dumbbells have no aligned neighbours. Figure A.8 shows the probabilities of the lengths of aligned Se_2^{2-} dumbbell chains.

5.3.4 Pair Distribution Function Refinements

Disorder of molecular groups is relatively rare in the crystal structures of inorganic compounds compared to the crystal structures of organic compounds. To verify that the disordered atomic coordinates are not just an artifact of twinning in the single-crystal XRD data, the local structures of $Ba_6Ge_2Se_{12}$ and $Ba_7Ge_2Se_{17}$ were investigated *via* PDF analysis. Unlike diffraction

experiments that summarize the average structure, the PDF analysis probes the local environment within a structure. Thus, the PDF analysis provides a direct description of the disorder, or lack thereof, within $Ba_6Ge_2Se_{12}$ and $Ba_7Ge_2Se_{17}$.

Small-box modelling was used to analyze the PDF data. Three models were used to describe experimental data: (1) Case A: PART1 and PART2 fixed at 100% and 0%, respectively; (2) Case B: PART1 and 2 fixed at 0% and 100%, respectively; and (3) Disordered: occupancies of PART1 and 2 were refined. Figure 5.9 depicts the PDF refinements for both structures using the three models. The lowest R_w was achieved with the disordered model for both $Ba_6Ge_2Se_{12}$ and $Ba_7Ge_2Se_{17}$. This demonstrates that the disordered models best describe the experimental data and supports the evidence of disorder provided by single-crystal XRD. In addition, the refined occupancies are within error of the model provided by diffraction experiments ($Ba_6Ge_2Se_{12}$: PART1 = 73%, PART2 = 27%; $Ba_7Ge_2Se_{17}$: PART1 = 79%, PART2 = 21%), thus providing quantitative validation for the degree of disorder in $Ba_6Ge_2Se_{12}$ and $Ba_7Ge_2Se_{17}$. The agreement of structural models obtained from diffraction and PDF data shows that the average structure accurately describes the local structure, and that disorder within the novel barium seleno-germanates is present on both the average and local scale.

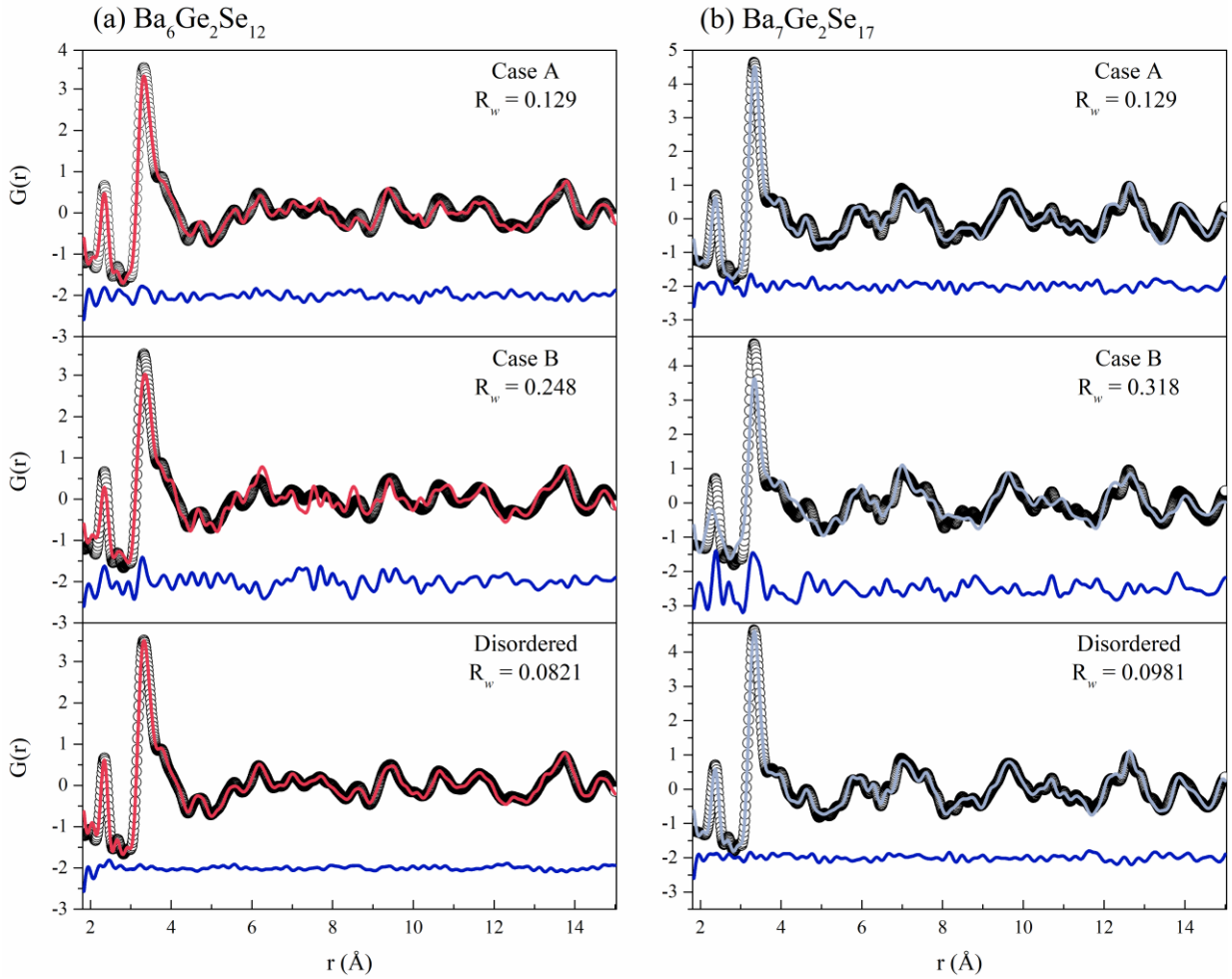

Figure 5.9. Small-box modelling of X-ray pair distribution function (PDF) data collected on (a) $Ba_6Ge_2Se_{12}$; and (b) $Ba_7Ge_2Se_{17}$. PDF fits were derived from two ordered models (Case A and Case B) and a disordered model. Ordered models for each system only contain PART1 or PART2 for Case A and B, respectively. Disordered models for each system do not constrain PART 1 and PART2 occupancies. Black open circles = experimental data, red and grey lines = calculated fit, blue line = difference.

5.4 Theoretical Studies

The new barium compounds models of the unit cells had to be constructed to calculate the electronic structures due to their disordered elements. Since only specific atom groups are disordered, the models kept the original unit cell parameters and set the occupancies of PART1 or 2 to either 100% or 0%.

The band structure of $Ba_6Ge_2Se_{12}$ dramatically depends upon the orientation of the Se_2^{2-} dumbbells. When the Se_2^{2-} are aligned along the *a* axis, their p_x orbitals change steeply in energy parallel to *a** (Y – Γ and Z – C in Figure 5.10). In the model with Se_2^{2-} aligned perpendicular to the *a* axis, the bands have slight variation and remain primarily flat (Figure 5.10). The total energy of the $Ba_6Ge_2Se_{12}$ model with PART1 occupied was 0.48 eV formula unit^{-1} lower in energy than the model with PART2 occupied. The calculated indirect band gap changes therefore substantially from 0.79 eV to 1.38 eV (Figure A.11). Experimental diffuse reflectance measurements give an experimental band gap of 1.75 eV, which better agrees with the structural model without the staggered Se chain. From the statistical analysis, it is unlikely to have long sequences of aligned Se_2^{2-}.

Since the electronic structures of the $Ba_6Ge_2Se_{12}$ models vary greatly, and supercell model was created to have 75% of the Se3 and Se12 sites occupied and 25% of the Se5 and Se13 sites occupied. The supercell was doubled in the *a* direction, and the density of the *k* point grid was lowered accordingly in the *a** direction to 3 × 6 × 2. Depending on which pairs of Se atoms are deleted in the supercell, the symmetry can be reduced from $P2_1/c$ (no. 14) to either $P2_1$ (no. 4) or *Pc* (no. 7). The model was created by removing all the symmetry of the supercell to remove Se atoms individually. Once the desired Se sites had been removed, symmetry was added back with

the "ADDSYM" command in the PLATON program.[134,135] The band structure of the $Ba_6Ge_2Se_{12}$ supercell is plotted in Figure 5.10. Compared to the $Ba_6Ge_2Se_{12}$ model with only the highly occupied Se dumbbells, the calculated band gap increased from 0.79 eV to 1.09 eV. The extreme variation in the *a** direction between Y – Γ and Z – C has also been dampened.

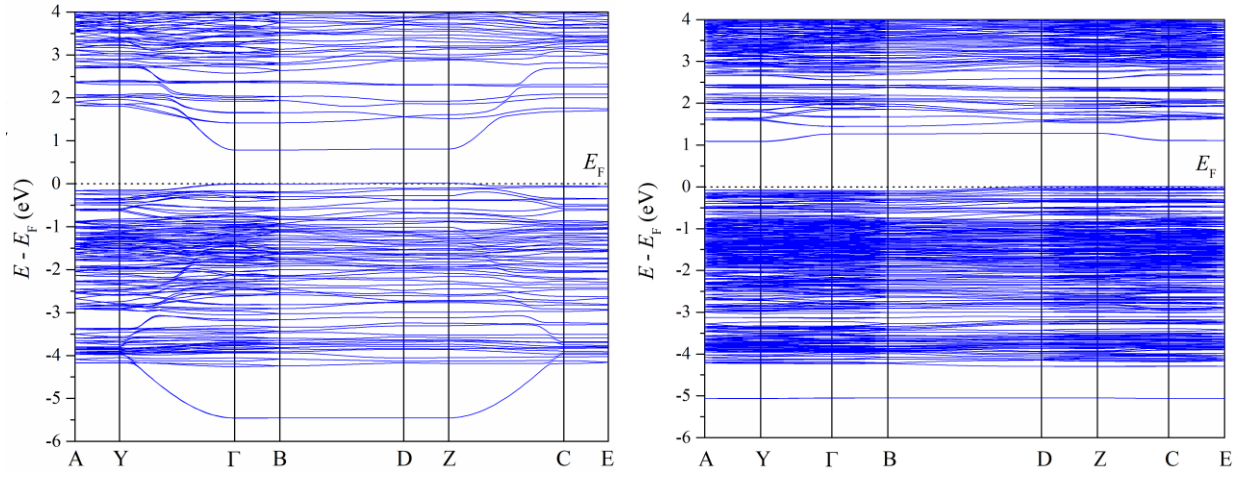

Figure 5.10. Band structures of two $Ba_6Ge_2Se_{12}$ models. The more highly occupied Se dumbbells (left) and the 2 × 1 × 1 supercell with 75% of Se atoms in the more highly occupied sites (right).

As with $Ba_6Ge_2Se_{12}$, two structural models were also constructed for $Ba_7Ge_2Se_{17}$. Since the disordered $[GeSe_5]^{4-}$ anion in this structure type does not contribute to long-range structural motifs, the two models have similar results. The band structures of both models have flat bands throughout the top of valence bands suggesting low electrical conductivity if *p*-type (Figure 5.11). As with the electronic structures of $Ba_6Ge_2Se_{12}$, the most significant energy changes are present in the lowest Se-based conduction bands of $Ba_7Ge_2Se_{17}$. As expected, changing the orientation of the isolated $[GeSe_5]^{4-}$ anions does not significantly affect the electronic structure. The total energy of the $Ba_7Ge_2Se_{17}$ model with PART1 occupied was 1.09 eV formula unit^{-1} lower in energy than the model with PART2 occupied. The two models' calculated indirect band gaps are 0.70 eV (Figure

A.13). This is lower than the band gaps of the $Ba_6Ge_2Se_{12}$ models caused by the two lowest-lying conduction bands.

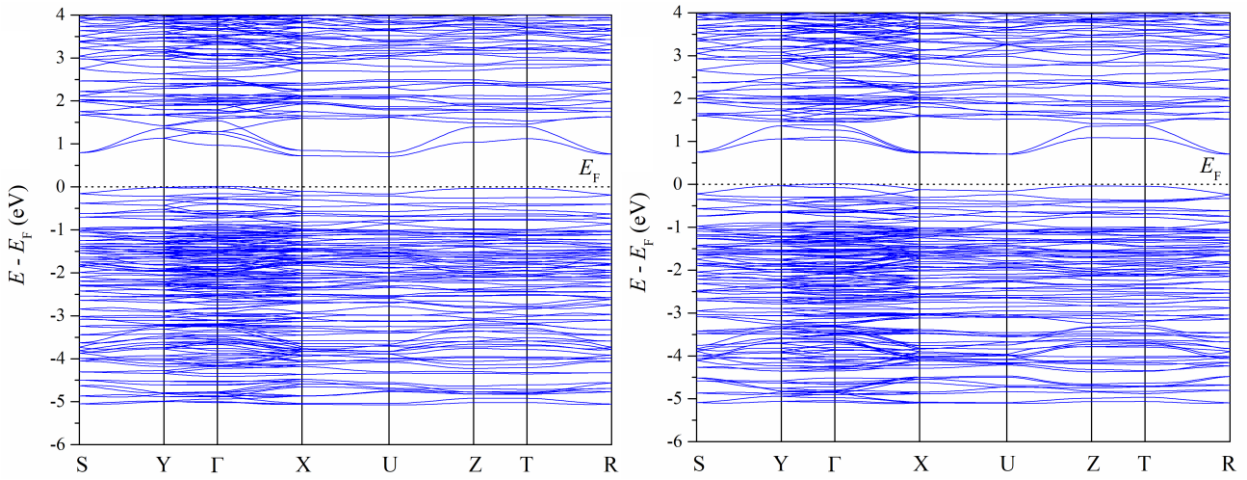

Figure 5.11. Band structures of the two $Ba_7Ge_2Se_{17}$ models. The more highly occupied $[GeSe_5]^{4-}$ anion (left) and the less occupied $[GeSe_5]^{4-}$ anion (right).

5.5 Physical Properties

5.5.1 UV-Vis-NIR Spectroscopy

The experimental band gaps of $Ba_6Ge_2Se_{12}$ and $Ba_7Ge_2Se_{17}$ were obtained by converting the diffuse reflectance spectra into the absorbance spectra *via* the Kubelka-Munk equation (Figure 5.12). The optical band gaps were obtained by extending the baseline absorbance until it intercepted the linear tangent of the absorption edge. The experimental band gaps for $Ba_6Ge_2Se_{12}$ and $Ba_7Ge_2Se_{17}$ were thus found to be 1.75 eV and 1.51 eV, respectively. This agrees with the brown colour of $Ba_6Ge_2Se_{12}$ and the black colour of $Ba_7Ge_2Se_{17}$.

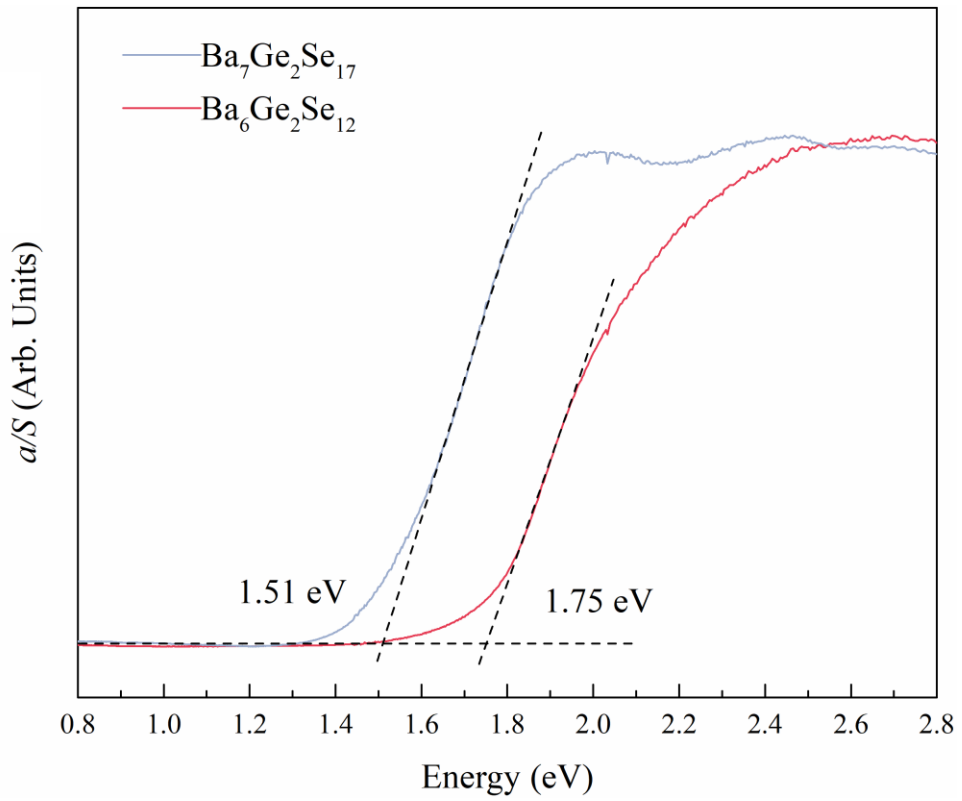

Figure 5.12. Absorbance spectra of the $Ba_6Ge_2Se_{12}$ and $Ba_7Ge_2Se_{17}$ samples.

5.5.2 Differential Scanning Calorimetry

Differential scanning calorimetry (DSC) was performed from room temperature up to 673 K for $Ba_6Ge_2Se_{12}$ and $Ba_7Ge_2Se_{17}$. The compounds are stable after completing a heating and cooling cycle up to 673 K. There is no indication in the DSC plots that a phase transition is affecting the 1D chains in $Ba_6Ge_2Se_{12}$, such as a Peierls distortion.

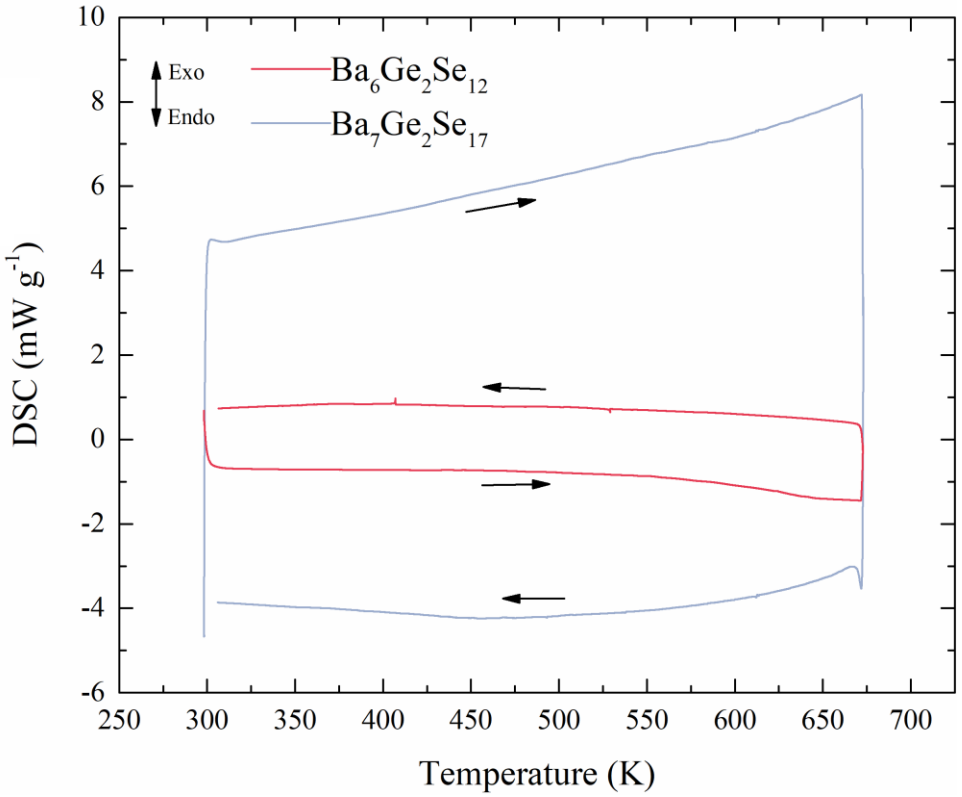

Figure 5.13. DSC of the $Ba_6Ge_2Se_{12}$ and $Ba_7Ge_2Se_{17}$ samples from room temperature up to 673 K.

5.5.3 Thermal Conductivity

The diffuson model predicted the hot-pressed pellets' minimum thermal conductivity (κ_{diff}).[49] The sound velocity (v_s) was measured by coupling the hot-pressed pellets to a transducer with silicone oil. The sound velocities were determined to be 3750 m s^{-1} and 2735 m s^{-1} for $Ba_6Ge_2Se_{12}$ and $Ba_7Ge_2Se_{17}$, respectively. The κ_{diff} is given by the expression $\kappa_{diff} \approx 0.76\, n^{2/3}\, k_B\, \frac{1}{3}(2 v_T + v_L)$, where n is the number density of the compound (atoms m^{-3}), k_B is the Boltzmann constant, v_T is the transverse sound velocity and v_L the longitudinal sound velocity. The velocities v_T and v_L are related to v_s by the expression $v_s = \frac{1}{3}(2v_T + v_L)$. κ_{diff} was calculated to be 0.40 W m^{-1} K^{-1} and

0.30 W m^{-1} K^{-1} for $Ba_6Ge_2Se_{12}$ and $Ba_7Ge_2Se_{17}$, respectively. These values assume 100% density of the pellets since *n* is evaluated from the crystallographic data.

For the final calculation of κ_{tot}, the C_P values derived from the Dulong-Petit law were used since experimental values did not approach the Dulong-Petit limit at higher temperatures. Plots of the temperature-dependent C_P and *D* are depicted in Figures A.14 and A.15. The κ_{tot} of these selenides is remarkably low (Figure 5.14). Both selenides have extremely similar thermal conductivity values from room temperature to 573 K due to their large unit cell volumes and similar compositions. The κ_{tot} decreases over the temperature range until a minimum value of 0.33 W m^{-1} K^{-1} was achieved in both samples at 573 K. The low κ_{tot} is in line with other selenides that have been studied for their thermoelectric applications, for example, Cu_2Se with 1.0 W m^{-1} K^{-1} at 300 K,[141] single crystal SnSe with 0.46 W m^{-1} K^{-1} at 300 K,[142] $AgCrSe_2$ with 0.7 W m^{-1} K^{-1} at 300 K,[143] Tl_3VSe_4 with 0.30 W m^{-1} K^{-1} at 300 K,[144] and $CdAg_2Bi_6Se_{11}$ with 0.54 W m^{-1} K^{-1} at 300 K.[145] Due to the low number of intrinsic charge carriers and relatively wide band gap of these compounds, the total thermal conductivity (κ_{tot}) is approximately equivalent to the lattice thermal conductivity (κ_{lat}), since the electrical, thermal conductivity (κ_{ele}) is essentially zero at these temperatures.

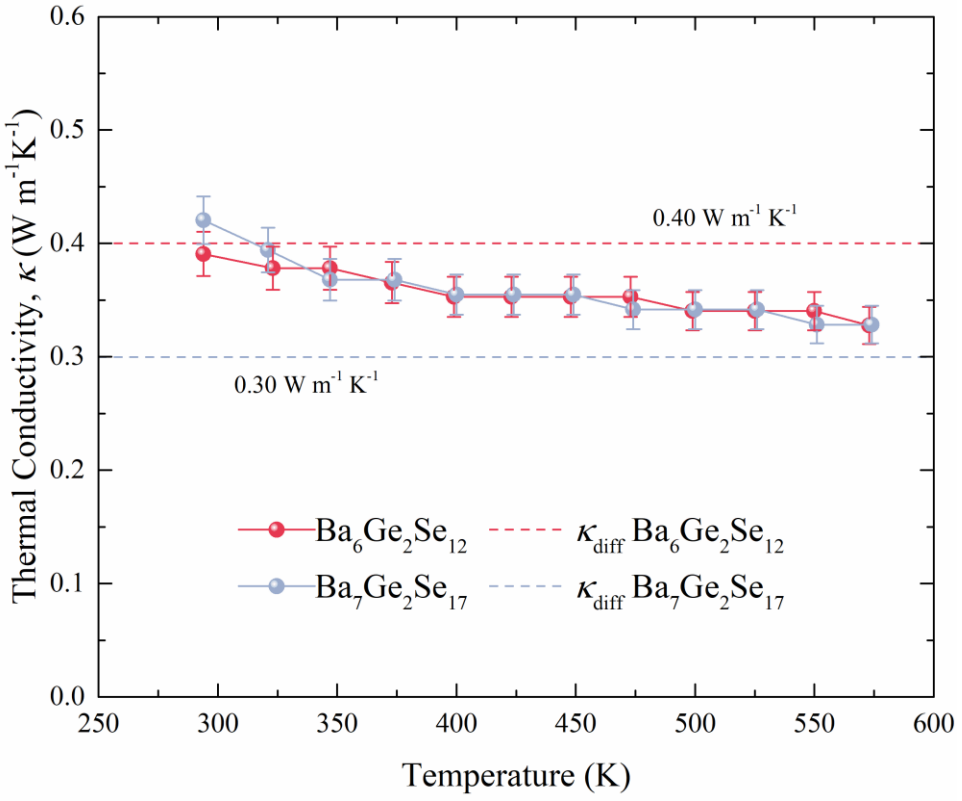

Figure 5.14. Experimental thermal conductivity for $Ba_6Ge_2Se_{12}$ and $Ba_7Ge_2Se_{17}$ alongside their theoretical minimum $\kappa_{diff.}$

5.6 Conclusion

The two previously unreported compounds $Ba_6Ge_2Se_{12}$ and $Ba_7Ge_2Se_{17}$ have been successfully synthesized, and their structural and physical properties analyzed. Before this work, Ba_2GeSe_4 and $Ba_2Ge_2Se_5$ were the only discovered ternary compounds in this phase space. $Ba_6Ge_2Se_{12}$ and $Ba_7Ge_2Se_{17}$ crystallize in new centrosymmetric structure types with large unit cells. Both crystal structures possess anion disorder which is rare in inorganic compounds. This disorder was confirmed in the average structure *via* a single crystal and Rietveld refinements, and the local structure was confirmed *via* PDF analysis. During the heating and cooling cycles of the

DSC experiment, there are no exothermic or endothermic peaks in the plot that would indicate a change in the ordering in the ordering of their structures.

The thermal conductivity values of these two compounds are extraordinarily low. The minimum κ_{tot} of $Ba_6Ge_2Se_{12}$ and $Ba_7Ge_2Se_{12}$ is 0.33 W m^{-1} K^{-1} at 573 K for both samples. The low values of κ_{tot} can be attributed to the large unit cells and disorder in these structure types. These low values of κ_{tot} are comparable to the values achieved by state-of-the-art thermoelectric materials, but the relatively wide band gaps and flat bands in the electronic structure limit their performance in these applications without being highly doped.

CHAPTER 6

$Ba_6Si_{2-x}Ge_xSe_{12}$ ($x = 0, 0.5, 1, 1.5$)

Portions of this chapter have been reprinted with permission from

Dalton Trans., 2023, 52, 15831-15838.

6.1 Introduction

Investigations into the phase space of metal chalcogenides have produced several novel compounds for use as non-linear optical (NLO) materials in the infrared region. Chalcogens such as S and Se readily form isolated $[TtQ_4]^{4-}$ (tetrel *Tt* = Si, Ge, Sn; *Q* = S, Se) tetrahedra when paired with group 14 elements. Combining these tetrahedral anions with cations has often resulted in new NLO active compounds with excellent properties, such as Hg_2GeSe_4 (space group $I\bar{4}$),[34] γ-Sr_2GeSe_4 (*Ama*2),[118,119] $SrHgGeSe_4$ (*Ama*2),[146] $BaHgGeSe_4$ (*Ama*2),[146] $A_2SrTtSe_4$ ($I\bar{4}2m$ and *R*3*c*) (*A* = Li, Na; *Tt* = Ge, Sn),[147] Li_2CdGeS_4 ($Pmn2_1$),[148] Li_2CdSnS_4 ($Pmn2_1$),[148] and $Na_2Ge_2Se_5$ ($Pna2_1$).[149] A cursory search reveals that the number of silicon chalcogenides lags behind the number of germanium and tin chalcogenides. Previously, only two barium silicon selenides were reported, namely Ba_2SiSe_4 ($P2_1/m$)[150] and Ba_3SiSe_5 (*Pnma*).[151] Neither of these compounds exhibits second harmonic generation (SHG) due to their centrosymmetric symmetry.

Our investigations into this phase space led to the discovery of the new compound $Ba_6Si_2Se_{12}$ ($P\bar{1}$). This compound does not exhibit NLO properties but adopts a new triclinic structure type with disordered Se_2^{2-} dumbbells. Interestingly this disorder is also observed in the

monoclinic germanium variant, $Ba_6Ge_2Se_{12}$ ($P2_1/c$).[152] The Se_2^{2-} disorder was investigated *via* single-crystal and Rietveld refinements. A thorough investigation of the phase width revealed that up to 75% of the Si atoms in the $Ba_6Si_2Se_{12}$ structure type can be replaced with Ge atoms. $Ba_6Si_2Se_{12}$ is a reddish-brown solid. To study the optical properties of this material, the Raman spectra were obtained for samples of $Ba_6Si_{2-x}Ge_xSe_{12}$ with x = 0, 0.5, 1, and 1.5.

6.2 Synthesis

Single crystals of $Ba_6Si_2Se_{12}$ were first prepared by adding stoichiometric amounts of pure elements (Ba: pieces, 99.7%, Strem Chemicals; Si: pieces, 99.9%, Alfa Aesar; Se: powder, 99.999%, Alfa Aesar) into a carbon-coated silica tube inside a dry Ar filled glove box. The tubes were then evacuated to a minimum pressure of 10^{-4} mbar and sealed using a torch. Next, the sealed ampoules were placed inside a programmable resistance furnace, heated to 673 K at a rate of 100 K h^{-1}, and left to dwell at this temperature for 24 h. The furnace was then heated to 1123 K at 100 K h^{-1}. The furnace was held at this temperature for another 24 hours to completely react the elements before slowly cooling to 300 K at a rate of 5.5 K h^{-1}. The furnace was turned off at that point.

To prepare bulk samples of $Ba_6Si_{2-x}Ge_xSe_{12}$ (x = 0, 0.5, 1, and 1.5), the elements (Ge, pieces, 99.999%, Strem Chemicals) were weighed in the desired rations and placed into carbon-coated silica tubes inside the glovebox. The sealed ampoules were heated to 923 K over 24 h to heat these samples. The samples were held at this temperature for 48 h to react with the elements completely, and the furnace was turned off and allowed to cool to room temperature. The sealed ampoules were then opened, and their contents were ground into homogenous powders and

resealed in new silica tubes. Finally, the sealed powders were heated in a manual furnace for one week at 923 K.

While determining the limit of Ge substitution in the phase, samples with nominal x = 1.6 and 1.8 were also prepared. According to the powder X-ray diffraction (pXRD) patterns, these samples contained the target compound and peaks associated with the ternary compound Ba_2GeSe_4. Therefore, the phase width of $Ba_6Si_{2-x}Ge_xSe_{12}$ is $0 \leq x \leq 1.5$.

For thermal conductivity measurements, the bulk samples were hot-pressed into dense pellets. An Oxy-Gon model FR-210-30T hot-press was used to create 12.7 mm diameter pellets by heating the powders in a graphite die for 5 h at 673 K under 54 MPa and an argon atmosphere. The pellets' densities were measured using the Archimedes method and determined to all be > 90% of their theoretical densities.

To solve the crystal structure of $Ba_6Si_2Se_{12}$, single crystal X-ray diffraction (sXRD) was performed with a Bruker Kappa Apex II CCD with Mo-Kα radiation. ω scans were used to collect the data and corrected for Lorentz and polarization effects. The correction method was the multi-scan method *via* SADABS, included in the APEX II software.[101] The crystal structure of $Ba_6Si_2Se_{12}$ was solved and refined with the SHELXTL package.[44,45] The final atomic coordinates of the structure were standardized using the Tidy procedure in the PLATON software.[134,135] Disordered Se_2^{2-} dumbbells were observed; when the occupancies of the Se sites were not tied together, the occupancies were refined 64.9(8)%, 64.0(8)%, 35.1(8)%, and 36.0(8)%. Due to the apparent correlation between the two pairs of Se sites, their occupancies were constrained to be equal, and the total occupancy of the two sites was fixed at 100%. We decided to refer to the title compound as $Ba_6Si_2Se_{12}$ rather than "Ba_3SiSe_6" due to the number of unique crystallographic sites and to reflect the relation to the germanium selenide $Ba_6Ge_2Se_{12}$. The poor single crystal quality of

$Ba_6Si_2Se_{12}$ led to the final refinement having large *R*-factors but was sufficient to create a valuable model of the crystal structure of the compound.

Due to the difficulty of growing high-quality single crystals for this compound, we decided to refine the final structure using pXRD. As laboratory pXRD instruments could not produce a large enough signal-to-background ratio for the many high-angle reflections of this triclinic structure, pXRD were collected at the High Energy Wiggler Beamline (BXDS-WHE) of the Canadian Light Source's (CLS). The wavelength of that beamline is 0.34970 Å. The energy of the X-ray photons was tuned to be 35 keV to avoid the Ba absorption edge (37.4 keV), well above the Si (1.8 keV), Ge (11.1 keV), and Se (12.7 keV) absorption edges. The pXRD patterns were collected for 60 s with the sample stage constantly spinning.

Rietveld refinements were performed on the powder diffraction patterns of $Ba_6Si_{2-x}Ge_xSe_{12}$ (x = 0, 0.5, 1, and 1.5) using GSAS-II (Figures A.16 – A.18).[46] Specifically, GSASIIscriptable was used to utilize its scripting interface and perform identical refinements on all diffraction patterns. For each refinement, the phase was manually edited to reflect the nominal composition of the sample before starting. The sample displacement was never refined in any of the refinements since sample displacement is highly correlated to the lattice cell parameters. The pXRD of a Ni standard was collected in the same session as the four $Ba_6Si_{2-x}Ge_xSe_{12}$ (x = 0, 0.5, 1, and 1.5) samples. A Rietveld refinement was performed on the Ni standard to obtain an instrument parameter file that could be used for all the samples. The *u*, *v*, and *w*, Gaussian constants were determined to be 1.1, -0.1, and 0.39, respectively. The data limits were set from 2.9º to 27º. The anisotropic thermal displacement parameters (U_{ani}) from the single crystal refinement were converted to isotropic thermal displacement parameters (U_{iso}). Due to the low symmetry and multiple crystallographic sites, the U_{iso} of like species were constrained to be equal (Ba^{2+}, Se^{2-}, and Se_2^{2-}). The U_{iso} of the

Si^{4+} and Ge^{4+} sites were not refined since they make up such a small part of the total electron density of the compound. Attempts to refine the U_{iso} of Si^{4+} and Ge^{4+} would make them impossibly small or multiple times larger than the U_{iso} of any other atom. When the Si sites were constrained to have equal U_{iso}, the final value was ~0.047 $Å^2$, more than double that of any other atom. For this reason, the U_{iso} for Si1/Ge1 and Si2/Ge2 were fixed at the values obtained from the initial sXRD experiment. Additionally, the atomic coordinates and fractional occupancies were also refined where applicable. The atomic coordinates of the disordered Si/Ge sites were constrained to have the same *x*, *y*, and *z* values. The final steps of the refinements were to perform a refinement cycle in the GSASII graphical user interface (GUI) to add restraints to the model since this is impossible in GSASIIscriptable. Bond restraints were added to prevent the Si atoms from moving too significantly from their original positions in the model. It was observed that the Si atoms in the structure were significantly displaced because their influence was weak, and the scattering of Ba and Se atoms dominated the pXRD pattern. The bond restraints were customized for each refinement. The ideal Si-Se and Ge-Se bond lengths were arbitrarily defined as 2.25 and 2.35 Å, respectively. The bond restraint for the x = 0, 0.5, 1, and 1.5 samples was determined using the linear combination: Bond Restraint = (1 - x/2)(2.25 Å) + x/2(2.35 Å). Finally, Rietveld refinements were repeated for all four samples without the less occupied Se_2^{2-} dumbbell to compare the final refined U_{iso} and residual values between the models and to provide more evidence for the existence of the disorder.

Energy dispersive X-ray analysis (EDAX) was used to determine the composition of four $Ba_6Si_{2-x}Ge_xSe_{12}$ samples with x = 0, 0.5, 1, and 1.5 to verify the refined Si/Ge ratios. EDAX was done using a QuantaFeg 250/Oxford Instrument x-act instrument. Multiple area scans of the hot-pressed pellets were acquired and averaged to determine the average compositions and their

standard deviations in all the samples. The tabulated results are summarized in Figures A.19 – A.22. For example, the atomic-% of $Ba_6SiGeSe_{12}$ was found to be 30.2(9)%, 7.5(9)%, 6.0(9)%, and 56.3(5)% for Ba, Si, Ge, and Se, respectively. Given that the corresponding nominal at.-% are 30%, 5%, 5%, and 60%, the elemental analysis agrees well with the intended target. Similar results were obtained for $Ba_6Si_2Se_{12}$, $Ba_6Si_{1.5}Ge_{0.6}Se_{12}$, and $Ba_6Si_{0.5}Ge_{1.5}Se_{12}$.

The electronic structure of $Ba_6Si_2Se_{12}$ was calculated using density functional theory (DFT) and the WIEN2K package.[102,153] Since deficiencies cannot be handled directly, the two Se sites corresponding to the more highly occupied Se_2^{2-} dumbbell were included, and the two less occupied Se sites were discarded. The Perdew-Burke-Ernzerhof (PBE) functional and the generalized gradient approximation (GGA) were used until the structure had met its convergence criteria of < 0.001 Ry for energy and < 0.001 e^- for the charge.[54] A fine mesh of 9 × 7 × 7 *k* points in the first Brillouin zone was used to perform the calculation. To construct the path of *k* points for the band structure, XCrySDen was used to create a path that passes through all the high symmetry points in the first Brillouin zone.[136]

Diffuse reflectance spectroscopy was performed on a PerkinElmer Lambda 1050 UV/vis/NIR spectrometer. The sample of $Ba_6Si_2Se_{12}$ was prepared by adhering the powdered sample to a glass slide substrate *via* double-sided tape. The reflectance (*R*) spectrum was collected from 300 nm to 1000 nm and converted to an absorbance (α) spectrum using the Kubelka-Munk equation: $\alpha/S = (1-R)^2/(2R)$, where *S* is a scattering factor which is effective for particle sizes > 5 μm.

The Raman microscopy spectra were collected using a Renishaw inVia Reflex instrument. Single crystals were targeted after searching the magnified powder sample. The 532 nm laser was used, and the integration time of each spectrum was 15 s.

Thermal diffusivities (D) were measured on the pellets of $Ba_6Si_{2-x}Ge_xSe_{12}$ *via* the Laser Flash DLF-1 (Environmental Module EM-1200, TA Instruments) under an argon atmosphere. The samples' specific heat ($C_{.P.}$) was determined simultaneously using a Vespel standard measured alongside the samples. The samples were measured up to 573 K. Thermal conductivity values (κ) of the four samples were calculated using the thermal diffusivity, density (ρ), and specific heat: $\kappa = D\rho C_P$. The experimental error of the thermal conductivity is estimated to be ±5%. The minimum thermal conductivity was also approximated using the sound velocity (v_s) through a pellet, as obtained by coupling the pellet to a 5.0 MHz Walfront Smart Sensor Sound Velocity Meter with silicone oil.

6.3 Crystal Structures

$Ba_6Si_2Se_{12}$ adopts a new structure type in the triclinic centrosymmetric space group $P\bar{1}$, and a thorough description of crystallographic details is presented in Table 6.1. As seen in Figure 6.1, the crystal structure comprises isolated $[SiSe_4]^{4-}$ tetrahedra and Se_2^{2-} dumbbells with Ba^{2+} cations packed between. Notably, this structure contains positional disorder in one of the Se_2^{2-} units. Furthermore, all atoms in this structure sit on 2*i* Wyckoff positions; thus, many unique crystallographic sites exist, as seen in Table A.5 – A.8. In total, there are 14 Se sites, but four are partially occupied and combined only account for two Se atoms; therefore, the charge-balanced formula may be written as $(Ba^{2+})_6(Si^{4+})_2(Se^{2-})_8(Se_2^{2-})_2$.

Table 6.1. Crystallographic information for the $Ba_6Si_{2-x}Ge_xSe_{12}$ compounds.

	x = 0	x = 0.5	x = 1	x = 1.5
Crystal System	Triclinic	Triclinic	Triclinic	Triclinic
Space group	$P\bar{1}$ (no. 2)	$P\bar{1}$ (no. 2)	$P\bar{1}$ (no. 2)	$P\bar{1}$ (no. 2)
a (Å)	9.1821(7)	9.1883(6)	9.1954(8)	9.1986(5)
b (Å)	12.2634(15)	12.2785(13)	12.2964(16)	12.3114(11)
c (Å)	12.3636(18)	12.3890(16)	12.426(2)	12.4532(14)
α (º)	109.278(3)	109.269(3)	109.259(3)	109.250(2)
β (º)	104.732(2)	104.737(2)	104.774(3)	104.7701(19)
γ (º)	100.4061(16)	100.4291(15)	100.4122(17)	100.4056(12)
Unit cell volume ($Å^3$)	1216.38(4)	1221.08(3)	1227.40(4)	1232.15(3)
Formula units per unit cell, *Z*	2	2	2	2
Molecular weight (g mol^{-1})	1827.67	1849.92	1872.18	1894.43
Density (g cm^{-3})	4.9902	5.031	5.066	5.106
Radiation wavelength (Å)	0.34970	0.34970	0.34970	0.34970
Temperature (K)	300	300	300	300
F(000)	1544	1562	1580	1598
wR_p*	0.0422	0.0385	0.0433	0.0447

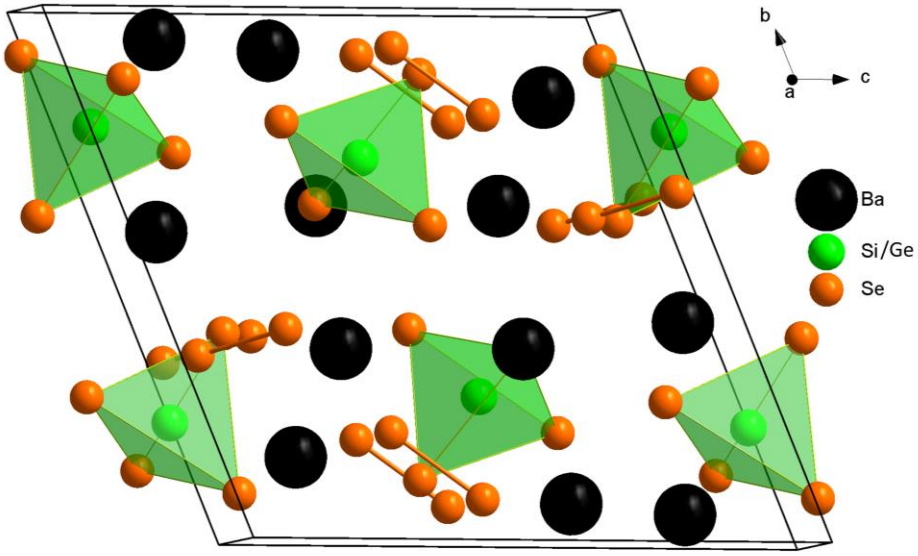

Figure 6.1. Crystal structure of $Ba_6Si_{2-x}Ge_xSe_{12}$. Se4 and Se14 have been excluded for clarity.

Starting with $Ba_6Si_{1.5}Ge_{0.5}Se_{12}$, the Si/Ge ratios of the two tetrel sites are very similar and only differ by 2%. As more Ge is substituted into the structure, the Si/Ge ratio between the Si1/Ge1 and Si2/Ge2 sites becomes increasingly disparate, as seen in Table 6.2. In $Ba_6Si_{0.5}Ge_{1.5}Se_{12}$, the difference in the Si/Ge ratio between the two tetrel sites is 10.4%. This increased site selectivity suggests that the structure is becoming increasingly strained and that we are reaching the limit of how much Ge may be substituted. This would explain why $Ba_6Ge_2Se_{12}$ adopts a different crystal structure. However, when analyzing the bond angles of the $[Ge1Se_4]^{4-}$ and $[Ge2Se_4]^{4-}$ as well as the Ba-Se distances to the nearest Ba neighbours, there was no obvious explanation as to why the Ge atoms with their larger radius would prefer the Si1/Ge1 site in $Ba_6Si_{0.5}Ge_{1.5}Se_{12}$ over the Si2/Ge2.

Table 6.2. Si/Ge disorder occupancies and Se-dumbbell disorder in the $Ba_6Si_{2-x}Ge_xSe_{12}$ series of compounds.

	x = 0	x = 0.5	x = 1	x = 1.5
Si1/Ge1	1/0	0.759(18)/ 0.241	0.49(2)/ 0.51	0.201(14)/ 0.799
Si2/Ge2	1/0	0.741(18)/ 0.259	0.51(2)/ 0.49	0.299(14)/ 0.701
Se3-Se5/ Se4-Se14	0.666(10)/ 0.334	0.650(8)/ 0.340	0.615(9)/ 0.385	0.604(8)/ 0.396

The structure contains both ordered Se_2^{2-} dumbbells (Se1/Se2) and disordered dumbbells (Se3/Se5 and Se4/Se14). The occupancies of the Se3/Se5 and Se4/Se14 dumbbells are 0.666(10) and 0.334(10), respectively. The Se pairs are angled approximately 90º to each other, as depicted in Figure 6.2. The Se3-Se5 and Se4-Se14 bond distances are equivalent with 2.32 Å and 2.33 Å, respectively. As Ge is substituted into the structure, the Se3/Se5 to Se4/Se14 ratio systematically decreases to 0.604(8):0.396(8) for $Ba_6Si_{0.5}Ge_{1.5}Se_{12}$.

Figure 6.2. Disordered Se_2^{2-} anion (left) vs. the 100% occupied Se_2^2 (right). Se3 and Se5 have an occupancy of 0.667(10), and Se4 and Se14 of 0.333(10).

Comparisons with $Ba_6Ge_2Se_{12}$ are instructive because of their similar stoichiometries and Se_2^{2-} dumbbell disorder; however, in the Ge case, the different orientations of the Se pairs create polyselenide chains of varying length in the *a* direction of the lattice. In $Ba_6Si_2Se_{12}$, Se3, Se4, Se5, and Se14 are isolated and do not make 1D chains with themselves or Se1 and Se2.

The Si-Se bonds in $Ba_6Si_2Se_{12}$ range from 2.25 to 2.31 Å. These bond distances align with other barium silicon selenides Ba_2SiSe_4 and Ba_3SiSe_5. In Ba_2SiSe_4 and Ba_3SiSe_5, the Si-Se bonds range from 2.25 to 2.28 Å and 2.24 to 2.27 Å, respectively.[150,151] Figure 6.3 compares the coordination environments of the Si1/Ge1 site throughout the series of $Ba_6Si_{2-x}Ge_xSe_{12}$ compounds. As Ge is substituted into the structure, the range of bond distances in the $[(Si,Ge)Se_4]^{4-}$ tetrahedra increases slightly to 2.26 to 2.36 Å in the case of $Ba_6Si_{0.5}Ge_{1.5}Se_{12}$.

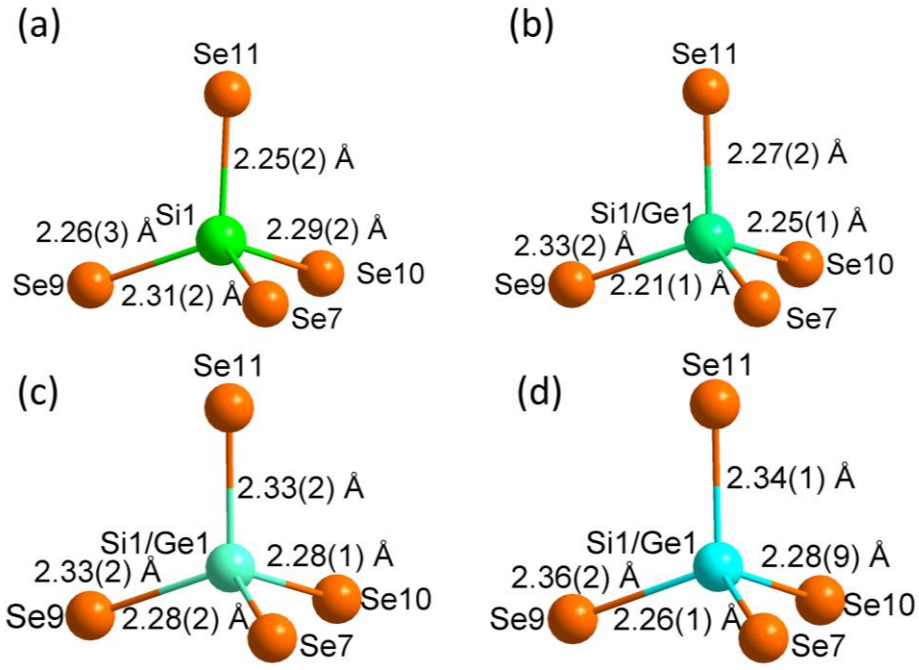

Figure 6.3. Si1/Ge1 tetrahedral coordination environnements in (a) $Ba_6Si_2Se_{12}$, (b) $Ba_6Si_{1.5}Ge_{0.5}Se_{12}$, (c) $Ba_6SiGeSe_{12}$, and (d) $Ba_6Si_{0.5}Ge_{1.5}Se_{12}$.

The Ba atoms are always coordinated to 10 Se atoms (C.N. 10) regardless of which disordered Se sites are coordinated to the Ba atom. Figure 6.4 shows the coordination environment of Ba2, which is coordinated to the ordered Se_2^{2-} and Ba4, which is coordinated to the disordered Se_2^{2-} dumbbells. The Ba-Se bonds range from 3.4 to 3.7 in $Ba_6Si_2Se_{12}$. The Ba-Se bond lengths in this compound occupy a wide bond length range; however, Ba-Se bonds vary depending on the exact coordination environment of the Ba atom. In Ba_2SnSe_4, the Ba1 and Ba2 atoms are C.N. 9 and C.N. 8, respectively and range from 3.20 – 3.79 Å.[120]

The Ba4-Se14 bond is approximately 0.2 Å shorter than any other disordered Se_2^{2-} sites, possibly explaining why the Se4/Se14 dumbbell is less preferred than the Se3/Se5 orientation. However, all Ba-Se bond lengths lie within an acceptable range for C.N. 10 Ba.

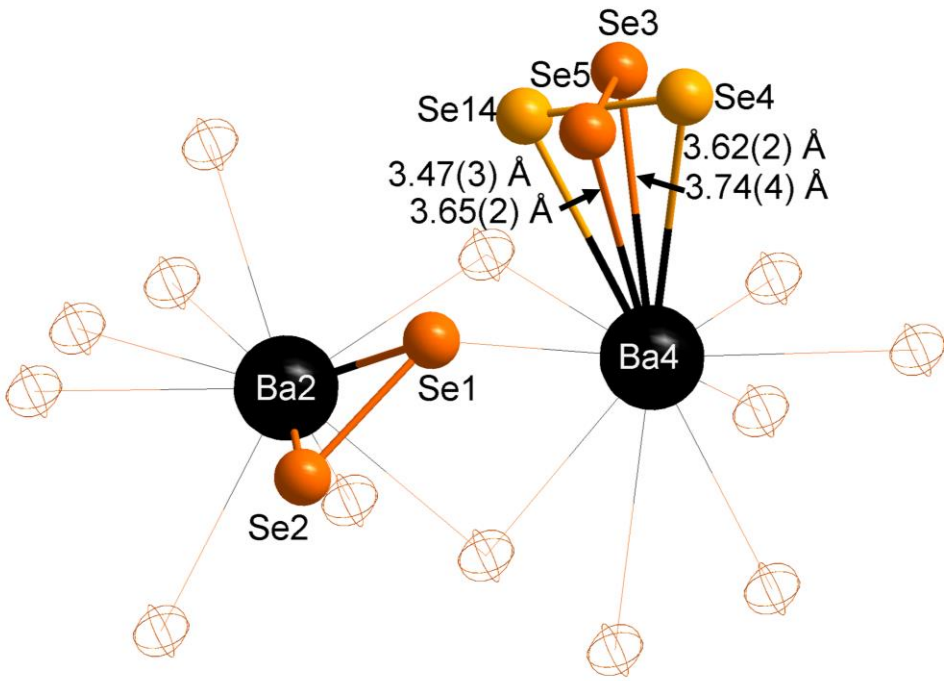

Figure 6.4. Coordination spheres around Ba2 and Ba4. Se^{2-} anions are depicted only as outlines.

The Rietveld refinements of the $Ba_6Si_{2-x}Ge_xSe_{12}$ samples were performed to determine the lattice parameters and occupancies of the disordered Si, Ge, and Se sites. The final fit of the experimental data is presented in Figure 6.5 for the sample with x = 0. The additional Rietveld refinements are depicted in Figures A.16, A.17 and A.18 for samples with x = 0.5, 1, and 1.5, respectively.

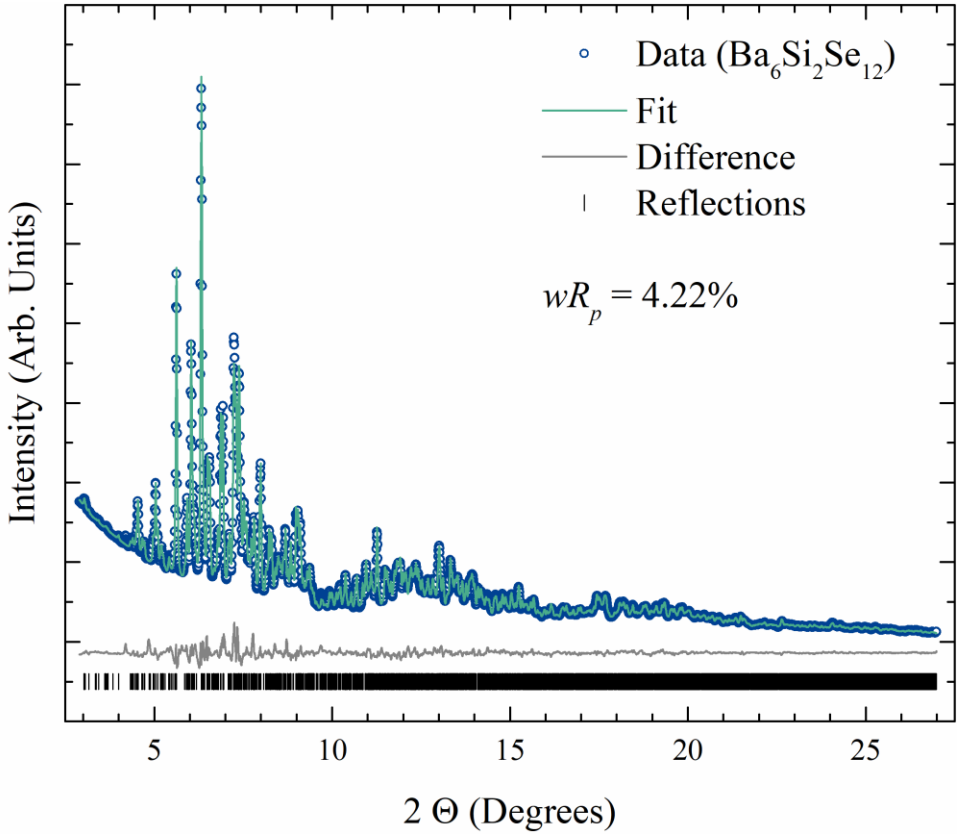

Figure 6.5. The Rietveld refinements of $Ba_6Si_2Se_{12}$, including the weighted profile *R*-factor, wR_p.

The Rietveld refinements of the ordered models were also attempted. In the ordered models, Se4 and Se14 were removed since they were the less occupied crystallographic sites and the occupancies of Se3 and Se5 were fixed at 100%. There is a significant difference in the U_{iso} of the Se_2^{2-} atoms in the disordered and ordered models. In the disordered models, the U_{iso} of Se_2^{2-} atoms vary from 0.013(3) - 0.023(3) $Å^2$ and in the ordered models their U_{iso} range from 0.069(3)

– 0.082(3) Å^2. The U_{iso} of the ordered Se3/Se5 sites is approximately four times larger than in the model where these sites are split into Se3/Se5 and Se4/Se14 positions. The large thermal displacement parameters of Se3 and Se5 are good evidence that they are deficient sites in the ordered models and have a positional disorder in the structure.

Additionally, the Rietveld refined lattice parameters are plotted with respect to sample composition in Figure 6.6. Vegard's Law predicts that the change in lattice parameters of a unit cell is linearly dependent with respect to the composition of the unit cell. As seen in Figure 6.6, the lattice parameters *a*, *b*, and *c* increase linearly from 0% Ge substitution up to 75% Ge substitution. Initially, the unit cell volume of $Ba_6Si_2Se_{12}$ is 1216.4 Å^{3,} but as Ge is substituted into the compound, the unit cell volumes of $Ba_6Si_{1.5}Ge_{0.5}Se_{12}$, $Ba_6SiGeSe_{12}$, and $Ba_6Si_{0.5}Ge_{1.5}Se_{12}$ increase to 1221.1 Å^3, 1227.4 Å^3, and 1232.2 Å^3. If the samples all contained the nominal amount of Ge, it could be determined that the unit cells increased on average 10.3 Å^3 per Ge atom.

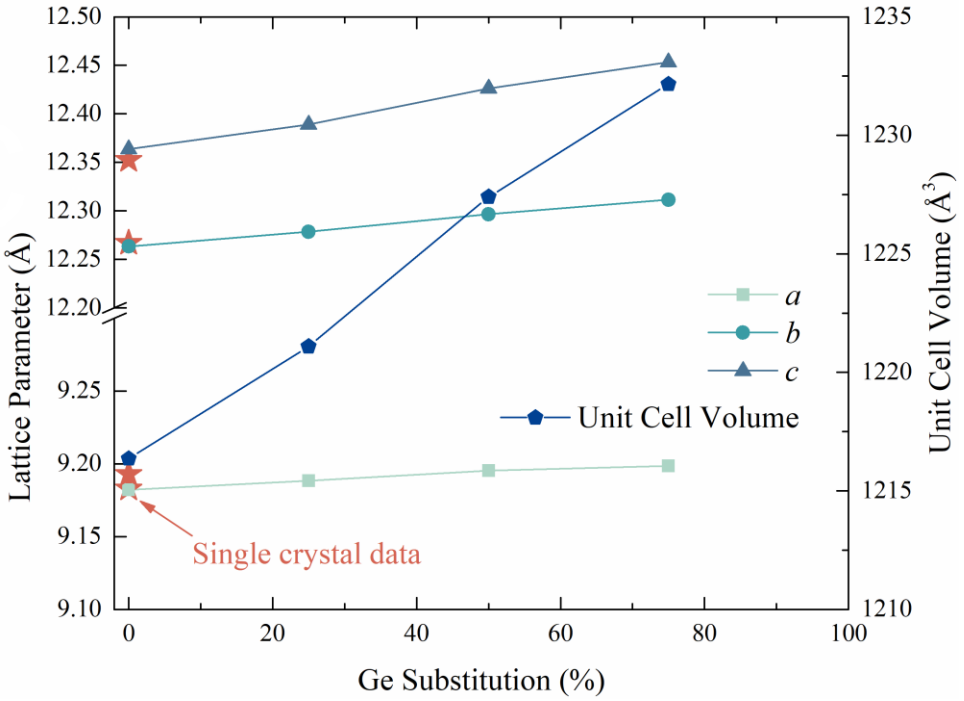

Figure 6.6. Composition-dependent lattice parameters as determined *via* Rietveld refinements. The initial lattice parameters obtained *via* laboratory sXRD experiments are also plotted for comparison.

6.4 Theoretical Studies

DFT calculations of $Ba_6Si_2Se_{12}$ were done using the ordered model with Se3 and Se5 at 100% occupancy, and the Se4 and Se14 sites were excluded. The calculated band structure and density of states (DOS) are depicted in Figure 6.7. The band structure was found to possess an indirect band gap between the X point of the valence band and the V point of the valence band. The calculated value of the band gap was determined to be 1.74 eV. This is slightly lower than the experimental value of 1.89 eV because regular DFT calculations rarely relax the structure to a global energy minimum. The lowest energy conduction band comprises the Se–Se antibonding 4*p* orbitals of the Se1/Se2 dumbbell. The second and third lowest conduction bands contain the 3*s*

orbitals of the two Si atoms in the unit cell. From the flatness of the bands and relatively wide band gap, this material can be expected to have low intrinsic electrical conductivity.

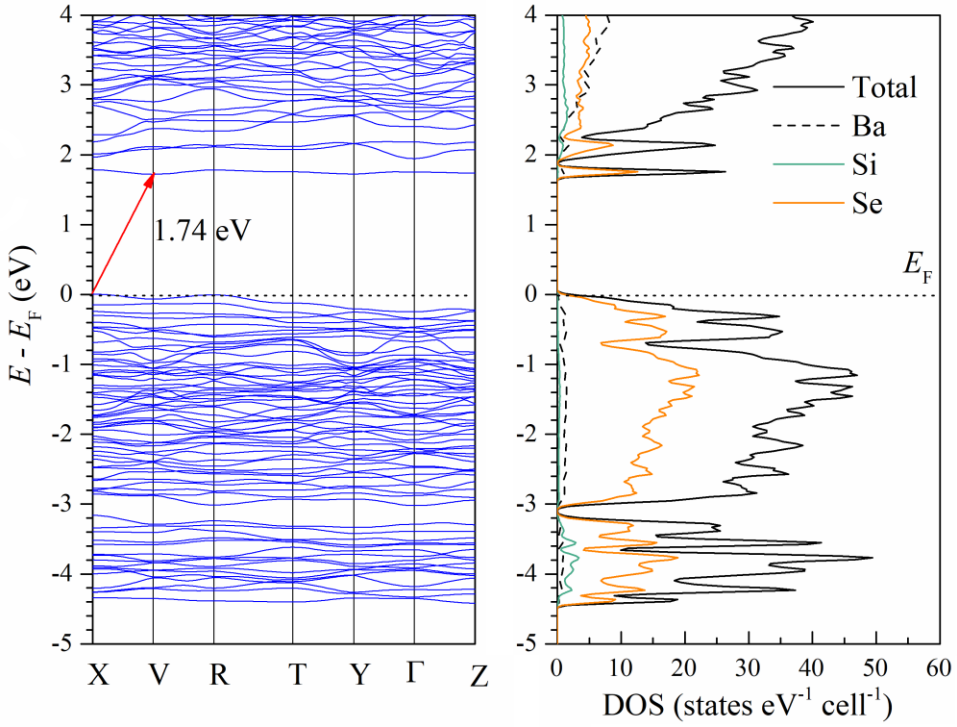

Figure 6.7. Band structure and DOS of $Ba_6Si_2Se_{12}$.

6.5 Physical Properties

6.5.1 UV-Vis-NIR Spectroscopy

The optical band gap of the parent compound was determined to be 1.89 eV *via* diffuse reflectance spectroscopy, shown in Figure 6.8. This is slightly larger than in the case of $Ba_6Ge_2Se_{12}$, which possesses an optical band gap of 1.75 eV. The wider band gap is due to the increased ionic character of the Si-Se bond compared to the Ge-Se bond.

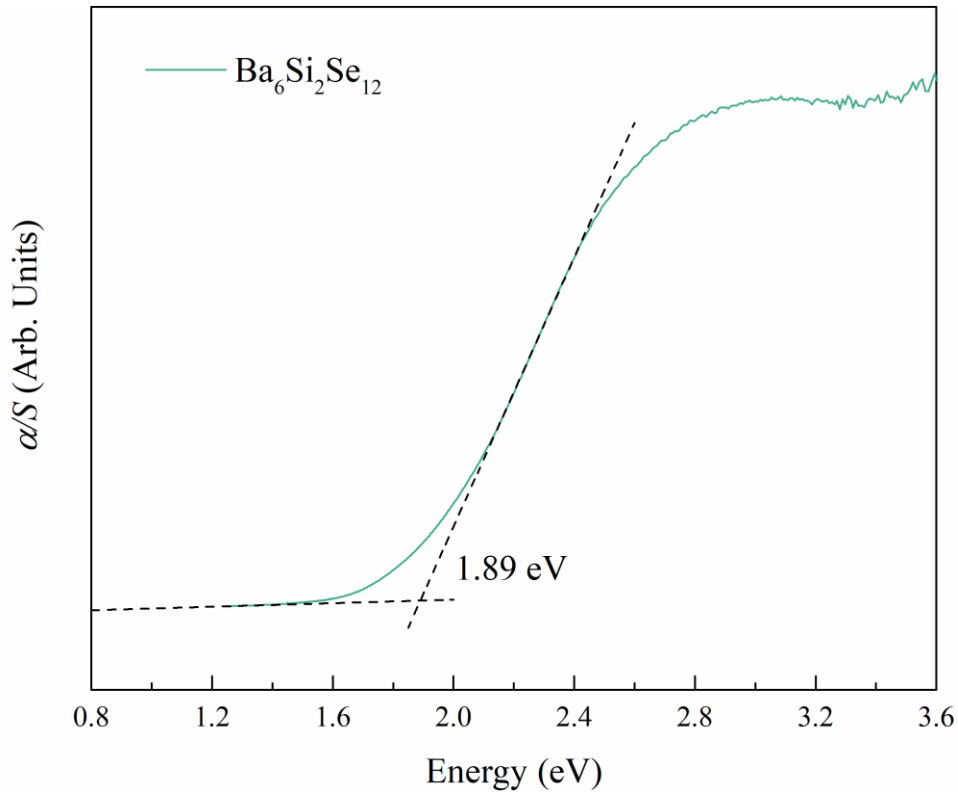

Figure 6.8. Experimental band gap determination *via* the absorption spectrum of $Ba_6Si_2Se_{12}$.

6.5.2 Raman Spectroscopy

The Raman spectra were obtained for samples with x = 0, 0.5, 1, and 1.5. The normalized Raman spectra are plotted in Figure 6.9. The Si-Se bonds' asymmetric and symmetric stretching modes create identifiable peaks around 220 and 280 cm^{-1}. For the x = 1 sample, the Ge-Se stretching mode at 254 cm^{-1} becomes visible in addition to the Si-Se peaks. For the x = 1.5 sample, the 251 cm^{-1} Ge-Se peak is now more significant than the Si-Se peak, which has been suppressed to 272 cm^{-1}. The asymmetric and symmetric Ge-Se Raman modes in Mg_2GeSe_4 correspond to 197 and 243 cm^{-1} peaks.[120] In the title compounds, the intense 197 cm^{-1} peak is shifted up to 216 – 220 cm^{-1}. is shifted to higher energy. The various Ba-Se vibrational modes create a broad peak between 100 and 150 cm^{-1}.

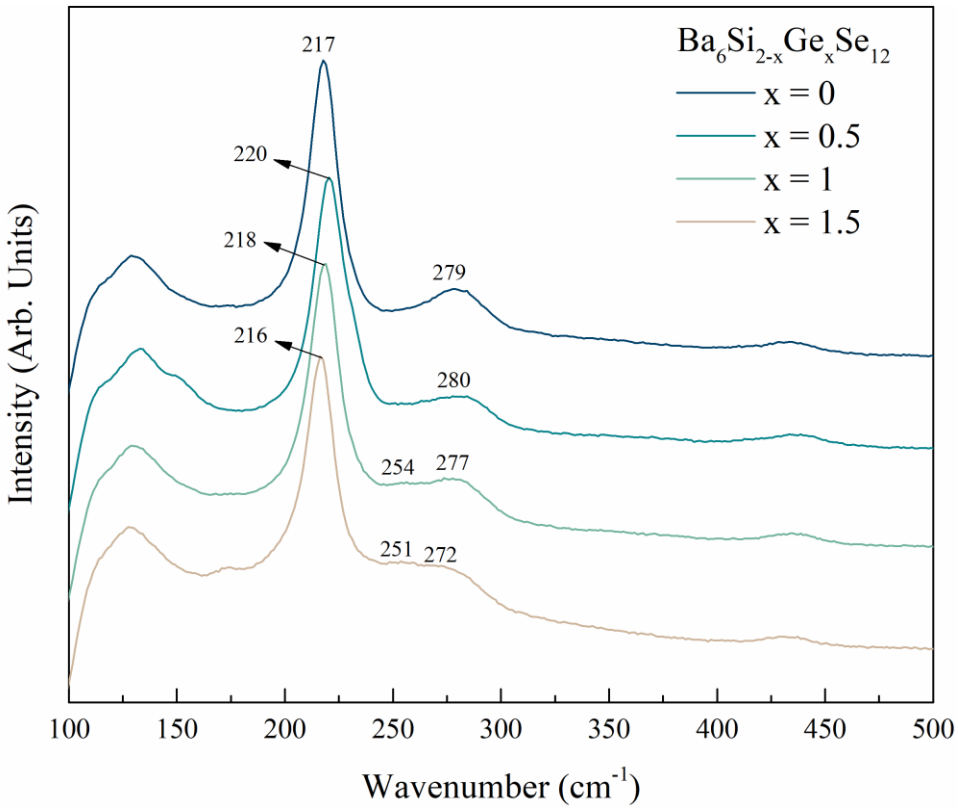

Figure 6.9. Normalized Raman spectra of $Ba_6Si_{2-x}Se_{12}$ with x = 0, 0.5, 1, and 1.5.

6.5.3 Thermal Conductivity

The κ of the series of $Ba_6Si_{2-x}Ge_xSe_{12}$ samples range between 0.3 and 0.5 W m^{-1} K^{-1} (Figure 6.10). The minimum thermal conductivity was approximated using the diffuson model ($\kappa_{diff.}$) developed by Snyder *et al*. This model uses the sound velocity (v_s), Boltzmann's constant (k_B), and the number density (n; atoms m^{-3}) to determine the minimum κ_{diff} *via* the approximation $\kappa_{diff} \approx 0.76 n^{2/3} k_B v_s$.[49] The κ_{diff} of $Ba_6Si_2Se_{12}$ was determined to be 0.31 W m^{-1} K^{-1} from its measured sound velocity of 2916 m s^{-1}. The κ_{diff} of $Ba_6Si_2Se_{12}$ is plotted as a continuous line in Figure 6.10, and the κ_{diff} of the other compositions would vary slightly due to their different sound velocities. The $Ba_6SiGeSe_{12}$ sample has thermal conductivity values of that order.

In contrast, the remaining three samples have slightly higher thermal conductivity values, beginning at approximately 0.5 W m^{-1} K^{-1} and decreasing somewhat over the temperature range to about 0.4 W m^{-1} K^{-1}. The lowest κ of $Ba_6SiGeSe_{12}$ may be because it has the most significant configurational entropy out of all the samples. Configurational entropy is maximized when different atoms equally occupy a disordered crystallographic site. The mismatch in the Si^{4+} and Ge^{4+} cation size creates distortions in the lattice that can strongly scatter the heat-carrying phonons, thus lowering κ.[154]

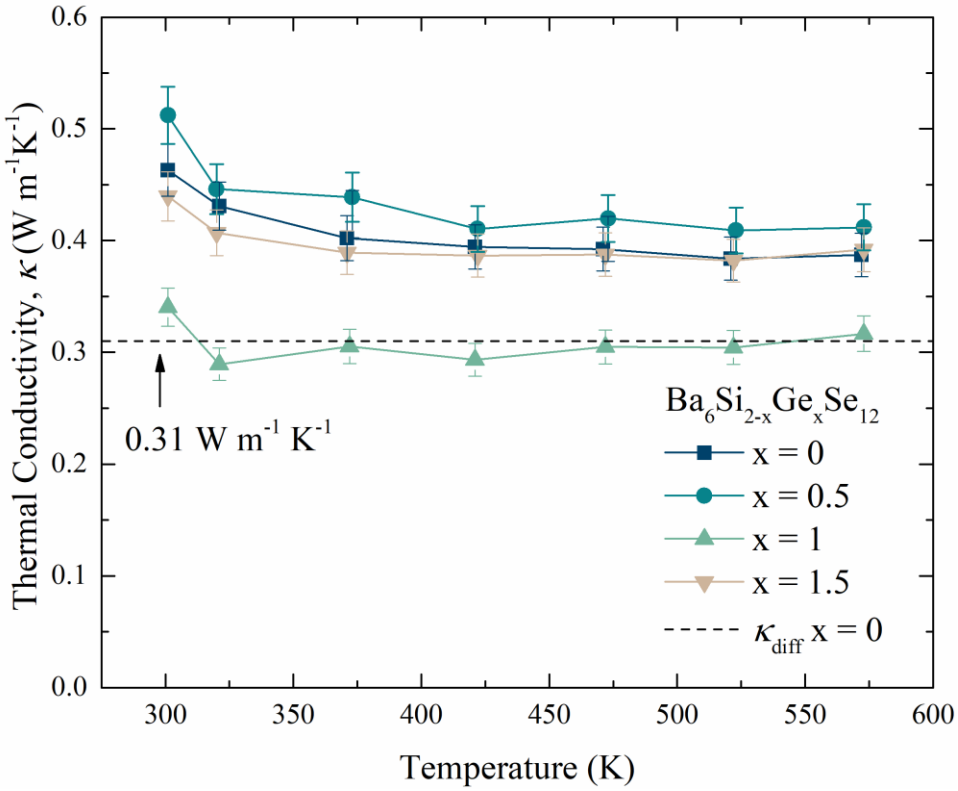

Figure 6.10. Thermal conductivity curves for $Ba_6Si_{2-x}Ge_xSe_{12}$ with x = 0, 0.5, 1, and 1.5, and theoretical $\kappa_{diff.}$ for $Ba_6Si_2Se_{12}$.

6.6 Conclusion

In this investigation, the authors report the new phase $Ba_6Si_2Se_{12}$. This compound adopts a new structure type in the triclinic $P\bar{1}$ space group. Upon exploration of the phase space, it was discovered that up to 75% of the Si atoms in the structure could be replaced by Ge atoms while maintaining the same structure type. Furthermore, the lattice parameters increased linearly with increased Ge composition, as predicted by Vegard's law. We studied the occupancies of the disordered Se3, Se4, Se5, and Se14 sites through the Rietveld refinements. Rietveld refinements using the ordered models contained large U_{iso} values for Se3 and Se5 when their counterparts were removed, indicating that these sites should not be 100% occupied and that the positional disorder observed in the single crystal data is accurate. Notably, the stoichiometrically similar compounds $Ba_6Si_2Se_{12}$ and $Ba_6Ge_2Se_{12}$ possess positional disorder in their Se_2^{2-} dumbbells despite their different structure types.

The calculations of the electronic structure of $Ba_6Si_2Se_{12}$ indicate that it is a semiconductor with a moderate band gap (below 2 eV) and that the valence and conduction bands are relatively flat, meaning that the intrinsic electrical conductivity is poor. These qualities limit the thermoelectric applications of the compound despite its remarkably low thermal conductivity.

CHAPTER 7

$Sr_8Ge_4Se_{17}$ and $Ba_8Sn_4Se_{17}$

The contents of this chapter will be submitted to the journal

Inorganic Chemistry (American Chemical Society)

7.1 Introduction

Exploratory research into alkaline earth chalcogenides has successfully resulted in several compounds for applications in nonlinear optics,[146,155–157] thermoelectrics,[4,158–160] and photovoltaics.[161–164] Herein, we compare two new alkaline earth selenides' crystal structures and physical properties with the same elemental ratios. While exploring the *Ae*–*Tt*-*Q* phase space (*Ae* = alkaline earth metal; *Tt* = tetrel, *Q* = chalcogenide), $Sr_8Ge_4Se_{17}$ and $Ba_8Sn_4Se_{17}$ were discovered. Despite their same elemental ratios, these compounds crystallize in different crystal systems. In the pursuit of developing materials with enhanced thermoelectric properties, researchers have found several compounds with complex structures and ultra-low thermal conductivities. The unique crystal structures of these compounds are characterized by large unit cells, which have been established as a crucial factor in reducing thermal conductivity. In solids, thermal energy is transferred by phonons. The wavelength of the phonons is limited by the lattice parameters of the unit cell of the compound.[25] Additionally, large unit cells scatter phonons more efficiently through Umklapp processes by shrinking the reciprocal unit cell volume, leading to a higher density of phonon wave vectors.[24] The increased density of phonon wave vectors enhances the probability of phonon-phonon scattering.

The Sr-Ge-Se and Ba-Sn-Se phase spaces include the compounds γ-Sr_2GeSe_4,[2] $Sr_2Ge_2Se_5$,[6] Ba_2SnSe_4,[165] Ba_2SnSe_5,[123–125] $Ba_7Sn_3Se_{13}$,[128] and $Ba_6Sn_6Se_{13}$.[166] Notably, the 8:4:17 stoichiometry of $Sr_8Ge_4Se_{17}$ and $Ba_8Sn_4Se_{17}$ may be regarded as derivatives of the 2:1:4 compounds with an additional ¼ Se per formula unit (2:1:4.25). The slight excess of Se leads to the formation of Se-Se bonds in these compounds in the form of Se_2^{2-} dumbbells, absent in the structures of γ-Sr_2GeSe_4 and Ba_2SnSe_4. $Sr_8Ge_4Se_{17}$ crystallizes in the triclinic $P\bar{1}$ space group, and $Ba_8Sn_4Se_{17}$ crystallizes in the monoclinic $C2/c$ space group. At first glance, there appears to be no relation between the two structure types. However, when the smaller triclinic cell is expanded eight times at large, it becomes clear that the $Ba_8Sn_4Se_{17}$ unit cell is a supercell of the smaller $Sr_8Ge_4Se_{17}$ unit cell with some notable differences. This work compares the structural similarities of $Sr_8Ge_4Se_{17}$ and $Ba_8Sn_4Se_{17}$ and their physical properties, including their ultra-low thermal conductivities.

7.2 Synthesis

Both $Sr_8Ge_4Se_{17}$ and $Ba_8Sn_4Se_{17}$ can be synthesized by traditional solid-state synthesis. Sr (Alfa Aesar, granules, 99%), Ba (Strem Chemicals, pieces, 99.7%), Ge (Strem Chemicals, pieces, 99.999%), Sn (Alfa Aesar, granules, 99.99%), and Se (Alfa Aesar, powder, 99.999%) were added in stoichiometric ratios into C-coated fused silica tubes inside a dry Ar filled glovebox. The tubes were evacuated to $< 2.5 \times 10^{-3}$ mbar before being sealed using an H_2/O_2 torch. To produce crystals for single-crystal X-ray diffraction (sXRD), the samples were heated up to 1073 K over 24 h and slowly cooled to 573 K at a rate of 2.5 K h^{-1}. To prepare phase pure bulk samples, the samples must be ground entirely after the first heating, resealed in silica ampoules, and annealed in a resistance furnace at 923 K for one week. The hypothetical quaternary variants "$Sr_8Ge_2Sn_2Se_{17}$", "$Ba_8Ge_2Sn_2Se_{17}$", and "$Sr_4Ba_4Ge_2Sn_2Se_{17}$" could not be synthesized using this procedure.

The laboratory sXRD experiments were performed on a Bruker Kappa Apex II CCD with Mo-Kα radiation. A red block-shaped crystal of $Sr_8Ge_4Se_{17}$ and a red block-shaped crystal of $Ba_8Sn_4Se_{17}$ were mounted onto a glass fibre for data collection. Each frame of data was collected for 30 s of exposure. Both crystal structures were solved using the SHELXTL package.[44,45] The atoms were assigned based on their coordination environments and bond distances to their closest neighbours. Due to their equivalent stoichiometric ratios, both compounds can be written with the charge-balanced formula $(Sr^{2+},Ba^{2+})_8(Ge^{4+},Sn^{4+})_4(Se^{2-})_{15}(Se_2^{2-})$. $Ba_8Sn_4Se_{17}$ contains 16 Ba sites, 8 Sn sites, and 34 Se sites. However, rather than reporting the formula as "$Ba_{16}Sn_8Se_{34}$", this was simplified to highlight the same elemental ratios between the two compounds. The final refined model of $Sr_8Ge_4Se_{17}$ was satisfactory, but the $Ba_8Sn_4Se_{17}$ refinement contained large residual values, common in unit cells with extremely large lattice parameters.[167] Additionally, the $Ba_8Sn_4Se_{17}$ sXRD data included unaccounted-for electron density resulting in creating two large Q peaks with 9 e $Å^{-3}$ and 6 e $Å^{-3}$ of electron density. However, these discrepancies may be negligible given that there are 19647 electrons per unit cell.

To overcome the limitations of laboratory sXRD instruments, phase pure powder samples of $Sr_8Ge_4Se_{17}$ and $Ba_8Sn_4Se_{17}$ were sent to the High Energy Wiggler Beamline (BXDS-WHE) at the Canadian Light Source (CLS) for powder X-ray diffraction (pXRD). The wavelength of the beamline is 0.34970 Å, and the energy of the photons was set to 35 keV to avoid the absorption edge of Ba (37.4 keV), which is well above the absorption edges of Sr (16.1 keV), Ge (11.1 keV), Sn (29.2 keV) and Se (12.7 keV). The 2D pXRD patterns were collected for 60 s each, with the sample constantly spinning to account for any texturing in the samples. A Ni standard was also measured during the same session to determine the instrument parameters for the Rietveld

refinements of $Sr_8Ge_4Se_{17}$ and $Ba_8Sn_4Se_{17}$. The Gaussian parameters *u*, *v*, and *w* were determined to be 1.1, -0.1, and 0.39, respectively, after refining the Ni pXRD pattern.

The final refinements were performed using GSAS-II using the models initially solved from sXRD data.[46] Before starting the Rietveld refinement, the atomic positions of both models were standardized using the Tidy program in the PLATON package.[134] The data limits were set from 2.5º to 27º. During the refinement, the background and scale were never refined simultaneously due to their high correlation. Once the background, scale, particle size, and lattice parameters had all been optimized, bond restraints were added to prevent atoms from moving too far from their original positions. In $Sr_8Ge_4Se_{17}$, the 39 crystallographic sites are all on the 2*i* Wyckoff positions, whereas in $Ba_8Sn_4Se_{17,}$ all 78 crystallographic sites belong to 8*f* Wyckoff positions. These Wyckoff positions do not correspond to any symmetry elements in the unit cell, meaning that no constraints are imposed on the fractional coordinates of the atoms. The atoms would often move to unrealistically short or long bonds without imposing bond restraints. The Ge-Se bonds were restrained to an ideal value of 2.35 Å, and the Sn-Se bonds were restrained to an ideal value of 2.52 Å. Additionally, during the Rietveld refinements, the anisotropic displacement (U_{ani}) values of the original single-crystal model were converted to isotropic displacement (U_{iso}). The U_{iso} of the same species (Ba^{2+}, Ge^{4+}, Sn^{4+}, Se^{2-}, and Se_2^{2-}) were constrained to be equal. The results of the Rietveld refinement are shown in Figure 7.1, and the refined crystal data in Table 7.1. Atomic coordinates and U_{iso} acquired from the Rietveld refinements are summarized in Tables A.9 and A.10.

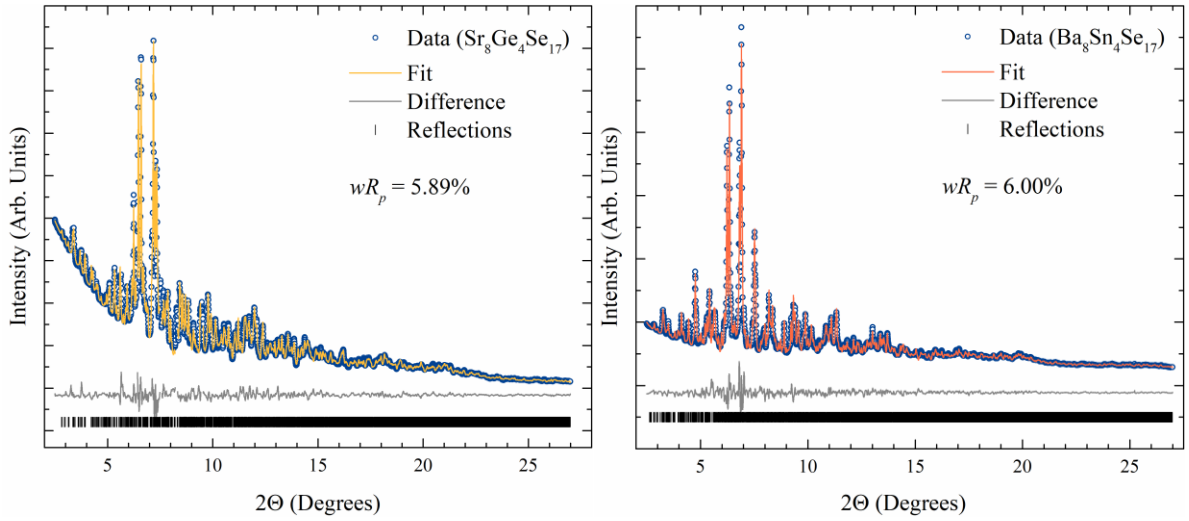

Figure 7.1. Rietveld refinement fits of $Sr_8Ge_4Se_{17}$ (left) and $Ba_8Sn_4Se_{17}$ (right) data.

The electronic structure of $Sr_8Ge_4Se_{17}$ and $Ba_8Sn_4Se_{17}$ were computed using density functional theory (DFT) through the Wien2K software.[102,153] Utilizing the Perdew-Burke-Ernzerhof (PBE) functional and the generalized gradient approximation (GGA), the electronic structure underwent iterations until it achieved convergence, with energy changes reaching below 0.001 Ry and charge changes below 0.001 e^-.[54] Due to their low symmetry and high number of atoms per unit cells, a moderate number of *k* points were used in reciprocal space. For $Sr_8Ge_4Se_{17}$, 6 × 6 × 5 *k* points were used in the Brillouin zone and for $Ba_8Sn_4Se_{17}$, 4 × 1 × 4 *k* points were used. Note that in $Ba_8Sn_4Se_{17}$, the *b** is much larger than *a** and *c**. When calculating the band structures of the two compounds, a *k* point path was constructed using XCrySDen to create pathways in the triclinic and monoclinic Brillouin zones.[136]

Table 7.1. Crystallographic details of $Sr_8Ge_4Se_{17}$ and $Ba_8Sn_4Se_{17}$ from the Rietveld refinement.

Empirical Formula	$Sr_8Ge_4Se_{17}$	$Ba_8Sn_4Se_{17}$
Crystal System	Triclinic	Monoclinic
Space group	$P\bar{1}$ (no. 2)	$C2/c$ (no. 15)
a (Å)	11.8429(18)	47.286(3)
b (Å)	12.172(3)	12.6294(5)
c (Å)	13.624(3)	25.7303(15)
α (º)	114.472(5)	90
β (º)	97.396(5)	104.585(5)
γ (º)	107.040(5)	90
Unit cell volume (Å^3)	1636.94(9)	14871.0(9)
Formula units per unit cell, Z	2	16
Molecular weight (g mol^{-1})	2333.64	2915.72
Density (g cm^{-3})	4.7346	5.2093
Radiation, wavelength (Å)	0.34970	0.34970
Temperature (K)	300	300
F(000)	2020	19616
wR_p	0.0589	0.0600

The optical band gaps of these compounds were probed using diffuse reflectance spectroscopy. The ground powdered samples were adhered to a mount using double-sided tape. The sample was loaded into a PerkinElmer Lambda 1050 UV/vis/NIR spectrometer and run in reflectance mode over the visible and near-infrared regions. The reflectance (R) was converted to

absorbance (α) using the Kubelka-Munk equation: $\alpha/S = (1 - R)^2 / (2 R)$. S is the scattering factor of the sample, effectively constant for particle sizes much larger than the probed wavelengths.

The Raman spectra of the samples were also measured using a Renishaw inVia Reflex instrument. Using a microscope, the 532 nm laser targeted single crystals in the samples. Red crystals present in the $Sr_8Ge_4Se_{17}$ and $Ba_8Sn_4Se_{17}$ were targetted in their respective samples. The Raman spectra were collected for ten 15 s scans and averaged.

The total thermal conductivity (κ_{tot}) may be taken as the sum of the vibrational lattice component (κ_{lat}) and the component transferred by charge carriers (κ_{ele}). To measure the $\kappa_{tot,}$ the bulk samples had to be pressed into dense pellets. An Oxy-Gon model FR-210-30T hot-press was used to press the powders into pellets at high temperatures. 12.7 mm diameter pellets were formed by pressing the powdered samples in graphite dies in an inert Ar atmosphere at 773 K for 5 h. The Archimedes method was used to verify that the densities of the pellets were > 90% of the theoretical densities of the compounds. The κ_{tot} of the pellets was determined by taking the product of the density (ρ), specific heat (C_P), and thermal diffusivity (D). The D was determined *via* a TA Instruments DLF 1200 instrument which utilizes the laser flash method. A Vespel standard was used as an external standard to determine the C_P of the samples. The final measurement error of the κ was approximately 5%. The diffuson thermal conductivity model can predict the minimum thermal conductivity.[49] This model calculates the minimum experimental $\kappa_{diff.}$ based on the sound velocity (v_s) *via* the equation $\kappa_{diff} \approx 0.76 n^{2/3} k_B v_s$. Here, k_B is Boltzmann's constant and n is the number density of the material (atoms m^{-3}). The v_s of the materials was measured by coupling the 5 MHz transducer of a Walfront Smart Sensor Sound Velocity Meter with silicone oil. The v_s of $Sr_8Ge_4Se_{17}$ and $Ba_8Sn_4Se_{17}$ were determined to be 2117 m s^{-1} and 2916 m s^{-1}, respectively.

7.3 Crystal Structures

7.3.1 $Sr_8Ge_4Se_{17}$

Compared to the unit cell of $Ba_8Sn_4Se_{17}$, the unit cell of $Sr_8Ge_4Se_{17}$ can be viewed as a ¼ × 1 × ½ subcell of the large $Ba_8Sn_4Se_{17}$ unit cell. Therefore, we opted to depict the unit cell of $Sr_8Ge_4Se_{17}$ as a 4 × 1 × 2 supercell in Figure 7.2 to highlight its similarities with $Ba_8Sn_4Se_{17}$. Both structures feature A and B layers that alternate on the (200) planes. The A layers are composed of $[GeSe_4]^{4-}$ tetrahedra sheets of tetrahedra that align antiparallel with each neighbour (Figure 7.2a). The B layers comprise columns that run parallel to the *b* axis. There are two varieties of columns which alternate in the B layer. One type of column exclusively has stacked $[GeSe_5]^{4-}$ tetrahedra, whereas the other type of column exclusively has stacked $[GeSe_4]^{4-}$ tetrahedra (Figure 7.2b). Seating $[GeSe_4]^{4-}$ and $[GeSe_5]^{4-}$ tetrahedra into their respective columns is an essential distinction between the structure types.

Four crystallographically unique Ge atoms are in the unit cell of $Sr_8Ge_4Se_{17}$, each coordinated to four Se atoms. The Ge-Se bonds range from 2.21 Å to 2.44 Å as seen in Figure 7.3. The range of Ge-Se bonds in $Sr_8Ge_4Se_{17}$ is broader than the range of Ge-Se bonds found in the γ-Sr_2GeSe_4 structure (2.35 Å – 2.37 Å).[2] The Sr-Se bond distances in $Sr_8Ge_4Se_{17}$ range from 3.02 Å to 3.35 Å. Within this range Sr is coordinated to six Se (Sr8), seven Se (Sr1, Sr2, Sr3, Sr4, and Sr6), and eight Se atoms (Sr5, Se7). Sr8 adopts a distorted octahedral environment and is centred between the vertices of three $[GeSe_4]^{4-}$ and a $[GeSe_5]^{4-}$ anions, limiting its number of Se neighbours. The coordination environments observed in γ-Sr_2GeSe_4 are similar, with Sr1 being coordinated to eight Se atoms and Sr2 being coordinated to seven Se atoms.

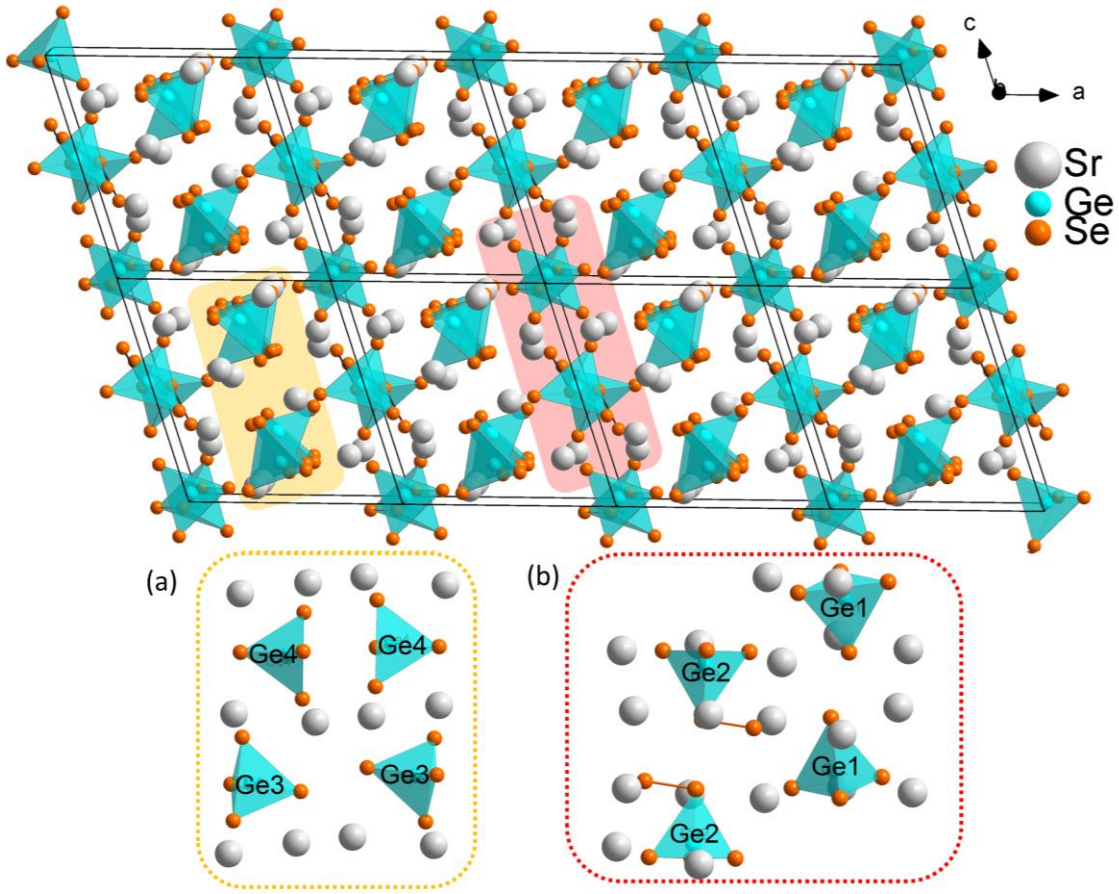

Figure 7.2. The crystal structure of $Sr_8Ge_4Se_{17}$ is depicted as a 4 × 1 × 2 supercell to highlight the structural similarities with the unit cell of $Ba_8Sn_4Se_{17}$. The yellow area highlights the arrangement of $[GeSe_4]^{4-}$ tetrahedra in the A layers of the structure (a). The red area highlights the columns of $[GeSe_4]^{4-}$ and $[GeSe_5]^{4-}$ tetrahedra that make up the B layers (b).

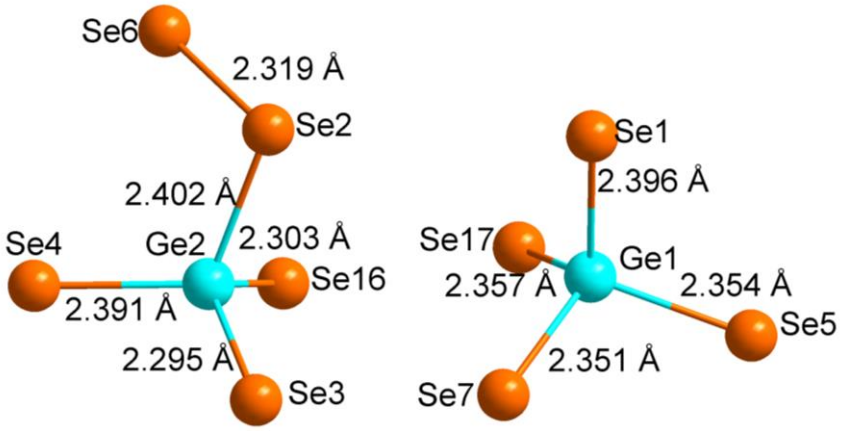

Figure 7.3. Examples of $[GeSe_5]^{4-}$ anions (left) and $[GeSe_4]^{4-}$ anions (right) that are found in $Sr_8Ge_4Se_{17}$.

7.3.2 $Ba_8Sn_4Se_{17}$

The structure of $Ba_8Sn_4Se_{17}$ has many similarities to the one of $Sr_8Ge_4Se_{17}$. The A and B planes that can be observed in $Sr_8Ge_4Se_{17}$ are still present, but they are more distorted, meaning that there are now four sets of A and B layers per $Ba_8Sn_4Se_{17}$ unit cell instead of the one pair that is in $Sr_8Ge_4Se_{17}$. In addition, because of the increased *c* axis, the A and B layers now alternate on the (800) set of planes. The sheets of $[SnSe_4]^{4-}$ in the A layers align in pairs (Figure 7.4a) as opposed to the $[GeSe_4]^{4-}$ in The A layers of $Sr_8Ge_4Se_{17}$ which align antiparallel to all their neighbours. Because of this pairing up of $[SnSe_4]^{4-}$ in $Ba_8Sn_4Se_{17}$, the *c* axis of the $Ba_8Sn_4Se_{17}$ structure type is double that of the $Sr_8Ge_4Se_{17}$ structure type. Contrary to the arrangement of $[GeSe_4]^{4-}$ and $[GeSe_5]^{4-}$ in the B layers of $Sr_8Ge_4Se_{17}$, in $Ba_8Sn_4Se_{17}$, the $[SnSe_4]^{4-}$ and $[SnSe_5]^{4-}$ do not segregate into their columns. Instead, each column comprises alternating $[SnSe_5]^{4-}$ and $[SnSe_4]^{4-}$ tetrahedra, as seen in Figure 7.4b.

The Sn-Se bonds in $Ba_8Sn_4Se_{17}$ range from 2.40 Å to 2.65 Å. The Ba-Se bonds go from 3.21 Å to 3.67 Å as shown in Figure 7.5. Likewise, the coordination number of the Ba sites increases relative to the Sr counterpart. There exist Ba atoms that are coordinated to seven Se (Ba10), eight Se (Ba3), and nine Se (Ba1). These Ba atoms can orient themselves in standard geometries. For example, Ba10 adopts a nearly undistorted pentagonal bipyramidal geometry with five equatorial Se atoms and two axial Se atoms. For comparison, the Ba-Se bond lengths of Ba_2SnSe_4 range from 3.2 Å to 3.65 Å.[165]

An interesting quality of these structures is that although their structures are similar, their space group relations cannot be understood through the perspective of *translationengleiche* or *klassengleiche* subgroups, as neither the translational nor point group symmetries are the same between the structures. Additionally, the subgroup cannot have a smaller unit cell than the supergroup; however, with these structures, the higher symmetry compound possesses a larger unit cell and more crystallographic sites.

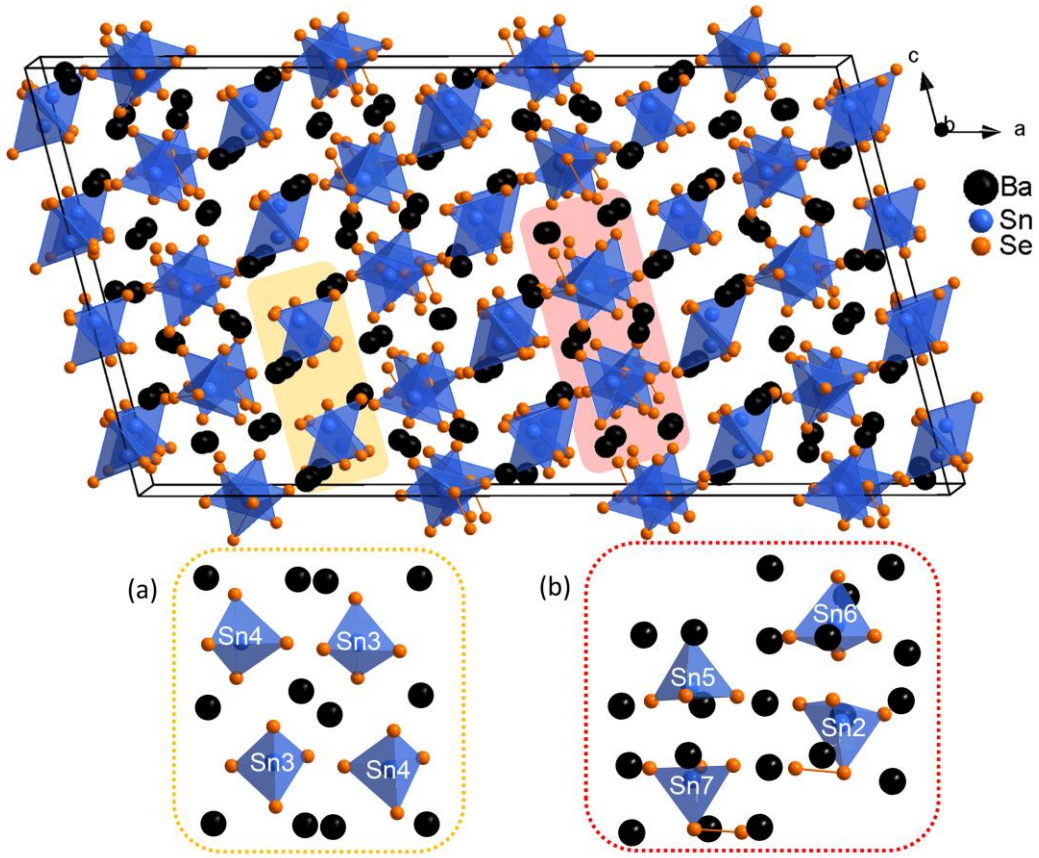

Figure 7.4. The unit cell of $Ba_8Sn_4Se_{17}$. The yellow area highlights the pairs of $[SnSe_4]^{4-}$ which align antiparallel to neighbouring pairs in the A layers (a). The red area highlights the columns of alternating $[SnSe_4]^{4-}$ and $[SnSe_5]^{4-}$ tetrahedra that make up the B layers (b).

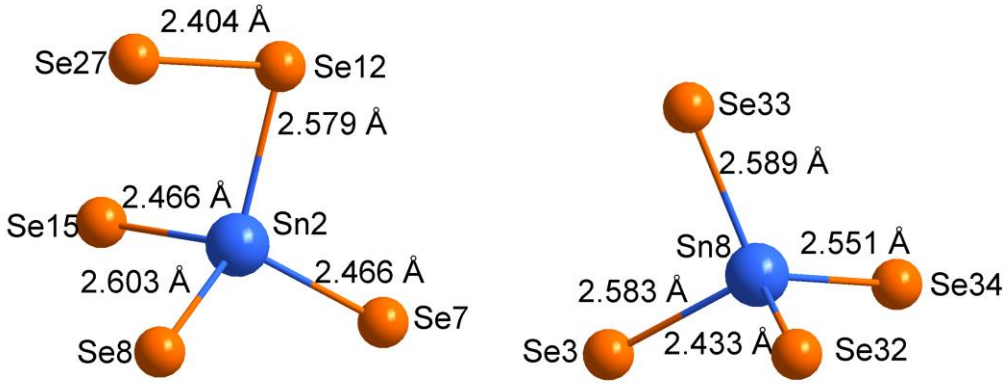

Figure 7.5. Examples of the $[SnSe_5]^{4-}$ anions (left) and $[SnSe_4]^{4-}$ anions (right) that can be found in $Ba_8Sn_4Se_{17}$.

7.4 Theoretical Studies

The electronic structures of the selenides reveal that both compounds have relatively flat bands and large density of states (DOS) near the Fermi energy (E_F). Flat bands are typical in structures with low dimensionalities, such as isolated tetrahedral anions.[5] Contributions from Se orbitals dominate the valence band, whereas, in the conduction bands, the Sr and Ba orbitals are the dominant contributors. In both compounds, there is a significant contribution from the interstitial states to the total DOS, as seen in Figure 7.6.

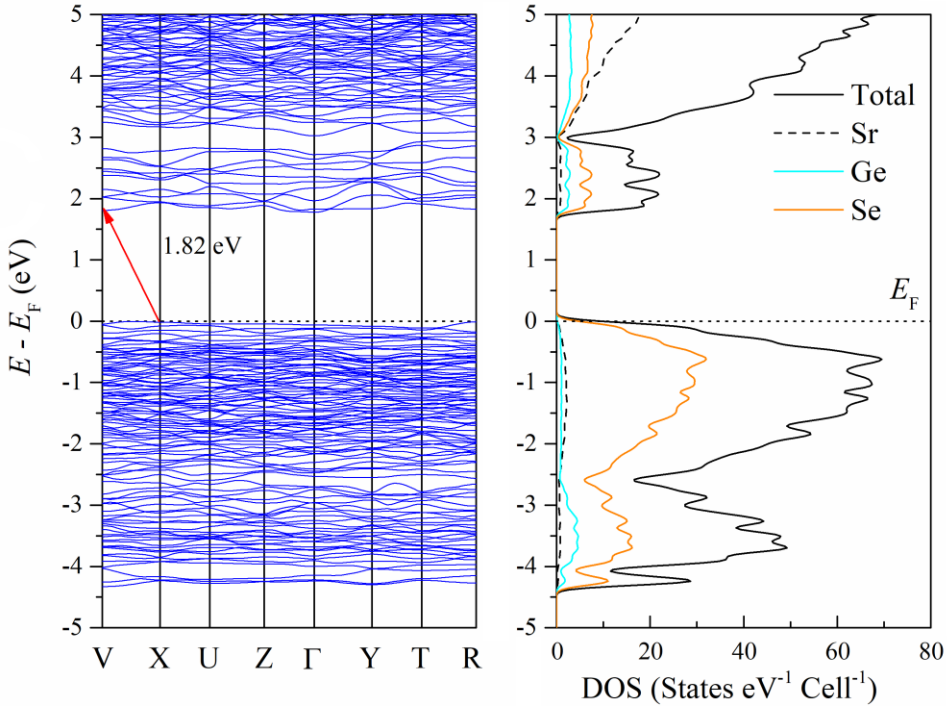

Figure 7.6. Band Structure and density of states of $Sr_8Ge_4Se_{17}$.

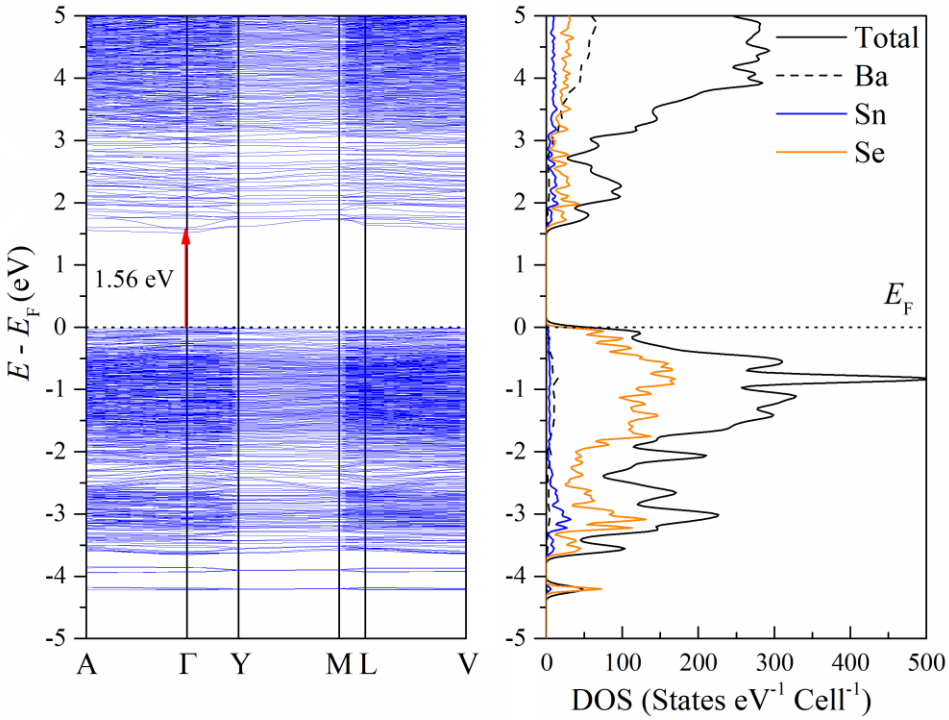

Figure 7.7. Band structure and density of states of $Ba_8Sn_4Se_{17}$.

7.5 Physical Properties

7.5.1 UV-Vis-NIR Spectroscopy

The optical band gaps of $Sr_8Ge_4Se_{17}$ and $Ba_8Sn_4Se_{17}$ were determined by intercepting the absorbance spectra baseline with the linear region of the absorption edge (Figure 7.8). The experimentally obtained band gaps of $Sr_8Ge_4Se_{17}$ and $Ba_8Sn_4Se_{17}$ were thus determined to be 1.88 eV and 1.93 eV, respectively. This agrees with their colours and qualitatively with the band gaps determined by DFT calculations. There is a more significant discrepancy between the calculated and experimental bandgaps of $Ba_8Sn_4Se_{17}$, which likely arises from the smaller number of *k* points not finding the global minimum when relaxing the structure.

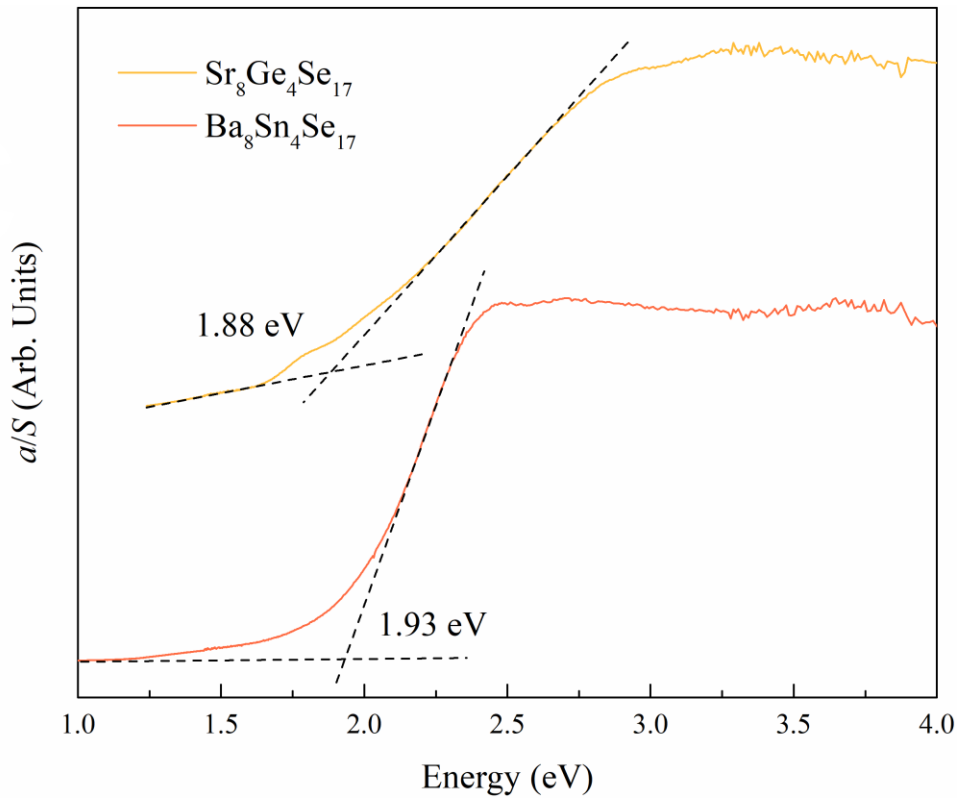

Figure 7.8. Optical band gap determination of $Sr_8Ge_4Se_{17}$ and $Ba_8Sn_4Se_{17}$.

7.5.2 Raman Spectroscopy

The Raman spectra (Figure 7.9) contained the characteristic peak associated with the Ge-Se and Sn-Se stretching modes at ~200 cm^{-1}. In Mg_2GeSe_4, the Ge-Se stretching modes are associated with 197 and 243 cm^{-1} peaks.[165] In the $Sr_8Ge_4Se_{17}$ and $Ba_8Sn_4Se_{17}$ compounds, both $[(Ge,Sn)Se_4]^{4-}$ and $[(Ge,Sn)Se_5]^{4-}$ are present which each have slightly different vibrational energies that are observed as overlapping peaks near 200 cm^{-1}. In $Sr_8Ge_4Se_{17}$, the symmetric and asymmetric vibrational modes of the Ge-Se bonds correspond to 200, 211, 235 and 280 cm^{-1}. In $Ba_8Sn_4Se_{17}$, the Sn-Se vibrational modes correspond to 193, 200, 218, and 256 cm^{-1} peaks. The Raman peaks in the $Ba_8Sn_4Se_{17}$ spectra are much broader since the structure contains many

symmetrically inequivalent $[SnSe_4]^{4-}$ and $[SnSe_5]^{4-}$ units that are slightly different in their vibrational energies.

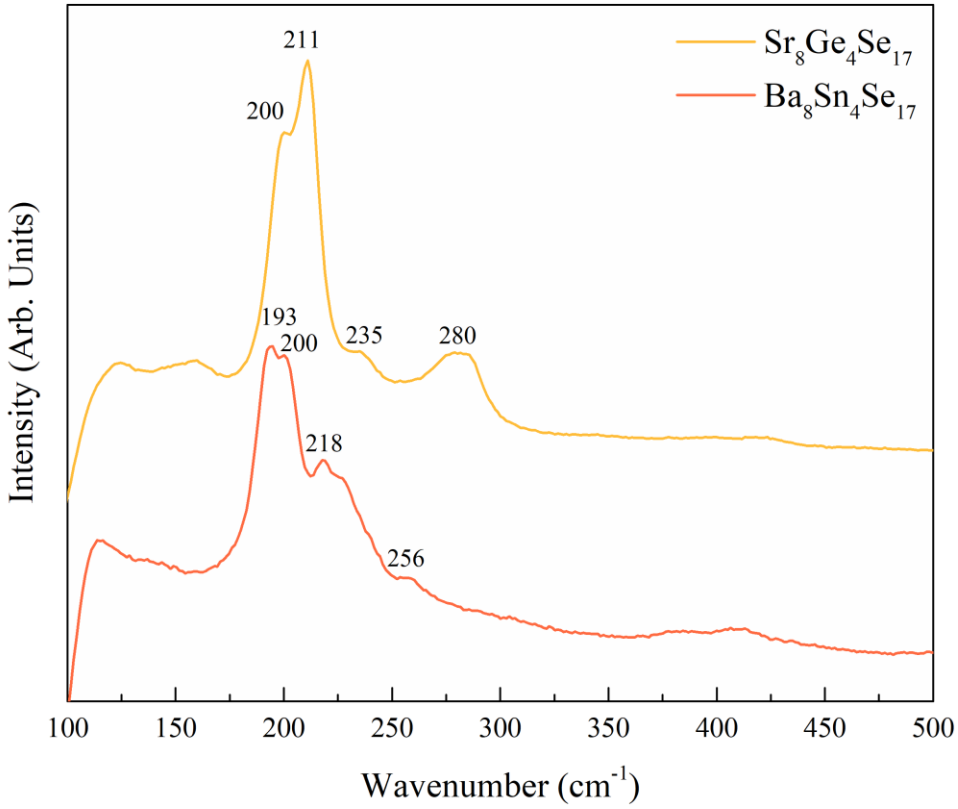

Figure 7.9. Normalized Raman spectra of $Sr_8Ge_4Se_{17}$ and $Ba_8Sn_4Se_{17}$.

7.5.3 Thermal Conductivity

The ultra-low κ_{tot} of the two title compounds are displayed in Figure 7.10. These κ_{tot} are based on the C_P and D experimentally determined in Figures A.25 and A.26, respectively. The C_P may be determined theoretically based on the Dulong-Petit law ($C_P = 3\,R\,/\,M_{avg.}$), where R is the ideal gas constant, and M_{avg} is the average molar mass of the compound. Theory dictates that the experimental C_P will approach the Dulong-Petit limit at elevated temperatures. This is observed in our experimental measurements as the C_P of $Sr_8Ge_4Se_{17}$ and $Ba_8Sn_4Se_{17}$ are below the Dulong-Petit limits at room temperature and comes up to match the Dulong-Petit limits once the

temperature reaches approximately 475 K in both compounds. Neither C_P measurement contained any anomalous trends that could be associated with phase transitions. The κ_{tot} of $Sr_8Ge_4Se_{17}$ and $Ba_8Sn_4Se_{17}$ are as low as 0.45 W m^{-1} K^{-1} (350 K) and 0.31 W m^{-1} K^{-1} (422 K), respectively. These κ_{tot} are comparable with the κ_{tot} of the complex Ba selenides $Ba_6Ge_2Se_{12}$ and $Ba_7Ge_2Se_{17}$ (0.33 W m^{-1} K^{-1} at 573 K).[152] There is a greater discrepancy between the κ_{tot} and κ_{diff} in the Sr compound than in the Ba compound. A similar discrepancy was observed when comparing the κ_{tot} and κ_{diff} of the Sr oxyselenide $Sr_6Ge_3OSe_{11}$ which had a 0.50 W m^{-1} K^{-1} at 573 K and a κ_{diff} of 0.22 W m^{-1} K^{-1}.[168]

Multiple mechanisms lead to low κ_{tot}. It is well understood that κ_{lat} is is lower in complex crystal structures.[169] The lattice can only possess (optical) vibrational modes with wavelengths greater than the length of its lattice parameters. Extremely large lattice parameters prohibit thermal transport by eliminating short wavelength vibrational spectrum regions. Additionally, phonon-phonon scattering *via* Umklapp processes is more efficient in the smaller reciprocal unit cell of $Ba_8Sn_4Se_{17}$. The result is that $Ba_8Sn_4Se_{17}$ has nearly identical κ_{tot} to that of $Ba_6Ge_2Se_{12}$ and $Ba_7Ge_2Se_{17}$, which have low κ_{tot} due to positional disorder of anions that effectively scatter short wavelength phonons.

Modern advances in thermoelectric research have been successful in discovering several new selenides with ultra-low thermal conductivities, such as $AgCrSe_2$ with 0.7 W m^{-1} K^{-1} at 300 K,[143] Tl_3VSe_4 with 0.30 W m^{-1} K^{-1} at 300 K,[144] and $CdAg_2Bi_6Se_{11}$ with 0.54 W m^{-1} K^{-1} at 300 K.[145] A thermoelectric material requires good intrinsic electric conductivity which typically arises from their narrow band gaps and not too flat bands. These compounds were too resistive to have their

electrical properties measured on our ULVAC ZEM-3 instrument, suggesting that their electric conductivity values are < 0.01 Ω^{-1} cm^{-1}.

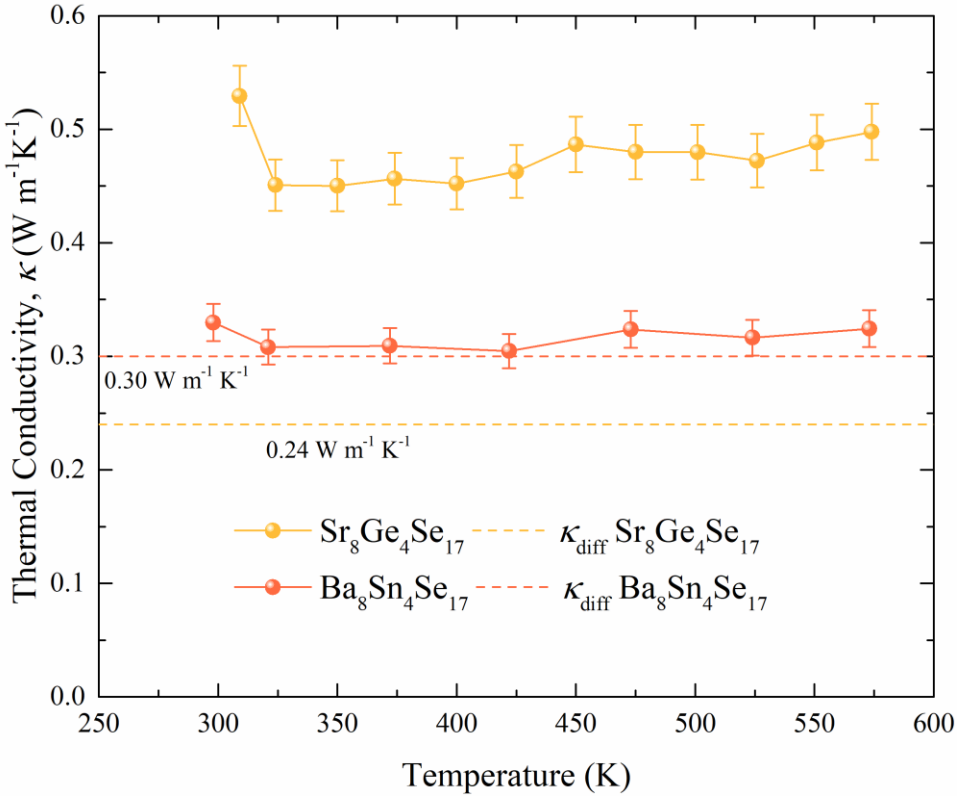

Figure 7.10. Thermal conductivities of $Sr_8Ge_4Se_{17}$ and $Ba_8Sn_4Se_{17}$ and their theoretical minimum thermal conductivities derived from the diffuson model.

7.6 Conclusion

In this investigation, the alkaline earth chalcogenides $Sr_8Ge_4Se_{17}$ and $Ba_8Sn_4Se_{17}$ and their properties are reported for the first time. Both compounds possess remarkably low thermal conductivities that are on par with the ultra-low thermal conductivities of state-of-the-art thermoelectric materials. The origin of their ultra-low thermal conductivities lies in their large unit cells, complex structures, and large unit cells that efficiently scatter phonons. However, alkaline earth metal selenides tend to have high ionicity and wide band gaps that limit their intrinsic

electrical conductivity. Compounded with the fact that the bands of these compounds are relatively flat due to their isolated $[(Ge,Sn)Se_4]^{4-}$ and $[(Ge,Sn)Se_5]^{4-}$ tetrahedra, these compounds have low electrical conductivities that limit their thermoelectric performance without significant doping.

The $Sr_8Ge_4Se_{17}$ and $Ba_8Sn_4Se_{17}$ structure types are also fascinating due to their subcell–supercell relationship. Unusually, the subcell structure adopts a lower symmetry structure since supercells tend to be less symmetrical due to long-range ordering. However, when the structural motifs shared between the structures are compared, differences significantly distinguish the two structure types.

CHAPTER 8

$Sr_6Ge_3OSe_{11}$

8.1 Introduction

Nonlinear optical (NLO) materials have attracted attention for their ability to convert laser wavelengths to ordinarily inaccessible regions of the light spectrum. NLO crystals have been in remote sensing,[170] environmental monitoring,[171] communication systems,[172] tissue imaging,[173] and minimally invasive surgeries.[92,174] To optimize the second harmonic generation (SHG) of these crystals, researchers have developed NLO materials specifically for the ultraviolet (UV), visible, and infrared (IR) spectral regions. In the mid-IR region, the chalcopyrite crystals $AgGaS_2$ (AGS), $AgGaSe_2$ (AGSe), and $ZnGeP_2$ (ZGP) are regarded as the benchmarks for their relatively large NLO susceptibility coefficients (d_{ij}) of 13 pm V^{-1}, 33 pm V^{-1}, and 75 pm V^{-1} respectively.[33] However, these compounds suffer from low laser damage thresholds (LDT) due to their relatively small optical band gaps. The bandgap of an NLO crystal must be large enough to not absorb the fundamental photons of the laser or the photons with twice the energy that SHG produces. To increase the band gap while maintaining large polarizability a strategy of combining oxygen with less electronegative anions in a single compound has been developed. This has been implemented successfully to produce several new noncentrosymmetric (NCS) oxychalcogenides such as

$SrZn_2OS_2$ (space group = $Pmn2_1$),[175] $SrGeOS_2$ ($P2_12_12_1$),[176] $BaGeOS_2$ ($P2_12_12_1$), [176] $Ba_3Ge_2O_4Te_3$ ($R3m$),[177] $Ba_5Ga_2SiO_4S_6$ (Cc),[31] $Sr_4Pb_{1.5}Sb_5O_5Se_8$ (Cm),[178] and $Sr_2MGe_2OS_6$ ($P\bar{4}2_1m$) where M = Mn, Zn, or Cd.[179]

Herein, we outline the strategy used to synthesize the NCS compound $Sr_6Ge_3OSe_{11}$. Previously, our groups had studied the effects of elemental substitution in the NLO properties of γ-Sr_2GeSe_4.[119] To perform partial isovalent anion substitution (PIAS) on this compound ⅓ of a mol of Se was replaced with ⅓ of a mol of O. This yielded crystals of the novel compound $Sr_6Ge_3OSe_{11}$ (i.e. $Sr_2GeO_{0.33}Se_{3.67}$). $Sr_6Ge_3OSe_{11}$ ($P3m1$) crystallizes in a new NCS structure type and is the third quaternary compound consisting of Sr, Ge, O and Se. Remarkably the other three quaternary compounds in this family, $SrGeOSe_2$ ($P2_12_12_1$),[29] $Sr_3Ge_2O_4Se_3$ ($R3m$),[180] and $Sr_3Se[GeOSe_3]$ ($Pca2_1$)[181] also adopt NCS crystal structures. Likewise, the quaternary Ba variant $BaGeOSe_2$ ($P2_12_12_1$) also adopts an NCS crystal structure.[182] This work aims to highlight oxychalcogenides as a promising materials class for NLO research and that PIAS is a valuable strategy for making NCS structures.[183,184]

8.2 Synthesis

The synthesis of the $Sr_6Ge_3OSe_{11}$ compound was carried out using traditional solid-state synthesis. The source of O in this preparation was SrO, although our experimentation showed that $Sr_6Ge_3OSe_{11}$ could also be synthesized using SeO_2 as a source of O. Before using the SrO, it was dried in an alumina boat for 1 h in a 973 K resistance furnace to remove any water that may have been absorbed. The samples were prepared in a glove box with a dry Ar atmosphere by weighing Sr, Ge, Se, and SrO in a 5:3:11:1 ratio (Sr: granules, 99%, Alfa Aesar; Ge: pieces, 99.999%, Strem

Chemicals; Se: powder, 99.999%, Alfa Aesar; SrO: powder, 99.9%, Sigma Aldrich) and adding them to a C-coated silica tube. The filled silica tubes were evacuated to < 2.5×10^{-3} bar and sealed with an H_2/O_2 torch. The sealed ampoule was heated to 673 K at a rate of 100 K/h and held at this temperature for 36 h to completely react with the Se powder. The temperature was then increased to 923 K at 100 K h^{-1} and held for another 36 h before turning the furnace off and allowing the sample to cool to room temperature. At this point, there were crystals suitable for single-crystal X-ray diffraction (XRD). For phase pure $Sr_6Ge_3OSe_{11}$, the bulk sample needed to be ground, resealed in an ampoule and annealed in a resistance furnace at 923 K for a final 72 h. This procedure could not synthesize analogous compounds with the same stoichiometry made with Ba, Si, or S.

Thermal conductivity measurements and SHG intensity measurements require dense samples. To create dense samples of $Sr_6Ge_3OSe_{11}$, phase-pure samples were hot-pressed into 12.7 mm pellets using an Oxy-Gon model FR-210-30T hot-press. The samples were loaded into graphite dies and pressed under 54 MPa of pressure at 773 K in an inert Ar atmosphere for 5 h.

Single-crystal XRD experiments were performed using a Bruker Kappa Apex II CCD diffractometer with Mo-Kα radiation. A yellow block-shaped crystal of $Sr_6Ge_3OSe_{11}$ was mounted, and each ω scan was collected for 30 s. Within SADABS the multi-scan method was used as the correction method.[133] The crystal structure of $Sr_6Ge_3OSe_{11}$ was solved using the SHELXTL program.[44,45] Finally, the fractional coordinates within the unit cell were standardized using the "TIDY" program within the PLATON package.[134,135] The final refined structure had a low Flack parameter of 0.027(7), indicating that the refined structure is in the correct absolute orientation. Initially, the SHELXTL program did not automatically identify the O atom in the

structure and instead labelled it as a Q peak with 9 e A^{-1}. This Q position was manually labelled as an O atom which resulted in the following charge-balanced formula: $(Sr^{2+})_6(Ge^{4+})_3(O^{2-})(Se^{2-})_{11}$. A summary of the crystallographic details is given in Table 8.1, and the fractional coordinates of atoms within the unit cell are presented in Table A.11.

Powder XRD patterns were collected on an Inel XRG 3000 diffractometer. GSAS-II was used to perform the Rietveld refinement of the bulk sample.[46] Neither single crystal nor Rietveld refinements indicated any O/Se mixing on the O site. The isotropic thermal displacement parameters (U_{iso}) were refined due to the lower spatial resolution of the detector of the powder XRD compared to the 2D detector of the single crystal diffractometer. When refining the U_{iso} values, the U_{iso} of O1 and Se1 were constrained to be equivalent since they are part of the $[GeOSe_3]^{4-}$ anion and the U_{iso} of Se2, Se3, Se4, and Se5 were constrained in the same manner because they make up the $[GeSe_4]^{4-}$ anions.

The electronic structure of $Sr_6Ge_3OSe_{11}$ was calculated using the Wien2K program to solve the Kohn-Sham equations *via* the full potential linear augmented plane wave model. [78,102] The Perdew-Burke-Ernzerhof (PBE) functional was used as the generalized gradient approximation (GGA) for the exchange-correlation energy.[54] A dense 10 × 10 × 15 grid of *k* points was used for the calculations. The energy convergence and electric charge convergence criteria were set to < 0.001 Ry and < 0.001 e for the self-consistent cycles. Once the convergence criteria were met, the band structure and density of states (DOS) were calculated. To create the path in *k* space for the band structure, XCrySDen created a continuous path that passes through all the high symmetry points of the first Brillouin zone.[136]

The Elk code was used to calculate the energy-dependent optical properties such as refractive indices and d_{ij}.[56] This software computes NLO susceptibilities from first principles using the sum-over-state formalism.[63] Elk was also used to produce an electron localization function (ELF) of $Sr_6Ge_3OSe_{11}$. The exchange-correlation functionals, convergence criteria, and *k* point mesh were all set to match the parameters of the Wien2K calculations.

The thermal conductivity (κ) of the hot-pressed $Sr_6Ge_3OSe_{11}$ pellet was measured on the TA Instruments DLF 1200 instrument up to 573 K under an Ar atmosphere. κ is defined as the product of thermal conductivity (D), specific heat (C_P), and density (ρ). The D is measured directly *via* the laser flash method, the C_P is measured relative to a Vespel standard, and ρ is measured by the Archimedes method. The experimental error of κ is estimated to be 5%. Additionally, the minimum thermal conductivity (κ_{diff}) can be calculated from the sound velocity of a medium.[49] A 5.0 MHz Walfront Smart Sensor Sound Velocity Meter was coupled to the pellets using silicone oil to obtain the sound velocity through the pellet.

The absorbance spectrum of the powdered $Sr_6Ge_3OSe_{11}$ sample was determined *via* diffuse reflectance spectroscopy using a PerkinElmer Lambda 1050 UV/vis/NIR spectrometer. The samples were prepared by adhering the $Sr_6Ge_3OSe_{11}$ powder to a glass substrate using double-sided tape. The percent reflectance (R) spectrum was converted to an absorbance spectrum (α/S) *via* the Kubelka-Munk equation ($\alpha/S = (1 - R)^2 / (2 R)$). Additionally, Fourier transform IR (FTIR) spectroscopy was performed on a Bruker Tensor 27 FTIR spectrometer to observe the transparency of the sample in the IR region.

The experimental SHG measurements were carried out using the Kurtz-Perry technique.[51] The hot-pressed pellets were crushed and sieved to separate the sample by particle size. The particle size ranges were as follows: < 20 μm, 20 – 45 μm, 45 – 63 μm, 63 – 75 μm, 75 – 90 μm, 90 – 125 μm, and 125 – 150 μm. The powders were loaded into silica tubes according to their size. KH_2PO_3 (KDP) standards of the same particle sizes were used as references for the relative SHG intensities. The samples were struck by a 1064 nm Nd:YAG laser, which led to the production of 532 nm by the NCS medium. These scattered 532 nm photons were focused at a photomultiplier tube (PMT) to detect the SHG signal. A short pass filter is placed before the PMT to prevent scattered 1064 nm photons from being detected.

8.3 Crystal Structure

$Sr_6Ge_3OSe_{11}$ adopts a new trigonal structure type which is depicted in Figure 8.1. The $Sr_6Ge_3OSe_{11}$ structure type consists of two different structural motifs oriented 120º to each other, creating trigonal symmetry. All the Ge tetrahedra are aligned, which makes the space group symmetry NCS. There are three crystallographic Ge positions in the $Sr_6Ge_3OSe_{11}$ structure type. These exist in the 1a, 1b, and 1c Wycoff positions. The Ge in site 1a forms the partially substituted $[GeOSe_3]^{4-}$ anion, whereas the Ge atoms in the 1b and 1c sites form the familiar $[GeSe_4]^{4-}$ anions. The 3-fold rotational symmetry in this structure originates from the partial substitution of Se with O in the Ge tetrahedra.

Table 8.1. Crystallographic Data for $Sr_6Ge_3OSe_{11}$ from the Single-Crystal XRD Measurement.

Parameter	$Sr_6Ge_3OSe_{11}$
Crystal system	Trigonal
Space group	*P*3*m*1 (no. 156)
a (Å)	10.268(5)
b (Å)	10.268(5)
c (Å)	6.363(3)
γ (°)	120
Unit cell volume ($Å^3$)	580.9(7)
Crystal size (mm)	0.06 × 0.2 × 0.4
Formula units per unit cell, *Z*	1
Molecular weight (g mol^{-1})	1628.20
Density (g cm^{-3})	4.654
Radiation, wavelength (Å)	0.71073 (Mo Kα)
Temperature (K)	300(2)
F(000)	706
Absorption coefficient, μ (mm^{-1})	34.701
Goodness-of-fit	1.019
R_1 [I > 2σ(I)]	0.0104
wR_2 [I > 2σ(I)]	0.0208
Largest diff. peak, hole (e $Å^{-3}$)	0.389, -0.445

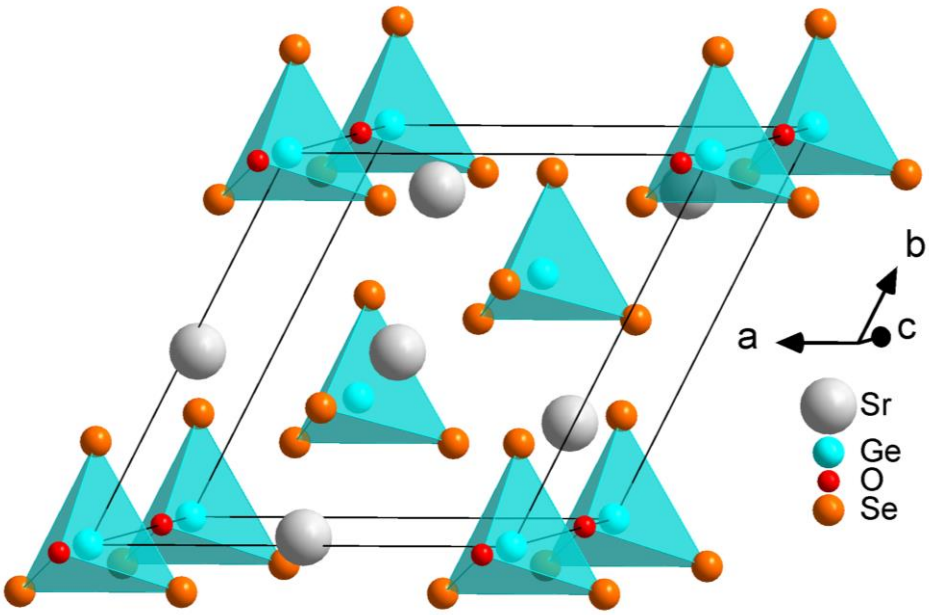

Figure 8.1. Crystal structure of $Sr_6Ge_3OSe_{11}$.

The two primary structural motifs in $Sr_6Ge_3OSe_{11}$ extend infinitely in the *c* direction of the lattice and are visualized in Figure 8.2. In the $\{Sr_3GeSe_4\}$ motif, the trigonal plane of strontium atoms is staggered with the three selenium atoms that make up the base of the tetrahedron below, whereas in the $\{Sr_3GeOSe_3\}$ motif, the trigonal plane of strontium atoms eclipses the base of the tetrahedron below it. We postulate that the alignment of the individual dipoles in these motifs leads to a large NLO response.

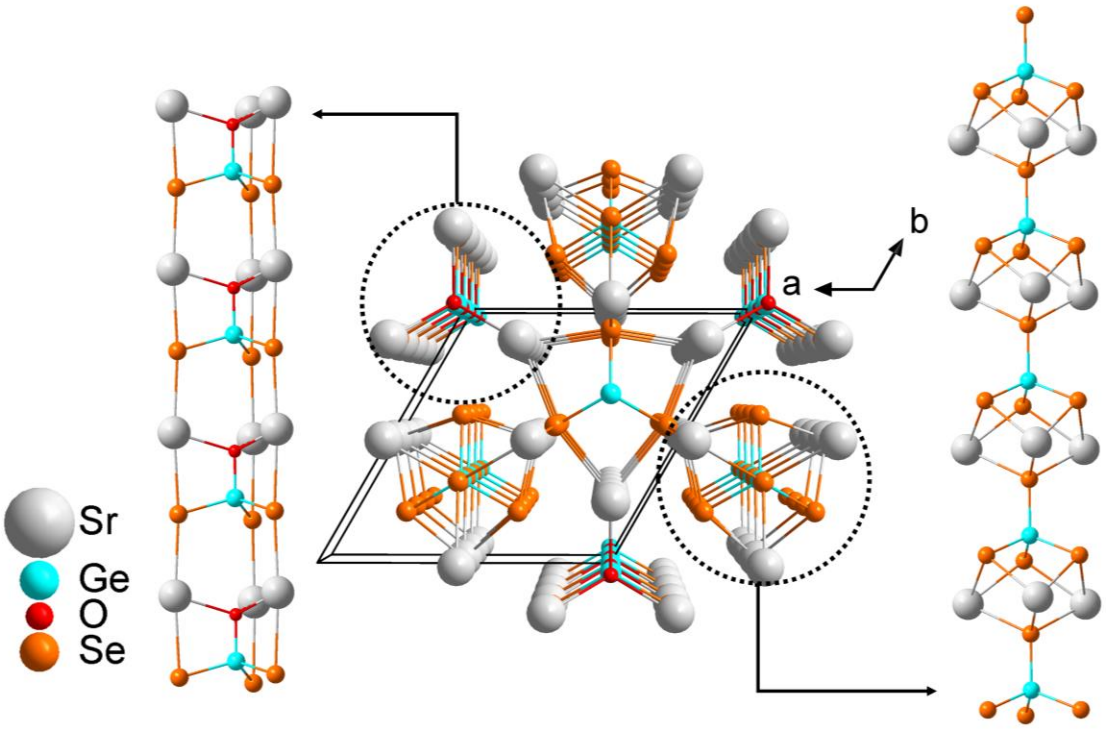

Figure 8.2. 1D $\{Sr_3GeOSe_3\}$ and $\{Sr_3GeSe_4\}$ structural motifs in $Sr_6Ge_3OSe_{11}$.

The oxygen atom has a coordination number of four with three 2.51 Å bonds to Sr2 atoms and one 1.82 Å bond to Ge1. For comparison, in $SrGeOSe_2$ and $Sr_3Ge_2O_4Se_3$, the Ge-O bonds are 1.78 Å to 179 Å and 1.76 Å, respectively.[29,180] The Ge-Se bond distances range from 2.32 Å to 2.39 Å in $Sr_6Ge_3OSe_{11}$, as seen in Table 8.2 and Figure 8.4. The Ge-O bonds in $Sr_6Ge_3OSe_{11}$ and $Sr_3Ge_2O_4Se_3$ are slightly longer than those in $SrGeOSe_2$ because the latter contains $[GeO_2Se_2]^{4-}$ anions. Due to the higher electronegativity of O compared to Se ($\chi_O = 3.44$ vs $\chi_{Se} = 2.55$), the Ge atom coordinated to two O atoms will have less electron density around it, thus shortening its bonds. Single-crystal refinements and the Rietveld refinement in Figure 8.4 did not indicate any O/Se mixing on the O1 or Se sites.

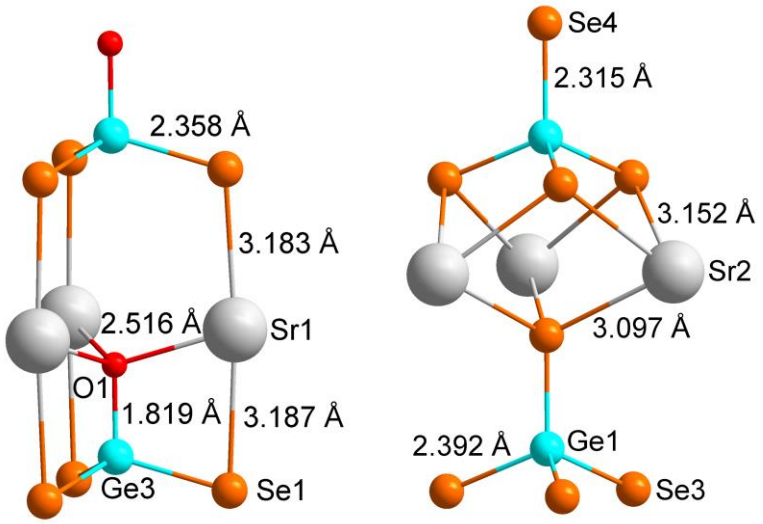

Figure 8.3. Coordination environments and bond distances of the $[GeOSe_3]^{4-}$ (left) and $[GeSe_4]^{4-}$ (right) anions in $Sr_6Ge_3OSe_{11}$.

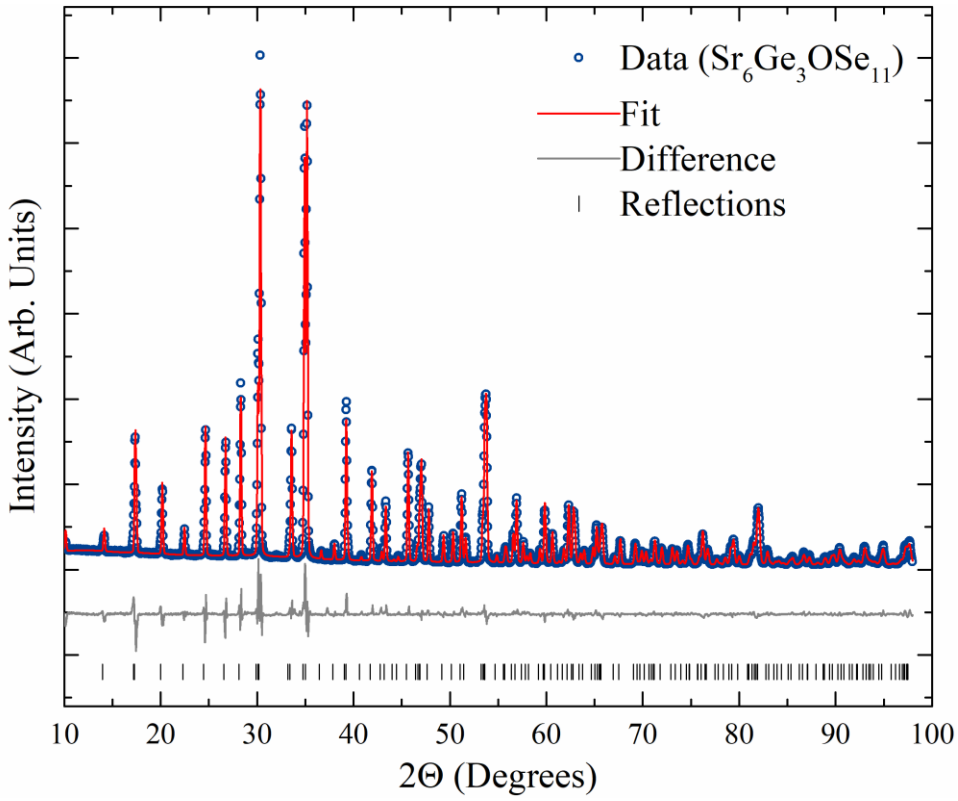

Figure 8.4. Rietveld refinement fit of a ground sample of $Sr_6Ge_3OSe_{11}$.

Table 8.2. Selected Interatomic Distances (in Å) for $Sr_6Ge_3OSe_{11}$.

Atom pair	Distance	Atom pair	Distance
Sr1–O1	2.516(2)	Sr2–Se4	3.097(1)
Sr1–Se2	2× 3.131(2)	Sr2–Se5	3.130(2)
Sr1–Se1	3.183(2)	Sr2–Se2	3.147(2)
Sr1–Se1	3.187(2)	Sr2–Se3	2× 3.152(1)
Sr1–Se3	2× 3.388(2)	Sr2–Se1	2× 3.453(2)
		Sr2–Se2	3.477(2)
Ge1–Se4	2.315(2)		
Ge1–Se3	3× 2.392(1)	Ge3–O1	1.819(5)
		Ge3–Se1	3× 2.358(1)
Ge2–Se2	3× 2.342(1)		
Ge2–Se5	2.358(2)		

8.3.1 Electronic Structure

The electronic structure of $Sr_6Ge_3OSe_{11}$ is depicted in Figure 8.5. $Sr_6Ge_3OSe_{11}$ was calculated to have a direct band gap of 1.80 eV at the A point in the Brillouin zone. The three lowest unfilled bands of the conduction band arise from the empty 4*s* orbitals of the three Ge atoms in the unit cell.[185] The bands are relatively flat because the isolated Ge tetrahedra suggest this compound has high resistivity.

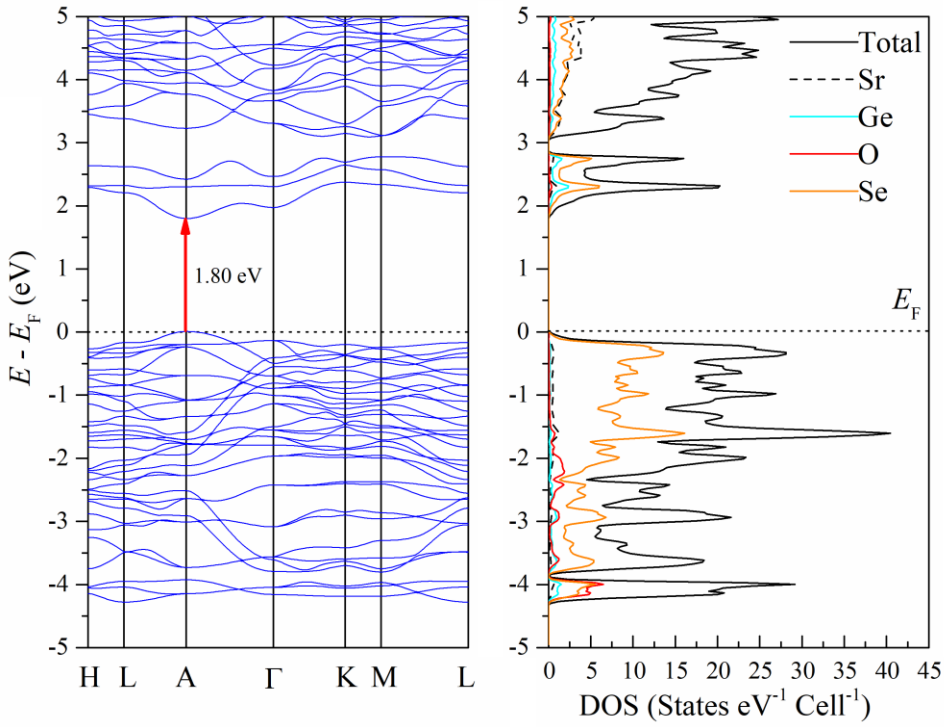

Figure 8.5. Band structure (left) and DOS (right) of $Sr_6Ge_3OSe_{11}$.

Modelling the ELF of the crystal structure shows covalent bonding between Ge and neighbouring O and Se atoms. The electron density around the O atoms is far more concentrated than that around the Se atoms in the $[GeOSe_3]^{4-}$ or $[GeSe_4]^{4-}$ tetrahedra. Moreover, the bonding between Sr and the O and Se anions is essentially ionic, increasing the band gap while not diminishing the polarizable nature of the polyatomic anions.

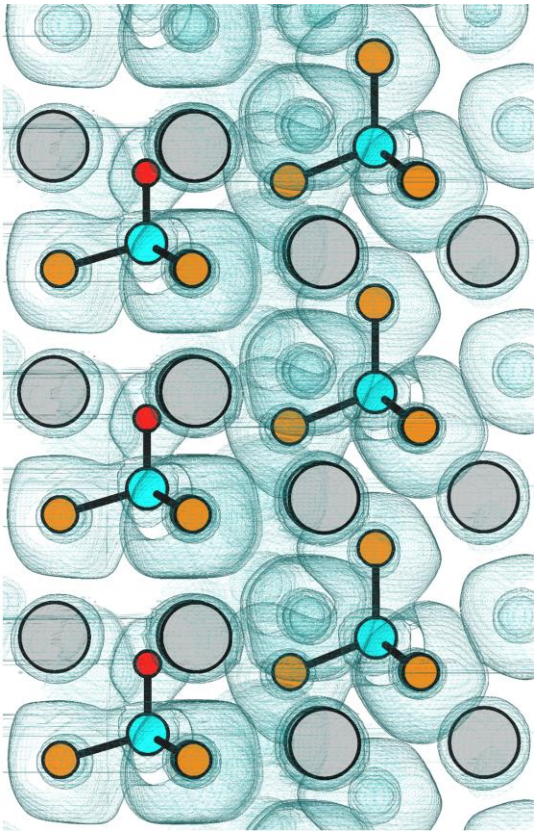

Figure 8.6. ELF isosurface plot of $Sr_6Ge_3OSe_{11}$ overlaid with the atomic structure. Sr atoms: gray; Ge: blue; O: red; Se: orange.

8.3.2 Optical Properties

To calculate the optical properties, including refractive indices and second-order nonlinear susceptibilities, a scissor operator was used to elevate the conduction bands to align with the experimental band gap since the GGA method often underestimates the actual band gap value. $Sr_6Ge_3OSe_{11}$ crystallizes in the *P*3*m*1 space group, meaning that $a = b \neq c$ is part of a uniaxial crystal system. Uniaxial crystal systems have two unique refractive indices: n_{xx} and n_{zz}. Figure 8.7 shows that the energy-dependent refractive indices of n_{xx} and n_{zz} are 2.45 and 2.36 at 1064 nm, respectively. The birefringence is defined as the difference in refractive indices. For NLO materials in the IR region, the ideal birefringence is $0.03 \leq \Delta n \leq 0.09$ to meet the phase-matching conditions

for SHG. Figure 8.7 shows that n_{xx}(1064 nm) = n_{zz}(532 nm), meaning that $Sr_6Ge_3OSe_{11}$ is phase matchable at this wavelength. This agrees with the results of the experimental SHG experiment.

$Sr_6Ge_3OSe_{11}$ belongs to the 3*m* space group. Under Kleinman symmetry conditions, the 3*m* space group has three unique tensor elements: d_{15}, d_{22}, and d_{33}.[50] Additionally, the effective nonlinear susceptibility, d_{eff}, for a powdered sample was calculated using the formula developed by Kurtz and Perry.[51] Figure 8.7 highlights the d_{ij} elements at 1064 nm because the experimental SHG intensity was measured at this wavelength. The calculated d_{ij} elements at 1064 nm were determined to be -12.9 pm V^{-1}, -15.4 pm V^{-1}, 15.0 pm V^{-1} and 17.0 pm V^{-1} for d_{15}, d_{22}, d_{33}, and d_{eff} respectively. Relative to other oxyselenides like $SrGeOSe_2$ (d_{ij} = 3.16 pm V^{-1}, 1.3 × AGS), $Sr_3Ge_2O_4Se_3$ (2.96 pm V^{-1}, 0.8 × AGS), and $BaGeOSe_2$ (4.1 pm V^{-1}, 0.5 × AGS) the calculated d_{lj} elements of $Sr_6Ge_3OSe_{11}$ are significantly larger in magnitude. The SHG response may be more significant if measured in the IR region.

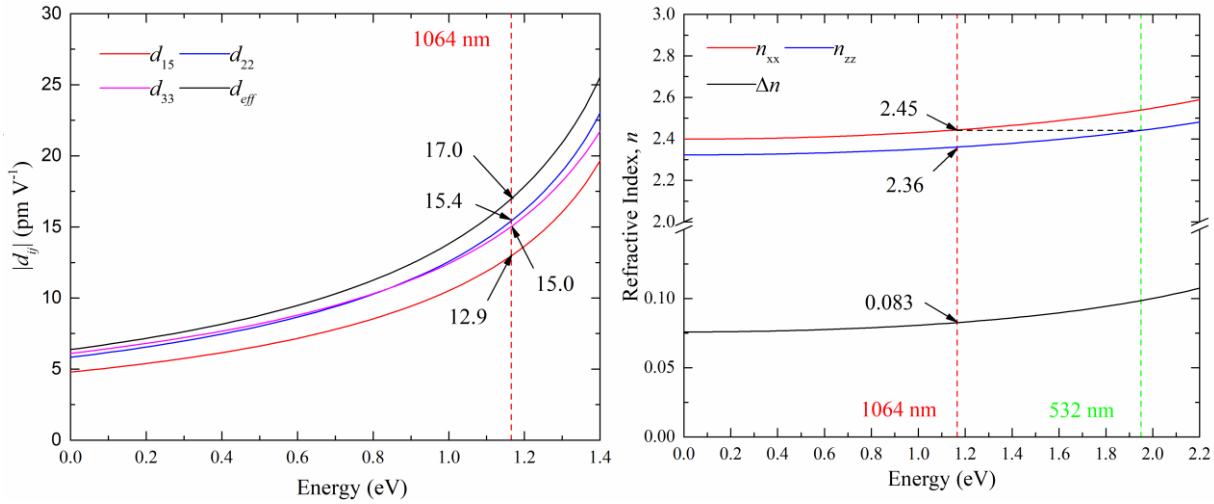

Figure 8.7. Calculated *d*-tensor elements (left) and the calculated refractive indices (right).

8.4 Physical Properties

8.4.1 Thermal Conductivity

The experimental κ of $Sr_6Ge_3OSe_{11}$ decreased slightly from 0.57 W m^{-1} K^{-1} at 923 K to 0.50 W m^{-1} K^{-1} at 573 K. $Sr_6Ge_3OSe_{11}$ has extremely low κ resulting from its complex crystal structure. The temperature-dependent C_P and D plots are available in Figures A.27 and A.28, respectively. The smooth trend suggests no phase transitions in this temperature range. The theoretical minimum thermal conductivity, κ_{diff}, which is based on the sound velocity through the material, was equal to 0.35 W m^{-1} K^{-1}. This is comparable to the κ of the seleno-germanates $Ba_6Ge_2Se_{12}$ and $Ba_7Ge_2Se_{17}$ (0.33 W m^{-1} K^{-1} at 573 K).[152]

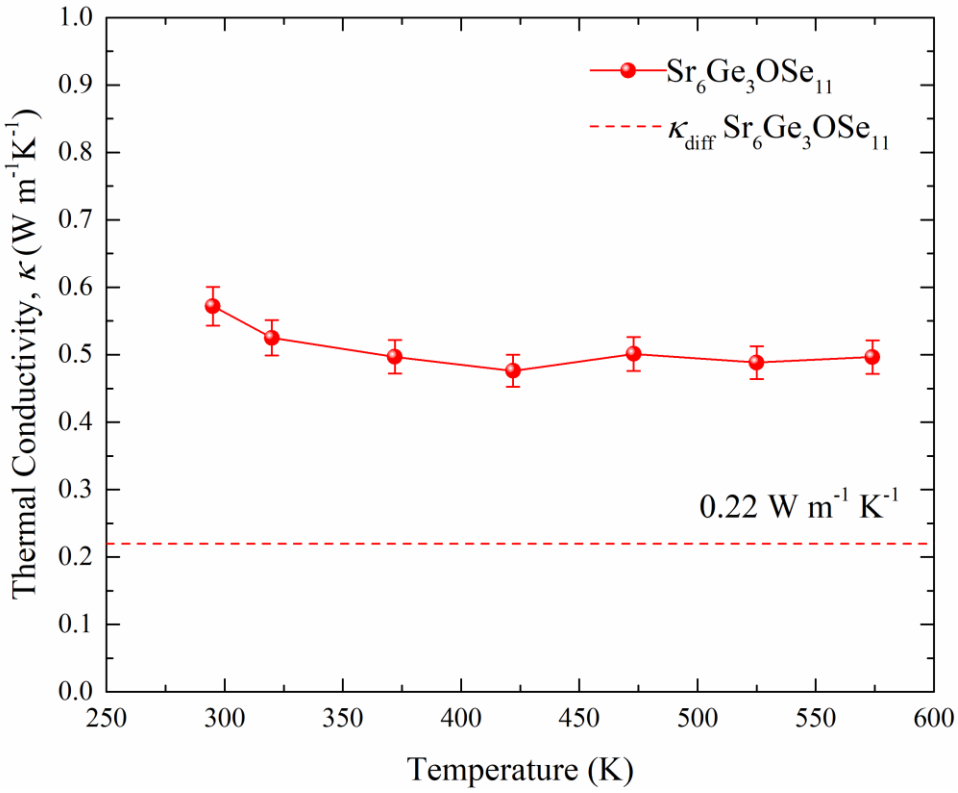

Figure 8.8. Thermal conductivity of $Sr_6Ge_3OSe_{11}$.

8.4.2 UV-Vis-NIR Spectroscopy

The spectroscopic studies of $Sr_6Ge_3OSe_{11}$ reveal an optical band gap of 2.39 eV and a wide transparency range in the IR region. Despite having similar stoichiometries, the band gap is approximately 20% larger than that of γ-Sr_2GeSe_4 (band gap = 2.00 eV). Compared to the quaternaries $SrGeOSe_2$ (3.16 eV) and $Sr_3Ge_2O_4Se_3$ (2.96 eV), $Sr_6Ge_3OSe_{11}$ has a smaller band gap because of the smaller atomic ratio of O.

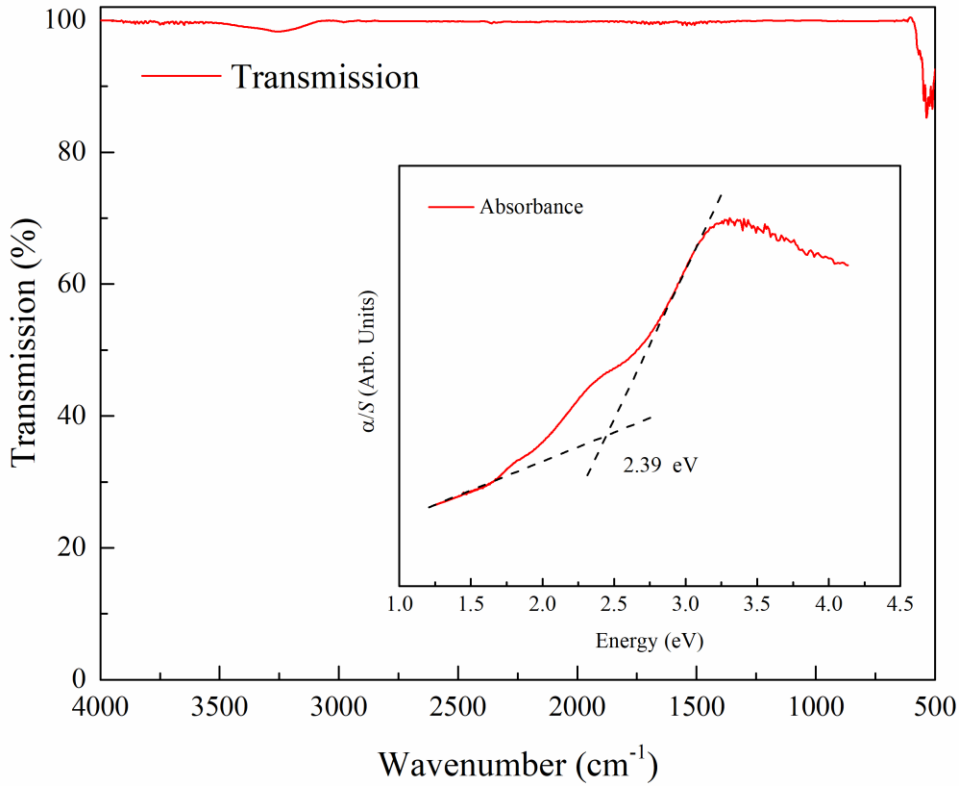

Figure 8.9. IR transmission spectrum and UV−vis absorbance spectrum (inset) of $Sr_6Ge_3OSe_{11}$.

8.4.3 Second Harmonic Generation

When $Sr_6Ge_3OSe_{11}$ was exposed to a 1064 nm laser beam, it produced 532 nm photons through SHG. Seven samples of various particle sizes were exposed to the fundamental beam, and

their intensities were compared to the SHG intensity of a KDP standard. The logarithmic trend of SHG intensity with increasing particle size indicates phase-matching behaviour. Phase matching is an indication that the birefringence of the compound is of suitable magnitude to prevent a phase mismatch ($\Delta k \neq 0$) when the wave vectors of the fundamental photons, $2 \times k(\omega)$, are converted to $k(2\omega)$ *via* SHG.[186]

The SHG intensity of $Sr_6Ge_3OSe_{11}$ was 0.62 × KDP for the largest particle sizes. Given that $Sr_6Ge_3OSe_{11}$ is yellow, there may have been two-photon absorption by the sample reducing its output of SHG photons. Therefore, it remains to be seen whether or not the performance of $Sr_6Ge_3OSe_{11}$ would be improved by testing the sample under a fundamental source in the IR region, such as a 2090 nm Ho:YAG laser. Other selenogermanates that have been studied for the NLO properties in the IR region include $SrCdGeSe_4$ (5.3 × AGS),[187] $SrHgGeSe_4$ (5 × AGS),[146] $BaHgGeSe_4$ (4.7 × AGS),[146] $BaZnGeSe_4$ (1 × AGS),[117] Hg_2GeSe_4 (2.1 × AGSe),[34] $Li_2SrGeSe_4$ (0.5 × AGS),[147] and $Na_2SrGeSe_4$ (0.5 × AGS).[147]

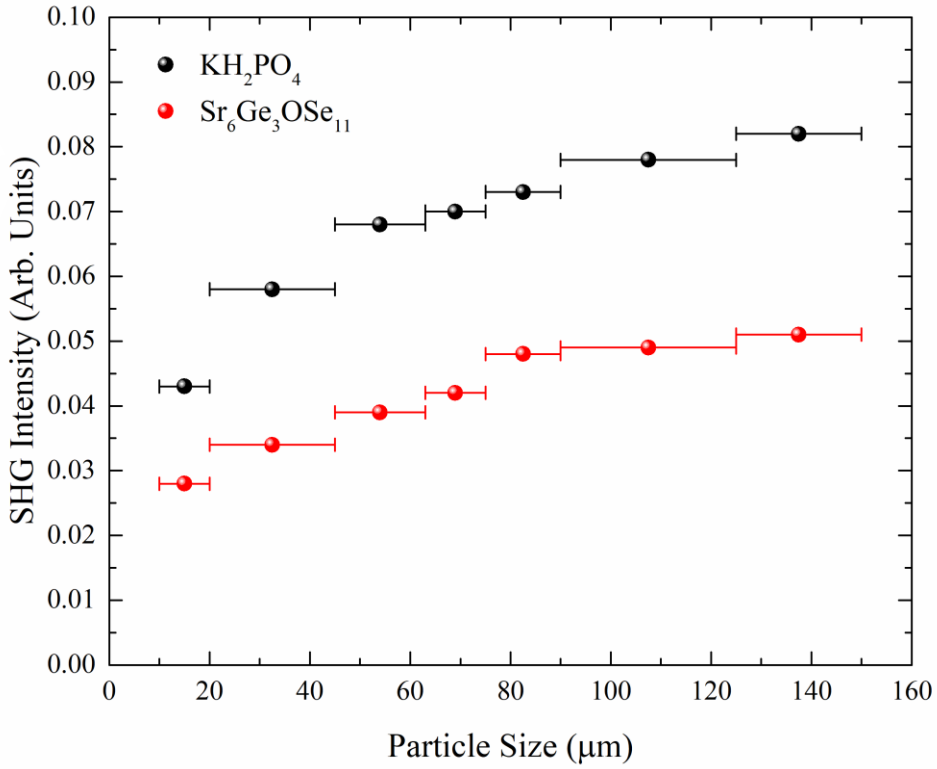

Figure 8.10. Size-dependent SHG intensities of $Sr_6Ge_3OSe_{11}$ and the KH_2PO_4 standard.

8.5 Conclusion

The new NCS quaternary oxyselenide $Sr_6Ge_3OSe_{11}$ was successfully synthesized, and the NLO properties were studied. $Sr_6Ge_3OSe_{11}$ has a significant NLO susceptibility (d_{eff} = 17.0 pm V^{-1}) compared to other oxychalcogenides that have been reported so far. This may arise from the alignment of the dipoles in the $\{Sr_3GeOSe_3\}$ and $\{Sr_3GeSe_4\}$ structural motifs that run in the *c* direction of the lattice. Unfortunately, the experimental SHG intensity did not reflect these large values, likely because the 2.39 eV band gap absorbed some of the SHG from the Nd:YAG laser source. It remains to be seen whether measuring the NLO response in the IR region would be comparable to the performance of the IR NLO benchmark AGS.

Along with $SrGeOSe_2$, $Sr_3Ge_2O_4Se_3$, and $Sr_3Se[GeOSe_3]$, $Sr_6Ge_3OSe_{11}$ is the third member of this phase space; all of which adopt NCS structures. For chemists performing exploratory work into new NCS compounds, PIAS is a promising strategy for finding unidentified NCS compounds. In this phase space, PIAS has been employed by replacing O with Se in the case of $SrGeO_3$ and Se with O in the case of γ-Sr_2GeSe_4. If we take these two examples as prototypes, it may be beneficial to start with chalcogen-rich compounds and introduce O into them so that the polarizable chalcogen anions preserve polarizability while the O increases ionicity and LDT.

CHAPTER 9

Conclusion

9.1 Conclusion

This thesis delves into the intricate realm of crystal structure exploration and characterization, shedding light on links between the structural aspects and physical properties. The materials $TlLa_2Sb_3Se_9$, $La_{12}Sb_9S_{38}$, $Ba_6Si_{2-x}Ge_xSe_{12}$, $Ba_7Ge_2Se_{17}$, $Sr_8Ge_4Se_{17}$, $Ba_8Sn_4Se_{17}$, and $Sr_6Ge_3OSe_{11}$ were systematically investigated showcasing a diverse array of structural motifs present in group 14 and 15 chalcogenides. We report several complex chalcogenides that possess positional disorder, either S_2^{2-}, Se_2^{2-}, or $[GeSe_5]^{4-}$ anions that aid in the reduction of lattice thermal conductivity. Since positional disorder is typically uncommon in inorganic compounds and we have multiple examples of it among a relatively small number of compounds, this type of disorder may be more likely to appear in chalcogen-rich compounds with large cations such as Ba^{2+} or La^{3+}. Disorder at the atomic scale is one of the factors leading to these materials having ultra-low thermal conductivities. In addition, several of these compounds, such as $La_{12}Sb_9S_{38}$, $Ba_6Ge_2Se_{12}$, and $Ba_7Ge_2Se_{17}$, have optical band gaps below 1.8 eV, which is the optimal range for photovoltaic materials. Currently, their electrical conductivity is too low for this application, but they enrich the pool of compounds that can be tailored for various functionalities.

From the outset of these projects, our exploratory syntheses were focused on cations with lone pairs (Sb^{3+}) or that adopt tetrahedral coordination environments (Si^{4+}, Ge^{4+}, Sn^{4+}) because these are commonly employed design strategies for discovering novel noncentrosymmetric

compounds for nonlinear optical materials. While not an exhaustive sampling of this phase space, it is evident that these strategies are not a reliable means of creating noncentrosymmetric compounds. The tetrahedral anions tend to align antiparallel in the crystal structures, eliminating the purpose of introducing them in the first place. The one compound that is nonlinearly active (beyond $TlLa_2Sb_3Se_9$) was $Sr_6Ge_3OSe_{11}$, which has a strong second-harmonic response due to the aligned dipoles in its structure. We employed partial isovalent anion substitution by replacing 1/12 of the Se atoms in Sr_2GeSe_4 with O atoms to produce the new noncentrosymmetric compound $Sr_6Ge_3OSe_{11}$. To the best of our knowledge, all other Sr/Ge/O/Se quaternaries ($SrGeOSe_2$, $Sr_3Ge_2O_4Se_3$, and $Sr_3Se[GeOSe_3]$) are also noncentrosymmetric crystal structures. This is a remarkable success rate when considering that the sample size is small, and more compounds of these four elements may be discovered. Moving forward, it would be worthwhile to explore chalcogen-rich compounds that incorporate oxygen or halogen atoms into their structure with the goal of aligning the noncentrosymmetric building blocks head-to-tail as in $Sr_6Ge_3OSe_{11}$. The consequence would be preserving the polarizability of the electron-rich chalcogenides while widening the optical band gap with electronegative oxygen or halogen atoms to improve the laser damage thresholds of the materials.

References

1. Liao, J. H. *et al.* α- and β-$A_2Hg_3M_2S_8$ (A = K, Rb; M = Ge, Sn): Polar quaternary chalcogenides with strong nonlinear optical response. *J Am Chem Soc* **125**, 9484–9493 (2003).

2. Pocha, R. *et al.* Crystal structures and properties of the thiostannates Eu_2SnS_4 and Sr_2SnS_4 and the selenogermanate γ-Sr_2GeSe_4. *Z Anorg Allg Chem* **629**, 1379–1384 (2003).

3. Denev, S. A., Lummen, T. T. A., Barnes, E., Kumar, A. & Gopalan, V. Probing Ferroelectrics Using Optical Second Harmonic Generation. *J Am Ceram Soc* **94**, 2699–2727 (2011).

4. Assoud, A., Soheilnia, N. & Kleinke, H. From Yellow to Black: New Semiconducting Ba Chalcogeno-Germanates. *Z Naturforsch B* **59**, 975–979 (2004).

5. Kanatzidis, M. G. Discovery-Synthesis, Design, and Prediction of Chalcogenide Phases. *Inorg Chem* **56**, 3158–3173 (2017).

6. Johrendt, D. & Tampier, M. Strontium Selenogermanate(III) and Barium Selenogermanate(II,IV): Synthesis, Crystal Structures, and Chemical Bonding. *Chem Eur J* **6**, 994–998 (2000).

7. Graf, C., Assoud, A., Mayasree, O. & Kleinke, H. Solid State Polyselenides and Polytellurides: A Large Variety of Se–Se and Te–Te Interactions. *Molecules* **14**, 3115–3131 (2009).

8. Yin, W., Iyer, A. K., Li, C., Yao, J. & Mar, A. When one becomes two: $Ba_{12}In_4Se_{20}$, not quite isostructural to $Ba_{12}In_4S_{19}$. *J Solid State Chem* **253**, 29–34 (2017).

9. Chen, J. H. & Dorhout, P. K. The synthesis and structural and physical characterization of a new family of rare-earth metal chalcoantimonates(III): $K_2(RE)_{2-x}Sb_{4+x}Sb_4Se_{12}$, RE= La, Ce, Pr and Gd. *J Alloys Compd* **249**, 199–205 (1997).

10. Sheldrick, W. S. & Kaub, J. Darstellung und Kristallstruktur von $CsSb_2Se_4$. *Z Anorg Allg Chem* **536**, 114–118 (1986).

11. Hinderman, J. D. *Thermoelectric Materials Evaluation Program. Annual technical report for fiscal years 1980/1981*. http://www.osti.gov/servlets/purl/5049266-Pm8oxS/ (1981) doi:10.2172/5049266.

12. Yang, Y., Wei, X.-J. & Liu, J. Suitability of a thermoelectric power generator for implantable medical electronic devices. *J Phys D Appl Phys* **40**, 5790–5800 (2007).

13. Leonov, V. & Vullers, R. J. M. Wearable electronics self-powered by using human body heat: The state of the art and the perspective. *J Renew Sustain Energy* **1**, 1–14 (2009).

14. Francioso, L. *et al.* Flexible thermoelectric generator for ambient assisted living wearable biometric sensors. *J Power Sources* **196**, 3239–3243 (2011).

15. Hamid Elsheikh, M. *et al.* A review on thermoelectric renewable energy: Principle parameters that affect their performance. *Renew Sustain Energy Rev* **30**, 337–355 (2014).

16. Sharma, S., Dwivedi, V. K. & Pandit, S. N. A Review of Thermoelectric Devices for Cooling Applications. *Int J Green Energy* **11**, 899–909 (2014).

17. Yang, L., Chen, Z., Dargusch, M. S. & Zou, J. High Performance Thermoelectric Materials: Progress and Their Applications. *Adv Energy Mater* **8**, 1701797 (2018).

18. Dai, Y. J., Wang, R. Z. & Ni, L. Experimental investigation on a thermoelectric refrigerator driven by solar cells. *Renew Energy* **28**, 949–959 (2003).

19. Shin, W., Imai, K., Izu, N. & Murayama, N. Thermoelectric thick-film hydrogen gas sensor operating at room temperature. *Jap J Appl Phys Lett* **40**, 1232–1234 (2001).

20. Park, N.-H., Akamatsu, T., Itoh, T., Izu, N. & Shin, W. Calorimetric Thermoelectric Gas Sensor for the Detection of Hydrogen, Methane and Mixed Gases. *Sensors* **14**, 8350–8362 (2014).

21. Swan, M. Sensor Mania! The Internet of Things, Wearable Computing, Objective Metrics, and the Quantified Self 2.0. *J Sens Actuator Networks* **1**, 217–253 (2012).

22. Zaia, E. W., Gordon, M. P., Yuan, P. & Urban, J. J. Progress and Perspective: Soft Thermoelectric Materials for Wearable and Internet-of-Things Applications. *Adv Electron Mater* **5**, 1800823 (2019).

23. Freer, R. & Powell, A. V. Realising the potential of thermoelectric technology: a Roadmap. *J Mater Chem C* **8**, 441–463 (2020).

24. Ma, N., Li, Y.-Y., Chen, L. & Wu, L.-M. α-$CsCu_5Se_3$: Discovery of a Low-Cost Bulk Selenide with High Thermoelectric Performance. *J Am Chem Soc* **142**, 5293–5303 (2020).

25. Toberer, E. S., May, A. F. & Snyder, G. J. Zintl Chemistry for Designing High Efficiency Thermoelectric Materials. *Chem Mater* **22**, 624–634 (2010).

26. Mutailipu, M., Zhang, M., Yang, Z. & Pan, S. Targeting the Next Generation of Deep-Ultraviolet Nonlinear Optical Materials: Expanding from Borates to Borate Fluorides to Fluorooxoborates. *Acc Chem Res* **52**, 791–801 (2019).

27. Han, G., Wang, Y., Zhang, B. & Pan, S. Fluorooxoborates: Ushering in a New Era of Deep Ultraviolet Nonlinear Optical Materials. *Chemistry - A European Journal* vol. 24 17638–17650 at https://doi.org/10.1002/chem.201802787 (2018).

28. Jantz, S. G. *et al.* $Sn[B_2O_3F_2]$-The First Tin Fluorooxoborate as Possible NLO Material. *Adv Opt Mater* **6**, 1800497 (2018).

29. Ran, M.-Y. *et al.* Partial Isovalent Anion Substitution to Access Remarkable Second-

Harmonic Generation Response: A Generic and Effective Strategy for Design of Infrared Nonlinear Optical Materials. *Chem Mater* **32**, 5890–5896 (2020).

30. Ran, M. Y. *et al.* Enhanced Second-Harmonic-Generation Efficiency and Birefringence in Melillite Oxychalcogenides $Sr_2MGe_2OS_6$(M = Mn, Zn, and Cd). *Chem Mater* **34**, 3853–3861 (2022).

31. Shi, Y.-F. *et al.* $Ba_5Ga_2SiO_4S_6$: a Phase-Matching Nonlinear Optical Oxychalcogenide Design via Structural Regulation Originated from Heteroanion Introduction. *Inorg Chem* **62**, 464–473 (2023).

32. Ayeb, Y. *et al.* Elucidating linear and nonlinear optical properties of defect chalcopyrite compounds ZnX_2Te_4 (X=Al, Ga, In) from electronic transitions. *Solid State Sci* **87**, 39–48 (2019).

33. Bai, L., Lin, Z., Wang, Z., Chen, C. & Lee, M.-H. Mechanism of linear and nonlinear optical effects of chalcopyrite $AgGaX_2$ (X=S, Se, and Te) crystals. *J Chem Phys* **120**, 8772–8778 (2004).

34. Guo, Y. *et al.* Nonbonding Electrons Driven Strong SHG Effect in Hg_2GeSe_4: Experimental and Theoretical Investigations. *Inorg Chem* **57**, 6795–6798 (2018).

35. Chen, H. *et al.* Experimental and theoretical studies on the NLO properties of two quaternary non- centrosymmetric chalcogenides: $BaAg_2GeS_4$ and $BaAg_2SnS_4$. *Dalt Trans* **47**, 429–437 (2018).

36. Luo, X., Li, Z., Guo, Y., Yao, J. & Wu, Y. Recent progress on new infrared nonlinear optical materials with application prospect. *J Solid State Chem* **270**, 674–687 (2019).

37. Pearson, R. G. The second-order Jahn-Teller effect. *J Mol Struct THEOCHEM* **103**, 25–34 (1983).

38. Lee, D. W., Oh, S. J., Halasyamani, P. S. & Ok, K. M. New Quaternary Tellurite and Selenite: Synthesis, Structure, and Characterization of Centrosymmetric $InVTe_2O_8$ and Noncentrosymmetric $InVSe_2O_7$. *Inorg Chem* **50**, 4473–4480 (2011).

39. Khyzhun, O. Y. *et al.* Single crystal growth and the electronic structure of orthorhombic Tl_3PbBr_5: A novel material for non-linear optics. *Opt Mater* **35**, 1081–1089 (2013).

40. Aliev, A. *et al.* Revised Bismuth Chloroselenite System: Evidence of a Noncentrosymmmetric Structure with a Giant Unit Cell. *Cryst Growth Des* **14**, 3026–3034 (2014).

41. Cao, X.-L., Hu, C.-L., Kong, F. & Mao, J.-G. Explorations of New SHG Materials in the Alkali-Metal−Nb^{5+}−Selenite System. *Inorg Chem* **55**, 10978–10984 (2015).

42. Suryanarayana, C. Mechanical alloying and milling. *Prog Mater Sci* **46**, 1–184 (2001).

43. Lefèvre, R. *et al.* Polar Transition-Metal Chalcogenide: Structure and Properties of the New Pseudo-Hollandite $Ba_{0.5}Cr_5Se_8$. *Chem Mater* **27**, 7110–7118 (2015).

44. Sheldrick, G. M. *SHELXTL*. (Siemens Analytical X-Ray Systems, 1995).

45. Sheldrick, G. M. A short history of SHELX. *Acta Crystallogr A* **64**, 112–122 (2008).

46. Toby, B. H. & Von Dreele, R. B. *GSAS-II* : the genesis of a modern open-source all purpose crystallography software package. *J Appl Crystallogr* **46**, 544–549 (2013).

47. Toby, B. H. *R* factors in Rietveld analysis: How good is good enough? *Powder Diffr* **21**, 67–70 (2006).

48. Farrow, C. L. *et al.* PDFfit2 and PDFgui: Computer programs for studying nanostructure in crystals. *J Phys Condens Matter* **19**, (2007).

49. Agne, M. T., Hanus, R. & Snyder, G. J. Minimum thermal conductivity in the context of: Diffuson -mediated thermal transport. *Energy Environ Sci* **11**, 609–616 (2018).

50. Kleinman, D. A. Nonlinear Dielectric Polarization in Optical Media. *Phys Rev* **126**, 1977–1979 (1962).

51. Kurtz, S. K. & Perry, T. T. A Powder Technique for the Evaluation of Nonlinear Optical Materials. *J Appl Phys* **39**, 3798–3813 (1968).

52. Liu, S. *et al.* Resonantly Enhanced Second-Harmonic Generation Using III-V Semiconductor All-Dielectric Metasurfaces. *Nano Lett* **16**, 5426–5432 (2016).

53. Ok, K. M., Chi, E. O. & Halasyamani, S. Bulk characterization methods for non-centrosymmetric materials: second-harmonic generation, piezoelectricity, pyroelectricity, and ferroelectricity. *Chem Soc Rev* **35**, 710–717 (2006).

54. Perdew, J. P., Burke, K. & Ernzerhof, M. Generalized gradient approximation made simple. *Phys Rev Lett* **77**, 3865–3868 (1996).

55. Gonze, X. *et al.* The Abinit project: Impact, environment and recent developments. *Comput Phys Commun* **248**, 107042 (2020).

56. Dewhurst, J. K. elk.sourceforge.net. (Date accessed: 2018-05-29)

57. Kresse, G. & Furthmüller, J. Efficient iterative schemes for ab initio total-energy calculations using a plane-wave basis set. *Phys Rev B* **54**, 11169–11186 (1996).

58. Fang, Z. *et al.* Computational design of inorganic nonlinear optical crystals based on a genetic algorithm. *CrystEngComm* **16**, 10569–10580 (2014).

59. Luo, Z. Z. *et al.* SHG materials $SnGa_4Q_7$ (Q = S, Se) appearing with large conversion efficiencies, high damage thresholds, and wide transparencies in the mid-infrared region. *Chem Mater* **26**, 2743–2749 (2014).

60. Clark, S. J. *et al.* First principles methods using CASTEP. *Z Kristallogr* **220**, 567–570 (2005).

61. Aversa, C. & Sipe, E. Nonlinear optical susceptibilities of semiconductors: Results with a length-gauge analysis. *Phys Rev B* **52**, 14636–14645 (1995).

62. Hughes, J. L. P. & Sipe, J. E. Calculation of second-order optical response in semiconductors. *Phys Rev B* **53**, 10751–10763 (1996).

63. Sharma, S. & Ambrosch-Draxl, C. Second-Harmonic Optical Response from First Principles. *Phys Scr* **T109**, 128 (2004).

64. Veithen, M., Gonze, X. & Ghosez, P. Nonlinear optical susceptibilities, Raman efficiencies, and electro-optic tensors from first-principles density functional perturbation theory. *Phys Rev B - Condens Matter Mater Phys* **71**, 1–14 (2005).

65. Assoud, A., Kleinke, K. M. & Kleinke, H. Synthesis, structure, and electronic structure of the ternary sulfide $La_7Sb_9S_{24}$. *Chem Mater* **18**, 1041–1046 (2006).

66. Assoud, A. & Kleinke, H. Crystal structure, electronic structure and electrical conductivity of the antimony selenide $BaLaSb_2Se_6$. *Solid State Sci* **12**, 919–923 (2010).

67. Kim, S.-J., Park, S. & Yim, S. Synthesis and Crystal Structure of a New Quaternary Chalcoantimonide: $KLa_2Sb_3S_9$ and $KSm_2Sb_3Se_8$. *Bull Korean Chem Soc* **25**, 485–490 (2004).

68. Hsu, K. F. *et al.* Cubic $AgPb_mSbTe_{2+m}$: Bulk Thermoelectric Materials with High Figure of Merit. *Science (80-)* **303**, 818–821 (2004).

69. Heo, J., Laurita, G., Muir, S., Subramanian, M. A. & Keszler, D. A. Enhanced Thermoelectric Performance of Synthetic Tetrahedrites. *Chem Mater* **26**, 2047–2051 (2014).

70. Zhu, C. *et al.* Achieving high power factor and thermoelectric performance through dual substitution of Zn and Se in tetrahedrites $Cu_{12}Sb_4S_{13}$. *Appl Phys Lett* **115**, 182102/1–5 (2019).

71. Bell, L. E. Cooling, heating, generating power, and recovering waste heat with thermoelectric systems. *Science (80-)* **321**, 1457–1461 (2008).

72. Kleinke, H. New bulk materials for thermoelectric power generation: clathrates and complex antimonides. *Chem Mater* **22**, 604–611 (2010).

73. Snyder, G. J. & Toberer, E. S. Complex thermoelectric materials. *Nat Mater* **7**, 105–114 (2008).

74. Shi, Y., Sturm, C. & Kleinke, H. Chalcogenides as thermoelectric materials. *J Solid State Chem* **270**, 273–279 (2019).

75. Shi, X. L., Zou, J. & Chen, Z. G. Advanced thermoelectric design: From materials and structures to devices. *Chem Rev* **120**, 7399–7515 (2020).

76. *M86-Exx078 APEX2 User Manual*. (Bruker AXS Inc., 2006).

77. Gelato, L. M. & Parthé, E. STRUCTURE TIDY– a computer program to standardize crystal structure data. *J Appl Crystallogr* **20**, 139–143 (1987).

78. Blaha, P., Schwarz, K. & Madsen, G. K. H. WIEN2K, An Augmented Plane Wave+ Local Orbitals Program for Calculating Crystal Properties (TU Wien, Austria, 2001). *Isbn 3-9501031-1-2* **2**, 254 (2001).

79. Xu, J., Assoud, A., Cui, Y. & Kleinke, H. Crystal structure, electronic structure and physical properties of a new semiconducting thallium antimony selenide: $Tl_{2.35}Sb_{8.65}Se_{14}$. *Solid State Sci* **10**, 1159–1165 (2008).

80. Derakhshan, S., Assoud, A., Taylor, N. J. & Kleinke, H. Crystal and Electronic Structures and Physical Properties of Two Semiconductors: $Pb_4Sb_6Se_{13}$ and $Pb_6Sb_6Se_{17}$. *Intermetallics* **14**, 198–207 (2006).

81. Matsushita, Y. & Ueda, Y. Structure and Physical Properties of 1D Magnetic Chalcogenide, Jamesonite ($FePb_4Sb_6S_{14}$). *Inorg. Chem.* **42**, 7830–7838 (2003).

82. Derakhshan, S., Assoud, A., Soheilnia, N. & Kleinke, H. Electronic structure and thermoelectric properties of the thioantimonate $FePb_4Sb_6S_{14}$. *J Alloys Compd* **390**, 51–54 (2005).

83. Assoud, A., Soheilnia, N. & Kleinke, H. Crystal and electronic structure of the red semiconductor $Ba_4LaSbGe_3Se_{13}$ comprising the complex anion $[Ge_2Se_7\text{-}Sb_2Se_4\text{-}Ge_2Se_7]^{14-}$. *J Solid State Chem* **177**, 2249–2254 (2004).

84. Assoud, A. & Kleinke, H. A Polyselenide with a Novel Se_7^{8-} Unit: the Structure of $Sr_{19-x}Pb_xGe_{11}Se_{44}$ with x = 5.0 and 6.4. *Eur J Inorg Chem* **2017**, 5515–5520 (2017).

85. Shannon, R. D. Revised effective ionic radii and systematic studies of interatomic distances in halides and chalcogenides. *Acta Crystallogr Sect A* **32**, 751–767 (1976).

86. Xu, Z. J., Hu, L. P., Ying, P. J., Zhao, X. B. & Zhu, T. J. Enhanced thermoelectric and mechanical properties of zone melted p-type $(Bi,Sb)_2Te_3$ thermoelectric materials by hot deformation. *Acta Mater* **84**, 385–392 (2015).

87. Zeier, W. G. *et al.* Thinking Like a Chemist: Intuition in Thermoelectric Materials. *Angew Chemie Int Ed* **55**, 6826–6841 (2016).

88. Zhao, H.-J. & Zhou, L.-J. A Series of Noncentrosymmetric Antimony Sulfides $Ln_8Sb_2S_{15}$ (Ln = La, Pr, Nd) - Syntheses, Crystal and Electronic Structures, and NLO Properties. *Eur J Inorg Chem* **2015**, 964–968 (2015).

89. Chen, M. C., Li, L. H., Chen, Y. B. & Chen, L. In-phase alignments of asymmetric building units in Ln_4GaSbS_9 (Ln = Pr, Nd, Sm, Gd-Ho) and their strong nonlinear optical responses in middle IR. *J Am Chem Soc* **133**, 4617–4624 (2011).

90. Zhao, H. J., Zhang, Y. F. & Chen, L. Strong Kleinman-Forbidden Second Harmonic Generation in Chiral Sulfide: La_4InSbS_9. *J Am Chem Soc* **134**, 1993–1995 (2012).

91. Zhao, H. J. Synthesis, Crystal Structure, and NLO Property of the Chiral Sulfide Sm_4InSbS_9. *Z Anorg Allg Chem* **642**, 56–59 (2016).

92. Chung, I. & Kanatzidis, M. G. Metal Chalcogenides: A Rich Source of Nonlinear Optical Materials. *Chem Mater* **26**, 849–869 (2014).

93. Assoud, A., Kleinke, K. M. & Kleinke, H. Synthesis, Structure and Electronic Structure of the Ternary Sulfide $La_7Sb_9S_{24}$. *Chem. Mater.* **18**, 1041–1046 (2006).

94. Babo, J. M. & Albrecht-Schmitt, T. E. Two new ternary lanthanide antimony chalcogenides: $Yb_4Sb_2S_{11.25}$ and $Tm_4Sb_2Se_{11.68}$ containing chalcogenide Q^{2-} and dichalcogenide $(Q_2)^{2-}$ anions. *J Solid State Chem* **187**, 264–268 (2012).

95. Guseinov, G. G., Mamedov, F. K., Amiraslanov, I. R. & Mamedov, K. S. Crystal structure of praseodymium antimony sulfide ($Pr_8Sb_2S_{15}$). *Kristallogr.* **26**, 831–833 (1981).

96. Zhao, H. J. & Zhong, X. A. Synthesis, crystal structure, and optical properties of the noncentrosymmetric sulfide $Ce_8Sb_2S_{15}$. *J Solid State Chem* **251**, 65–69 (2017).

97. Lemoine, P., Carré, D. & Guittard, M. Structure du sulfure deuropium et d'antimoine $Eu_3Sb_4S_9$. *Acta Crystallogr B* **37**, 1281–1284 (1981).

98. Jin, G. *et al.* Europium antimony sulfide, $Eu_6Sb_6S_{17}$. *Acta Crystallogr E* **61**, i116–i119 (2006).

99. Goerigk, F. C. & Schleid, T. Composition and Crystal Structure of $SmSb_2O_4Cl$ Revisited – and the Analogy of $Sm_{1.5}Sb_{1.5}O_4Br$. *Z Anorg Allg Chem* **645**, 1079–1084 (2019).

100. Katsuyama, S., Tanaka, Y., Hashimoto, H., Majima, K. & Nagai, H. Effect of substitution of La by alkaline earth metal on the thermoelectric properties and the phase stability of γ-La_3S_4. *J Appl Phys* **82**, 5513–5519 (1997).

101. Bruker. APEX2, SAINT and SADABS. *APEX II* Bruker AXS Inc., Madison, Wisconsin, USA. (2009).

102. Schwarz, K. DFT calculations of solids with LAPW and WIEN2k. *J Solid State Chem* **176**, 319–328 (2003).

103. Wang, H. *et al.* Transport Properties of Bulk Thermoelectrics: An International Round-Robin Study, Part II: Thermal Diffusivity, Specific Heat, and Thermal Conductivity. *J Electron Mater* **42**, 1073–1084 (2013).

104. Föppl, H., Busmann, E. & Frorath, F. K. Die Kristallstrukturen von a-Na_2S_2 und K_2S_2, b-Na_2S_2 und Na_2Se_2. *Z Anorg Allg Chem* **314**, 12–29 (1962).

105. Dugué, J., Carré, D. & Guittard, M. Structure cristalline du polysulfure de lanthane LaS_2. *Acta Crystallogr B* **34**, 403–406 (1978).

106. Khan, A. U. *et al.* Sb Doping of Metallic $CuCr_2S_4$ as a Route to Highly Improved Thermoelectric Properties. *Chem Mater* **29**, 2988–2996 (2017).

107. Shahmohamadi, H. & Naghavi, S. S. Sulfide Perovskites for Thermoelectricity. *ACS Appl Mater Interfaces* **13**, 14189–14197 (2021).

108. Johnsen, S. *et al.* Nanostructures boost the thermoelectric performance of PbS. *J Am Chem Soc* **133**, 3460–3470 (2011).

109. Skoug, E. J. & Morelli, D. T. Role of lone-pair electrons in producing minimum thermal conductivity in nitrogen-group chalcogenide compounds. *Phys Rev Lett* **107**, 235901/1–5 (2011).

110. Qiu, P., Zhang, T., Qiu, Y., Shi, X. & Chen, L. Sulfide bornite thermoelectric material: A natural mineral with ultralow thermal conductivity. *Energy Environ Sci* **7**, 4000–4006 (2014).

111. Cahill, D. G., Watson, S. K. & Pohl, R. O. Lower limit to the thermal conductivity of disordered crystals. *Phys Rev B* **46**, 6131–6140 (1992).

112. Iyer, R. G., Aitken, J. A. & Kanatzidis, M. G. Noncentrosymmetric cubic thio- and selenogermanates: $A_{0.5}M_{1.75}GeQ_4$ (A=Ag, Cu, Na; M=Pb, Eu; Q=S, Se). *Solid State Sci* **6**, 451–459 (2004).

113. Gulay, L. D., Huch, M. R., Wołcyrz, M. & Olekseyuk, I. D. Crystal structure of new selenosilicates $Pb_{1.75}M_{0.5}SiSe_4$ (M = Cu and Ag). *J Alloys Compd* **402**, 115–117 (2005).

114. Poduska, K. M., Cario, L., DiSalvo, F. J., Min, K. & Halasyamani, P. S. Structural studies of a cubic, high-temperature (α) polymorph of Pb_2GeS_4 and the isostructural $Pb_{2-x}Sn_xGeS_{4-y}Se_y$ solid solution. *J Alloys Compd* **335**, 105–110 (2002).

115. Vu, T. V. *et al.* Electronic band-structure and optical constants of Pb_2GeS_4: *Ab initio* calculations and X-ray spectroscopy experiments. *J Mater Sci* **29**, 16088–16100 (2018).

116. Susa, K. & Steinfink, H. Ternary sulfide compounds AB_2S_4: The crystal structures of $GePb_2S_4$ and $SnBa_2S_4$. *J Solid State Chem* **3**, 75–82 (1971).

117. Yin, W., Iyer, A. K., Li, C., Yao, J. & Mar, A. Noncentrosymmetric chalcogenides $BaZnSiSe_4$ and $BaZnGeSe_4$ featuring one-dimensional structures. *J Alloys Compd* **708**, 414–421 (2017).

118. Barde, A. & Joubert, D. P. Investigation of structural, mechanical, dynamic, electronic and optical properties of seleno-germanates A_2GeSe_4 (A = Mg, Ca and γ-Sr) from first principles. *Mater Today Commun* **22**, 100785 (2020).

119. Menezes, L. T., Assoud, A., Zhang, W., Halasyamani, P. S. & Kleinke, H. Effect of Pb Substitution in $Sr_{2-x}Pb_xGeSe_4$ on Crystal Structures and Nonlinear Optical Properties Predicted by DFT Calculations. *Inorg Chem* **59**, 15028–15035 (2020).

120. Wu, K., Su, X., Yang, Z. & Pan, S. An investigation of new infrared nonlinear optical material: $BaCdSnSe_4$, and three new related centrosymmetric compounds: Ba_2SnSe_4, Mg_2GeSe_4, and $Ba_2Ge_2S_6$. *Dalt Trans* **44**, 19856–19864 (2015).

121. Duan, R.-H. *et al.* Modifying Disordered Sites with Rational Cations to Regulate Band-Gaps and Second Harmonic Generation Responses Markedly: Ba6Li2ZnSn4S16 vs Ba6Ag2ZnSn4S16 vs Ba6Li2.67Sn4.33S16. *Cryst Growth Des* **18**, 5609–5616 (2018).

122. Pocha, R. & Johrendt, D. Crystal Structures of $Sr_4Sn_2Se_9$ and $Sr_4Sn_2Se_{10}$ and the Oxidation State of Tin in an Unusual Geometry. *Inorg. Chem.* **43**, 6830–6837 (2004).

123. Assoud, A., Soheilnia, N. & Kleinke, H. The new semiconducting polychalcogenide Ba_2SnSe_5 exhibiting Se_3^{2-} units and distorted $SnSe_6$ octahedra. *J Solid State Chem* **178**, 1087–1093 (2005).

124. Graf, C., Assoud, A., Zelinska, M. & Kleinke, H. The metastable m-Ba_2SnSe_5 - Synthesis, Phase Transition, Crystal Structure, Structural Relations and Electronic Structure. *Z Anorg Allg Chem* **636**, 1821–1826 (2010).

125. Zelinska, M., Assoud, A., Graf, C. & Kleinke, H. Reversible Reconstructive Phase Transition of Ba_2SnSe_5: A New High Temperature Modification with Completely Different Structural Motifs. *Inorg Chem* **49**, 1090–1093 (2010).

126. Assoud, A., Derakhshan, S., Soheilnia, N. & Kleinke, H. Electronic structure and physical properties of the semiconducting polytelluride Ba_2SnTe_5 with a unique Te_5^{4-} unit. *Chem Mater* **16**, 4193–4198 (2004).

127. Duan, R. H., Liu, P. F., Lin, H., Huangfu, S. X. & Wu, L. M. Syntheses and characterization of three new sulfides with large band gaps: Acentric $Ba_4Ga_4SnS_{12}$, centric $Ba_{12}Sn_4S_{23}$ and $Ba_7Sn_3S_{13}$. *Dalt Trans* **46**, 14771–14778 (2017).

128. Assoud, A. & Kleinke, H. Unique Barium Selenostannate−Selenide: Ba7Sn3Se13 (and Its Variants $Ba_7Sn_3Se_{13-\delta}Te_\delta$) with $SnSe_4$ Tetrahedra and Isolated Se Anions. *Chem Mater* **17**, 4509–4513 (2005).

129. Luo, Z. *et al.* Syntheses, Characterization, and Optical Properties of Ternary Ba–Sn–S System Compounds: Acentric $Ba_7Sn_5S_{15}$, Centric $BaSn_2S_5$, and Centric $Ba_6Sn_7S_{20}$. *Inorg Chem* **52**, 273–279 (2013).

130. Luo, Z.-Z. *et al.* $Ba_8Sn_4S_{15}$: A Strong Second Harmonic Generation Sulfide with Zero-Dimensional Crystal Structure. *Chem Mater* **26**, 1093–1099 (2014).

131. Cruz-Cabeza, A. J., Day, G. M. & Jones, W. Structure prediction, disorder and dynamics in a DMSO solvate of carbamazepine. *Phys Chem Chem Phys* **13**, 12808–12816 (2011).

132. Velázquez-Carmona, M. Á., Bernès, S., Ríos-Merino, F. J. & Ortega, Y. R. Crystal structure of trans-N,N'-bis(3,5-di-tert-butyl-2-hydroxyphenyl)oxamide methanol monosolvate. *Acta Crystallogr Sect E Crystallogr Commun* **72**, 918–921 (2016).

133. *SAINT*. (Siemens Analytical X-ray Instruments Inc., 1995).

134. Spek, A. L. Single-crystal structure validation with the program PLATON. *J Appl Crystallogr* **36**, 7–13 (2003).

135. Spek, A. L. Structure validation in chemical crystallography. *Acta Crystallogr D* **65**, 148–155 (2009).

136. Kokalj, A. XCrySDen—a new program for displaying crystalline structures and electron densities. *J Mol Graph Model* **17**, 176–179 (1999).

137. Zeljkovic, I. D. ConsecutiveRNG. *GitHub Repository* https://github.com/idzidz/ConsecutiveRNG (2021).

138. Orr, M., Hebberd, G. R., McCabe, E. E. & Macaluso, R. T. Structural Diversity of Rare-Earth Oxychalcogenides. *ACS Omega* **7**, 8209–8218 (2022).

139. Tuxworth, A. J., Wang, C. H. & Evans, J. S. O. Synthesis, characterisation and properties of rare earth oxyselenides $A_4O_4Se_3$ (A = Eu, Gd, Tb, Dy, Ho, Er, Yb and Y). *Dalt Trans* **44**, 3009–3019 (2015).

140. Strobel, S., Choudhury, A., Dorhout, P. K., Lipp, C. & Schleid, T. Rare-earth metal(III) oxide selenides $M_4O_4Se[Se_2]$ (M = La, Ce, Pr, Nd, Sm) with discrete diselenide units: Crystal structures, magnetic frustration, and other properties. *Inorg Chem* **47**, 4936–4944 (2008).

141. Liu, H. *et al.* Copper ion liquid-like thermoelectrics. *Nat Mater* **11**, 422–425 (2012).

142. Zhao, L. D. *et al.* Ultralow thermal conductivity and high thermoelectric figure of merit in SnSe crystals. *Nature* **508**, 373–377 (2014).

143. Gascoin, F. & Maignan, A. Order–Disorder Transition in $AgCrSe_2$: a New Route to Efficient Thermoelectrics. *Chem Mater* **23**, 2510–2513 (2011).

144. Mukhopadhyay, S. *et al.* Two-channel model for ultralow thermal conductivity of crystalline Tl_3VSe_4. *Science (80-)* **360**, 1455–1458 (2018).

145. Zhao, J. *et al.* Six Quaternary Chalcogenides of the Pavonite Homologous Series with Ultralow Lattice Thermal Conductivity. *Chem Mater* **31**, 3430–3439 (2019).

146. Guo, Y. *et al.* $BaHgGeSe_4$ and $SrHgGeSe_4$: Two New Hg-Based Infrared Nonlinear Optical Materials. *Chem. Mater* **31**, 3034–3040 (2019).

147. Wu, K., Chu, Y., Yang, Z. & Pan, S. $A_2SrM^{IV}S_4$ (A = Li, Na; M^{IV} = Ge, Sn) concurrently exhibiting wide bandgaps and good nonlinear optical responses as new potential infrared nonlinear optical materials. *Chem Sci* **10**, 3963–3968 (2019).

148. Lekse, J. W. *et al.* Second-Harmonic Generation and Crystal Structure of the Diamond-like Semiconductors Li_2CdGeS_4 and Li_2CdSnS_4. *Inorg Chem* **48**, 7516–7518 (2009).

149. Chung, I., Song, J. H., Jang, J. I., Freeman, A. J. & Kanatzidis, M. G. $Na_2Ge_2Se_5$: A highly nonlinear optical material. *J Solid State Chem* **195**, 161–165 (2012).

150. Brinkmann, C., Eisenmann, B. & Schäfer, H. Darstellung und Struktur der Verbindungen Ba2SiTe4 und Ba2SiSe4. *Z Anorg Allg Chem* **524**, 83–89 (1985).

151. Cheng, H. *et al.* Design and synthesis of Ba_3SiSe_5 with suitable birefringence modulated via M IV atoms in the Ba–M IV –Q (M IV = Si, Ge; Q = S, Se) system. *Dalt Trans* **50**, 11999–12005 (2021).

152. Menezes, L. T. *et al.* $Ba_6Ge_2Se_{12}$ and $Ba_7Ge_2Se_{17}$: Two Centrosymmetric Barium Seleno-Germanates with Polyatomic Anion Disorder. *Inorg Chem* **62**, 285–294 (2023).

153. Blaha, P. *et al.* WIEN2k: An APW+lo program for calculating the properties of solids. *J Chem Phys* **152**, 074101 (2020).

154. Jiang, B. *et al.* High-entropy-stabilized chalcogenides with high thermoelectric performance. *Science (80-)* **371**, 830–834 (2021).

155. Badikov, V. *et al.* Phase-matching properties of $BaGa_4S_7$ and $BaGa_4Se_7$: Wide-bandgap nonlinear crystals for the mid-infrared. *Phys Status Solidi* **5**, 31–33 (2011).

156. Guo, Y., Zhou, Y., Lin, X., Chen, W. & Ye, N. Growth and characterizations of $BaGa_4S_7$ crystal. *Opt Mater* **36**, 2007–2011 (2014).

157. Li, X. *et al.* $BaGa_2SnSe_6$: a new phase-matchable IR nonlinear optical material with strong second harmonic generation response. *J Mater Chem C* **3**, 10998–11004 (2015).

158. Guo, W. *et al.* Two Mixed-Anion Semiconductors in the Ba-Sn-Te-S System with Low Thermal Conductivity. *ACS Appl Energy Mater* **6**, 2508–2514 (2023).

159. Cui, Y., Mayasree, O., Assoud, A. & Kleinke, H. Different clusters within the $Ba_4M_{4-x}A_2Te_9$ (M = Cu, Ag, Au; A = Si, Ge) series: Crystal structures and transport properties. *J Alloys Compd* **493**, 70–76 (2010).

160. Jafarzadeh, P. *et al.* $BaCuSiTe_3$: A Noncentrosymmetric Semiconductor with $CuTe_4$ Tetrahedra and Ethane-like Si_2Te_6 Units. *Inorg Chem* **58**, 11656–11663 (2019).

161. Azam, S., Khan, S. A. & Goumri-Said, S. Exploring the electronic structure and optical properties of the quaternary selenide compound, $Ba_4Ga_4SnSe_{12}$: For photovoltaic applications. *J Solid State Chem* **229**, 260–265 (2015).

162. Zhu, T. *et al.* I_2–II–IV–VI_4 (I = Cu, Ag; II = Sr, Ba; IV = Ge, Sn; VI = S, Se): Chalcogenides for Thin-Film Photovoltaics. *Chem Mater* **29**, 7868–7879 (2017).

163. Shin, D. *et al.* $BaCu_2Sn(S,Se)_4$: Earth-Abundant Chalcogenides for Thin-Film Photovoltaics. *Chem Mater* **28**, 4771–4780 (2016).

164. Shin, D. *et al.* Earth-Abundant Chalcogenide Photovoltaic Devices with over 5% Efficiency Based on a $Cu_2BaSn(S,Se)_4$ Absorber. *Adv Mater* **29**, 1606945 (2017).

165. Wu, K., Su, X., Yang, Z. & Pan, S. An investigation of new infrared nonlinear optical material: $BaCdSnSe_4$, and three new related centrosymmetric compounds: Ba_2SnSe_4, Mg_2GeSe_4, and $Ba_2Ge_2S_6$. *Dalt Trans* **44**, 19856–19864 (2015).

166. Feng, K. *et al.* $Ba_6Sn_6Se_{13}$: A new mixed valence selenostannate with NLO property. *Dalt*

Trans **42**, 13635–13641 (2013).

167. Tranchitella, L. J., Fettinger, J. C., Dorhout, P. K., Van Calcar, P. M. & Eichhorn, B. W. Commensurate Columnar Composite Compounds: Synthesis and Structure of $Ba_{15}Zr_{14}Se_{42}$ and $Sr_{21}Ti_{19}Se_{57}$. *J Am Chem Soc* **120**, 7639–7640 (1998).

168. Menezes, L. T. *et al.* $Sr_6Ge_3OSe_{11}$: A Rationally Designed Noncentrosymmetric Oxyselenide with Polar [$GeOSe_3$] Building Blocks. *Chem Mater* **35**, 3033–3040 (2023).

169. Snyder, G. J. & Toberer, E. S. Complex TE meterials. *Nat Mater* **7**, 105–114 (2008).

170. Arriola, A. *et al.* Mid-infrared astrophotonics: study of ultrafast laser induced index change in compatible materials. *Opt Mater Express* **7**, 698–711 (2017).

171. Pestov, D. *et al.* Single-shot detection of bacterial endospores via coherent Raman spectroscopy. *Proc Natl Acad Sci* **105**, 422–427 (2008).

172. Wooten, E. L. *et al.* A review of lithium niobate modulators for fiber-optic communications systems. *IEEE J Sel Top Quantum Electron* **6**, 69–82 (2000).

173. Zhao, Z. *et al.* Mid-infrared supercontinuum covering 2.0–16 μm in a low-loss telluride single-mode fiber. *Laser Photonics Rev* **11**, 1–5 (2017).

174. Lan, H. *et al.* Langasite Family Midinfrared Nonlinear Optical Oxide Materials: Structure, Property, and Applications. *Int J Opt* **2017**, 1–13 (2017).

175. Tsujimoto, Y. *et al.* Function of Tetrahedral ZnS_3O Building Blocks in the Formation of $SrZn_2S_2O$: A Phase Matchable Polar Oxysulfide with a Large Second Harmonic Generation Response. *Chem Mater* **30**, 6486–6493 (2018).

176. Zhang, X. *et al.* Synthesis, crystal structures and optical properties of noncentrosymmetric oxysulfides $AeGeS_2O$ (Ae = Sr, Ba). *Dalt Trans* **48**, 14662–14668 (2019).

177. Sun, M. *et al.* Highly polarized [$GeOTe_3$] motif-driven structural order promotion and an enhanced second harmonic generation response in the new nonlinear optical oxytelluride $Ba_3Ge_2O_4Te_3$. *J Mater Chem C* **10**, 150–159 (2022).

178. Wang, Y. *et al.* $Sr_4Pb_{1.5}Sb_5O_5Se_8$: a new mid-infrared nonlinear optical material with a moderate SHG response. *CrystEngComm* **22**, 3526–3530 (2020).

179. Ran, M.-Y. *et al.* Enhanced Second-Harmonic-Generation Efficiency and Birefringence in Melillite Oxychalcogenides $Sr_2MGe_2OS_6$ (M = Mn, Zn, and Cd). *Chem Mater* **34**, 3853–3861 (2022).

180. Xing, W. *et al.* Two Mixed-Anion Units of [$GeOSe_3$] and [GeO_3S] Originating from Partial Isovalent Anion Substitution and Inducing Moderate Second Harmonic Generation Response and Large Birefringence. *Inorg Chem* **59**, 16716–16724 (2020).

181. Cui, S. *et al.* The Antiperovskite-Type Oxychalcogenides $Ae_3Q[GeOQ_3]$ (Ae = Ba, Sr; Q = S, Se) with Large Second Harmonic Generation Responses and Wide Band Gaps. *Adv Sci*

10, 2204755 (2023).

182. Liu, B.-W. *et al.* Oxychalcogenide $BaGeOSe_2$: Highly Distorted Mixed-Anion Building Units Leading to a Large Second-Harmonic Generation Response. *Chem Mater* **27**, 8189–8192 (2015).

183. Shi, Y. F., Wei, W. B., Wu, X. T., Lin, H. & Zhu, Q. L. Recent progress in oxychalcogenides as IR nonlinear optical materials. *Dalt Trans* **50**, 4112–4118 (2021).

184. Zhang, Y., Wu, H., Hu, Z. & Yu, H. Oxychalcogenides: A Promising Materials Class for Nonlinear Optical Crystals with Mixed-anion Groups. *Chem – A Eur J* **279**, 4510–4524 (2022).

185. Assoud, A., Soheilnia, N. & Kleinke, H. Band Gap Tuning in New Strontium Seleno-Stannates. *Chem Mater* **16**, 2215–2221 (2004).

186. Zhang, W., Yu, H., Wu, H. & Halasyamani, P. S. Phase-Matching in Nonlinear Optical Compounds: A Materials Perspective. *Chem Mater* **29**, 2655–2668 (2017).

187. Dou, Y. *et al.* $SrCdGeS_4$ and $SrCdGeSe_4$: Promising Infrared Nonlinear Optical Materials with Congruent-Melting Behavior. *Cryst Growth Des* **19**, 1206–1214 (2019).

Appendix

Table A.1. Atomic positions and U_{eq} values of $TlLa_2Sb_3Se_9$. All sites are 100% occupied.

Atom	Site	x	y	z	U_{eq} (Å^2)
Tl1	4*a*	0.2603(4)	0.00304(7)	0.30311(4)	0.0321(3)
La1	4*a*	0.2469(5)	0.15831(9)	0.64784(6)	0.0228(4)
La2	4*a*	0.3233(4)	0.0807(1)	0.47901(6)	0.0182(4)
Sb1	4*a*	0.2137(6)	0.3397(1)	0.06379(8)	0.0331(5)
Sb2	4*a*	0.2355(6)	0.2434(1)	0.21848(6)	0.0215(4)
Sb3	4*a*	0.6997(6)	0.0918(1)	0.09929(7)	0.0219(5)
Se1	4*a*	0.1969(8)	0.5020(2)	0.09287(9)	0.0166(6)
Se2	4*a*	0.207(1)	0.1202(2)	0.0132(1)	0.0280(8)
Se3	4*a*	0.2150(9)	0.0523(2)	0.16464(9)	0.0208(7)
Se4	4*a*	0.2169(8)	0.2005(1)	0.38019(9)	0.0163(6)
Se5	4*a*	0.2414(9)	0.3922(1)	0.27149(8)	0.0165(6)
Se6	4*a*	0.2962(8)	0.4262(1)	0.43186(9)	0.0151(6)
Se7	4*a*	0.3819(7)	0.2678(2)	0.5428(1)	0.0178(7)
Se8	4*a*	0.694(1)	0.2980(2)	0.1378(1)	0.0327(9)
Se9	4*a*	0.6988(8)	0.1799(2)	0.2770(1)	0.0237(7)

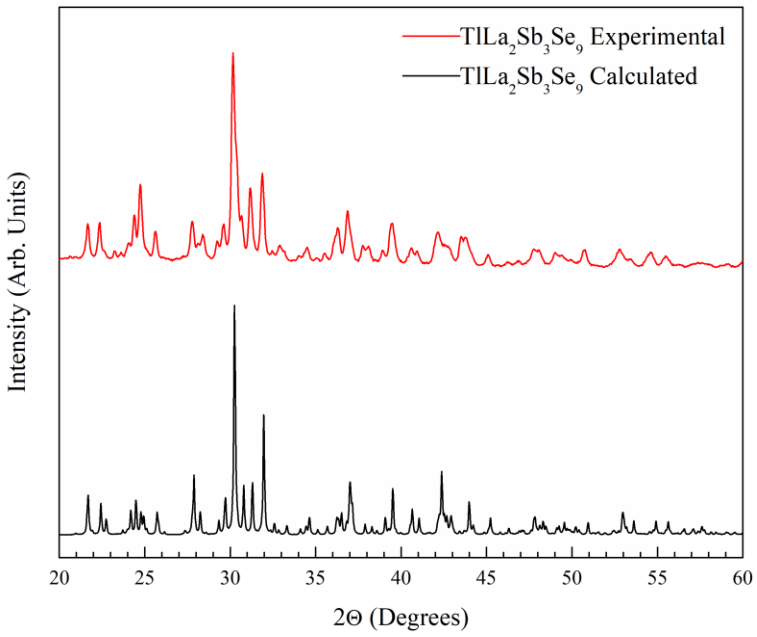

Figure A.1. Powder X-ray diffraction pattern of $TlLa_2Sb_3Se_9$.

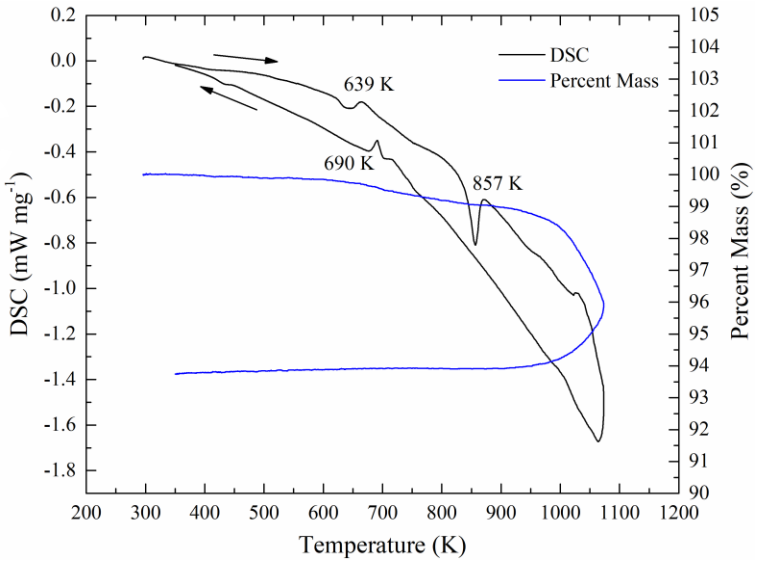

Figure A.2. Heating and cooling curves of the DSC/TGA of $TlLa_2Sb_3Se_9$.

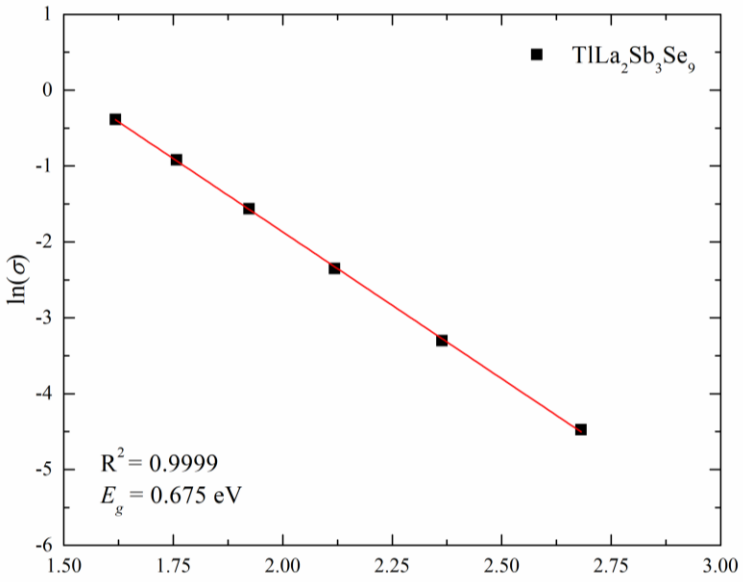

Figure A.3. Band gap determination of $TlLa_2Sb_3Se_9$ from the temperature dependent electrical conductivity.

Table A.2. Atomic positions, U_{eq} values and occupancy factors of $La_{12.17(1)}Sb_{8.59(2)}S_{37.86(3)}$.

Atom	Site	x	y	z	U_{eq} (Å^2)	occ.
La1	8i	0.26879(1)	0.26879(1)	0.26879(1)	0.01032(6)	1
La2	6e	0.35667(7)	0	0	0.0185(2)	0.529(2)
Sb2	6e	0.2750(1)	0	0	0.0428(4)	0.432(3)
La3	1b	½	½	½	0.0105(1)	1
Sb1	12j	0	0.46966(4)	0.32801(4)	0.0156(1)	½
S1	12k	½	0.17772(7)	0.15549(7)	0.0133(2)	1
S2	12k	½	0.23611(7)	0.40646(7)	0.0105(1)	1
S3	12j	0	0.2438(1)	0.2463(1)	0.0279(2)	1
S4	8i	0.0518(3)	0.0518(3)	0.0518(3)	0.022(1)	0.232(4)

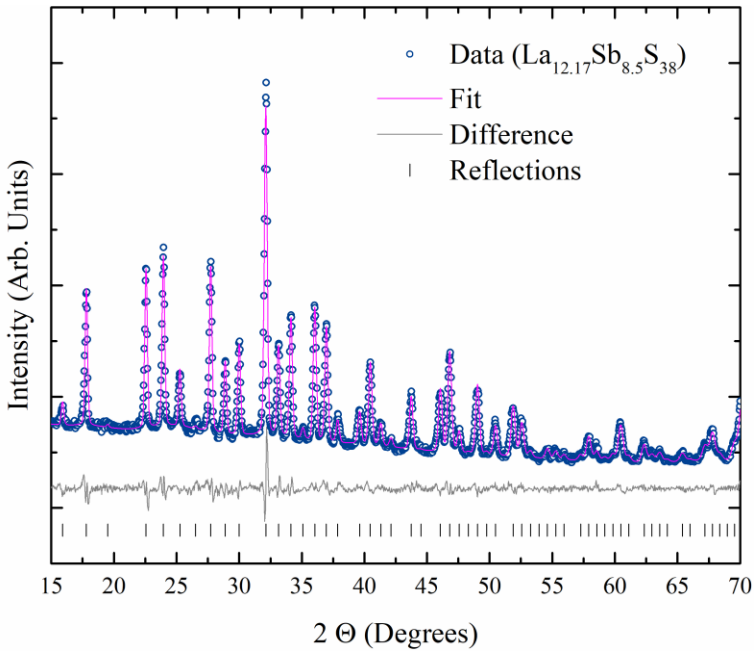

Figure A.4. Rietveld refinement of sample with $La_{12.17}Sb_{8.5}S_{38}$ nomical composition.

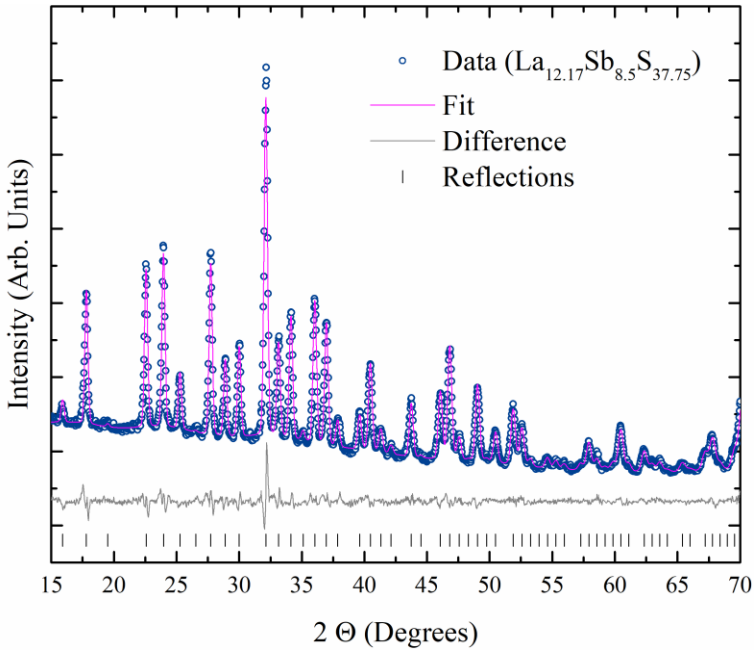

Figure A.5. Rietveld refinement of a sample with $La_{12.17}Sb_{8.5}S_{37.75}$ nominal composition.

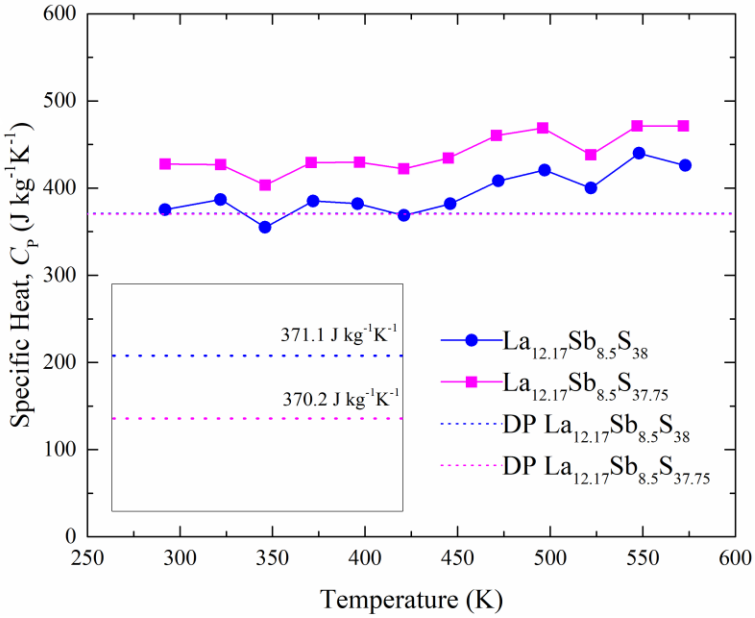

Figure A.6. Specific heat of $La_{12.17}Sb_{8.5}S_{38}$ and $La_{12.17}Sb_{8.5}S_{37.35}$ in comparison to the Dulong-Petit (DP) limits.

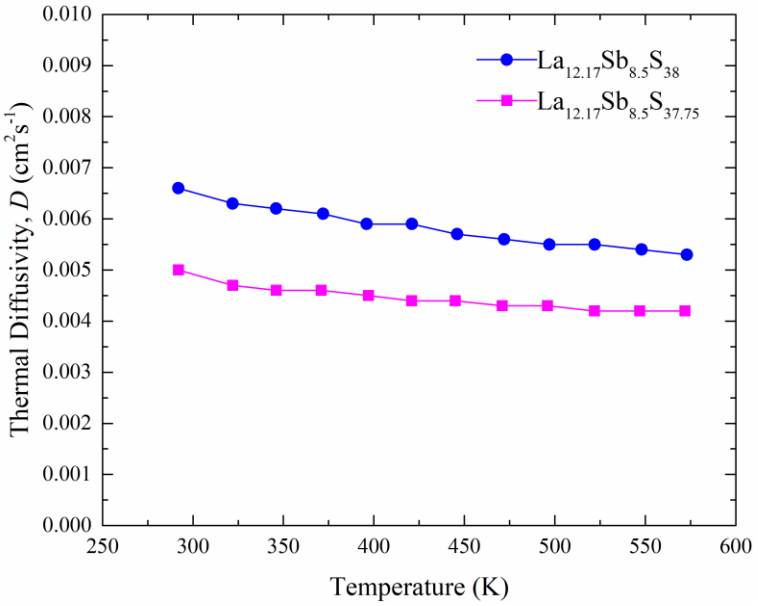

Figure A.7. Thermal diffusivity of $La_{12.17}Sb_{8.5}S_{38}$ and $La_{12.17}Sb_{8.5}S_{37.35}$.

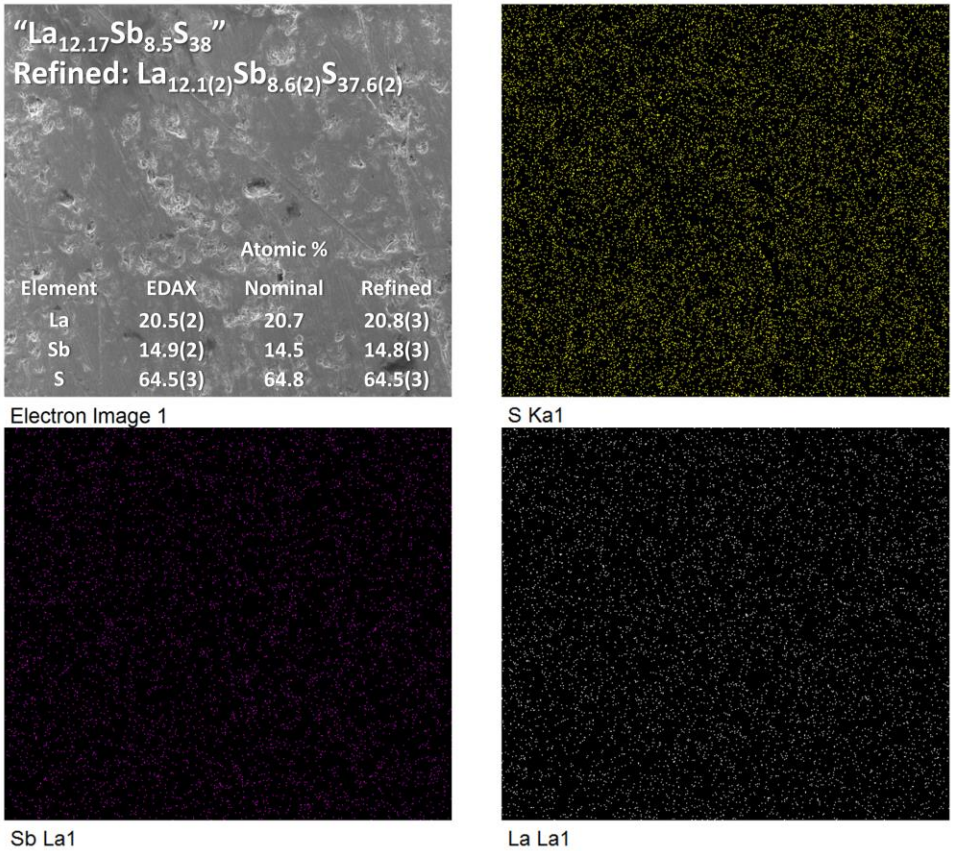

Figure A.8. SEM maps and EDAX results of the pellet of nominal composition $La_{12.17}Sb_{8.5}S_{38}$ in comparison to the formula obtained from the Rietveld refinement.

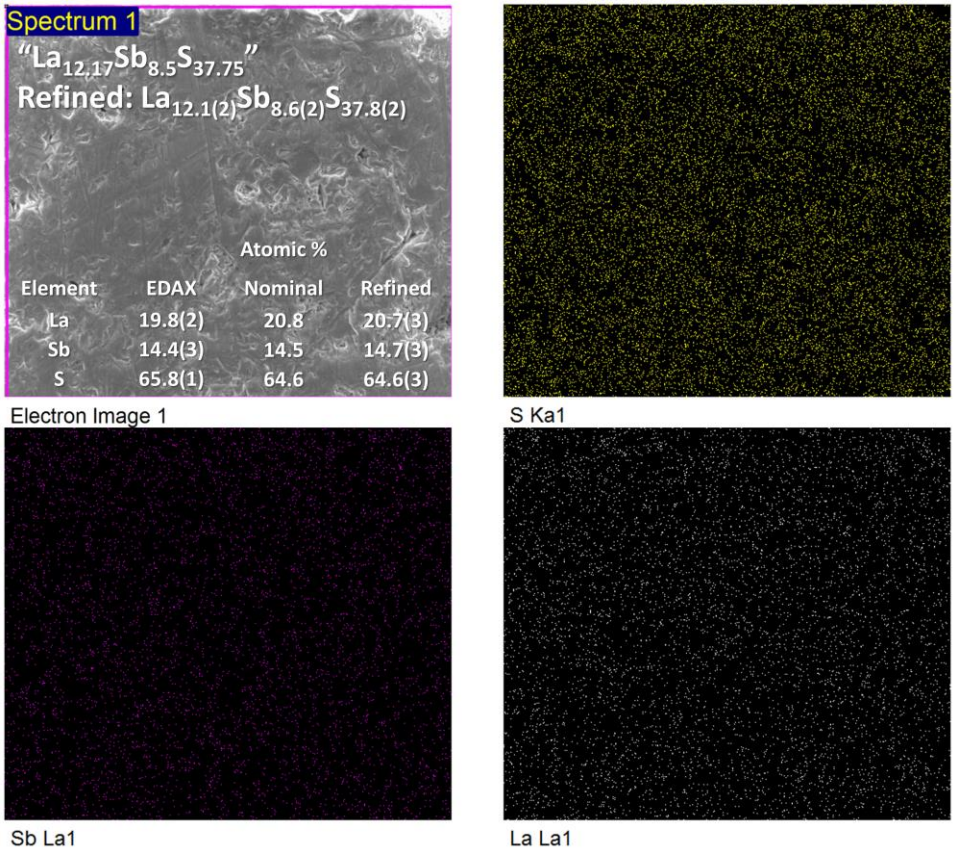

Figure A.9. SEM maps and EDAX results of the pellet of nominal composition $La_{12.17}Sb_{8.5}S_{37.5}$ in comparison to the formula obtained from the Rietveld refinement.

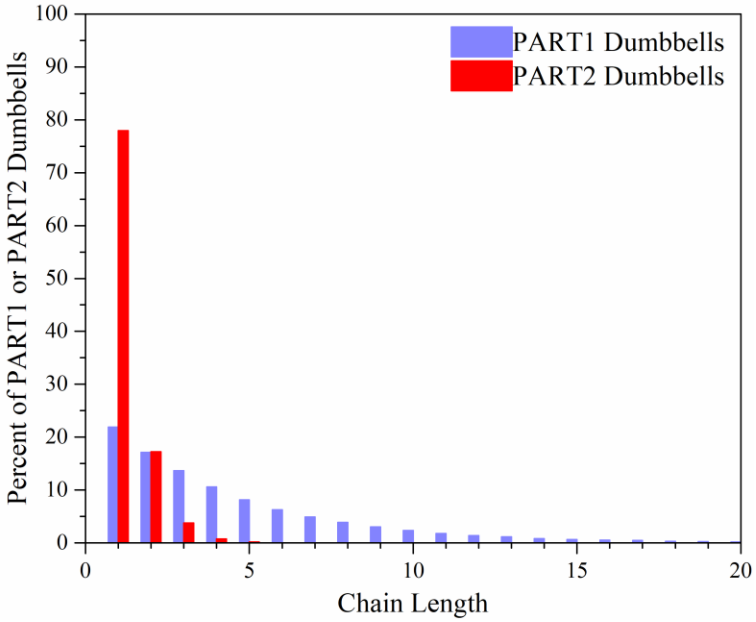

Figure A.10. The simulated number of consecutive Se_2^{2-} dumbbells in $Ba_6Ge_2Se_{12}$ in each orientation, when the occupancies of PART1 and PART2 are 78% and 22%, respectively.

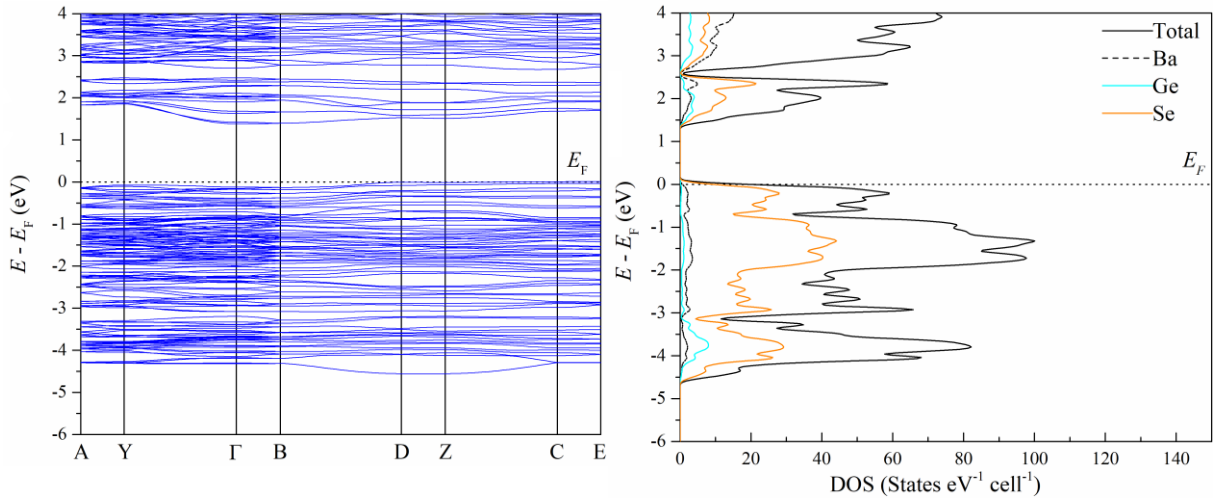

Figure A.11. Band structure (left) and DOS (right) of the $Ba_6Ge_2Se_{12}$ model with only the less occupied Se dumbbells occupied.

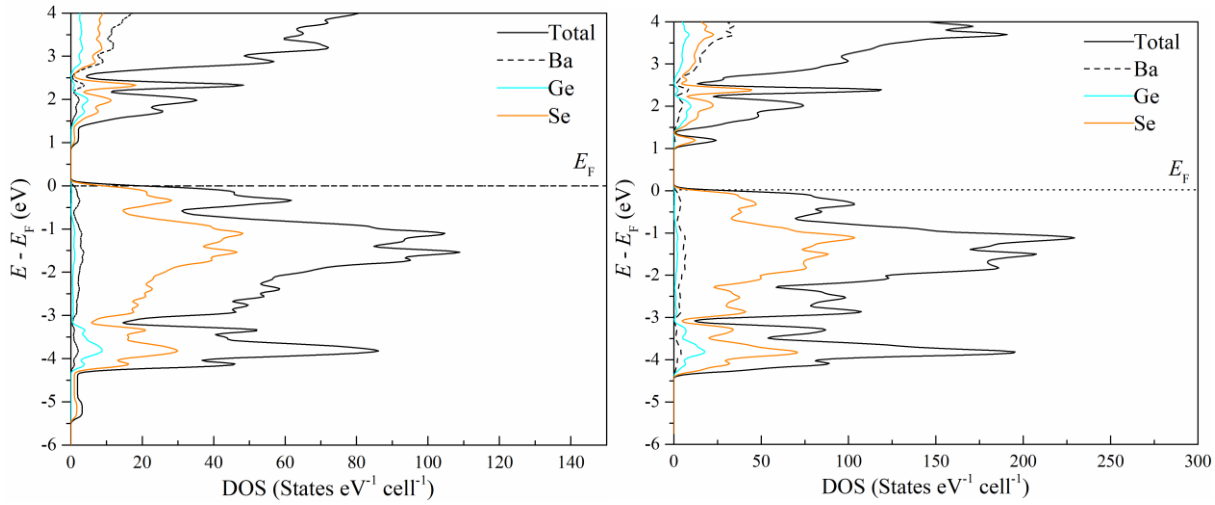

Figure A.12. DOS of the two $Ba_6Ge_2Se_{12}$ models. Left: the more highly occupied Se dumbbells; right: 2 × 1 × 1 supercell with 75% of Se atoms in the more highly occupied sites.

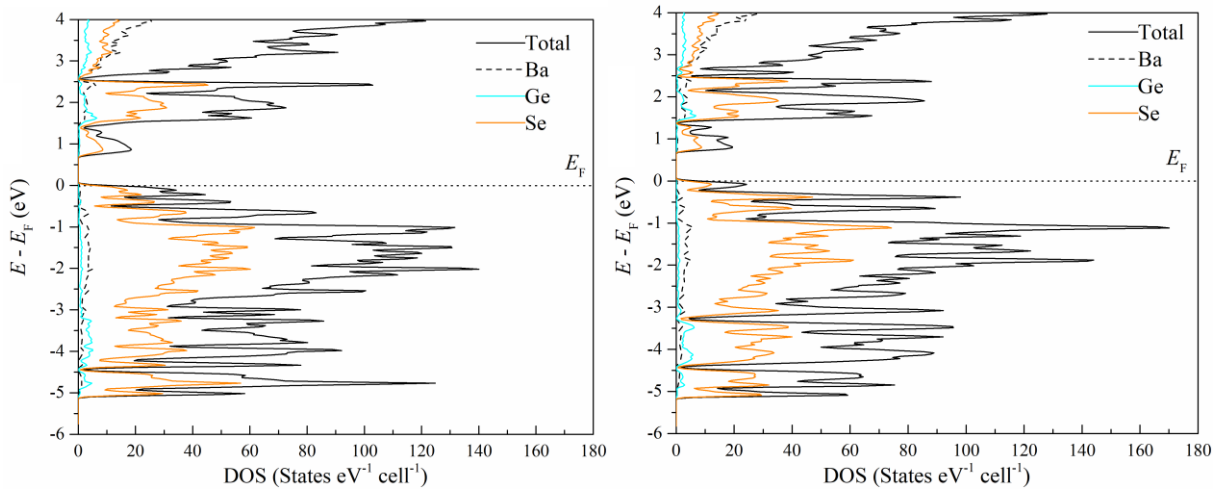

Figure A.13. DOS of the two $Ba_7Ge_2Se_{17}$ models. The more highly occupied $[GeSe_5]^{4-}$ anions are depicted on the left and the less occupied anions are on the rig

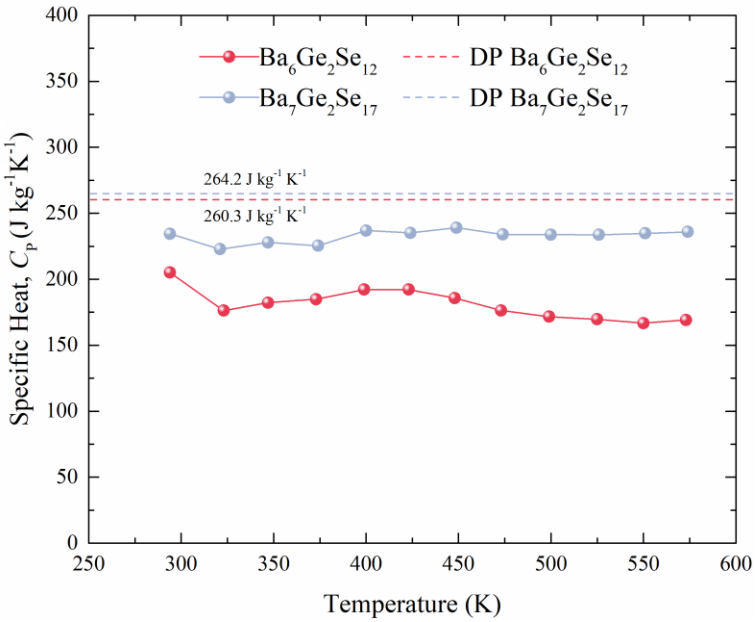

Figure A.14. C_P measurements of the $Ba_6Ge_2Se_{12}$ and $Ba_7Ge_2Se_{17}$ pellets, including the C_P calculated via the Dulong-Petit law.

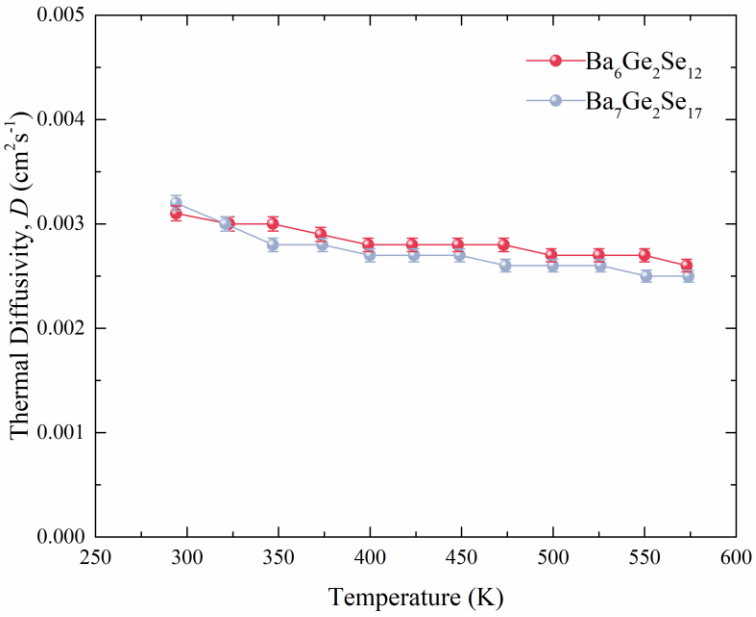

Figure A.15. Thermal diffusivity measurements of the $Ba_6Ge_2Se_{12}$ and $Ba_7Ge_2Se_{17}$ pellets. Error bars represent 2.3%.

Table A.3. Atomic positions, U_{eq} values and occupancy factors of $Ba_6Ge_2Se_{12}$ from sXRD.

Atom	Site	*x*	*y*	*z*	U_{eq} (Å^2)	occ.
Ba1	4*e*	0.00681(4)	0.49003(4)	0.21290(2)	0.01877(8)	1
Ba2	4*e*	0.02453(4)	0.29379(5)	0.04804(2)	0.02146(9)	1
Ba3	4*e*	0.24775(4)	0.43920(4)	0.37325(2)	0.02333(9)	1
Ba4	4*e*	0.25194(4)	0.80652(4)	0.09424(2)	0.02225(8)	1
Ba5	4*e*	0.48140(4)	0.29355(5)	0.04817(2)	0.02299(9)	1
Ba6	4*e*	0.54251(4)	0.40665(4)	0.22036(2)	0.01966(8)	1
Ge1	4*e*	0.24823(7)	0.03644(7)	0.41924(2)	0.01296(12)	1
Ge2	4*e*	0.25143(7)	0.16963(6)	0.17799(2)	0.01309(12)	1
Se1	4*e*	0.05259(7)	0.16360(8)	0.40523(3)	0.02176(14)	1
Se2	4*e*	0.05369(7)	0.05750(8)	0.15352(3)	0.02299(15)	1
Se4	4*e*	0.17844(6)	0.78368(7)	0.21645(2)	0.01572(12)	1
Se6	4*e*	0.25264(7)	0.53018(7)	0.00739(2)	0.01954(13)	1
Se7	4*e*	0.25812(7)	0.38983(7)	0.13479(2)	0.01841(13)	1
Se8	4*e*	0.26594(7)	0.19806(7)	0.26819(2)	0.01909(13)	1
Se9	4*e*	0.29839(7)	0.60546(7)	0.26194(3)	0.01948(13)	1
Se10	4*e*	0.43944(6)	0.04618(8)	0.14899(3)	0.02041(14)	1
Se11	4*e*	0.44415(7)	0.15471(8)	0.40064(3)	0.0290(2)	1
Se14	4*e*	0.76377(7)	0.32737(7)	0.12993(2)	0.01762(13)	1
Se3	4*e*	0.13277(2)	0.51382(13)	0.49553(5)	0.0596(5)	0.784(2)
Se12	4*e*	0.63187(2)	0.00840(14)	0.00802(4)	0.0611(5)	0.784(2)
Se5	4*e*	0.2519(4)	0.1085(4)	0.0152(2)	0.0449(13)	0.216(2)
Se13	4*e*	0.7530(3)	0.1053(3)	0.03081(14)	0.0242(8)	0.216(2)

Table A.4. Atomic positions, U_{eq} values and occupancy factors of $Ba_7Ge_2Se_{17}$ from the sXRD experiment.

Atom	Site	*x*	*y*	*z*	U_{eq} (Å^2)	occ.
Ba1	8*d*	0.12874(2)	0.14248(2)	0.74350(2)	0.01547(6)	1
Ba2	8*d*	0.37134(2)	0.10723(2)	0.02470(2)	0.01856(7)	1
Ba3	8*d*	0.38234(2)	0.11063(2)	0.48147(2)	0.01749(7)	1
Ba4	4*c*	0.12714(4)	¼	0.30548(4)	0.03053(1)	1
Se3	8*d*	0.12087(4)	0.58832(2)	0.25328(3)	0.01405(9)	1
Se7	8*d*	0.36331(4)	0.01982(2)	0.25367(3)	0.01450(9)	1
Se9	8*d*	0.37463(5)	0.19117(3)	0.25173(4)	0.02361(12)	1
Se10	4*c*	0.02767(6)	¼	0.55680(5)	0.01631(13)	1
Se11	4*c*	0.10348(9)	¼	0.00980(7)	0.0471(3)	1
Se12	4*c*	0.21927(5)	¼	0.56131(5)	0.01546(13)	1
Se13	4*c*	0.26256(7)	¼	0.90889(6)	0.0268(2)	1
Se14	4*c*	0.46901(7)	¼	0.61938(7)	0.0287(2)	1
Ge1	8*d*	0.17946(6)	0.02225(3)	0.27580(7)	0.01220(14)	0.809(1)
Se2	8*d*	0.11597(5)	0.10219(3)	0.14825(5)	0.01726(13)	0.809(1)
Se5	8*d*	0.12876(5)	0.07582(3)	0.43720(5)	0.0220(2)	0.809(1)
Se8	8*d*	0.37011(5)	0.55231(3)	0.47097(5)	0.01536(12)	0.809(1)
Ge2	8*d*	0.1800(3)	0.01807(2)	0.2260(3)	0.0135(6)	0.191(1)
Se1	8*d*	0.1109(2)	0.09897(1)	0.3516(2)	0.0169(6)	0.191(1)
Se4	8*d*	0.1242(2)	0.04981(1)	0.5280(2)	0.0155(5)	0.191(1)
Se6	8*d*	0.1322(2)	0.05544(1)	0.0542(2)	0.0206(6)	0.191(1)

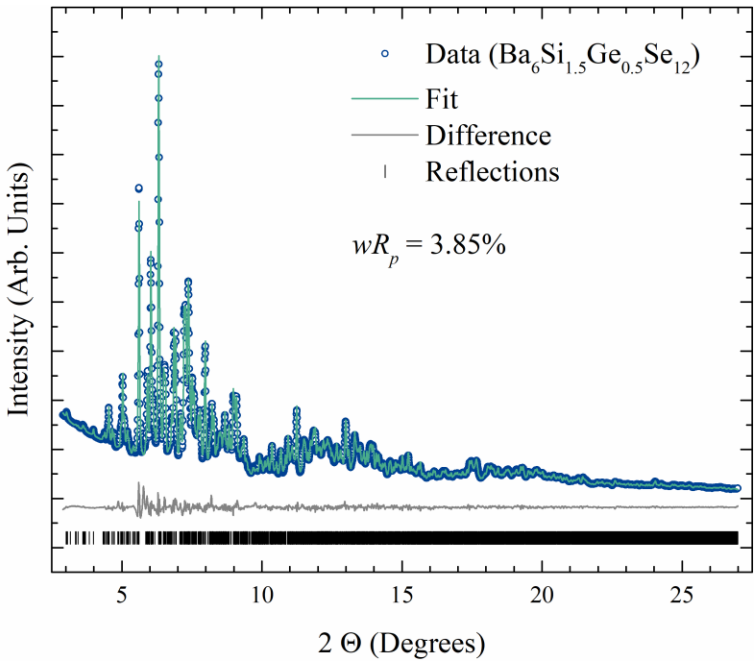

Figure A.16. Rietveld refinement plot for $Ba_6Si_{2-x}Ge_xSe_{12}$ for x = 0.5 including the Se4 and Se14 sites.

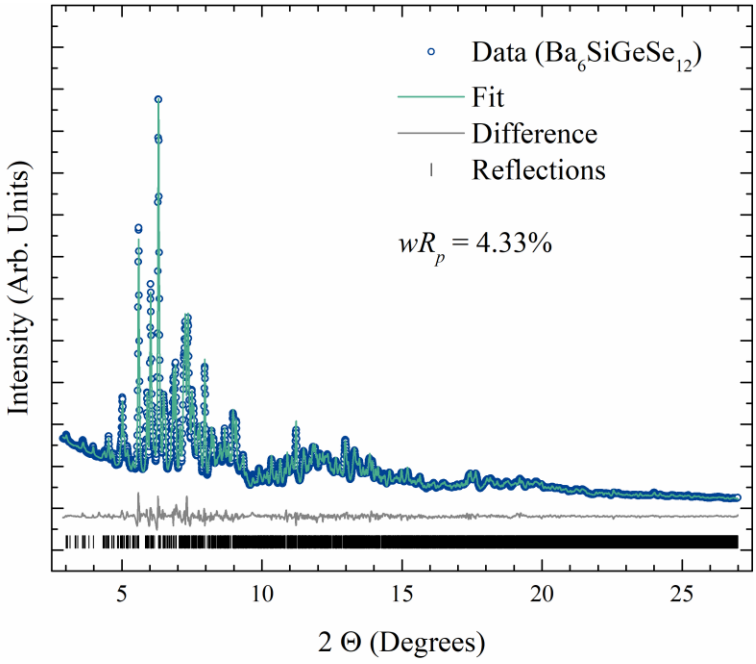

Figure A.17. Rietveld refinement plot for $Ba_6Si_{2-x}Ge_xSe_{12}$ for x = 1 including the Se4 and Se14 sites.

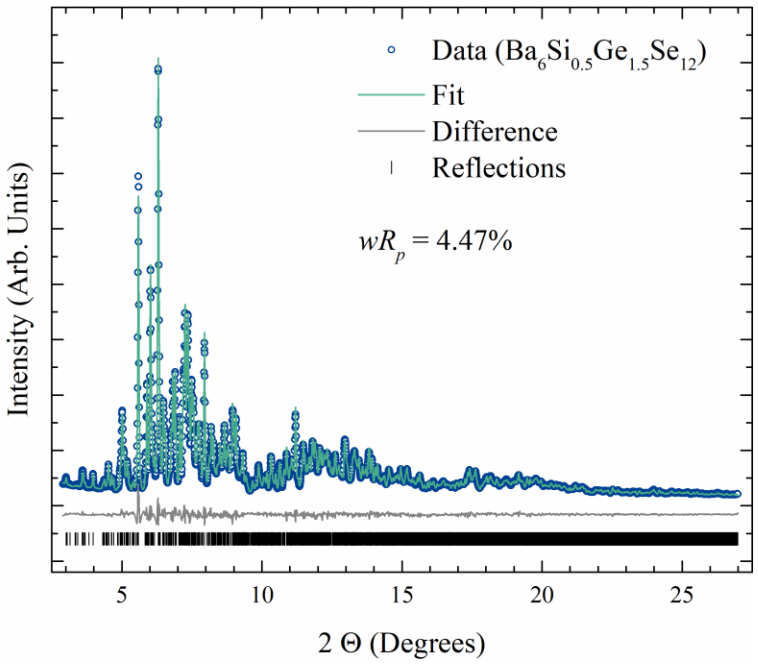

Figure A.18. Rietveld refinement plot for $Ba_6Si_{2-x}Ge_xSe_{12}$ for x = 1.5 including the Se4 and Se14 sites.

Table A.5. Rietveld refned atomic positions, U_{iso}, and occupancies of the $Ba_6Si_2Se_{12}$ sample.

Atom	Site	x	y	z	U_{iso} (Å^2)	occ.
Ba1	2*i*	0.0742(8)	0.3597(6)	0.6023(6)	0.0214(5)	1
Ba2	2*i*	0.0942(8)	0.9395(6)	0.1750(6)	0.0214(5)	1
Ba3	2*i*	0.2870(8)	0.5731(6)	0.0611(6)	0.0214(5)	1
Ba4	2*i*	0.3159(8)	0.3620(6)	0.3019(6)	0.0214(5)	1
Ba5	2*i*	0.3429(8)	0.0760(6)	0.5964(6)	0.0214(5)	1
Ba6	2*i*	0.6513(8)	0.1582(6)	0.1674(7)	0.0214(5)	1
Si1	2*i*	0.6138(20)	0.2807(16)	0.5265(16)	0.0115	1
Si2	2*i*	0.630(2)	0.7801(18)	0.0415(16)	0.0123	1
Se1	2*i*	0.0062(11)	0.2017(9)	0.3163(10)	0.0176(6)	1
Se2	2*i*	0.0039(11)	0.0703(11)	0.4197(10)	0.0176(6)	1
Se3	2*i*	0.0253(18)	0.3462(15)	0.0332(14)	0.023(3)	0.666(10)
Se5	2*i*	0.0760(19)	0.6071(16)	0.8090(14)	0.023(3)	0.666(10)

Se4	2*i*	0.001(4)	0.480(3)	0.165(3)	0.023(3)	0.334(10)
Se14	2*i*	0.946(4)	0.271(3)	0.083(3)	0.023(3)	0.334(10)
Se6	2*i*	0.2037(13)	0.2679(9)	0.8181(9)	0.0176(6)	1
Se7	2*i*	0.2241(12)	0.7849(9)	0.3482(9)	0.0176(6)	1
Se8	2*i*	0.2474(12)	0.0896(10)	0.0203(10)	0.0176(6)	1
Se9	2*i*	0.2662(12)	0.5945(10)	0.5446(9)	0.0176(6)	1
Se10	2*i*	0.4484(12)	0.1174(9)	0.3561(9)	0.0176(6)	1
Se11	2*i*	0.4645(12)	0.3611(10)	0.6314(10)	0.0176(6)	1
Se12	2*i*	0.4578(12)	0.8662(11)	0.1174(10)	0.0176(6)	1
Se13	2*i*	0.5127(13)	0.3875(10)	0.1222(10)	0.0176(6)	1

Table A.6. Rietveld refned atomic positions, U_{iso}, and occupancies of the $Ba_6Si_{1.5}Ge_{0.5}Se_{12}$ sample.

Atom	Site	x	y	z	U_{iso} (Å ^{2})	occ.
Ba1	2*i*	0.0764(7)	0.3609(5)	0.6008(5)	0.0179(4)	1
Ba2	2*i*	0.0939(7)	0.9385(5)	0.1758(5)	0.0179(4)	1
Ba3	2*i*	0.2867(7)	0.5760(5)	0.0575(5)	0.0179(4)	1
Ba4	2*i*	0.3160(7)	0.3609(5)	0.3025(6)	0.0179(4)	1
Ba5	2*i*	0.3432(7)	0.0747(5)	0.5973(5)	0.0179(4)	1
Ba6	2*i*	0.6541(7)	0.1604(5)	0.1708(6)	0.0179(4)	1
Si1	2*i*	0.6107(15)	0.2742(13)	0.5297(13)	0.0115	0.759(18)
Ge1	2*i*	0.6107(15)	0.2742(13)	0.5297(13)	0.0115	0.241(18)
Si2	2*i*	0.6350(16)	0.7813(14)	0.0371(13)	0.0123	0.741(18)
Ge2	2*i*	0.6350(16)	0.7813(14)	0.0371(13)	0.0123	0.259(18)
Se1	2*i*	0.0056(10)	0.1957(9)	0.3090(9)	0.0233(6)	1
Se2	2*i*	0.0066(10)	0.0719(10)	0.4208(9)	0.0233(6)	1
Se3	2*i*	0.0352(15)	0.3436(13)	0.0345(12)	0.0161(2)	0.650(8)

Se5	2*i*	0.0586(16)	0.6060(13)	0.8052(13)	0.0161(2)	0.650(8)
Se4	2*i*	0.042(3)	0.498(2)	0.187(2)	0.0161(2)	0.350(8)
Se14	2*i*	0.945(3)	0.288(2)	0.091(2)	0.0161(2)	0.350(8)
Se6	2*i*	0.2008(11)	0.2661(8)	0.8195(8)	0.0233(6)	1
Se7	2*i*	0.2350(11)	0.7894(8)	0.3518(8)	0.0233(6)	1
Se8	2*i*	0.2440(11)	0.0832(9)	0.0211(9)	0.0233(6)	1
Se9	2*i*	0.2592(11)	0.5912(9)	0.5350(8)	0.0233(6)	1
Se10	2*i*	0.4501(11)	0.1186(8)	0.3572(9)	0.0233(6)	1
Se11	2*i*	0.4607(11)	0.3619(9)	0.6304(9)	0.0233(6)	1
Se12	2*i*	0.4695(10)	0.8703(10)	0.1226(9)	0.0233(6)	1
Se13	2*i*	0.5147(12)	0.3896(9)	0.1223(10)	0.0233(6)	1

Table A.7. Rietveld refned atomic positions, U_{iso}, and occupancies of the $Ba_6SiGeSe_{12}$ sample.

Atom	Site	x	y	z	U_{iso} (Å^2)	occ.
Ba1	2*i*	0.0763(8)	0.3579(6)	0.5978(6)	0.0196(5)	1
Ba2	2*i*	0.0968(8)	0.9407(5)	0.1749(6)	0.0196(5)	1
Ba3	2*i*	0.2797(8)	0.5749(6)	0.0568(6)	0.0196(5)	1
Ba4	2*i*	0.3180(8)	0.3616(6)	0.3000(7)	0.0196(5)	1
Ba5	2*i*	0.3415(8)	0.0740(6)	0.5952(6)	0.0196(5)	1
Ba6	2*i*	0.6534(8)	0.1605(6)	0.1683(7)	0.0196(5)	1
Si1	2*i*	0.6139(14)	0.2794(12)	0.5297(12)	0.0115	0.49(2)
Ge1	2*i*	0.6139(14)	0.2794(12)	0.5297(12)	0.0115	0.51(2)
Si2	2*i*	0.6342(15)	0.7804(13)	0.0418(12)	0.0123	0.51(2)
Ge2	2*i*	0.6342(15)	0.7804(13)	0.0418(12)	0.0123	0.49(2)
Se1	2*i*	0.0106(11)	0.1993(9)	0.3133(10)	0.0203(6)	1
Se2	2*i*	0.0014(11)	0.0683(11)	0.4189(10)	0.0203(6)	1
Se3	2*i*	0.0354(18)	0.3484(15)	0.0413(14)	0.013(3)	0.615(9)
Se5	2*i*	0.0694(19)	0.6115(15)	0.8053(14)	0.013(3)	0.615(9)

Se4	2*i*	0.026(3)	0.488(2)	0.181(2)	0.013(3)	0.385(9)
Se14	2*i*	0.968(3)	0.284(2)	0.087(2)	0.013(3)	0.385(9)
Se6	2*i*	0.2000(13)	0.2688(10)	0.8184(10)	0.0203(6)	1
Se7	2*i*	0.2231(12)	0.7841(9)	0.3490(10)	0.0203(6)	1
Se8	2*i*	0.2438(12)	0.0851(9)	0.0222(10)	0.0203(6)	1
Se9	2*i*	0.2659(13)	0.5883(10)	0.5409(9)	0.0203(6)	1
Se10	2*i*	0.4531(12)	0.1197(9)	0.3571(9)	0.0203(6)	1
Se11	2*i*	0.4573(12)	0.3642(9)	0.6333(10)	0.0203(6)	1
Se12	2*i*	0.4583(11)	0.8671(10)	0.1172(10)	0.0203(6)	1
Se13	2*i*	0.5168(13)	0.3936(10)	0.1209(10)	0.0203(6)	1

Table A.8. Rietveld refned atomic positions, U_{iso}, and occupancies of the $Ba_6Si_{0.5}Ge_{1.5}Se_{12}$ sample.

Atom	Site	x	y	z	U_{iso} (Å^2)	occ.
Ba1	2*i*	0.0779(6)	0.3600(4)	0.5985(4)	0.0177(3)	1
Ba2	2*i*	0.0945(6)	0.9395(4)	0.1766(5)	0.0177(3)	1
Ba3	2*i*	0.2802(6)	0.5755(4)	0.0557(5)	0.0177(3)	1
Ba4	2*i*	0.3173(6)	0.3621(4)	0.3015(5)	0.0177(3)	1
Ba5	2*i*	0.3443(6)	0.0739(4)	0.5965(5)	0.0177(3)	1
Ba6	2*i*	0.6532(6)	0.1596(4)	0.1678(5)	0.0177(3)	1
Si1	2*i*	0.6121(10)	0.2766(8)	0.5305(8)	0.0115	0.201(14)
Ge1	2*i*	0.6121(10)	0.2766(8)	0.5305(8)	0.0115	0.799(14)
Si2	2*i*	0.6372(11)	0.7803(9)	0.0428(9)	0.0123	0.299(14)
Ge2	2*i*	0.6372(11)	0.7803(9)	0.0428(9)	0.0123	0.701(14)
Se1	2*i*	0.0071(9)	0.2005(7)	0.3124(7)	0.0216(5)	1
Se2	2*i*	0.0062(8)	0.0715(8)	0.4207(8)	0.0216(5)	1
Se3	2*i*	0.0400(14)	0.3444(12)	0.0372(11)	0.017(2)	0.604(8)

Se5	2*i*	0.0588(15)	0.6087(12)	0.8036(12)	0.017(2)	0.604(8)
Se4	2*i*	0.032(2)	0.4929(16)	0.1827(18)	0.017(2)	0.396(8)
Se14	2*i*	0.958(2)	0.2926(17)	0.0827(17)	0.017(2)	0.396(8)
Se6	2*i*	0.1984(10)	0.2686(7)	0.8194(7)	0.0216(5)	1
Se7	2*i*	0.2262(9)	0.7889(7)	0.3515(7)	0.0216(5)	1
Se8	2*i*	0.2424(10)	0.0830(7)	0.0196(8)	0.0216(5)	1
Se9	2*i*	0.2610(9)	0.5895(8)	0.5390(7)	0.0216(5)	1
Se10	2*i*	0.4534(10)	0.1211(7)	0.3551(7)	0.0216(5)	1
Se11	2*i*	0.4588(10)	0.3640(7)	0.6368(8)	0.0216(5)	1
Se12	2*i*	0.4646(9)	0.8682(8)	0.1201(7)	0.0216(5)	1
Se13	2*i*	0.5153(10)	0.3951(7)	0.1209(8)	0.0216(5)	1

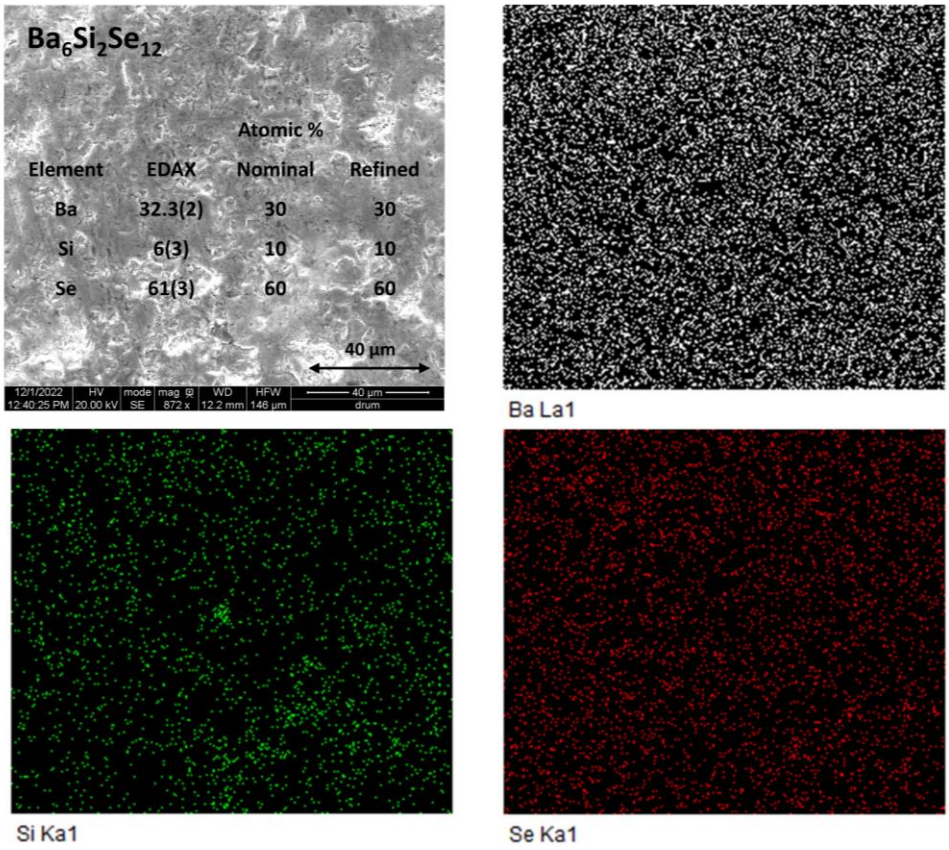

Figure A.19. EDAX and elemental mapping of hot-pressed $Ba_6Si_2Se_{12}$ pellet.

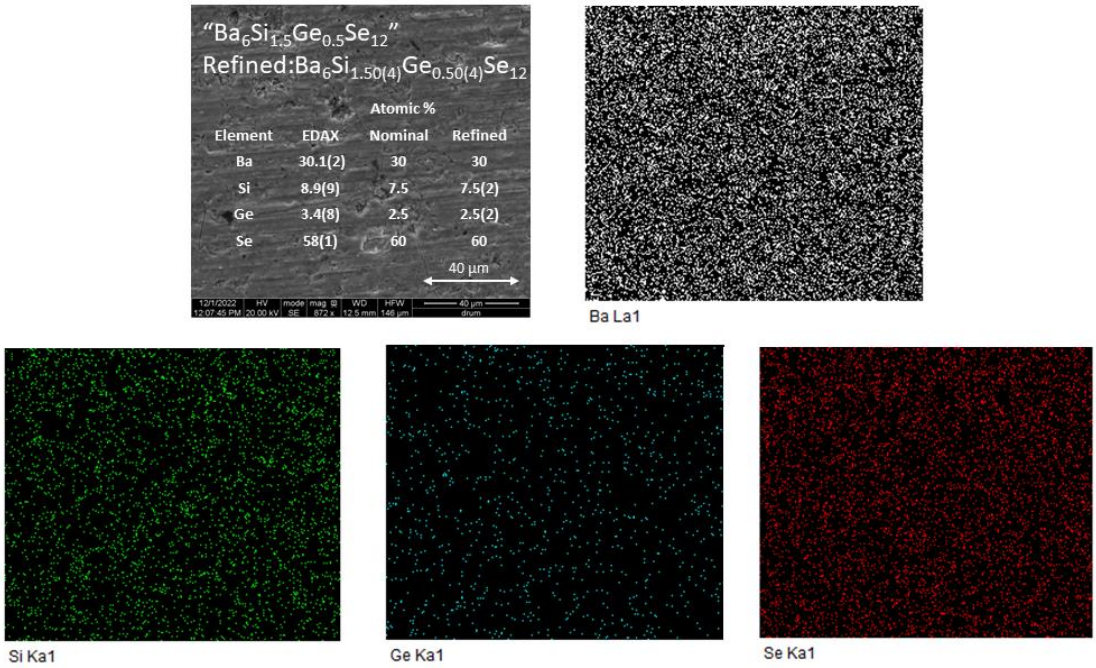

Figure A.20. EDAX and elemental mapping of hot-pressed $Ba_6Si_{1.5}Ge_{0.5}Se_{12}$ pellet.

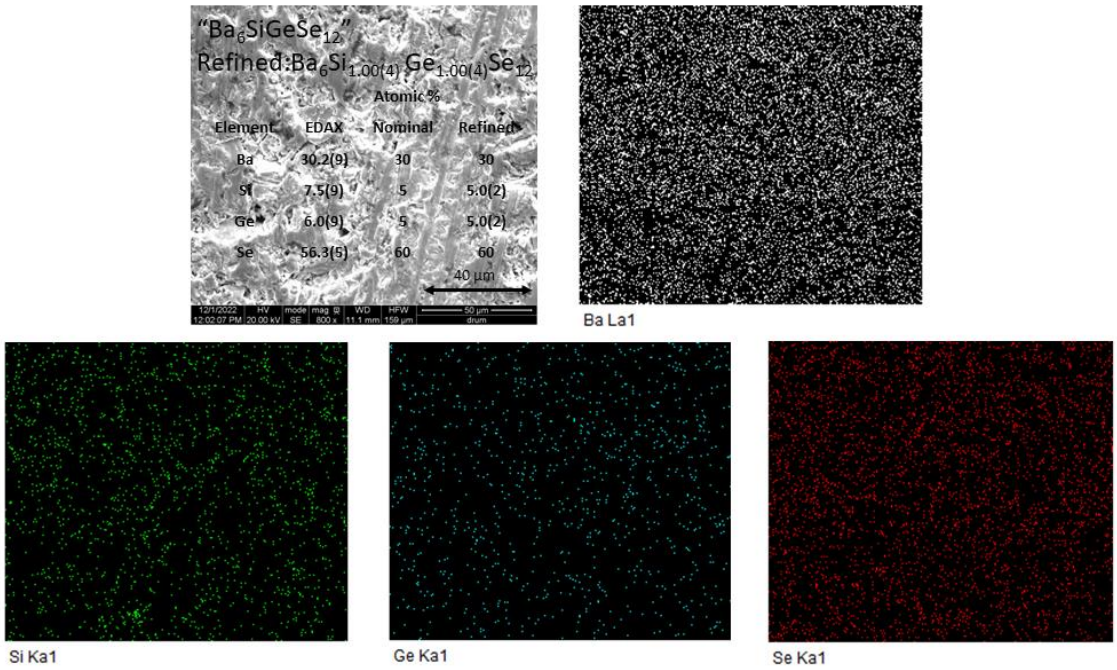

Figure A.21. EDAX and elemental mapping of hot-pressed $Ba_6SiGeSe_{12}$ pellet.

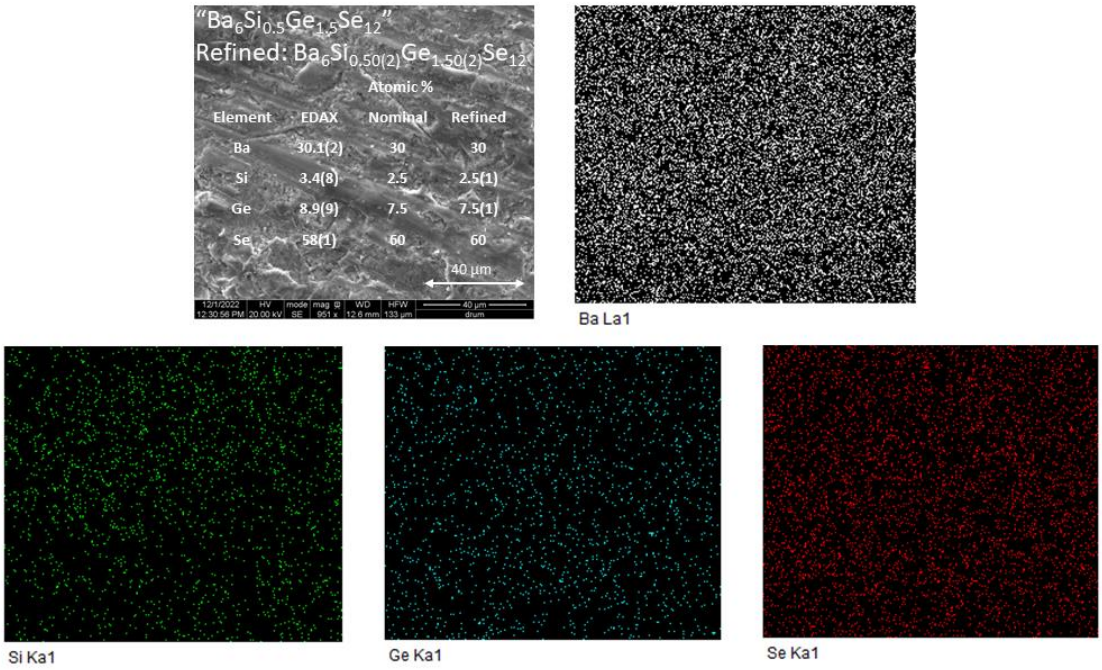

Figure A.22. EDAX and elemental mapping of hot-pressed $Ba_6Si_{0.5}Ge_{1.5}Se_{12}$ pellet.

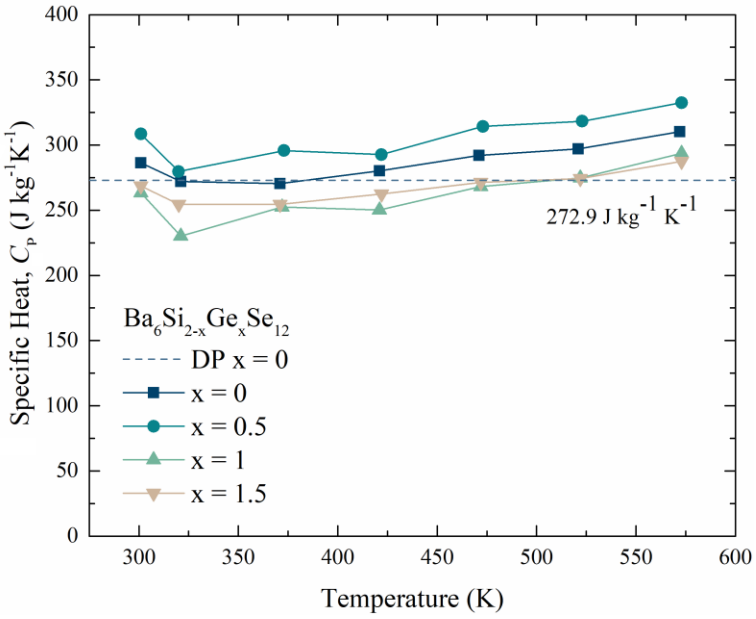

Figure A.23. Specific heat capacity curves of the $Ba_6Si_{2-x}Ge_xSe_{12}$ samples and the Dulong-Petit limit of $Ba_6Si_2Se_{12}$.

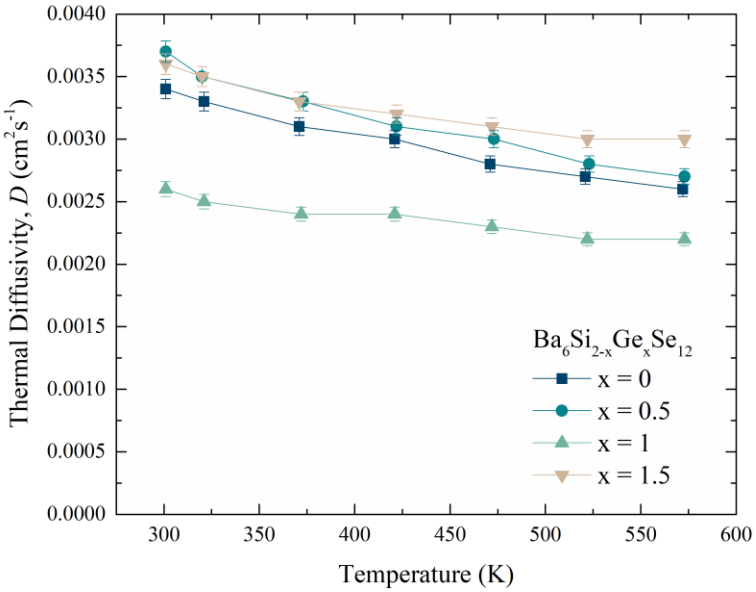

Figure A.24. Thermal diffusivity curves of the $Ba_6Si_{2-x}Ge_xSe_{12}$ samples.

Table A.9. Atomic positions, U_{iso} values of of $Sr_8Ge_4Se_{17}$ from the Rietveld refinement. All sites are 100% occupied.

Atom	Site	*x*	*y*	*z*	U_{iso} (Å^2)
Sr1	2*i*	0.1499(13)	0.7423(13)	0.2337(10)	0.0190(11)
Sr2	2*i*	0.1519(12)	0.0610(12)	0.7921(12)	0.0190(11)
Sr3	2*i*	0.1853(11)	0.3113(13)	0.3171(11)	0.0190(11)
Sr4	2*i*	0.3333(14)	0.2538(13)	0.5859(11)	0.0190(11)
Sr5	2*i*	0.3366(13)	0.0007(12)	0.0696(10)	0.0190(11)
Sr6	2*i*	0.3492(12)	0.4689(13)	0.0765(12)	0.0190(11)
Sr7	2*i*	0.6456(13)	0.2294(12)	0.4592(10)	0.0190(11)
Sr8	2*i*	0.8022(13)	0.4113(13)	0.1995(12)	0.0190(11)
Ge1	2*i*	0.0108(14)	0.2135(13)	0.0309(12)	0.0025(13)
Ge2	2*i*	0.0216(13)	0.8124(14)	0.4737(12)	0.0025(13)
Ge3	2*i*	0.4969(14)	0.8253(14)	0.1879(13)	0.0025(13)
Ge4	2*i*	0.5027(14)	0.3823(14)	0.3061(13)	0.0025(13)
Se1	2*i*	0.0655(15)	0.4284(14)	0.0496(14)	0.0196(10)
Se2	2*i*	0.0596(18)	0.6410(18)	0.4987(15)	0.037(5)
Se3	2*i*	0.0866(15)	0.1097(15)	0.4041(13)	0.0196(10)
Se4	2*i*	0.1099(13)	0.2734(14)	0.7112(13)	0.0196(10)
Se5	2*i*	0.1014(14)	0.9371(16)	0.1582(13)	0.0196(10)
Se6	2*i*	0.0999(15)	0.5401(15)	0.3286(13)	0.037(5)
Se7	2*i*	0.1991(14)	0.1867(14)	0.0572(12)	0.0196(10)
Se8	2*i*	0.2937(15)	0.5082(14)	0.5823(12)	0.0196(10)
Se9	2*i*	0.3099(15)	0.7217(14)	0.0630(12)	0.0196(10)
Se10	2*i*	0.4000(14)	0.2088(15)	0.3412(12)	0.0196(10)

Se11	2*i*	0.4052(14)	0.5395(15)	0.3344(12)	0.0196(10)
Se12	2*i*	0.5007(14)	0.2995(14)	0.1271(14)	0.0196(10)
Se13	2*i*	0.5435(14)	0.1232(17)	0.6350(13)	0.0196(10)
Se14	2*i*	0.6065(14)	0.0194(15)	0.1765(12)	0.0196(10)
Se15	2*i*	0.6135(14)	0.6906(14)	0.1589(12)	0.0196(10)
Se16	2*i*	0.7767(15)	0.0555(14)	0.4886(12)	0.0196(10)
Se17	2*i*	0.9065(14)	0.1833(14)	0.1595(12)	0.0196(10)

Table A.10. Atomic positions, U_{iso} values of $Ba_8Sn_4Se_{17}$ from the Rietveld refinement. All sites are 100% occupied.

Atom	Site	*x*	*y*	*z*	U_{iso} (Å^2)
Ba1	8*f*	0.0318(5)	0.2959(18)	0.4701(9)	0.0269(12)
Ba2	8*f*	0.0391(6)	0.2565(20)	0.2205(10)	0.0269(12)
Ba3	8*f*	0.0811(6)	-0.0127(20)	0.1009(11)	0.0269(12)
Ba4	8*f*	0.0853(6)	0.4765(23)	0.1120(11)	0.0269(12)
Ba5	8*f*	0.0856(6)	0.0176(22)	0.3649(11)	0.0269(12)
Ba6	8*f*	0.1648(5)	0.2544(18)	0.1466(11)	0.0269(12)
Ba7	8*f*	0.1653(6)	0.2282(20)	0.4045(10)	0.0269(12)
Ba8	8*f*	0.2099(5)	0.0076(19)	0.2875(11)	0.0269(12)
Ba9	8*f*	0.2086(6)	0.4804(22)	0.0314(11)	0.0269(12)
Ba10	8*f*	0.2117(6)	0.0062(21)	0.0352(11)	0.0269(12)
Ba11	8*f*	0.2121(5)	0.4635(20)	0.2872(12)	0.0269(12)
Ba12	8*f*	0.3302(6)	0.2358(22)	0.3511(10)	0.0269(12)
Ba13	8*f*	0.3350(6)	0.2151(19)	0.1249(10)	0.0269(12)
Ba14	8*f*	0.4175(6)	0.0137(21)	0.1550(11)	0.0269(12)

Ba15	8*f*	0.4545(6)	0.2682(22)	0.0435(11)	0.0269(12)
Ba16	8*f*	0.4592(7)	0.2935(21)	0.2814(11)	0.0269(12)
Sn1	8*f*	0.0020(6)	0.0122(20)	0.4073(11)	0.0032(13)
Sn2	8*f*	0.1242(5)	0.3091(20)	0.2674(10)	0.0032(13)
Sn3	8*f*	0.2514(6)	0.2383(20)	0.1570(10)	0.0032(13)
Sn4	8*f*	0.2496(6)	0.2269(20)	0.4029(10)	0.0032(13)
Sn5	8*f*	0.3694(6)	0.3103(22)	0.0171(10)	0.0032(13)
Sn6	8*f*	0.3771(6)	0.4310(19)	0.2501(10)	0.0032(13)
Sn7	8*f*	0.3790(5)	0.0444(21)	0.5127(10)	0.0032(13)
Sn8	8*f*	0.5064(6)	0.0246(20)	0.1478(10)	0.0032(13)
Se1	8*f*	0.0094(7)	0.0385(30)	0.3149(14)	0.0201(17)
Se2	8*f*	0.0224(7)	0.1717(25)	0.5837(12)	0.0201(17)
Se3	8*f*	0.0240(7)	0.3639(26)	0.3357(12)	0.0201(17)
Se4	8*f*	0.0294(7)	0.1694(25)	0.0818(12)	0.0201(17)
Se5	8*f*	0.0514(8)	0.0320(23)	0.4679(13)	0.0201(17)
Se6	8*f*	0.0754(7)	0.0272(24)	0.2285(12)	0.0201(17)
Se7	8*f*	0.0961(7)	0.2604(24)	0.3326(13)	0.0201(17)
Se8	8*f*	0.0988(7)	0.2330(27)	0.1732(14)	0.0201(17)
Se9	8*f*	0.1038(7)	0.2137(31)	0.0568(13)	0.0201(17)
Se10	8*f*	0.1043(7)	0.2696(28)	0.4862(13)	0.007(6)
Se11	8*f*	0.1390(7)	0.0055(29)	0.4839(15)	0.0201(17)
Se12	8*f*	0.1384(6)	0.5053(25)	0.2855(12)	0.007(6)
Se13	8*f*	0.1497(6)	0.4838(23)	0.4239(13)	0.0201(17)
Se14	8*f*	0.1518(7)	0.4950(24)	0.0834(13)	0.0201(17)
Se15	8*f*	0.1739(7)	0.2367(25)	0.2800(12)	0.0201(17)
Se16	8*f*	0.1819(7)	0.2427(25)	0.0059(12)	0.0201(17)

Se17	8*f*	0.2215(7)	0.0761(25)	0.1654(12)	0.0201(17)
Se18	8*f*	0.2214(7)	0.3998(26)	0.4191(13)	0.0201(17)
Se19	8*f*	0.2254(7)	0.3999(26)	0.1645(13)	0.0201(17)
Se20	8*f*	0.2246(7)	0.0629(26)	0.4206(12)	0.0201(17)
Se21	8*f*	0.2534(6)	0.2284(25)	0.3063(14)	0.0201(17)
Se22	8*f*	0.2600(7)	0.2133(31)	0.0673(14)	0.0201(17)
Se23	8*f*	0.3008(7)	0.2368(23)	0.2193(12)	0.0201(17)
Se24	8*f*	0.3017(7)	0.2433(23)	0.4622(11)	0.0201(17)
Se25	8*f*	0.3462(7)	0.4790(23)	0.1578(13)	0.0201(17)
Se26	8*f*	0.3491(7)	0.4928(23)	0.3208(13)	0.0201(17)
Se27	8*f*	0.3491(7)	-0.0018(24)	0.2994(11)	0.007(6)
Se28	8*f*	0.3875(8)	0.2426(29)	0.2562(17)	0.0201(17)
Se29	8*f*	0.4026(6)	0.2597(24)	0.1090(13)	0.0201(17)
Se30	8*f*	0.4034(7)	0.2339(24)	0.4283(12)	0.007(6)
Se31	8*f*	0.4308(7)	0.0212(24)	0.0281(12)	0.0201(17)
Se32	8*f*	0.4464(8)	0.0246(23)	0.2868(12)	0.0201(17)
Se33	8*f*	0.4759(7)	0.1783(25)	0.1723(12)	0.0201(17)
Se34	8*f*	0.5130(7)	0.0164(26)	0.0525(13)	0.0201(17)

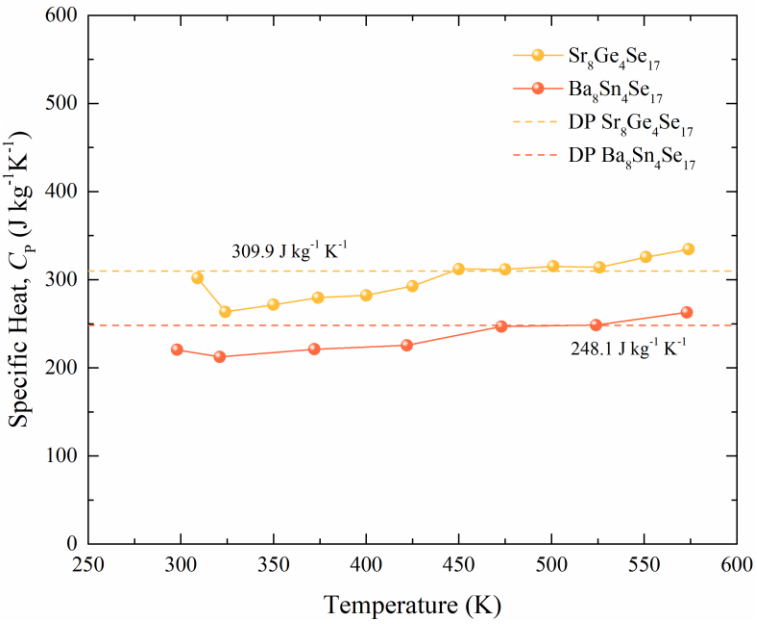

Figure A.25. Temperature dependent specific heat (C_P) plot of $Sr_8Ge_4Se_{17}$ and $Ba_8Sn_4Se_{17}$ along with the Dulong-Petit limits (DP).

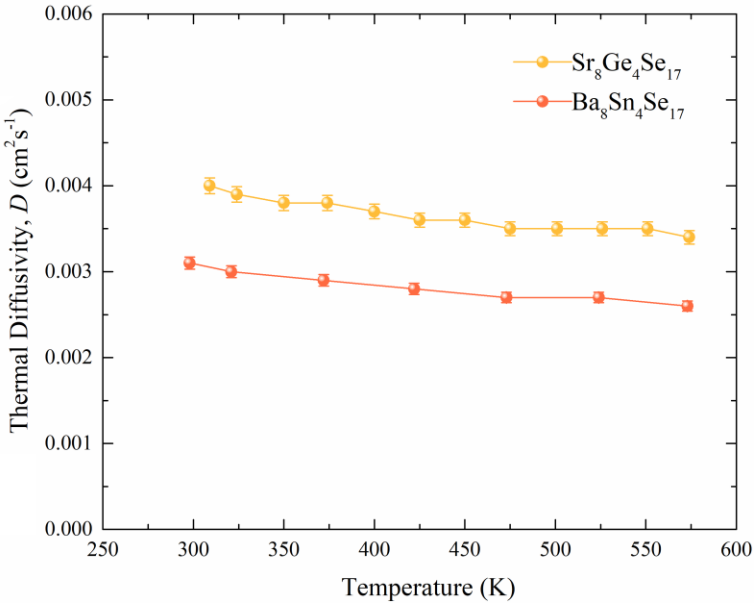

Figure A.26. Temperature dependent thermal diffusivity (D) plot of $Sr_8Ge_4Se_{17}$ and $Ba_8Sn_4Se_{17}$.

NLO calculations.

The non-linear optical susceptibility tensor for *3m* is:

$$\begin{bmatrix} 0 & 0 & 0 & 0 & d_{15} & -d_{22} \\ -d_{22} & d_{22} & 0 & d_{15} & 0 & 0 \\ d_{15} & d_{15} & d_{33} & 0 & 0 & 0 \end{bmatrix}$$

The d_{eff} expression for *mm*2 symmetry under Kleinman symmetry ($d_{15} = d_{31}$) is:

$$\langle (d_{eff})^2 \rangle = \frac{19}{105}(d_{33})^2 + \frac{26}{105}(d_{33}d_{15}) + \frac{144}{105}(d_{15})^2 + \frac{10}{21}(d_{22})^2$$

Table A.11. Atomic Positions and U_{eq} values of $Sr_6Ge_3OSe_{11}$ from the sXRD Measurement. All sites are 100% occupied.

Atom	Site	*x*	*y*	*z*	U_{eq} (Å^2)
Sr1	3*d*	0.13583(2)	0.86417(2)	0.60364(8)	0.01504(9)
Sr2	3*d*	0.50918(2)	0.49082(2)	0.03806(7)	0.01527(10)
Ge1	1*c*	2/3	1/3	0.60970(12)	0.00968(16)
Ge2	1*b*	1/3	2/3	0.38771(12)	0.00939(16)
Ge3	1*a*	0	0	0.00000(12)	0.00938(16)
O1	1*a*	0	0	0.7141(8)	0.0093(10)
Se1	3*d*	0.12727(2)	0.87273(2)	0.10399(8)	0.01438(10)
Se2	3*d*	0.45740(2)	0.54260(2)	0.51109(7)	0.01201(10)
Se3	3*d*	0.79157(3)	0.20843(3)	0.74914(7)	0.01195(10)
Se4	1*c*	2/3	1/3	0.24591(12)	0.01392(17)
Se5	1*b*	1/3	2/3	0.01711(12)	0.01222(16)

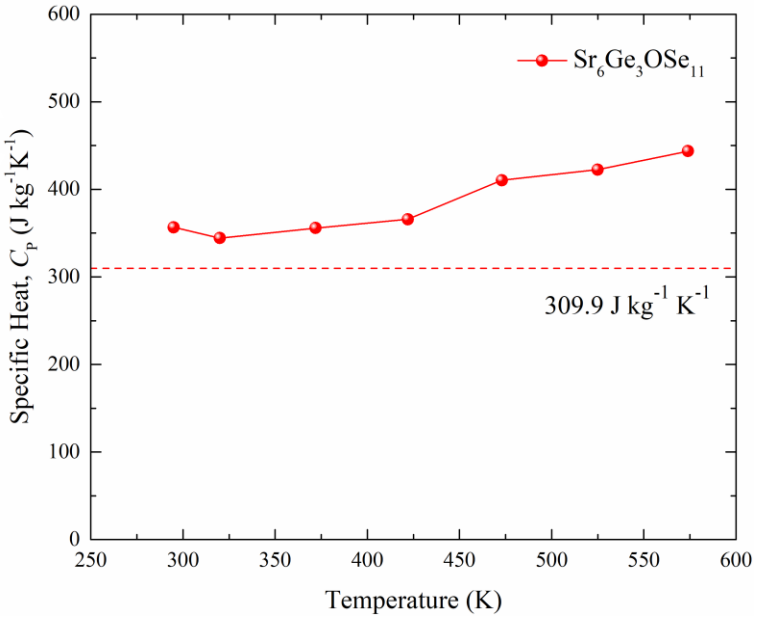

Figure A.27. Specific heat (C_P) measurements of hot-pressed $Sr_6Ge_3OSe_{11}$ pellets up to 573 K. The theoretical Dulong-Petit limit is represented by a red dashed line.

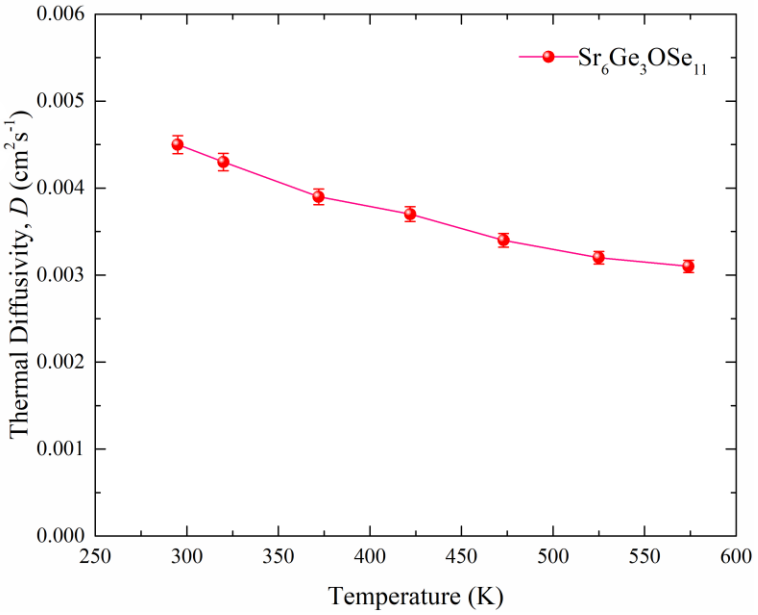

Figure A.28. Thermal diffusivity (D) measurements of hot-pressed $Sr_6Ge_3OSe_{11}$ pellets up to 573. Error bars represent 2.3%.